研究課題名：FEL による物質の光誘起構造変化・光誘起価数変化の研究と フォトメモリー材料開発への応用

研究代表者:望月　章介(日本大学文理学部物理学科)
共同研究者:浅地　哲夫(日本大学文理学部化学科)

【研究目的】

最近，我々の研究グループで酸化物の固体，薄膜，ナノ粒子膜が紫外レーザー光照射下での雰囲気交換(酸素→真空)に伴ってフォトルミネッセンス色が可逆的変化し，変化した状態はレーザー光を照射しなければ室内灯の下で如何なる雰囲気交換によっても永久的に保存される事を発見した．本研究はこれらの研究を基礎にして，室温で安定に起こる可逆(消去可能)なレーザー光誘起物性変化現象を示す物質の探索及び創製とこれら物質表面へのナノメートルサイズのカラードット記録について以下の研究を行う．

(1) 紫外レーザー光の照射で発光色が赤色から白色，青色から白色等に永久的に転移し(情報の記録に対応)，この転移が別の波長のレーザー光や異なる雰囲気での紫外レーザー光照射で元の発光色に戻せる(記録された情報の消去に対応)如くの性質を有する光メモリー物質を探索・創製する．

(2) 創製された光メモリー物質表面に情報を近接場光学顕微装置と結合させて，ナノメートルサイズの赤・青・白他のカラードット列として情報を超高密度記録する方法を確立する．

【研究概要】

①カラーフォトメモリー物質の探索・創製
紫外レーザー光で金属イオンの価数変化・酸素欠陥生成でフォトルミネッセンス色の変化が期待できる**金属酸化物やその複合体**，層間に種々の分子層を挿入して制御可能な多様なフォトルミネッセンス特性が期待できる**層状ペロブスカイト化合物**，また，電場発光も期待できる**有機化合物**等に着目して．レーザー光誘起発光色変化現象を研究する．

②レーザー光による分裂・融合・構造変化を含む転移の過渡現象を**計算機シミュレーション**によって解明する．

③近接場光学顕微分光装置との結合によるナノサイズカラードット列の記録
ナノメートル空間分解能近接場光学顕微分光装置により，創製した物質の表面に**ナノメーターサイズの赤・青・白他のカラードット列として情報を記録する実験**を行う．

その結果は以下のとおりである．

(1)希土類金属酸化物のカラーフォトメモリー現象のダイナミクスの研究

酸化ユーロピウム Eu_2O_3，酸化サマリウム Sm_2O_3 について，これまでの研究に続いてフォトルミネッセンススペクトルとラマン散乱スペクトルを詳細に測定し，レーザー光子場と物質との励起エネルギーのやり取りとしてカラーフォトメモリー現象のダイナミクスを研究した．この研究成果の一部は本年５月にフランス国 Rennes University 1 で開催される光誘起相転移に関する国際会議 the Second International Conference on Photo-Induced Phase Transitions Cooperative, non- linear and functional properties で下記の論文として公表する予定である．

Shosuke Mochizuki,Fumito Fujishiro,Ken'ichiro Ishiwata: Photo-induced valence-number changes and defects in Eu_2O_3

ほかに，γAl_2O_3-Eu_2O_3, AgI-anatase TiO_2, silica glass についてもカラーフォトメモリー現象を発

見し，そのダイナミクスを研究した.

(2)光触媒・量子常誘電体 $SrTiO_3$ のフォトメモリー現象の研究

光触媒性や量子常誘電性で興味が持たれているチタン酸ストロンチウム $SrTiO_3$ のフォトメモリー現象とフォトルミネッセンス現象の起源を研究し, この物質について初めて紫外レーザー光誘起フォトメモリー現象を発見した. そして, 従来この物質の量子常誘電性と関連付けて議論されていたフォトルミネッセンスは, この物質特有の結晶欠陥構造と化学的ヘテロ性に起源を持つ発光であることを明らかにした. この研究の概要は以下のとおりである.

無色透明なチタン酸ストロンチウム $SrTiO_3$ 単結晶試料が室温で真空中にて 325nm レーザー光で照射されると，2.4eV を中心とする幅広い発光帯がその発光強度を増大させる. この強い発光状態はレーザー光の照射が無ければ, 室内灯の下で如何なる雰囲気でも長期間保存される. 試料雰囲気を酸素ガスにすると，かかる紫外レーザー光の下で発光強度を弱めつつ，元の発光状態に戻る. このようなレーザー光誘起現象は低温 13K でも観測され，現象は純粋に $SrTiO_3$ 結晶の電子系の励起に関係したものであることを示している. この実験は，$SrTiO_3$ の as-grown 結晶やこれを $Ar\text{-}H_2$ 雰囲気中，973K でアニールして，無色透明結晶に至る過程についても行われた. 観測された現象は SrTiO3 結晶表面付近での，紫外レーザー光に誘起された光還元・光酸化として理解される. これらの研究成果より，この $SrTiO_3$ 結晶の表面を発光物質で修飾すると，新しいカラーフォトメモリー物質が創製できる可能性があることが分かった.

これまで $SrTiO_3$ 結晶については，2.4eV 発光が知られていたが，本研究ではこの物質のバンドギャップ以上のエネルギーの光，Nd^{3+}-YAG レーザーの第 3 高調波 355nm の励起で 2.4eV 発光のほかに 3.2eV を中心とするバンド端近傍発光と 2.9eV を中心とする A バンド発光を発見した. 2.4eV 発光は数秒まで続く長寿命残光性発光を特徴とするが，新しく見つけられた二つの発光は光励起後 50ns 以内に消滅してしまう短寿命妙発光であることが分かった. また，フォトルミネッセンスの励起レーザー光強度依存性を測定すると，2.4eV 発光は $4mJ/cm^2$ で最大値をとり，それ以上の対励起では発光効率は減少し始めるが， 3.2eV および 2.9eV 発光はどこまでも線形的に増え続けることが分かった. これは，2.4eV 発光がこれまで内外の研究者が主張してきた量子常誘電性に起源を持つ真性自己束縛励起子であることを否定する新事実である.

(3)超イオン導電体 AgI-anatase TiO_2, AgI-ZrO_2 のフォトメモリー現象の研究

すでに超イオン導電体 AgI-anatase TiO_2 の光誘起スペクトル変化の発見については論文で公表してあるが，今年度の研究ではこの詳細について実験すると伴に，同じ超イオン導電体の AgI-ZrO_2 を作製し，光メモリー性を研究した. この物質は室温で真空中にて 325nm レーザー光で照射されると，2.6eV を中心とする幅広い発光帯がその発光幅を増大させる. この幅広い発光状態はレーザー光の照射が無ければ, 室内灯の下で如何なる雰囲気でも長期間保存される. 試料雰囲気を酸素ガスにすると，かかる紫外レーザー光の下で，元の発光状態に戻る. このようなレーザー光誘起現象は低温 13K でも観測され，現象は純粋に ZrO_2 の電子系の励起に関係したものであることを示している.

また，この超イオン導電体の基礎材料の AgI の薄膜成長過程について，蒸着膜形成中およびアニール過程で光吸収スペクトル・フォトルミネッセンススペクトルの測定を行った。

この研究テーマについて現在，AgI-$SrTiO_3$ 系の試料を作製し，フォトルミネッセンス特性を調べている．

【まとめ】

これまでに発見した Eu_2O_3, Sm_2O_3, γAl_2O_3-Eu_2O_3, AgI-anatase TiO_2, silica glass 等のフォトメモリー物質の光誘起現象のダイナミクスを研究するとともに，光触媒物質 $SrTiO_3$ と超イオン導電体 AgI, AgI-ZrO_2 のフォトルミネッセンス特性を明らかにし，フォトメモリー現象を発見した．

【研究業績等】

・発表論文

(1) S. Mochizuki, F. Fujishiro and S. Minami "Photoluminescence and reversible photo-induced spectral change of $SrTiO_3$" Journal of Physics: Condensed Matter 17 (2005) 923-948.

(2) F. Fujishiro and S. Mochizuki "Photoluminescence studies on AgI-ZrO_2 composites" Journal of Luminescence **112** (2005) 71-74.

(3) S. Mochizuki, S. Minami and F. Fujishiro "The reversible UV-laser-light-induced spectral change and origin of the 2.4 eV luminescence band in $SrTiO_3$" Journal of Luminescence **112** (2005) 267-270.

(4) S. Mochizuki and F. Fujishiro "In situ real time optical study of films grown on low temperature substrates by vacuum evaporation of iodine and silver iodide: spectral transitions during deposition and annealing processes" Journal of Physics: Condensed Matter **16** (2004) 3239-3256.

(5) Y. Ishida, Y. Mita, M. Kobayashi, S. Endo and S. Mochizuki "Pressure-induced phase transition in α-MnS" Journal of Magnetism and Magnetic Materials **272-276** (2004) 428-429.

(6) F. Fujishiro and S. Mochizuki "Excitons in AgI-based-glasses and -composites" (accepted).

(7) F. Fujishiro and S. Mochizuki "Structural- and optical studies on mesoscopic defect structure in highly conductive AgI-ZnO composites" Physica B **340-342** (2003) 216-220.

(8) S. Mochizuki and H. Araki "Reversible photoinduced spectral transition in Eu_2O_3-γAl_2O_3 composites at room temperature" Physica B **340-342** (2003) 913-917.

(9) S. Mochizuki "Intense white-luminescence of Sm2O3 irradiated with ultraviolet laser light under vacuum" Physica B **340-342** (2003) 944-948.

(10) S. Mochizuki, T. Shimizu and F. Fujishiro "Photoluminescence study on defects in pristine anatase and anatase-based composites" Physica B **340-342** (2003) 956-959.

(11) S. Mochizuki and H. Araki "UV-laser-light-produced defects and reversible blue-white photoluminescence change in silica" Physica B **340-342** (2003) 969-973.

(12) S. Mochizuki and F. Fujishiro "Structural, electrical and optical studies on AgI-anatase composites" Journal of Physics: Condensed Matter **15** (2003) 5057-5072.

(13) S. Mochizuki and F. Fujishiro "Shallow and deep excited states of mesoscopic structure in AgI-γAl_2O_3 composites" physica status solidi (c) **0** (2002) 763-766.

(14) S. Mochizuki and F. Fujishiro "Shallow- and deep- luminescence centers in AgI- based superionic conductor glass" physica status solidi (c) **0** (2002) 767-770.

(15) F. Fujishiro and S. Mochizuki "The photoexcitation and relaxation of high ionicconductivity glasses $(AgI)_x(AgPO_3)_{1-x}$" Nonlinear Optics **29** (2002) 443-449.

(16) T. Nakanishi and S. Mochizuki "Exhanced photoluminescence of C_{70} porous glass composite" Nonlinear Optics **29** (2002) 603-608.

(17) Y. Mita, Y. Sakai, M. Kobayashi, S. Endo and S. Mochizuki "Magnetic phase transition in antiferromagnetic materials under high pressure" physica status solidi (a) **189** (2002) 935-938.

(18) S. Mochizuki, T. Nakanishi, Y. Suzuki and K. Ishi "Reversible photoinduced spectral change in Eu_2O_3 at room temperature" Applied Physics Letters **79** (2001) 3785-3787.

(19) S. Mochizuki "Stacking faults and excitons in AgI" Physica B **308-310** (2001) 1042-1045.

(20) S. Mochizuki, Y. Suzuki, T. Nakanishi and K. Ishi "Valence-change and defect-induced white

luminescence of Eu2O3" Physica B **308-310** (2001) 1046-1049

(21) Y. Mita, Y. Sakai, D. Izaki, M. Kobayashi, S. Endo and S. Mochizuki "Optical study of MnO under high pressure" physica status solidi (b) **223** (2001) 247-251.

(22) T. Asaji and T. Ishizaka; "Effect of Deuteration on Ammonium Motion and Structural Phase Transition Studied by Nuclear Quadrupole Resonance", Z.Naturforsch., 55a, 2000, 83-89

(23) H. Fujimori and T. Asaji; "35Cl NQR in Glassy Crystal of 2-chlorothiophene", Z.Naturforsch., 55a, 2000, 183-185

(24) Y. Kume and T. Asaji; "Hydrogen Isotope Effect on the Temperature Dependence of the 35Cl-NQR Frequency in (NH4)2IrCl6", Z.Naturforsch., 57a, 2002, 504-508

(25) H. Fujimori, T. Jinbo, and T. Asaji; "13C NMR Study of Liquid Crystals CBOOA", Proc. of Institute of Natural Sci., Nihon Univ., 39, 2004, 405-409

(26) T. Asaji, E. Akiyama, F. Tajima, K. Eda, M. Hashimoto, and Y. Furukawa; "Salts of tetrachloroauric acid with pyridine N-oxide having various base/acid ratios of 1/1, 4/3, 3/2 and 2/1. Crystal structures, 35Cl NQR and phase transitions", Polyhedron, 23, 2003, 1605-1611

・学会発表

口頭発表(日本物理学会)

(1) 望月章介, 藤代史, 四家井千英, 南聖子「$SrTiO_3$ ベルヌイ単結晶の光スペクトル : 濃青色 as-grown 結晶から透明結晶に至るまで」 日本物理学会 第 60 回年次大会 （東京理科大学）

(2) 藤代史，望月章介「$SrTiO_3$ の紫外・可視領域のフォトルミネセンス：表面効果，欠陥効果」 日本物理学会 第 60 回年次大会 （東京理科大学）

(3) 望月章介，南聖子「$SrTiO_3$ 単結晶のレーザー光誘起スペクトル変化現象Ⅰ」日本物理学会 2004 年秋季大会 （青森大学）平成 16 年 9 月

(4) 南聖子，望月章介「$SrTiO_3$ 単結晶のフォトルミネッセンスⅠ」日本物理学会 2004 年秋季大会 （青森大学）平成 16 年 9 月

(5) 望月章介，藤代史「ZrO_2 のフォトルミネッセンス」日本物理学会 2004 年秋季大会 （青森大学）平成 16 年 9 月

(6) 藤代史，望月章介「AgI-ZrO_2 複合体の電気物性・光物性」日本物理学会 2004 年秋季大会 （青森大学）平成 16 年 9 月

(7) 藤代史，望月章介「AgI の励起子：過剰ヨウ素効果，複合体化効果，積層欠陥効果ほか」日本物理学会第 59 回年次大会 （九州大学）平成 16 年 3 月

(8) 望月章介，藤代史「Ag，I，AgI の熱的蒸発過程と薄膜成長過程の分光学的研究」日本物理学会第 59 回年次大会 （九州大学）平成 16 年 3 月

(9) 藤代史，望月章介「AgI/酸化物複合物質の構造と光物性・電気物性」日本物理学会 2003 年秋季大会 （岡山大学）平成 15 年 9 月

(10) 望月章介，藤代史「AgI-anatase 複合体の可逆なレーザー光誘起スペクトル変化現象」日本物理学会 2003 年秋季大会 （岡山大学）平成 15 年 9 月

(11) 荒木寛之，望月章介「酸化物のレーザー光誘起光スペクトル変化現象Ⅰ」日本物理学会 2003 年秋季大会 （岡山大学）平成 15 年 9 月

(12) 清水貴嗣，藤代史，望月章介「アナターゼを含む高いイオン導電性複合体のラマン散乱Ⅱ」日本物理学会 2003 年秋季大会 （岡山大学）平成 15 年 9 月

(13) 藤代史，養田直人，佐野信介，望月章介「AgI/非遷移金属酸化物複合物質の原子的構造と光・電気物性」日本物理学会第 58 回年次大会 （東北大学）平成 15 年 3 月

(14) 望月章介，藤代史「AgI/遷移金属酸化物複合物質の原子的構造と光・電気物性」日本物理学会第 58 回年次大会　（東北大学）平成 15 年 3 月

(15) 荒木寛之，望月章介，渡嘉敷星司，中西太宇人，伊師君「Eu_2O_3・表面活性酸化物複合体の可逆的光誘起光スペクトル変化現象 II」日本物理学会　第 58 回年次大会　（東北大学）平成 15 年 3 月

(16) 清水貴嗣，望月章介「アナターゼを含む高いイオン導電性複合体のラマン散乱」日本物理学会第 58 回年次大会　（東北大学）平成 15 年 3 月

(17) 藤代史，望月章介「AgI の高濃度極限近傍での AgI 系導電性ガラスの原子的構造と光スペクトル：$(AgI)_x(AgPO_3)_{1-x}$」日本物理学会 2002 年秋季大会　（中部大学）平成 14 年 9 月

(18) 望月章介，藤代史「AgI-γAl2O3 複合物質の原子的構造と光スペクトル」日本物理学会 2002 年秋季大会　（中部大学）平成 14 年 9 月

(19) 荒木寛之，望月章介「Eu_2O_3・表面活性酸化物複合体の可逆的光誘起光スペクトル変化現象 I」日本物理学会 2002 年秋季大会　（中部大学）平成 14 年 9 月

(20) 望月章介，藤代史「AgI と AgI 系イオン導電性ガラスの光スペクトルⅡ」日本物理学会第 57 回年次大会　（立命館大学）平成 14 年 3 月

(21) 藤代史，望月章介「高イオン導電性ガラス$(AgI)_x(AgPO_3)_{1-x}$のフォトルミネッセンスと伝導Ⅰ」日本物理学会第 57 回年次大会　（立命館大学）平成 14 年 3 月

(22) 世良太郎，Raphael RUPPIN，望月章介「希土類金属のガス中蒸発と光スペクトル II -Sm，Eu，Yb クラスターの成長と電子状態-」日本物理学会第 57 回年次大会　（立命館大学）平成 14 年 3 月

(23) 藤代史，宇野良晴，望月章介「$(AgI)_x(AgPO_3)_{1-x}$系イオン導電性ガラスの光スペクトルⅠ」日本物理学会 2001 年秋季大会　（徳島文理大学）平成 13 年 9 月

(24) 望月章介，藤代史「AgI と AgI 系イオン導電性ガラスの光スペクトルⅠ」日本物理学会 2001 年秋季大会　（徳島文理大学）平成 13 年 9 月

(25) 鈴木祐也，中西太宇人，須貝宏行，伊師君弘，望月章介「光情報メモリー物質 Eu_2O_3 の光スペクトル」日本物理学会 2001 年秋季大会　（徳島文理大学）平成 13 年 9 月

(26) 中西太宇人，荒木寛之，望月章介「多孔ガラス中に分散した C_{60} クラスターの光学スペクトル」日本物理学会 2001 年秋季大会　（徳島文理大学）平成 13 年 9 月

(27) 中西太宇人，荒木寛之，望月章介「多孔ガラス中に分散した C_{70} クラスターの発光機構 II」日本物理学会 2001 年秋季大会　（徳島文理大学）平成 13 年 9 月

(28) 世良太郎，Raphael RUPPIN，望月章介「希土類金属のガス中蒸発と光スペクトル - Eu，Yb クラスターの成長と電子状態 - 」日本物理学会 2001 年秋季大会　（徳島文理大学）平成 13 年 9 月

(29) 望月章介「AgI の励起子」日本物理学会　第 56 回年次大会　（中央大学）平成 13 年 3 月

(30) 鈴木祐也, 望月章介, 曾根田忠和, 中西太宇人, 平野晋司, 宇野良清, 伊師君弘, Michele FAUCHER, Oon-Kyoung MOUNE，Jeannette DEXPERT-GHYS，Yolande KIHN「Eu_2O_3，Sm_2O_3 のフォトルミネッセンスの光誘起可逆的変化現象」日本物理学会　第 56 回年次大会　（中央大学）平成 13 年 3 月

(31) 望月章介，宇野良清，鈴木祐也，Michele Faucher，O. Kiyoung Moune，Jeannette Dexpert-Ghys，Yolande Zihn「Eu-O 凝縮系における Eu^{3+}イオンの光学遷移の結晶構造との相関Ⅰ」日本物理学会第 55 回年次大会　（新潟大学）平成 12 年 9 月

(32) 鈴木祐也，望月章介，中西太宇人，伊師君弘「Eu_2O_3 の可逆的光誘起価数変化現象」日本物理学会　第 55 回年次大会　（新潟大学）平成 12 年 9 月

(33) 大田有作，望月章介「AgI の超イオン導電相の光スペクトル」日本物理学会　第 55 回年次大会　（新潟大学）平成 12 年 9 月

(34) 中西太宇人，高橋節夫，望月章介「多孔ガラス中に分散した C_{70} クラスターの発光機構」日本物理学会　第 55 回年次大会　（新潟大学）平成 12 年 9 月

口頭発表(第 6 回超イオン導電体物性研究会)

(1) 藤代史，望月章介「高濃度 AgI の超イオン導電ガラスの構造と光物性」第 6 回超イオン導電体物性研究会　（ぱるるプラザ京都）平成 14 年 5 月

(2) 望月章介，藤代史「AgI の原子的構造と励起子構造」第 6 回超イオン導電体物性研究会　（ぱるるプラザ京都）平成 14 年 5 月

口頭発表(国際会議)

(1) 藤代史，望月章介「Excitons in AgI-based-glasses and -composites」The 1st International Discussion Meeting of Superionic Conductor Physics　（同志社大学）平成 15 年 9 月

ポスター発表(国際会議)

(1) 望月章介, 南聖子, 藤代史「The reversible UV-laser-light-induced spectral change and origin of the 2.4 eV luminescence band in $SrTiO_3$」6th International Conference on Excitonic Processes in Condenesd Matter　（Cracow）平成 16 年 7 月

(2) 藤代史, 望月章介「Photoluminescence studies on AgI-ZrO_2 composites」6th International Conference on Excitonic Processes in Condenesd Matter　（Cracow）平成 16 年 7 月

(3) 藤代史，望月章介「Structural- and optical studies on mesoscopic defect structure in highly conductive AgI-ZnO composites」the 22nd International conference on defects in semiconductors　（Aarhus）平成 15 年 7 月

(4) 望月章介，荒木寛之「Reversible photoinduced spectral transition in Eu_2O_3–γAl_2O_3 composites at room temperature」the 22nd International conference on defects in semiconductors　（Aarhus）平成 15 年 7 月

(5) 望月章介「Intense white-luminescence of Sm_2O_3 irradiated with ultraviolet laser light under vacuum」the 22nd International conference on defects in semiconductors　（Aarhus）平成 15 年 7 月

(6) 望月章介, 清水貴嗣, 藤代史「Photoluminescence study on defects in pristine anatase and anatase-based composites」the 22nd International conference on defects in semiconductors　（Aarhus）平成 15 年 7 月

(7) 望月章介，荒木寛之「UV-laser-light-produced defects and reversible blue-white photoluminescence change in silica」the 22nd International conference on defects in semiconductors　（Aarhus）平成 15 年 7 月

(8) 望月章介，　藤代史「Shallow and deep excited states of mesoscopic structure in AgI–γAl_2O_3 composites」10th International Conference on Shallow Level Centers in Semiconductors　（Warsaw）平成 14 年 7 月

(9) 望月章介，藤代史「Shallow- and deep- luminescence centers in AgI- based superionic conductor glass」10th International Conference on Shallow Level Centers in Semiconductors　（Warsaw）平成 14 年 7 月

(10) 藤代史，望月章介「The photoexcitation and relaxation of high ionicconductivity glasses $(AgI)_x(AgPO_3)_{1-x}$」5th International Conference on Excitonic Processes in Condenesd Matter　（Darwin）平成 14 年 7 月

(11) 中西太宇人，望月章介「Exhanced photoluminescence of C_{70} porous glass composite」5th International Conference on Excitonic Processes in Condenesd Matter　（Darwin）平成 14 年 7 月

Reversible photoinduced spectral change in Eu_2O_3 at room temperature

Shosuke Mochizuki,[a] Tauto Nakanishi, and Yuya Suzuki
Department of Physics, College of Humanities and Sciences, Nihon University, Tokyo 156-8550, Japan

Kimihiro Ishi
Institute of Multidisciplinary Research for Advanced Materials, Tohoku University, Sendai 980-8577, Japan

(Received 5 February 2001; accepted for publication 1 October 2001)

When Eu_2O_3 powder compact and film are irradiated with ultraviolet (UV) laser light in a vacuum, their photoluminescence (PL) spectra change from a red sharp-line structure to a white broad band, which can be clearly seen with the naked eye. After removing the UV laser light, the white PL continues for more than several months at room temperature under room light, in spite of any changes of atmosphere. By irradiating with the same UV laser light at room temperature under O_2 gas atmosphere, the original red PL state reappears. Such a reversible phenomenon may well yield materials for white-light-emitting devices and erasable optical storage. © *2001 American Institute of Physics.* [DOI: 10.1063/1.1425064]

Recently, considerable attention has been devoted to research for new materials to be used for erasable optical storage and for laser media for tunable wide-band lasers. The interest in photoluminescent materials showing photoinduced reversible spectral change at room temperature has significantly grown, because a combination of such reversible phenomenon and the near-field optical microscope[1] is very promising when applied to high-density optical storage with nanometer resolution. It is a hope that we can find white photoluminescence (PL) material, which is useful for the wide-band tunable-laser medium. Hitherto, X-ray- and photoinduced spectral change of rare-earth ions has been observed mainly on Eu-doped ionic crystals and glasses.[2–6] However, there is a limitation to dopant concentration. The storage density of such doped crystals cannot, in principle, prevail against that of rare-earth metal compounds (for example, Eu_2O_3 and Sm_2O_3). We have observed recently the reversible photoinduced phenomenon and white PL state in Eu_2O_3 powder compact and film. In this letter, we report the experimental results in detail.

Powder compact specimens are prepared by pressing Eu_2O_3 powder 99.98% in purity under a pressure of 0.2 GPa for 1 h at room temperature. They are then sintered at 1273 K in air for 24 h. X-ray diffraction analysis of every compact shows that they are cubic-phase Eu_2O_3.[7] Eu_2O_3 films are grown on a silica glass substrate in a planar diode of the radio-frequency-excited sputter deposition system. X-ray diffraction analysis of the films shows that they are the hexagonal-phase Eu_2O_3.[7] Irradiation is carried out with a continuous wave (cw) of He–Cd laser line ($\lambda = 325$ nm) with power densities between 31 and 840 kW/m^2. The illumination optics area is between 2.54×10^{-6} and 1.13×10^{-8} m^2. The same He–Cd laser line excites luminescence. Emitted light is dispersed and detected using a grating spectrograph equipped with a multichannel photodetection system. Excitation spectra are recorded in an apparatus consisting of a 150 W xenon lamp, a mechanical light chopper, two grating monochromators and a synchronous light detection system. The PL and excitation spectra are corrected, respectively, for the response of the optical measurement systems and the emission intensity spectrum of the light source. The values of the PL intensity are given in arbitrary units. In the film measurements, the sensitivity of the detections was twice that in the powder compact measurements.

Figures 1(a), 1(b), and 1(c) show the reversible spectral change of the Eu_2O_3 powder compact sintered at 1273 K in air. Measurements are carried out in alphabetical order: (a)→(b)→(c). Irradiation is carried out with a 325 nm laser line at room temperature. Irradiation time t_{ir} under a given atmosphere and kind of atmosphere are indicated by each spectrum. The spectrum shown in Fig. 1(a) corresponds to that of the as sintered Eu_2O_3 specimen, which is measured in O_2 gas of 1.01×10^5 Pa. Clear red emission can be seen with the naked eye. The specimen chamber is then evacuated below 1.33×10^{-4} Pa under UV light irradiation. With increasing t_{ir}, all the Eu^{3+} [$^5D_0\rightarrow{}^7F_J$ ($J=0,1,2,3,4$)] emission lines become weak, while a very broad emission band appears and spreads all over the visible light region, as seen in the spectrum shown in Fig. 1(b) as observed at 90 min later after the evacuation. At this stage, the bright white PL can be seen with the naked eye. Oxygen gas is again introduced in the chamber. The change from white PL emission to red emission can be seen with the naked eye. The spectrum as shown in Fig. 1(c) is obtained 150 min later after introducing the O_2 gas. It is found through many successive experiments that the spectral changes as shown in Figs. 1(b) and 1(c) are reversible. Similar experiments were carried out by changing the wavelength of the irradiating laser light. For example, a cw He–Cd laser ($\lambda = 442$ nm), a cw Ar^+ laser ($\lambda = 528.7$, 514.5, 501.7, 496.5, 488.0, 476.5, 472.2, 465.8, and 457.9 nm), and a pulsed Nd^{3+}:YAG laser ($\lambda = 266$, 354.7, 532, and 1064 nm) were used. No spectral change was observed with these lasers, which indicates that the cw UV light of the wavelength 325 nm is required to induce the spectral change. The speed of the change accelerates by increasing the power density of the activating light. The change to the white PL emission can also be observed at low temperatures down to 7

[a]Author to whom correspondence should be addressed; electronic mail: motizuki@physics.chs.nihon-u.ac.jp

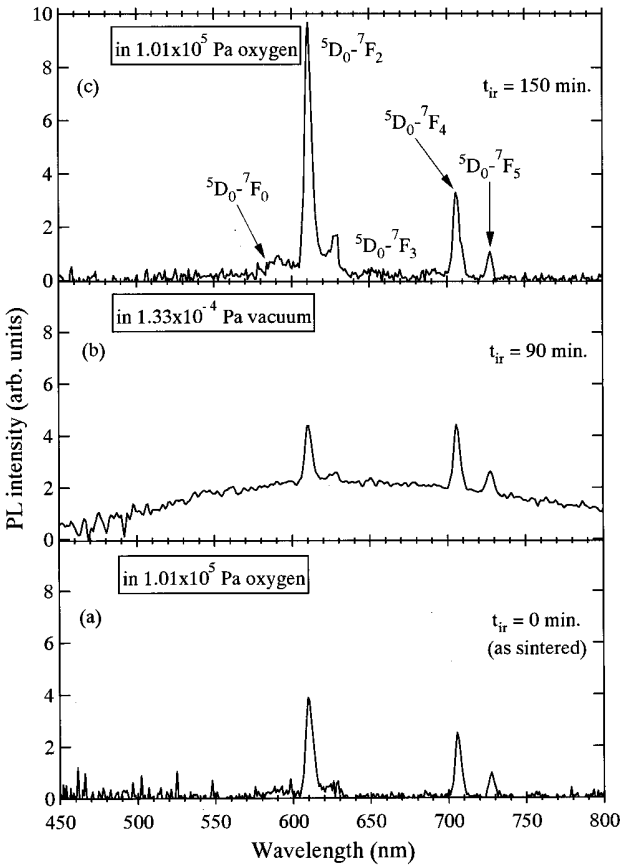

FIG. 1. Reversible photoinduced PL spectral change in Eu_2O_3 powder compact at room temperature. The powder compact was sintered at 1273 K in air. The atmosphere and irradiation time t_{ir} at 325 nm are indicated in the plots. Experiments were carried out in alphabetical order: (a)→(b)→(c).

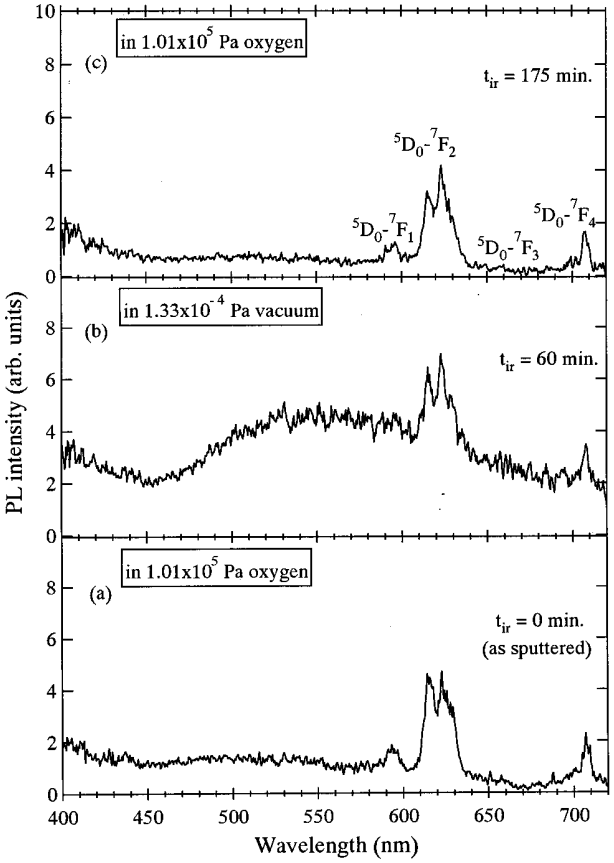

FIG. 2. Reversible photoinduced spectral change in Eu_2O_3 film at room temperature. The film was produced by the rf-sputtering method. The atmosphere and irradiation time t_{ir} at 325 nm are indicated in the plots. Experiments were carried out in alphabetical order: (a)→(b)→(c).

K, which indicates that the phenomenon does not arise from a phonon assisted process and that it is a purely electronic mechanism. In spite of the changing atmosphere (for example, O_2 gas and air exposures), the white PL state lasts for more than several months at room temperature after the removal of the laser light under room light, and the red PL state reappears only by irradiating with the same UV laser light under O_2 gas atmosphere.

Figures 2(a), 2(b), and 2(c) show the reversible spectral change of the Eu_2O_3 film under 325 nm irradiation at room temperature. Measurements are carried out in alphabetical order: (a)→(b)→(c). The results are quite similar to those of the powder compact specimen obtained both at room temperature and 7 K. The wavelength, however, at the intensity peak for the film specimen is at about 550 nm which is blueshifted by about 60 nm from that observed for the powder compact specimen. The observed spectral structure for the $^5D_0 \rightarrow {}^7F_2$ emission, incidentally, differs from that for the powder compact specimen (C phase Eu_2O_3) in which each Eu^{3+} ion is surrounded by six oxygen ions. Seven coordinate Eu^{3+} ions account for the spectral difference.[8]

The excitation (PL yield) spectra of the Eu_2O_3 powder compact and film were measured at room temperature for the $^5D_0 \rightarrow {}^7F_2$ emission and the white emission band. The results show that the 325 nm laser photons are slightly absorbed by the $^7F_0 \rightarrow {}^5L_J$ transitions.[9] The excitation spectrum for the white band does not show any yield peak due to intra-4f transitions from the excited $^5D_0$ level of Eu^{3+} ions. The yield at the CT band is depressed considerably which is due to decreased number of Eu^{3+} ions. Excitation spectra quite similar to the powder compact are also observed in the film specimen.

The present experimental results of the Eu_2O_3 powder compact and film specimens may be summarized as follows:

(1) Photoinduced reversible spectral change between red and white PL can be observed at different temperatures from 7 K to room temperature. The change is induced only by a 325 nm cw laser line. The 325 nm corresponds to transition onset wavelength for the charge transfer excitation and for excitation of the $^7F_0 \rightarrow {}^5L_J$ transitions. After removing the UV laser light irradiation, each PL state continues for more than several months at room temperature under room light, in spite of any change of atmospheres (1.01×10^5 Pa O_2 gas and air).

(2) The change to white PL occurs only as a result of the 325 nm cw laser light irradiation under vacuum, while we have not observed under any other reducing atmosphere; for example, Ar–H_2 mixture gas.

(3) The change to the white PL is accompanied by reduction of the $^5D_0 \rightarrow {}^7F_J$ ($J=0,1,2,3,4$) emissions of Eu^{3+} ions.

The result (1) indicates that the observed photoinduced spectral changes are purely electronic phenomena and are not phonon assisted. The result (2) indicates that the phenom-

enon is a photoinduced associative detachment of O_2 near the specimen surface.

The results above summarize how spectral change arises naturally from photoactivated oxidation and reduction. The reduction is accompanied both by a valence-number change of europium ions ($Eu^{3+} \rightarrow Eu^{2+}$) and by oxygen defect formation. Broadband emission is connected with Eu^{2+} ions and local structural changes arising from oxygen defects. It should be noted that EuO shows an absorption edge at about 1 eV and a photoluminescence band centered at 1.19 eV.[8,10] These energies are far away from those of the observed white luminescence. Therefore, the photogenerated Eu^{2+} ions and oxygen defects do not form any structure based on EuO crystal. Then, we examine other types of Eu^{2+} luminescent center as follows. First, we assume that the Eu^{2+} ions in Eu_2O_3 constitute different types of luminescent cluster with surrounding ions. The broad white PL band indicates that the energies of emitting centers are slightly different from each other, which may arise from the diversity of the cluster size, shape, and structure. Such diversity may also give the difference (about 60 nm) of the white PL intensity peak wavelength between the powder (cubic crystal structure) and the film (hexagonal one) specimens. Second, we assume that the Eu^{2+} ions are well isolated from each other in Eu_2O_3. They can be luminescent centers and also give rise to the broad PL band. The $4f^6 5d \rightarrow 4f^7$ transition gives a PL band at wavelengths from 400 to 520 nm, which has been observed in Eu^{2+}-doped crystals.[11–13] The oxygen vacancies are also responsible for the broad PL band of metal oxides.[14] Further studies, for example, the measurements on the electronic and crystal structures of Eu_2O_3 surface, are required in order to ascertain the validity of the cluster model and in order to clarify which mechanism is responsible for the observed broad white PL. Now, we will return to discussion of the result (2). Since the UV light (325 nm) cannot dissociate directly free O_2 as atmospheric gas, the photoinduced oxidation indicates that the photodissociation energy of O_2 is considerably decreased at the specimen surface by the interactions between O_2 and Eu_2O_3, as known since 1932 as dissociative adsorption of molecules on a metal surface.[15] The result (2) indicates that the UV light with shorter wavelength is needed for photoreduction in H_2 gas atmosphere. Incidentally, the photodissociation energy of free H_2 is about two times that of free O_2.[16]

To clarify the mechanism of the observed spectral change in detail, simultaneous measurements of the Raman scattering and PL spectra of Eu_2O_3 during UV light irradiation, together with the studies on surface electronic states, are now in progress.

This work is supported by Interdisciplinary General Joint Research Grant for Nihon University, and by Project Research Grant from The Institute of Information Sciences, College of Humanities and Sciences, Nihon University. This work is also partially supported by a Grant-in-Aid for Scientific Research from the Ministry of Education, Science, Sports, Culture and Technology, Japan.

[1] E. Bezig and J. K. Trautman, Science **257**, 189 (1992).
[2] B. Welber, J. Appl. Phys. **36**, 2744 (1965).
[3] W. Beck, A. Ya. Karasik, J. Arvanitidis, and D. Richard, Eur. Phys. J. D **10**, 131 (2000).
[4] K. Miura, J. Qui, T. Mitsuyu, and K. Hirao, Proc. SPIE **3618**, 141 (1999).
[5] V. Barbin, J. P. Jouart, and Th. D'Almeida, Chem. Geol. **130**, 77 (1996).
[6] K. Fujita, K. Tanaka, K. Yamashita, and K. Hirao, J. Lumin. **87–89**, 682 (2000).
[7] K. A. Gschneid, Jr. and L. R. Eyring, *Handbook on the Physics and Chemistry on Rare Earths* (North-Holland, Amsterdam, 1979), Vol. 3.
[8] S. Mochizuki, Y. Suzuki, R. Uno, M. Faucher, O. K. Moune, J. Dexpert-Ghys, and Y. Zihn, Meeting Abstracts Phys. Soc. Jpn. **55**, 627 (2000).
[9] G. Wakefield, H. A. Keron, P. J. Dobson, and J. L. Hutchison, J. Colloid Interface Sci. **215**, 179 (1999).
[10] G. Guntherodt and P. Wachter, AIP Conf. Proc. **10**, 1284 (1973).
[11] M. Akiyama, C. Xu, K. Nonaka, and T. Watanabe, Appl. Phys. Lett. **73**, 3046 (1998).
[12] T. Takasaki, S. Tanabe, and T. Harada, J. Ceram. Soc. Jpn. **104**, 322 (1996).
[13] T. Matsuzawa, Y. Aoki, N. Takeuchi, and Y. Murayama, J. Electrochem. Soc. **143**, 2670 (1996).
[14] Y. Kawabe, A. Yamanaka, E. Hanamura, T. Kimura, Y. Takiguchi, H. Kan, and Y. Tokura, J. Appl. Phys. **88**, 1175 (2000).
[15] J. E. Lennard-Jones, Trans. Faraday Soc. **28**, 333 (1932).
[16] G. Herzberg, I. Spectra of Diatomic Molecules, p. 351, p. 446, 1989.

ELSEVIER

Physica B 308–310 (2001) 1042–1045

PHYSICA B

www.elsevier.com/locate/physb

Stacking faults and excitons in AgI

S. Mochizuki*

Department of Physics, College of Humanities and Sciences, Nihon University, 3-25-40 Sakurajosui, Setagaya-ku, Tokyo 156-8550, Japan

Abstract

AgI powder is gradually evaporated in vacuum onto a substrate whose temperature is higher than the superionic transition point T_C. During the evaporation, the optical absorption spectrum of the film is measured as a function of time-elapsed after the beginning of evaporation. By increasing the time (i.e., with increasing film thickness), the shifts of the absorption edge and exciton energy are observed, which are due to exciton or carrier confinement effects in the averaged structure of α-AgI. Information as to the electronic structure of the averaged structure is deduced from analyzing the observed spectra. After stopping evaporation, the film is gradually cooled down to 131 K. Through the cooling process, the absorption spectrum is also measured as a function of temperature. New exciton absorption bands (H_1, H_2 and H_3) appear, together with the $Z_{1,2}$ and Z_3 excitons in the γ-AgI. The H_1, H_2 and H_3 excitons are assigned to a metastable disordered polytype structure of β-AgI, in the light of the X-ray diffraction data.

Keywords: Polytypism; Averaged structures; Excitons; Superionic conductor

1. Introduction

Silver iodide AgI is well known as a solid electrolyte and has three phases designated as α, β and γ at normal pressure in the order of decreasing temperature with the following properties [1]. At superionic transition point T_C (419 K), the superionic conductor α-phase transforms into semiconductor β-phase (wurtzite lattice). The α-phase has a body-centered cubic arrangement of I^- ion with highly mobile Ag^+ ions randomly distributed through the equivalent interstices, which has been known as the averaged structure. Extensive attention has been paid to the mechanisms of the superionic motion and to the electron–phonon interactions in the averaged structure for many years [2,3]. However, an in situ optical study on the electron states of α-AgI is limited in number and many basic problems remain to be solved. Moreover, the interest in AgI-based superionic conducting glasses and AgI : metal oxide composites has significantly grown and extreme conductivity enhancement has been observed at room temperature [4]. For this reason, also, it is necessary to clarify the electronic and ionic structures of α-AgI. At 408 K, the β-phase transforms mostly into the second semiconductor γ-phase (zinc blende lattice) with a small amount of the β-phase [5]. However, at temperatures lower than T_C, the effects of stacking faults and metastable structures need to be pointed out [6]. It is said that, if annealed and aged, the structures may convert into the wurtzite lattice. Therefore, in order to clarify the details of such a transition between the wurtzite and zinc blende structures, any measurement must be carried out in situ. The exciton absorption spectrum of AgI is very sensitive to such a crystal modification and local structural change [7,8]. While high-temperature α-AgI is cooled down to low temperature, it is useful to measure spectral transition in the exciton absorption.

2. Experimental

Vacuum evaporation experiments are carried out under a base pressure of 10^{-4} Pa. Optically flat-plates of silica glass, sapphire (R-cut) and MgO (1 0 0) are used as substrates. The surface temperature of the substrate is monitored with an alumel–chromel thermocouple. A platinum crucible containing nominally pure AgI

*Tel.: +81-3-5317-9733 ; fax: +81-3-5317-9771.
E-mail address: motizuki@physics.chs.nihon-u.ac.jp (S. Mochizuki).

0921-4526/01/$ - see front matter
PII: S0921-4526(01)00919-X

powder was gradually heated indirectly in an alumina crucible on which a tungsten-wire heater was wound. The thickness of AgI film on the substrate increases with time. During film deposition, the substrate temperature was maintained above T_C. The optical density spectrum of the film was measured as a function of the time t_d elapsed after the beginning of the evaporation with an optical multichannel analyzer system. The experimental procedure is almost the same as the experiments for microcrystals, except for introducing noble gas stream, which has been already reported [9]. After stopping the evaporation, the film is gradually cooled down to 131 K. Through the cooling process, the absorption spectrum of the film was also measured as a function of temperature.

3. Results and discussion

3.1. Optical absorption of α-AgI film

Fig. 1 shows the time evolution of the optical density spectrum of α-AgI. The substrate temperature is 453 K. Although one time-resolved spectrum consists of successive sixty-four spectra in this figure, only eight spectra are selected and presented in order to show clearly the time evolution. The time t_d is indicated in the plots. The final thickness of the film was about 300 nm. At the initial stage of the evaporation, a kink and an absorption edge appear at about 2.8 eV and at about 2.6 eV, respectively. With the progressing evaporation, the absorptions increase and the kink and the edge shift to lower energies, together with the growth of an absorption tail below 2.5 eV. In order to observe the detail, as shown in Fig. 2, we compared the spectrum measured at $t_d = 48.88$ s (curve A) with that measured at $t_d = 123.63$ s (curve B), by scaling the curve A, so that the optical density at 3 eV coincides with that of curve B. The curve C obtained by such scaling coincides with the curve B not only at the energy region between 3 and 4 eV, but also at the lowest photon energy (1.549 eV). The result shows that, with progressing evaporation, namely, the increasing film thickness, the steepness of the optical density curve in the neighborhood of the absorption edge decreases and the absorption-edge shifts from 2.57 eV to a lower energy 2.52 eV. The red shift nature observed arises from a decrease in the quantum confinement of carriers or excitons in α-AgI film. We investigated the absorption tail below 2.5 eV by replacing the silica glass substrate with a MgO (1 0 0) plate and a R-cut sapphire plate, and changing the evaporation speed. The results can be summarized as follows:

(1) With the increasing evaporation speed, the fabricated films become somewhat cloudy.
(2) Films on the MgO- and sapphire single-crystal substrates do not show a prominent tail below 2.5 eV.

Therefore, the absorption tail observed below 2.5 eV is closely connected with surface roughness, and with crystalline defects at the film/substrate interface.

3.2. Optical absorption of AgI film below T_C

After stopping the evaporation, the specimen was gradually cooled to 131 K with an average cooling rate

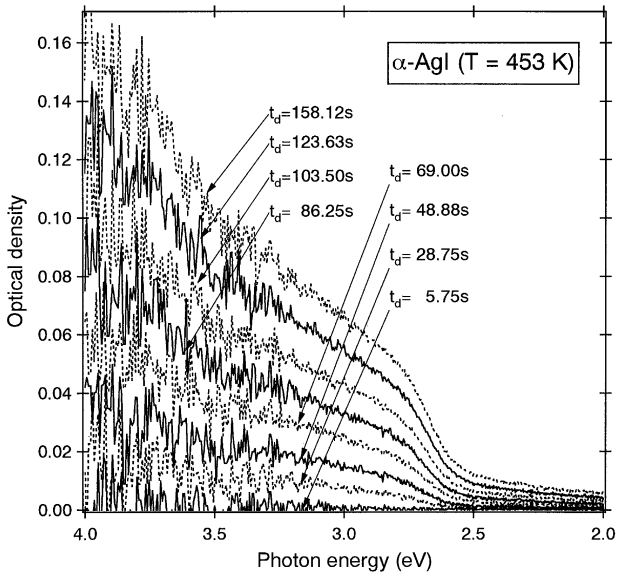

Fig. 1. Time evolution of the optical density spectrum of α-AgI film on a silica glass at 453 K during vacuum evaporation.

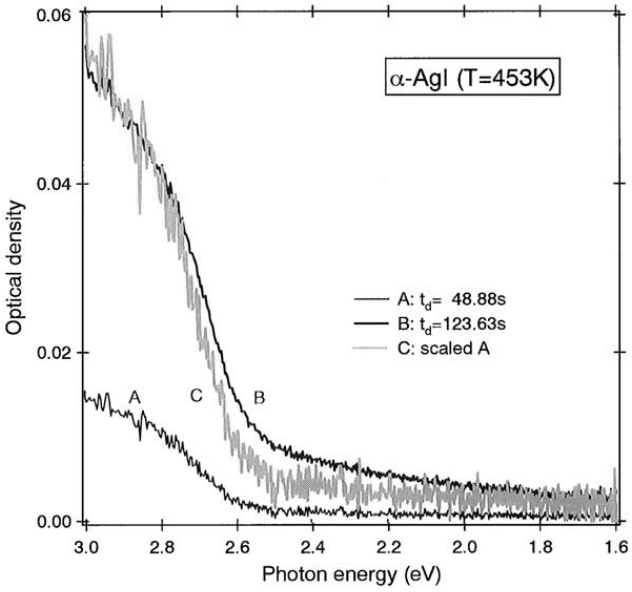

Fig. 2. Comparison of the optical density spectra of AgI film between the early and middle stages of the vacuum evaporation.

of 0.03 K/s. During the cooling process, the optical density spectrum was measured as a function of temperature, at temperature intervals of 5 K. Only the four spectra are presented in order to show clearly the temperature dependence. The result is shown in Fig. 3. During cooling from 453 to 398 K, the optical density spectrum is almost independent of temperature. Urbach rule does not hold in α-AgI. This indicates that the contribution from the electron–phonon interaction characteristic of the α-phase counterbalances that from the temperature-shift of the band gap energy due to thermal contraction of α-AgI. No remarkable spectral change was observed near T_C. This is due to the hysteresis of the superionic conduction transition [8]. At 393 K, several weak exciton absorption peaks and a shoulder appear faintly at 2.934, 2.975 (shoulder), 3.058, 3.110, 3.766 and 3.977 eV. On further cooling, these absorption peaks become prominent. In order to show the detailed spectral structure, the spectrum measured at 131 K is shown, together with that measured at 453 K, in Fig. 4. The X-ray diffraction (XRD) pattern of the AgI film was measured at room temperature. The XRD result shows a considerable amount of γ-AgI and the broadening of the (h 0 l) diffraction lines of β-AgI. The broadening arises from the stacking disorder in β-AgI hexagonal stacking sequence (ababab…), as pointed out by Lee et al. [10]. Taking into account the X-ray diffraction data, as indicated in the figure, the peaks, the absorption peaks and the shoulder observed at 2.934, 2.975 (shoulder) and 3.766 eV are assigned to the Z_1-, Z_2- and Z_3- exciton absorptions of γ-AgI [7,8], while the peaks observed at 3.058, 3.110 and 3.977 eV are assigned to the H_1-, H_2- and H_3-exciton absorptions of some

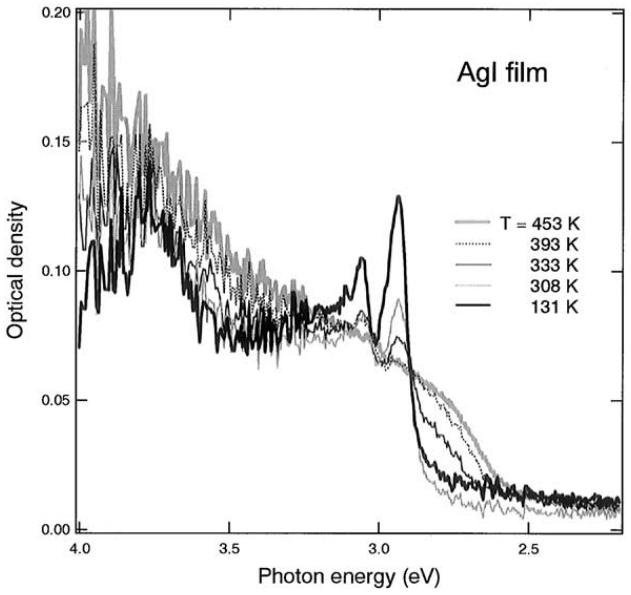

Fig. 3. Optical density spectra of AgI film on a silica glass at different temperatures during cooling process.

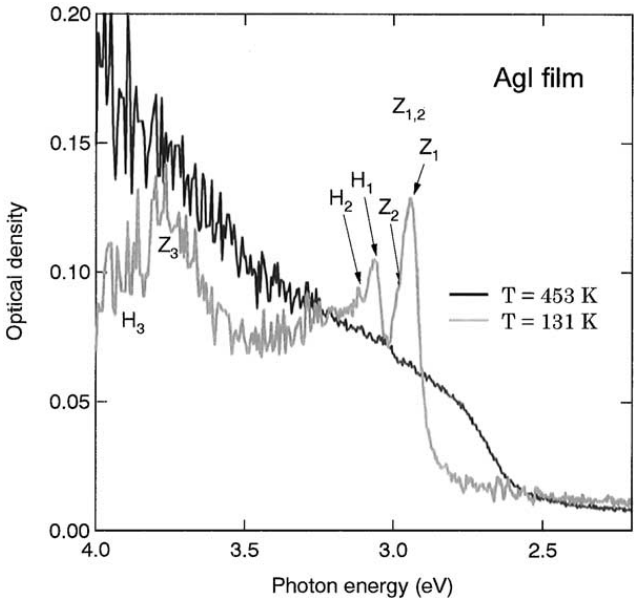

Fig. 4. Optical density spectra of AgI film at 131 and 453 K.

stacking-disorder-induced polytype structure of AgI. Quite a similar exciton absorption due to the polytype structure was found in CuI film evaporated onto a room-temperature substrate [7].

3.3. Miscellaneous

In Fig. 5, the absorption intensity peak energy and photoluminescence intensity peak energy of AgI film at 9 K are plotted as a function of the substrate temperature during vacuum evaporation. The observed absorption and photoluminescence (PL) peaks are due to the $Z_{1,2}$ exciton. The PL intensity peak appears several tens of meV lower than the absorption one, which indicates the existence of shallow exciton traps due to electron–phonon interactions or defects. With the increasing substrate temperature above about 450 K, the redshift becomes prominent. Silica glass substrate, which has an extremely small thermal expansion coefficient, gives a larger shift than that of sapphire. The results are qualitatively explained by the asymmetric stress at the interface coming from thermal shrinking with different thermal expansion coefficients between AgI and substrate material. The stress affects the electronic structure of AgI and induces an additional shift of the $Z_{1,2}$ exciton energy. This thermal stress may be one of the candidates for the cause of polytype structure formation. Our experiments show that the H_1, H_2 and H_3 absorptions are not observed in thick AgI films which were produced by the vacuum evaporation with a small evaporation rate. Thinner sample tends to be influenced by the thermal stress and, therefore, the H_1, H_2 and H_3 absorptions become more prominent. In addition to this stress effect, the effect of the deviation from

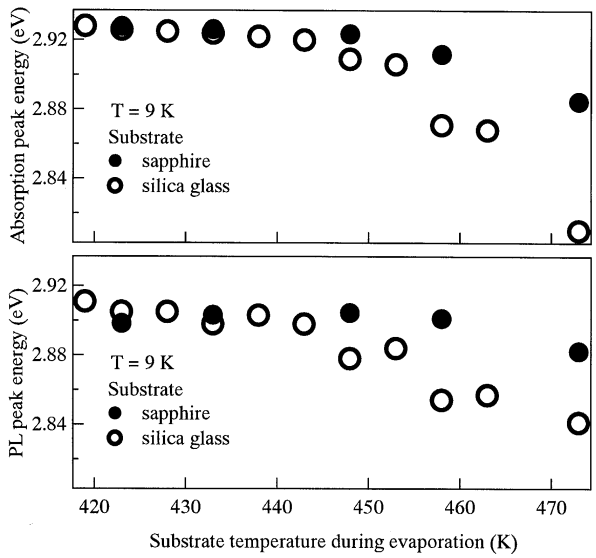

Fig. 5. Substrate temperature dependence of the absorption intensity peak and PL intensity peak energies at 9 K for the silica glass and sapphire substrates.

stoichiometry, Ag_1I_{1-x}, should also be considered at a high temperture for further discussion.

Effect of the stacking disorder observed in film specimens appears frequently even in the absorption spectra of nanocrystal specimens. Nanocrystals both on a substrate [11] and in a matrix [12] show faint absorption bands between 3.0 and 3.2 eV, which are in the H_1- and H_2 exciton energy region. This indicates that AgI nanocrystals contain a stacking disorder induced by some reconstruction of surface atoms and by the stress at the nanocrystal/matrix interface similar to CuI nanocrystals [13].

Acknowledgements

This work is supported by Interdisciplinary General Joint Research Grant for Nihon University and by Project Research Grant from The Institute of Information Sciences, College of Humanities and Sciences, Nihon University. This work is also partially supported by a Grant-in-Aid for Scientific Research from the Ministry of Education, Science, Sports, Culture and Technology, Japan.

References

[1] G. Burley, Amer. Min. 48 (1963) 1266.
[2] G. Eckold, K. Funke, J. Klaus, R.E. Lechner, J. Phys. Chem. Solids 37 (1976) 1097.
[3] A. Rakitin, M. Kobayashi, Phys. Rev. B 53 (1996) 3088.
[4] St. Adams, J. Maier, Sol. Stat. Ionics 105 (1998) 67.
[5] R. Bloch, H. Moller, Z. Phys. Chem. A125 (1931) 245.
[6] P.R. Prager, Acta. Cryst. A30 (1974) 369.
[7] M. Cardona, Phys. Rev. 129 (1963) 69.
[8] S. Mochizuki, Y. Ohta, J. Lumin. 87–89 (2000) 299.
[9] S. Mochizuki, J. Lumin. 70 (1996) 60.
[10] J.–S. Lee, S. Adams, J. Maier, J. Phys. Chem. Solids 61 (2000) 1607.
[11] S. Mochizuki, K. Umezawa, Phys. Lett. A 228 (1997) 111.
[12] G. Mshvelidse, et al., Phys. Stat. Sol. (b) 207 (1998) 369.
[13] A. Tanji, I. Akai, K. Kojima, T. Karasawa, T. Komatsu, J. Lumin. 87–89 (2000) 516.

ELSEVIER

Physica B 308–310 (2001) 1046–1049

PHYSICA B

www.elsevier.com/locate/physb

Valence-change- and defect-induced white luminescence of Eu_2O_3

S. Mochizuki[a,*], Y. Suzuki[a], T. Nakanishi[a], K. Ishi[b]

[a] *Department of Physics, College of Humanities and Sciences, Nihon University, 3-25-40 Sakurajosui, Setagaya-ku, Tokyo 156-8550, Japan*

[b] *Institute of Multidisciplinary Research for Advanced Materials, Tohoku University, Sendai 980-8577, Japan*

Abstract

Under irradiating with a CW UV laser light ($\lambda = 325$ nm) at room temperature in vacuum and oxygen gas atmosphere, the film, microcrystals and powder compacts of Eu_2O_3 exhibit a reversible photoluminescence (PL) spectral change between a red sharp-line structure and a white broad one. After stopping the UV irradiation, the ability of the white PL lasts for more than several months at room temperature under room light, in spite of changes of atmosphere. The reversible phenomena to be observed are interpreted as the results of both the valence-number change of europium ions ($Eu^{3+} \rightarrow Eu^{2+}$) and the oxygen vacancy formation.

Keywords: Defect structures; Valence change; White-light emission

1. Introduction

Eu_2O_3 is stable in air and has five phases designated by X, H, A, B and C at atmospheric pressure in order of decreasing temperature as follows [1]. At about 2553 K, the X phase transforms into the H phase which transforms to the A phase at 2413 K. At 2313 K, the A phase (hexagonal structure: space group D_{3d}) transforms into the B phase (monoclinic structure: space group C_{2h}^3). In the A phase, the europium atoms are seven-coordinate with four oxygen atoms closer than the other three, while, in the B phase, the europium atoms are six- and seven-coordinate. At about 1373 K, the B phase transforms into the C phase (cubic structure: space group T_h^7) in which the europium atoms are six-coordinate. At room temperature, the present authors have recently observed the reversible UV-laser-light-induced spectral transitions between the red- and white-luminescence states in Eu_2O_3-powder compacts and —films produced by the radio-frequency sputtering method [2,3]. The interest in photoluminescent materials showing such photo-induced reversible spectral change at room temperature has significantly grown, because a combination of the reversible phenomenon and the near-field optical microscope [4] is very promising when applied to high-density optical storage with nanometer resolution. It is also the hope that we can find white PL material, which is useful for the wide-band tunable-laser medium. Very recently, we have also observed the similar photoinduced spectral transition in Eu_2O_3 films produced by the pulsed laser ablation method in vacuum and Eu_2O_3 microcrystal films produced by the laser ablation in low-pressure oxygen gas atmosphere.

In this paper, an overview of our results obtained in the past three years will be given, together with a phenomenal model of the photoinduced spectral transition.

2. Experimental

All specimens were made from Eu_2O_3 powder of 99.98% purity. Powder compact specimens were prepared by pressing the Eu_2O_3 powder under a pressure of 0.2 GPa for 1 h at room temperature. They were then

*Corresponding author. Tel.: +81-3-5317-9733; fax: +81-3-5317-9771.

E-mail address: motizuki@physics.chs.nihon-u.ac.jp (S. Mochizuki).

0921-4526/01/$ - see front matter
PII: S0921-4526(01)00921-8

sintered at 1273 K in air for 24 h. First types of Eu_2O_3 films were grown on a silica glass substrate by the radio-frequency sputtering (RFS) method. They are named RFS films. Second-type of Eu_2O_3 films were grown on a silica glass substrate by the pulsed laser ablation (PLA) method in vacuum of 1.33×10^{-4} Pa. They are named PLA-films. Eu_2O_3 microcrystal-accumulated films were grown on a silica glass substrate by the PLA method in oxygen gas of the pressure lower than 100 Pa. They are named PLA-MC film. They are characterized by the X-ray diffraction (XRD) method and the scanning electron microscopy (SEM). Irradiations were carried out with a CW He–Cd laser line ($\lambda = 325$ nm) with power densities between 31438 and 840000 W/m^2. The same He–Cd laser line excites luminescence. Emitted light is dispersed and detected using a grating spectrograph equipped with a multichannel photodetection system.

3. Results and discussion

The XRD analysis of the produced specimens indicates that the powder compact, RFS film, PLA film, and PLA-MC film are respectively, the C phase, the H phase [1], a mixture of predominantly C phase with a little B phase, and a mixture of predominantly B phase with a little C phase of Eu_2O_3. The specimens were also examined by the SEM. The powder compacts consist of randomly oriented and connected rectangular-parallelepiped grains, as shown in Fig. 1(a). The RFS-films and the PLA ones have smooth surfaces and are optically transparent. The PLA-MC films consist of a lot of small particles whose sizes is approximately several hundred nanometers and little aggregates whose sizes can be several thousand nanometers, as shown in Fig. 1(b).

Figs. 2–5 show the photoinduced spectral changes at room temperature of the Eu_2O_3-powder compact, Eu_2O_3-RFS film, Eu_2O_3-PLA film and Eu_2O_3-PLA-MC film, respectively. In the measurements of the powder compact, the RFS films, the PLA films and the PLA-MC films, their relative sensitivities of the detections are 1, 8, 170 and 34, respectively. Experiments were carried out in alphabetical order: (a)→(b)→(c). Irradiation time t_{ir} under a given atmosphere and the kind of

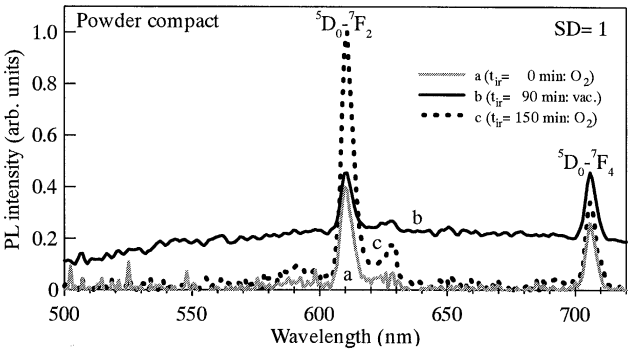

Fig. 2. Reversible spectral change of Eu_2O_3 powder compact.

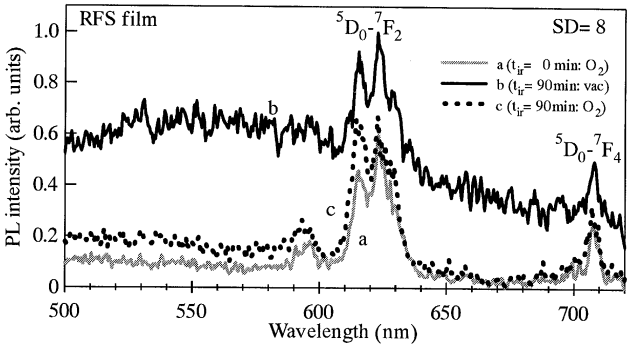

Fig. 3. Reversible spectral change of Eu_2O_3 film produce by the RF-sputtering method.

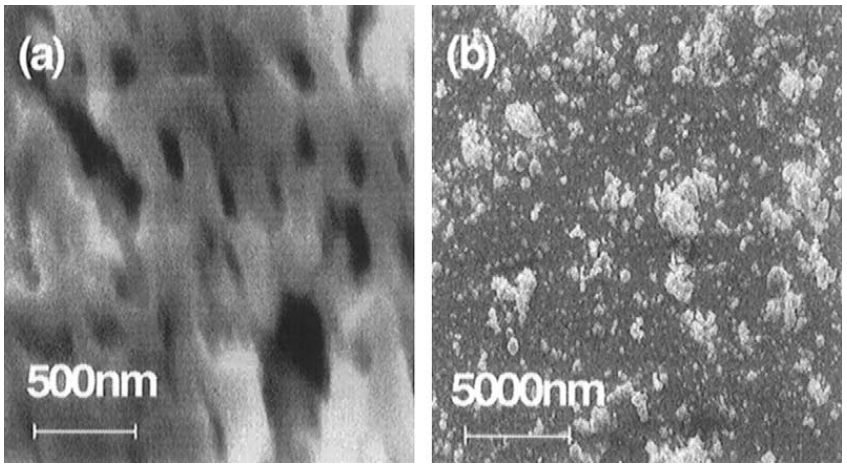

Fig. 1. SEM photographs of the Eu_2O_3-powder compact (a) and Eu_2O_3-PLA-microcrystal film (b).

atmosphere are indicated in each plot, together with the relative sensitivity of the detection, SD. First, these as-produced Eu_2O_3 specimens are irradiated with a 325 nm laser line at room temperature under oxygen atmosphere of a pressure 1.01×10^5 Pa. Under 325 nm excitation, these specimens show the red sharp $^5D_0 \rightarrow {}^7F_J$ ($J = 0, 1, 2, 3, 4$) emissions [5,6]. Depending on the crystal structure of the specimens, the detailed spectral structure of the $^5D_0 \rightarrow {}^7F_2$ emission differs each other [7,8]. Next, the specimen chamber is evacuated to 1.33×10^{-4} Pa. Under 325 nm irradiation in this vacuum, quite similar photoinduced spectral changes were observed in all the specimens. Namely, with increasing t_{ir}, the ($^5D_0 \rightarrow {}^7F_J$ ($J = 0, 1, 2, 3, 4$)) emission intensity of Eu^{3+} ions becomes weak, while a very broad emission band appears and spreads all over the visible light region. The wavelength of the intensity peak of the white PL band observed in all the specimens is between 540 and 620 nm. Especially, the relative intensity decreases of the $^5D_0 \rightarrow {}^7F_2$ emission of the powder compact, RFS film, PLA film and PLA-MC film are 75.3%, 15.6%, 34.5% and 15.4%, respectively. The intensity decrease indicates the decrease of number of Eu^{3+} ion, which is due to photoreduction ($Eu^{3+} \rightarrow Eu^{2+}$). At this stage, the bright white PL can be seen with the naked eye. The whitening speed of the PLA film specimen was the highest among all specimens. In addition, the wavelength of their intensity maximum of the white PL band is specimen-dependent. The spectral structures to be observed in the $^5D_0 \rightarrow {}^7F_2$ emission in the RFS film, PLA film and PLA-MC film, incidentally, differ from that for the powder compact specimen (C-phase Eu_2O_3) in which each Eu^{3+} ion is surrounded by six oxygen ions. Seven-coordinate Eu^{3+} ions account for the spectral difference [2,3,7,8].

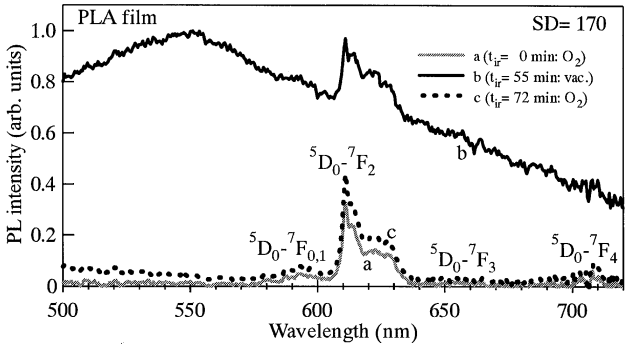

Fig. 4. Reversible spectral change of Eu_2O_3 film produced by the laser ablation method in vacuum.

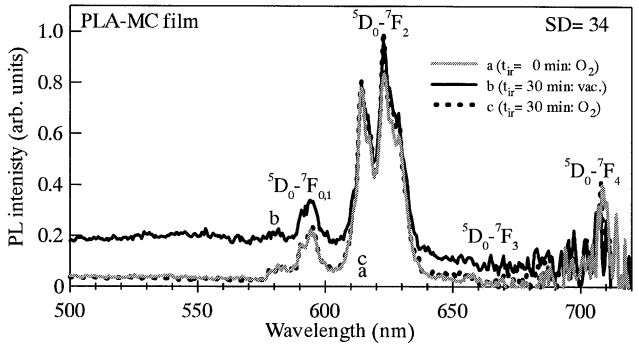

Fig. 5. Reversible spectral change of Eu_2O_3 microcrystal film by the laser ablation method in low-pressure oxygen gas atmosphere.

Oxygen gas is again introduced into the chamber. The change from white PL emission to red emission can be seen with the naked eye. It is found through many successive experiments that the spectral changes as shown in these figures are reversible. Similar experiments were carried out by changing the wavelength of the irradiating laser light. For example, a CW He–Cd laser ($\lambda = 442$ nm), a CW Ar^+ laser ($\lambda = 528.7$, 514.5, 501.7, 496.5, 488.0, 476.5, 472.2, 465.8, and 457.9 nm), and a pulsed Nd^{3+}:YAG laser ($\lambda = 266$, 354.7, 532, and 1064 nm) were used. No spectral change was observed with these lasers, which indicates that the CW UV laser light of the wavelength 325 nm is required to induce the spectral change. The speed of the spectral change is accelerated by increasing the power density of the activating light. The change to the white PL emission can also be observed at low temperatures down to 7 K, which indicates that the phenomenon does not arise from a phonon-assisted process and that it is a purely electronic mechanism. In spite of the changing atmosphere (for example, O_2 gas and air exposures), the white PL state lasts for more than several months at room temperature after the removal of the laser light under room light, and the red PL state re-appears only by irradiating with the same UV laser light under O_2 gas atmosphere of a pressure 1.01×10^5 Pa.

Finally, we turn to the observed photoinduced spectral change between the red- and white PL. Noting the result that the 325 nm photons are essential to induce the spectral change. The 325 nm irradiation in vacuum produces both valence change ($Eu^{3+} \rightarrow Eu^{2+}$) and oxygen vacancies. They then induce local structural relaxation (distortion) around photoexcited ions to form a metastable state. A simplified scheme is drawn in Fig. 6, omitting the detailed structure of the 4f electronic states of Eu^{3+} ions. The $^7F_0$, MS and X represent the ground state of Eu^{3+} ions, the metastable state, and one of some 4f excited energy level of Eu^{3+} ions or charge-transfer state, respectively. The coordinate Q expresses some local structural change due to both the valence number change of Eu^{3+} ions and the oxygen vacancy formation. The potential barrier of the height ΔE separates the metastable state from the ground state. In oxidizing atmosphere, the 325 nm radiation produces

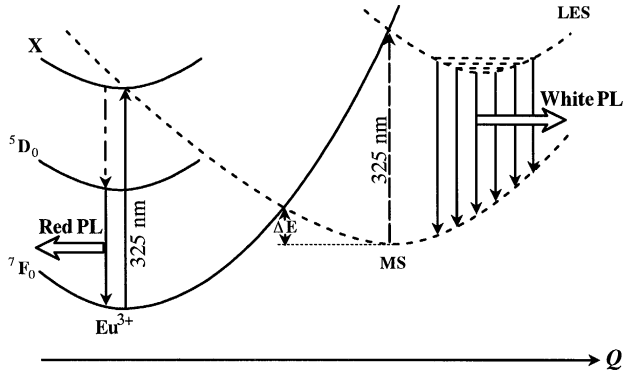

Fig. 6. Schematic energy diagram of the photoinduced reversible spectral change of Eu_2O_3.

the localized excitation of Eu^{3+} ions and the deexcitation of the photoexcited Eu^{3+} ions provides the red luminescence due to the $^5D_0 \rightarrow {}^7F_J$ transitions, via the nonradiative transitions (NR) to the $^5L_6$, ^5D_J ($J = 3, 2, 1, 0$) states. When the photoexcitation is carried out in vacuum, the excited state is relaxed through both a radiative recombination and the local structural relaxation to the metastable state. The 325 nm excitation of the metastable state induces both the backward transition and the transition to the localized electronic state (LES) originating from the Eu^{2+} and oxygen vacancy formations. Since the photoproduced metastable state is extremely stable even at room temperature in oxygen, air and vacuum atmospheres after stopping 325 nm irradiation as described above, the potential barrier separating the ground state ($^7F_0$) from the MS must be high enough to suppress the thermal-forward and -backward transitions between the $^7F_0$ state and MS. The LES is a luminescence center strongly coupled with lattice vibrations and, therefore, gives a broadband luminescence as observed. Our PL-excitation spectra measurements on all the specimens show that the laser wavelength 325 nm corresponds the lower-energy edge of the charge-transfer (CT) absorption band ($Eu^{3+} + O^{2-} \rightarrow Eu^{2+} + O^{1-}$) and the transition energy to higher excited states of Eu^{3+} ions; for example, $^7F_0 \rightarrow {}^5L_J$ transitions. Therefore, the CT and ^5L_J states are candidates for the origin of the X state. However, the observed spectral change is thought to be a surface phenomenon. The detailed surface electronic structure should be clarified for further discussion.

Acknowledgements

This work is supported by Interdisciplinary General Joint Research Grant for Nihon University, and by Project Research Grant from The Institute of Information Sciences, College of Humanities and Sciences, Nihon University. This work is also partially supported by a Grant-in-Aid for Scientific Research from the Ministry of Education, Science, Sports, Culture and Technology, Japan.

References

[1] K.A. Gschneid Jr., L.R. Eyring, in: Handbook on the Physics and Chemistry on Rare Earths, Vol. 3, North-Holland, Amsterdam, 1979.
[2] S. Mochizuki, T. Nakanishi, Y. Suzuki, K. Ishi, Book of Abstracts, International Chemical Congress of Pacific Basin Societies, Part 2, Honolulu, Hawai, 2000.
[3] S. Mochizuki, T. Nakanishi, Y. Suzuki, K. Ishi, Meeting Abstr. Phys. Soc. Jpn, Part 4, 55 (2) (2000) 627.
[4] E. Bezig, J.K. Trautman, Science 257 (1992) 189.
[5] G.H. Dieke, Spectra and Energy Levels of Rare Earth Ions in Crystal, Interscience, New York, 1968.
[6] H.M. Crosswhite, H.W. Moos (Eds.), Optical Properties of Ions in Crystals, Interscience, New York, 1967, p. vi.
[7] J. Dexpert-Ghys, M. Faucher, P. Caro, Phys. Rev. B 23 (1981) 607.
[8] G. Wakefield, H.A. Keron, P.J. Dobson, J.L. Hutchison, J. Colloid Interface Sci. 215 (1999) 179.

phys. stat. sol. (b) **223**, 247 (2001)

Subject classification: 78.30.Hv; S10.1

Optical Study of MnO under High Pressure

Y. MITA[1]) (a), Y. SAKAI (a), D. IZAKI (a), M. KOBAYASHI (a, c), S. ENDO (b, c), and S. MOCHIZUKI (d)

(a) Graduate School of Engineering Science, Osaka University, Osaka 560-8531, Japan

(b) Research Center for Materials Science at Extreme Conditions, Osaka University, Osaka 560-8531, Japan

(c) CREST, Japan Science and Technology Corporation, Kawaguchi, Saitama 332-0012, Japan

(d) College of Humanities and Sciences, Nihon University, Tokyo 156-8550, Japan

(Received October 10, 2000)

Raman and optical absorption studies of the antiferromagnetic insulator MnO were performed at several temperatures under high pressure. In Raman scattering at 2 K, it was observed that the two-magnon peak shifts to higher energy with increasing pressure and then disappears at around 20 GPa. This suggests that a change in spin arrangement occurs at that pressure. At 77 K the peak-vanishing pressure increases to 25 GPa. At room temperature, a jump of the Raman peak position was observed at 30 GPa and the peak vanishes at 89 GPa. These results are consistent with previous X-ray diffraction studies which showed phase transitions at 30 and 90 GPa. The vanishing of the Raman peak suggests a metallization transition. The pressure dependence of the Mn^{2+} d–d transition observed in optical absorptions was consistent with the crystal field theory up to around 25 GPa at room temperature.

Introduction MnO is well known as a Mott insulator and has antiferromagnetic character at temperatures lower than T_N = 118 K. It has type-II spin structure in which ferromagnetically ordered (111) sheets are stacked antiferromagnetically in the [111] direction. This causes the rock-salt (B1) structure to undergo a small trigonal lattice distortion below T_N, contracting along a [111] direction. Recently new phase boundaries have been observed at 30, 90 and 120 GPa by X-ray diffraction performed at room temperature [1] and theoretical works about the phase transitions have been reported [2]. There have been few experimental studies of the magnetic properties at low temperature and high pressure [3–5] and the highest reported value of applied pressure is only 3.3 GPa [4]. It is difficult to study aniferromagnetic materials by conventional magnetization measurement under high pressure, both because the magnetization signal is very weak on account of the anti-parallel spin configuration in antiferromagnetic materials and because of the small sample volume needed in the pressure cell. On the other hand, only 10^{-8} cm^3 of crystal is required for accurate Raman detection, which enables us to use a diamond anvil cell (DAC). Furthermore, the Raman shift due to the antiferromagnetic magnon is larger than that of a ferromagnetic one [6]. Since the posi-

[1]) Corresponding author; Tel.: +81-6-6850-6417; Fax: +81-6-6845-4632;
e-mail: mita@mp.es.osaka-u.ac.jp

tion and intensity of the magnon Raman peak are strongly affected by the spin configuration, drastic changes of the magnon Raman peak indicate changes in the spin arrangement. Thus magnon Raman scattering is one of the best ways to study magnetic phase transitions of antiferromagnetic materials under high pressure [7].

The localized d-states of Mn^{2+} ions are split into dε and dγ states by the octahedral crystal field created by surrounding O^{2-} ions. The validity of this crystal field model can be investigated from the effect of pressure on the d–d transition energy [8, 9]. In this paper we report studies of magnetic phase transitions and Mn^{2+} d–d transition of MnO under very high pressure by Raman scattering and absorption measurements.

Experiment Raman and absorption measurements were performed. The Raman study was carried out in back scattering geometry on single crystals of MnO in the pressure range 0–90 GPa at 2, 77 and 300 K. Samples were pressurized using a DAC. Liquid helium or a methanol–ethanol (4:1) solution was used as a pressure medium as occasion demands. For pressure calibration, the standard ruby fluorescence method was used. The excitation source was the 514.5 nm line of an argon ion laser. Scattered light was detected by a Jobin-Yvon triple monochromator T64000 and a Jobin-Yvon Spex Spectrum-one CCD (charge coupled device) system. Visible and near-infrared (IR) absorption measurements were also performed up to 80 GPa on powdered samples at room temperature. No pressure medium was used. Jobin-Yvon types H20 and H20IR monochromators were used in visible and near-infrared regions, respectively.

Results and Discussion Figure 1 shows pressure dependence of the Raman spectrum measured at 2 K. In the spectrum obtained at 1 GPa, two peaks are observed clearly around 500 and 550 cm^{-1}. These are a two-magnon (2M) and a two-TO phonon Raman peak, respectively [10, 11]. With increasing pressure, the 2M and 2TO peaks shift toward higher energy. The 2M peak becomes weak and disappears around 19 GPa. A relation between applied pressure and the peak position is illustrated in Fig. 2, here open circles and full squares represent 2M and 2TO Raman peaks, respectively. Up to 20 GPa, pressure coefficients of 2M and 2TO are 1.1 and 2.4 cm^{-1}/GPa,

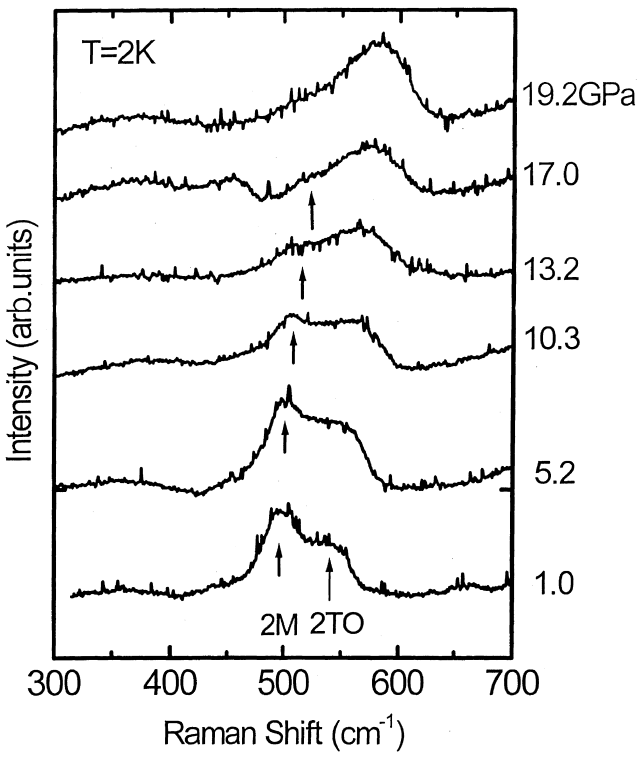

Fig. 1. Raman spectra of MnO under several pressures obtained at 2 K. A two-magnon (2M) and a 2TO phonon peak are seen. With increasing pressure, the former becomes weak and vanishes around 19 GPa

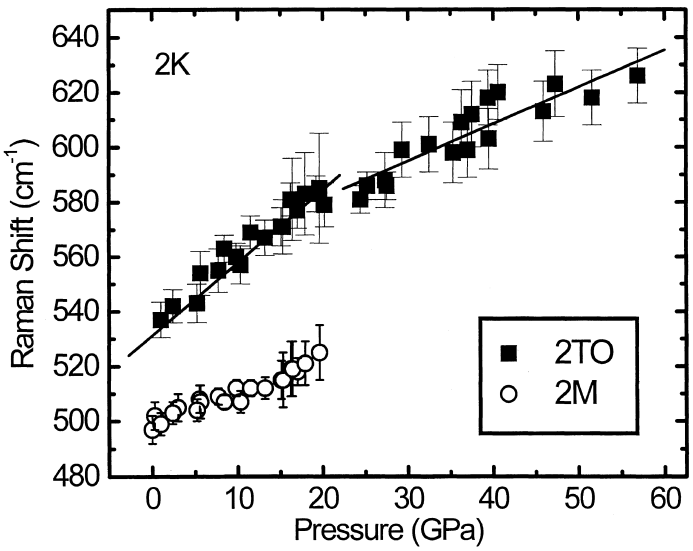

Fig. 2. Pressure dependence of Raman peak positions at 2 K. Full squares and open circles represent 2TO phonon and two-magnon (2M) Raman peaks, respectively. At around 20 GPa, the 2M peak vanishes and a change in pressure coefficient of the 2TO peak occurs from 2.4 to 1.3 cm^{-1}/GPa

respectively. Above 20 GPa, the 2M peak disappears and the pressure coefficient of the 2TO peak becomes 1.3 cm^{-1}/GPa. These results suggest that the antiferromagnetic spin configuration exists up to 20 GPa and a change in spin arrangement (magnetic phase transition) occurs around 20 GPa. However, we are unable to determine the precise spin arrangement in the higher pressure region. At 77 K, the 2M Raman peak disappears around 25 GPa. At room temperature, only the 2TO peak is observed, because the temperature is higher than T_N (Fig. 3). A small peak around 670 cm^{-1} is attributed to scattering associated with electronic excitation of impurities [10]. The 2TO peak vanishes at 89 GPa and we observed that the sample becomes highly reflective around the pressure. The metallic nature around 90 GPa has observed previously by Kondo et al. [1]. The pressure dependence of the 2TO peak position is illustrated in Fig. 4. A slight jump of the peak toward lower energy is seen around

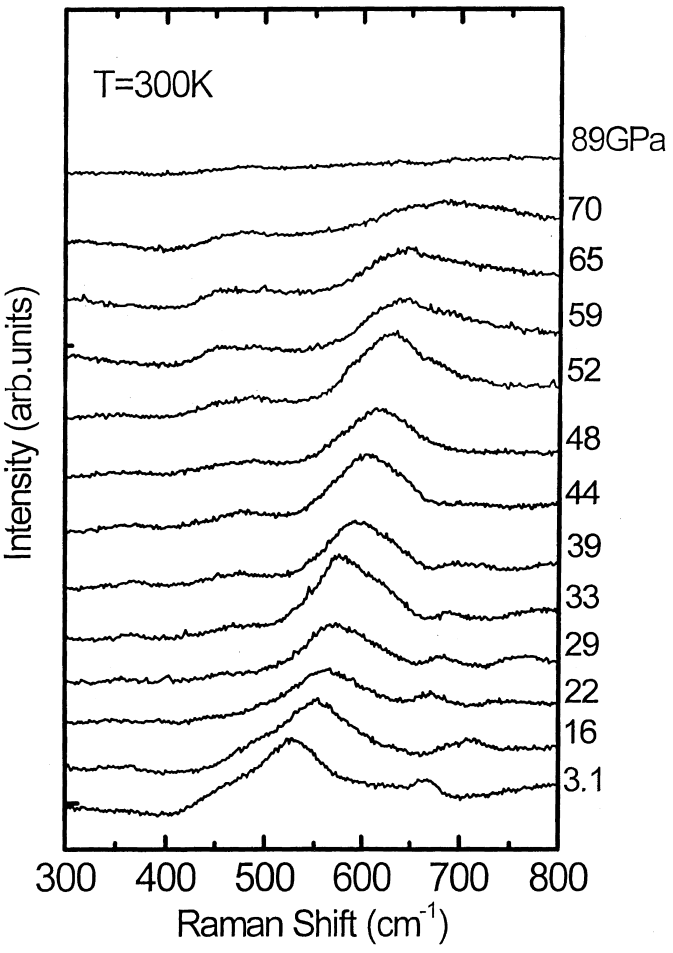

Fig. 3. Raman spectra at room temperature. The peak disappears at 89 GPa. Vanishing of the Raman peak suggests metallization of the sample

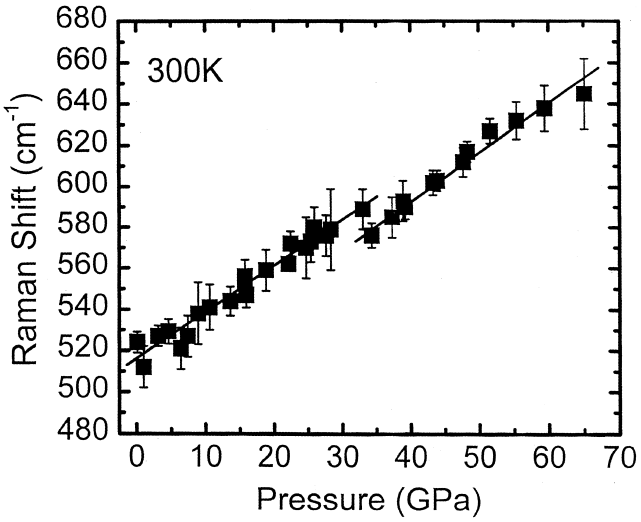

Fig. 4. Relation between Raman peak position and applied pressure at room temperature. A jump of the Raman peak toward lower energy is observed at 30 GPa, where the phase transition occurs

30 GPa. These changes around 30 and 90 GPa may be due to the phase transition observed by X-ray diffraction [1].

Figure 5 shows typical absorption spectra at room temperature under three different pressures. The observed peak, marked by arrows, is ascribed to the 3d crystal field splitting transition from the ground state $^6A_1$ to the excited state $^4T_1$ [12]. With increasing pressure, the peak shifts to lower energy which can be explained by the increase of the crystal field formed by O^{2-} ions. According to the crystal field theory [8], the crystal field splitting $10Dq$ is proportional to a^{-5}, where a is the lattice constant, and the $^6A_1 \rightarrow {}^4T_1$ transition energy (E) normalized to the Racah parameter B is given by $E/B = 32.5$, which is a constant. Figure 6 shows the relation between E and $(a/a_0)^{-5}$, where a_0 is the lattice parameter at ambient pressure, and the values of a were obtained from a pressure–volume relation obtained by X-ray analysis [1]. The highest pressure of the data point corresponds to 78 GPa. The slanting line in the figure is calculated by crystal field theory [8]. Up to $(a/a_0)^{-5} = 1.24$ (26.1 GPa), the agreement between theory and experimental result is good. However, the experimental data begin

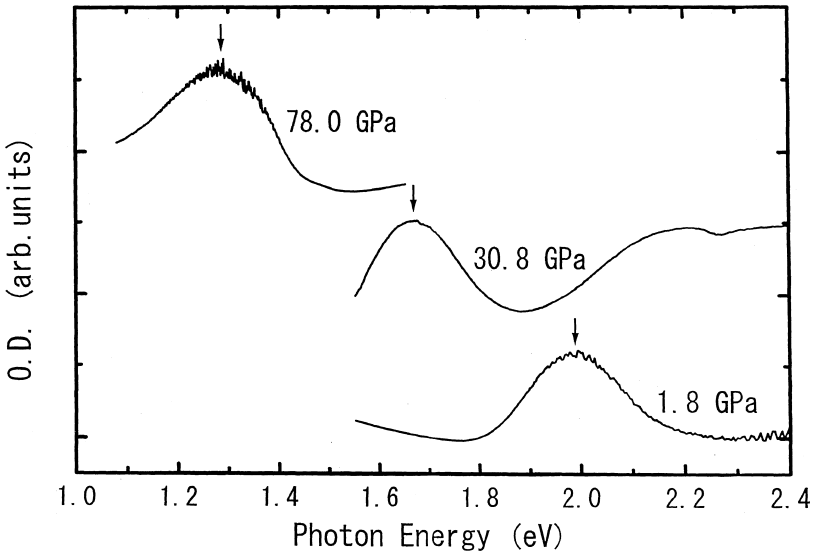

Fig. 5. Absorption spectra at room temperature under three different pressures

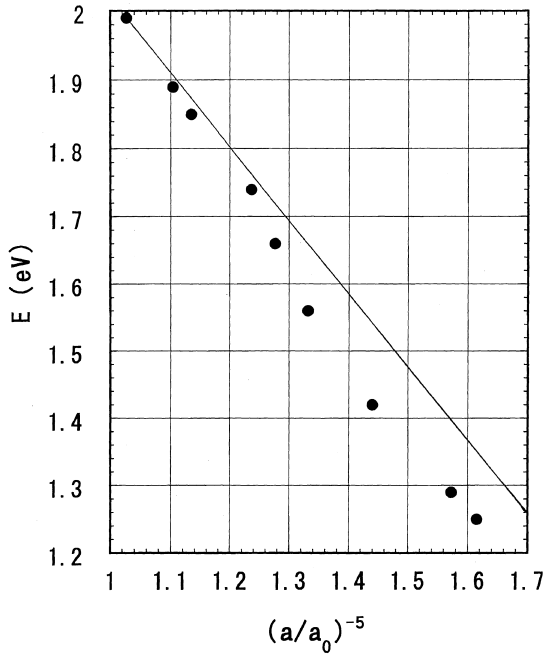

Fig. 6. Relation between $(a/a_0)^{-5}$ and 3d transition ($^6A_1 \rightarrow {}^4T_1$) energies of the Mn^{2+} ion

to deviate from the theoretical line with increasing pressure. This deviation suggests that Mn^{2+} ions are no longer behaving as isolated impurities and the effect of formation of an energy band is no longer ignorable.

Conclusions Raman scattering and absorption measurements of MnO were performed under high pressure. In Raman scattering at 2 K, it was observed that the two-magnon peak shifts toward higher energy with increasing pressure and disappears around 20 GPa. This suggests that a change in spin arrangement occurs at that pressure. At room temperature, a phase transition around 30 GPa is observed, as has previously been reported by X-ray diffraction experiments. Furthermore, vanishing of the 2TO Raman peak is observed around 90 GPa. It seems to correspond to the metallization transition reported previously. From absorption measurements, it appears that the crystal field theory which treats the Mn^{2+} ions as isolated impurities is valid up to around 25 GPa.

Acknowledgements The authors thank Dr. H. Furuta of Research Center for Material Science at Extreme Conditions of Osaka University for technical support, and Dr. G. J. Ackland of Edinburgh University for help with writing the manuscript.

References

[1] T. Kondo, T. Yagi, Y. Shono, T. Kikegawa, and O. Shimomura, Rev. High Press. Sci. Technol. **7**, 148 (1998).
[2] Z. Fang, I. V. Solovyev, H. Sawada, and K. Terakura, Phys. Rev. B **59**, 762 (1999).
[3] H. Barholin, D. Bloch, and R. Geoges, C.R. Acad. Sci. **264**, 360 (1967).
[4] D. Bloch and C. Vettier, J. Magn. Magn. Mater. **15/18**, 589 (1980).
[5] S. Tamura, High Temp. – High Press. **19**, 657 (1987).
[6] P. A. Fleury and R. Loudon, Phys. Rev. **166**, 514 (1968).
[7] Y. Mita, M. Kobayashi, and S. Endo, Phys. Rev. B **62**, 8891 (2000).
[8] Y. Tanabe and S. Sugano, J. Phys. Soc. Jpn. **9**, 766 (1954).
[9] M. Kobayashi, T. Nakai, S. Mochizuki, and N. Takayama, J. Phys. Chem. Solids **56**, 341 (1995).
[10] H.-H. Chou and H. Y. Fan, Phys. Rev. B **13**, 3924 (1976).
[11] H. Y. Fan, Indian J. Phys. A **55**, 218 (1981).
[12] D. R. Huffman, R. L. Wild, and M. Shinmei, J. Chem. Phys. **50**, 4092 (1969).

phys. stat. sol. (c) **0**, No. 2, 763–766 (2003) / **DOI** 10.1002/pssc.200306199

Shallow and deep excited states of mesoscopic structure in AgI–γAl_2O_3 composites

Shosuke Mochizuki* and **Fumito Fujishiro**

Department of Physics, College of Humanities and Sciences, Nihon University, 3-25-40 Sakurajosui, Setagaya-ku, Tokyo 156-8550, Japan

Received 24 July 2002, accepted 27 July 2002
Published online 30 January 2003

PACS 61.72.Nn, 68.35.Fx, 71.35.Cc, 78.55.Qr

The photoluminescence (PL) and PL excitation (PLE) spectra of superionic conducting AgI–γAl_2O_3 composites have been measured at different temperatures between 7 K and room temperature. The X-ray diffraction patterns of these composites have also been measured at room temperature. The PL intensity peak observed at 426 nm is closely connected with radiative decay of free excitons in AgI, while other emission bands are connected with shallow excited states in AgI and deep excited states at the AgI/γAl_2O_3 interface. With increasing excitation light intensity, the PL efficiencies of several emission bands become saturated, except for the free exciton band. These results may give important information about the origins of the high ionic motion in these composites.

1. Introduction Recently, there has been growing interest in fast ion conduction in composites and glasses because these may yield new solid electrolytes. They are also useful materials for studying cooperative phenomena between mobile ions and electrons in solids. Moreover, it is hoped that transparent electrical conductors can be found, which are useful for optoelectronic devices. Shahi and Wagner first reported the extremely high absolute values of electrical conductivity in AgI–γAl_2O_3 composites [1]. Hitherto, considerable work to clarify the mechanism of high ionic conductivity in the AgI–γAl_2O_3 system has been carried out by many workers [2, 3]. Many models to explain the high ionic conductivity have been proposed by noting the high ionic conductivity at the AgI/γAl_2O_3 boundary. However, a basic problem arises. What is the atomic structure of the AgI/γAl_2O_3 interface?

The AgI constituent material shows clear optical spectra due to excitons in the bulk [4], film [5–7] and microcrystals [8]. The exciton behavior is sensitive to the environment in which the excitons are moving, and, therefore, the optical spectra due to excitons may provide useful information about the AgI/γAl_2O_3 interface. In this paper, we report in detail on the optical and structural studies that we have conducted on AgI–γAl_2O_3 composites and propose an atomic structural model.

2. Experimental AgI–γAl_2O_3 composites were prepared by mixing AgI and wet γAl_2O_3 of particle size 60 nm, heating the mixture at about 873 K for 12 h in air and annealing at 373 K for 12 h. The atomic structural data of the composites were gathered using an X-ray diffraction (XRD) system with Cu Kα_1 radiation. Photoluminescence (PL) spectra were measured using an optical multichannel analyzer. A N_2 laser (wavelength $\lambda = 337.1$ nm, pulse width <1 ns), a Nd^{3+}:YAG laser ($\lambda = 355$ nm, pulse

* Corresponding author: e-mail: motizuki@physics.chs.nihon-u.ac.jp, Tel./Fax: +81 3 5317 9771

 1610-1634/03/00002-0763 $ 17.50+.50/0

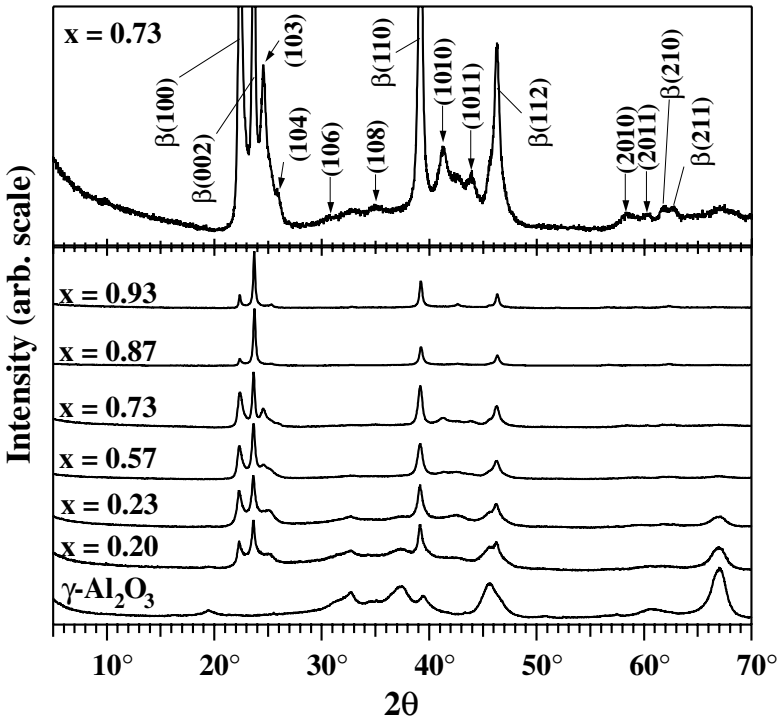

Fig. 1 XRD patterns for different $(AgI)_x(\gamma Al_2O_3)_{1-x}$.

width <5 ns) and a monochromatic light source consisting of a 150 W xenon lamp and a grating monochromator were used as the excitation source. PL excitation (PLE) spectra were recorded using an apparatus consisting of the same monochromatic light source described above, a grating monochromator and a synchronous light detection system.

3. Results and discussion The XRD patterns of different $(AgI)_x(\gamma Al_2O_3)_{1-x}$ composites were measured at room temperature and the results for x = 0, 0.20, 0.23, 0.57, 0.73, 0.87 and 0.93 are shown in Fig. 1. With increasing x, some broadening of the peaks and weakening of the (h0l) peaks of βAgI become pronounced at 2θ = 25.4°, 32.8°, 42.6°, 47.2°, 52.0° and 66.5°. However, new diffraction lines can be observed near reduced (h0l) peaks, as reported by Lee et al. [2]. They can be referred to a new stacking

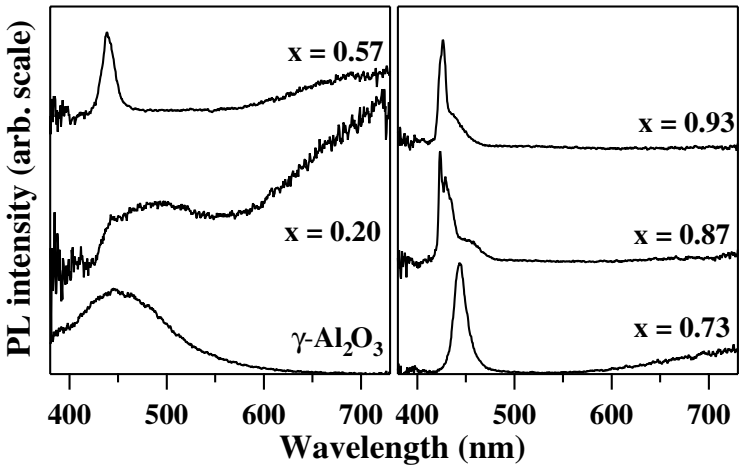

Fig. 2 PL spectra for different $(AgI)_x(\gamma Al_2O_3)_{1-x}$ at 10 K.

sequence of the close-packed planes in the wurtzite structure of AgI. They also explain the XRD features of AgI–γAl_2O_3 composites by taking account of seven-hexagonal-layer polytype AgI (7H-AgI) with the stacking sequence ABCBCAC [2, 9, 10]. The new diffraction lines at 24.5°, 25.8°, 30.7°, 34.8°, 41.5°, 43.9°, 58.2° and 60.2° seem to correspond to the (103), (104), (106), (108), (1010), (1011), (2010) and (2011) peaks of the polytype structure, respectively. On further increasing x, the XRD pattern becomes close to that of the Type II AgI specimen [9], which has the 7H structure.

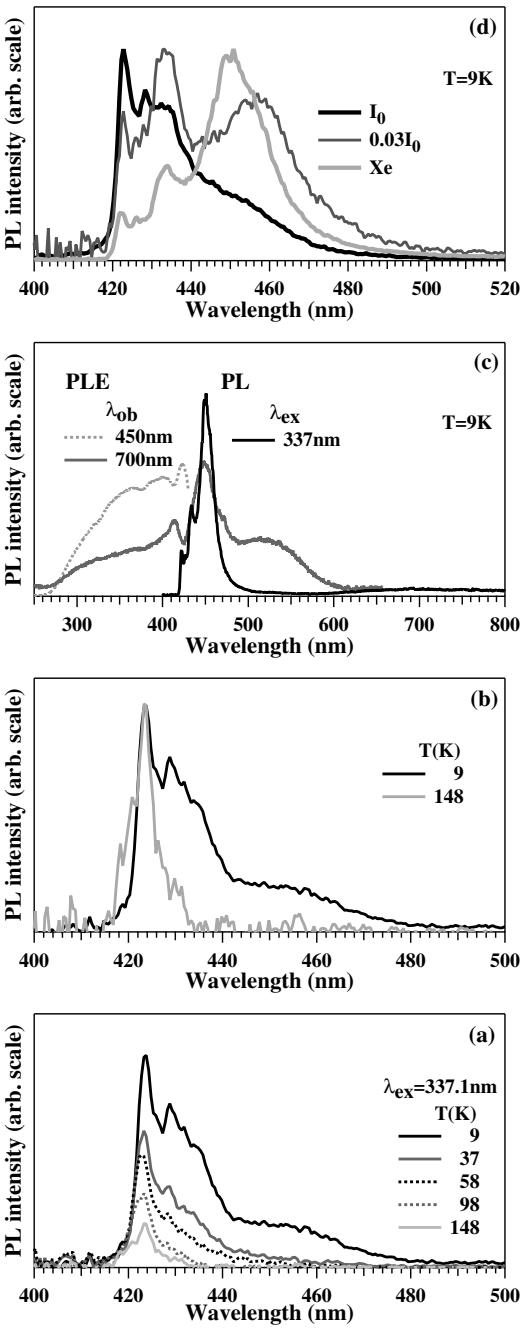

The PL spectra obtained for $(AgI)_x(\gamma Al_2O_3)_{1-x}$ with different compositions at 10 K are compared in Fig. 2. The PL was excited by the 337.1 nm laser line of the N_2 laser. Pure γAl_2O_3 shows a broad PL band centered at about 448 nm. Addition of a small amount of AgI, $x = 0.2$, leads to a decrease of the PL intensity at shorter wavelengths than about 425 nm which corresponds to the $Z_{1,2}$ exciton energy of pristine AgI. The light absorption by environmental AgI may decrease the intensity of light emitted from γAl_2O_3 particles. A very broad PL band centered at 720 nm appears, which may arise from the AgI/γAl_2O_3 interface. This broad band may be assigned to radiative decay of AgI excitons trapped by a deep potential at the AgI/γAl_2O_3 interface. On further increasing x, the PL intensity of the very broad band decreases and several PL bands around 440 nm become prominent. Since the $Z_{1,2}$ free-exciton energy is 2.915 eV (= 425 nm), the bands around 440 nm may be assigned to radiative decay of AgI excitons trapped by a shallow potential inside AgI domains in the AgI–γAl_2O_3 composite. At the higher x region ($x \geq 0.87$), the 425 nm emission due to free excitons in AgI appears clearly.

Figure 3a shows the temperature dependence of the PL spectrum of $(AgI)_x(\gamma Al_2O_3)_{1-x}$ for x = 0.87. With increasing temperature, free-exciton emission prevails against the shallow- and deep-level emissions. In Fig. 3b the PL spectra observed at 9 and 148 K are compared, which may be due to thermal activations from shallow and deep excited states to the free-exciton state. Figure 3c shows the PL and PLE spectra at 9 K. This

Fig. 3 PL spectra for $(AgI)_{0.87}(\gamma Al_2O_3)_{0.13}$: a, b) temperature dependence; c) PL and PLE spectra; d) excitation light intensity dependence.

indicates that the shallow and deep levels are below 0.16 and 0.56 eV from the bottom of the free-exciton band, respectively. The PLE peak at 413 nm is assigned to free-exciton absorption in polytype-structured AgI [7].

The excitation light intensity (I_{ex}) dependence of the PL spectrum was also studied. The results are summarized as follows. The free-exciton emission increases with I_{ex}, while the shallow and deep level emissions have higher yields than that of the free exciton, but they become saturated under intense excitation. These saturations arise from the finite number of shallow and deep level PL centers. In Fig. 3d the PL spectra under intense I_0 and weak $0.03I_0$ (peak power I_0 = 200 kW) excitations at 9 K are typically compared.

Finally, on the basis of the results described above, we propose a structural model for $AgI-\gamma Al_2O_3$ composites as follows. γAl_2O_3 particles are enveloped with the hexagonal-layer polytype AgI, which has high ionic conductivity. Both the interface and the polytype structure of AgI may play important roles in fast ion conduction. Through this interface, the mobile Ag^+-Ag^+ ion exchange responsible for fast ion conduction may occur. Free excitons are trapped by a shallow potential inside AgI domains and a deep potential at the $AgI/\gamma Al_2O_3$ interface. Since the mean free path of free excitons is finite, the effects of the interface on PL become obscured by the contribution from shallowly trapped excitons inside AgI domains with increasing AgI content (i.e. AgI domain size), as shown in Fig. 2.

Acknowledgements This work was supported in part by a Project Research Grant from the Institute of Information Sciences of the College of Humanities and Sciences (Nihon University), and by a Cooperative Research Grant from the Institute of Natural Sciences (Nihon University). This work was also partially supported by a Grant-in-Aid for Scientific Research from the Ministry of Education, Science, Sports, Culture and Technology, Japan.

References

[1] K. Shahi and J. B. Wagner Jr., J. Electrochem. Soc. **128**, 6 (1981).
[2] J.-S. Lee, S. Adams, and J. Maier, Solid State Ionics **136–137**, 1261 (2000).
[3] M. Nagai and T. Nishino, Solid State Ionics **117**, 317 (1999).
[4] S. Mochizuki and F. Fujishiro, in: Proc. 6th Forum Superionic Conductor Physics, Kyoto, Japan, 24–25 May 2002 (The Solid State Ionics Society of Japan, Kyoto, 2002), pp. 41–46.
[5] M. Cardona, Phys. Rev. **129**, 69 (1963).
[6] S. Mochizuki and Y. Ohta, J. Lumin. **87–89**, 299 (2000).
[7] S. Mochizuki, Physica B **308–310**, 1042 (2001).
[8] S. Mochizuki and K. Umezawa, Phys. Lett. A **228**, 111 (1997).
[9] J.-S. Lee, S. Adams and J. Maier, J. Phys. Chem. Solids **61**, 1607 (2000).
[10] B. L. Davis and L. R. Johnson, Cryst. Latt. Defects **5**, 235 (1974).

phys. stat. sol. (c) **0**, No. 2, 767–770 (2003) / **DOI** 10.1002/pssc.200306200

Shallow- and deep-luminescence centers in AgI-based superionic conductor glass

Shosuke Mochizuki* and **Fumito Fujishiro**

Department of Physics, College of Humanities and Sciences, Nihon University, 3-25-40 Sakurajosui, Setagaya-ku, Tokyo 156-8550, Japan

Received 24 July 2002, accepted 27 July 2002
Published online 30 January 2003

PACS 61.72.Nn, 68.35.Fx, 71.35.Cc, 78.55.Qr

The photoluminescence (PL), time-resolved photoluminescence (TRPL) and PL-excitation (PLE) spectra of superionic conductor glass $(AgI)_{0.85}(Ag_2WO_4)_{0.15}$ have been measured at different temperatures between 8 K and room temperature. The PL intensity peak is observed at 426 nm which corresponds to free exciton wavelength of pristine AgI. There are also different PL bands well related to the internal and interface states of mesoscopic AgI particles in Ag_2WO_4 glass matrix. This may give important information about the origins of superionic conduction. With increasing excitation light intensity, the PL efficiencies of several emission bands become saturated, except for the free exciton band.

1. Introduction In recent years, a growing interest has arisen in the study of highly ion-conducting glasses because the glasses may yield new solid electrolytes and are useful specimens for studying the interactions between mobile ions and electrons in solids. Progress in this research field on the high ionic conductor has been mainly achieved by studying the electrical and thermal properties [1, 2]. However, several fundamental problems arise. What are the atomic structures of glasses? What delocalizes some of the ions in glasses to exhibit fast ion conductions? In order to elucidate these problems, $(AgI)_x(Ag_2WO_4)_{1-x}$ glasses are chosen for the present study because they have high ionic conductivity due to Ag^+ ions. The AgI which is a constituent material shows clear optical spectra due to excitons in the bulk [3], film [4–6] and microcrystals [7]. The exciton behavior is sensitive to the environment in which excitons are moving, and therefore the optical spectra may provide useful information about glass structure. In the present paper, we report on the experimental results of the optical studies on $(AgI)_{0.85}(Ag_2WO_4)_{0.15}$ glasses in detail, and we deduce the glass structure by comparing the optical data with the XRD patterns.

2. Experiments $(AgI)_x(Ag_2WO_4)_{1-x}$ glasses were prepared by mixing AgI, Ag_2O, and WO_3 in air, by heating the mixture at about 873 K for 12 h and by cooling rapidly down to room temperature with a twin-roller. The glass structural data were gathered by a XRD system using Cu $K\alpha_1$ line.

The PL and TRPL spectra were measured by an optical multichannel analyzer system. A N_2-laser (wavelength $\lambda = 337.1$ nm, pulse width <1 ns), a Nd^{3+}:YAG laser ($\lambda = 355$ nm, pulse width <5 ns) and a monochromatic light source consisting of a 150 W xenon lamp and a grating monochromator were used as the excitation source. The PLE spectra were recorded in an apparatus consisting of the same monochromatic light source, a grating monochromator and a synchronous light detection system.

* Corresponding author: e-mail: motizuki@physics.chs.nihon-u.ac.jp, Phone/Fax: +81-3-5317-9771

 1610-1634/03/00002-0767 $ 17.50+.50/0

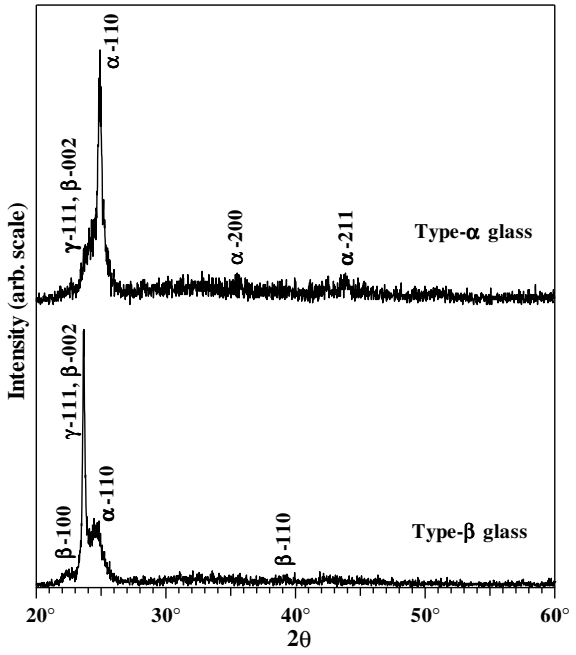

Fig. 1 X-ray diffraction patterns of different $(AgI)_{0.85}(Ag_2WO_4)_{0.15}$ glasses.

3. Results and discussion Depending on the cooling speed of the melt, two different types of specimen were obtained. As shown in Fig. 1, under rapid cooling condition, glass predominantly showing the XRD pattern of αAgI phase (Type-α glass) was obtained, while under less rapid cooling condition, glass predominantly exhibiting the XRD pattern of low-temperature AgI phases (Type-β glass) was obtained. It has been elsewhere reported that AgI precipitated in glass are particles whose sizes are several ten nanometers [8].

Figure 2 shows the PL and PLE spectra of the type-α glass at 9 K. The spectra are normalized in intensity. We have found that the PL for the type-α glass cannot be excited with any ultraviolet light, but with green light. The PL has very broad bandwidth and the intensity peak of the PLE spectra appears near the absorption edge wavelength (483 nm) [6] of αAgI. This indicates that the observed PL is due to excitons of αAgI particles precipitated in glass matrix. The PL spectrum is shifted by about 0.6 eV from the intensity peak of the PLE spectra. The shift may arise from deeply trapped exciton states due to strong electron–phonon interaction in αAgI particle or deeply trapping potential at αAgI/matrix glass interface. The observation wavelength dependence of PLE spectra may arise from different trapped states due to different shapes and sizes of the αAgI particles.

Figure 3 shows the PL spectrum of the type-β glass at different temperatures. The intensity peak at about 425 nm is assigned to radiative decay of free excitons in AgI particles [4, 5, 7], while the sideband at about 436 nm is assigned to radiative decay of excitons trapped by lattice defects and impurities. The broadband peak at about 484 nm is assigned to radiative decay of excitons trapped at β or αAgI/matrix glass interface. The TRPL measurements show that the PL decay times of the free exciton and board

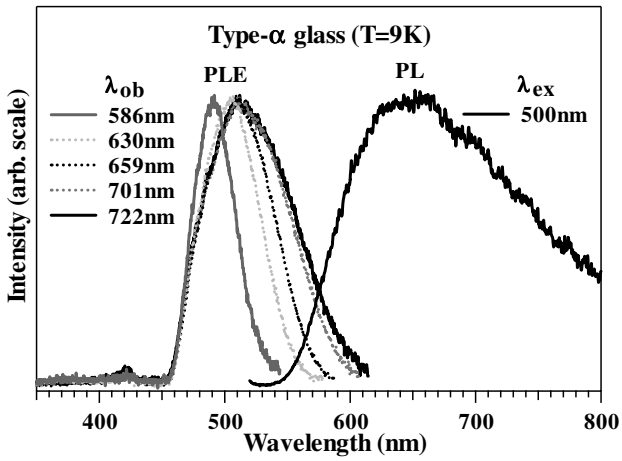

Fig. 2 PL and PLE spectra of type-α $(AgI)_{0.85}(Ag_2WO_4)_{0.15}$ glass at 9 K.

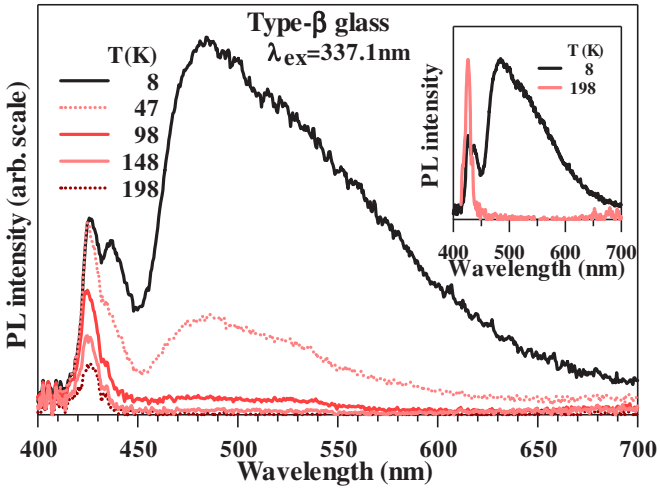

Fig. 3 (online colour at: www.interscience.wiley.com) Temperature dependence of the PL spectrum of type-β $(AgI)_{0.85}(Ag_2WO_4)_{0.15}$ glass.

bands are shorter than 10 ns, that is about 25 ns. As shown in the inset, the PL except for free excitons are weakened and only free exciton PL becomes prominent with increasing temperature, which may be due to a thermally activated reverse process from trapped states to free exciton state.

Figure 4 shows the excitation-light-intensity dependence of the PL spectrum of the type-β glass at 10 K. With increasing laser fluence (peak power I_0 = 200 kW), the intensity of PL due to free excitons increases linearly, while the intensity of PL due to trapped excitons increases and then becomes saturated at higher fluences. In the inset figure, the spectra for intense and weak-excitation limits are compared, which correspond to curves S and W, respectively. This excitation-light-intensity dependence shows that the PL centers due to trapped excitons have higher quantum yields than free excitons, but the number of the PL center is limited.

Finally, we apply the results of the present optical study to the ion conduction. Since the chemical potentials of Ag^+ in AgI and Ag_2WO_4 glass differ, a transition layer is formed at the interface between AgI particle and Ag_2WO_4 glass matrix. Many crystalline defects may be also contained at the interface, which gives rise to deep trap for free exciton and enhances ionic conductivity. The deeply trapped exciton states can be connected to the transition layer. Through this layer, the mobile Ag^+–Ag^+ ion exchange responsible for high ionic conduction occurs in the type-α and type-β glasses.

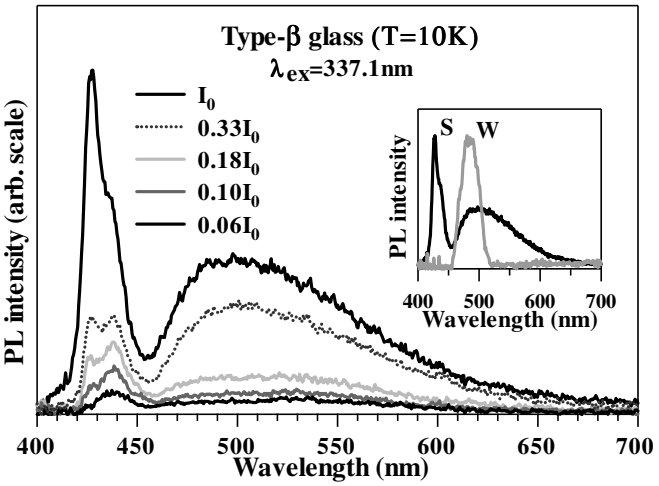

Fig. 4 Excitation-light-intensity dependence of the PL spectrum of type-β $(AgI)_{0.85}(Ag_2WO_4)_{0.15}$ glass at 10 K.

Acknowledgements This work was partially supported by Project Research Grant from The Institute of Information Sciences of College of Humanities and Sciences (Nihon University) and by Cooperative Research Grant from The Institute of Natural Sciences (Nihon University). This work was also partially supported by a Grant-in-Aid for Scientific Research from the Ministry of Education, Science, Sports, Culture and Technology, Japan.

References

[1] B. Roling and M. D. Ingram, Phys. Rev. B **56**, 13619 (1997).
[2] M. Hosono, J. Kawamura, H. Itoigawa, N. Kuwata, T. Kamiyama, and Y. Nakamura, J. Non-Cryst. Solids **244**, 81(1999).
[3] S. Mochizuki and F. Fujishiro, in: Proc. 6th Forum Superionic Conductor Physics, 24–25 May 2002, Kyoto, Japan (The Solid State Ionics Society of Japan, Kyoto, 2002), pp. 41–46.
[4] M. Cardona, Phys. Rev. **129**, 69 (1963).
[5] S. Mochizuki and Y. Ohta, J. Lumin. **87/89**, 299 (2000).
[6] S. Mochizuki, Physica B **308/310**, 1042 (2001).
[7] S. Mochizuki and K. Umezawa, Phys. Lett. A **228**, 111(1997).
[8] M. Tatsumisago, N. Itakura, and T. Minami, J. Non-Cryst. Solids **232/234**, 267 (1998).

Nonlinear Optics, 2002, Vol. 29(7–9), pp. 443–449

THE PHOTOEXCITATION AND RELAXATION OF HIGH IONIC-CONDUCTIVITY GLASSES $(AgI)_x(AgPO_3)_{1-x}$

FUMITO FUJISHIRO* and SHOSUKE MOCHIZUKI†

Department of Physics, College of Humanities and Sciences, Nihon University 3-25-40 Sakurajosui, Setagaya-ku, Tokyo 156-8550, Japan

(Received 22 July 2002; In final form 7 August 2002)

The photoluminescence (PL)-, time-resolved PL (TRPL)- and PL-excitation (PLE) spectra of $(AgI)_x(AgPO_3)_{1-x}$ glasses and Eu^{3+} ion-doped $(AgI)_x(AgPO_3)_{1-x}$ glasses have been measured at different temperatures between 7 K and room temperature. The X-ray diffraction (XRD) data have been also obtained. Comparing the obtained optical spectra with the XRD patterns of these glasses, the local structure and fast Ag^+ ion conduction of $(AgI)_x(AgPO_3)_{1-x}$ glasses are discussed.

Keywords: Photoluminescence; Glass structure; Super ionic conductor; Exciton

1 INTRODUCTION

AgI-based glasses attract much attention because the glasses may yield new solid electrolyte and present useful specimens for studying cooperative phenomena between mobile ions and electrons in solid. Progress in this research field on the high ionic conductor has been mainly achieved by studying the electrical and thermal properties [1]. However, there arise some fundamental problems. What are the atomic structures of AgI dis-

* Corresponding author. E-mail: fumito@phys.chs.nihon-u.ac.jp
† HP URL: http://web.phys.chs.nihon-u.ac.jp/~motizuki/

ISSN 1058-7268 print; ISSN 1029-2500 online
DOI: 10.1080/1058726021000044550

solved in a glass matrix? How does AgI doping delocalize some of Ag^+ ions in glasses to exhibit fast ion conductions? In order to elucidate these problems, $(AgI)_x(AgPO_3)_{1-x}$ glasses are chosen for the present study because they can be easily prepared over large composition ranges and have been widely investigated. Moreover, AgI shows clear optical spectra due to excitons in the bulk [2], films [3–5] and microcrystal [6]. The exciton behavior is sensitive to the environment in which excitons are moving and therefore the optical spectra may provide useful information about glass structure. In the present paper, we report upon the optical studies on $(AgI)_x(AgPO_3)_{1-x}$ glasses and we arrive at a view on the glass structure by comparing the optical data with XRD patterns.

2 EXPERIMENTS

$(AgI)_x(AgPO_3)_{1-x}$ glasses were prepared by mixing AgI, $AgNO_3$ and $NH_4H_2PO_4$ in air, by heating the mixture at about 873 K for 12 h and by cooling rapidly down to room temperature with a twin-roller. By adding Eu_2O_3 to the mixtures, Eu^{3+} ion-doped $(AgI)_x(AgPO_3)_{1-x}$ glasses were produced with the same procedure. The glass structural data were gathered by a XRD system using Cu $K\alpha_1$ line.

The PL and TRPL spectra were acquired by an optical multichannel analyzer (OMA) system. A N_2-laser (wavelength $\lambda = 337.1$ nm, pulse width <1 ns), a Nd^{3+} YAG laser ($\lambda = 355$ nm, pulse width <5 ns) and a monochromatic light source consisting of a Xe lamp and a grating monochromator were used as the excitation source. The PLE spectra were recorded in an apparatus consisting of the same monochromatic light source, a grating monochromator and a synchronous light detection system.

3 RESULTS AND DISCUSSION

We have measured XRD patterns of different $(AgI)_x(AgPO_3)_{1-x}$ glasses at room temperature for $x = 0$, 0.2, 0.4, 0.6 and 0.8 shown in Figure 1(a). The glass scattering of the $AgPO_3$ host glass at about 31 degrees is not greatly changed by the introduction of AgI. This indicates that the AgI dopant does not greatly alter the short-range covalent bonding of the phosphorous–oxygen network but is primarily introduced into voids of the host phosphate glass structure. This structure within the glass also gives rise to the prepeak at about 12 degrees. With increasing x, the prepeak shifts toward smaller

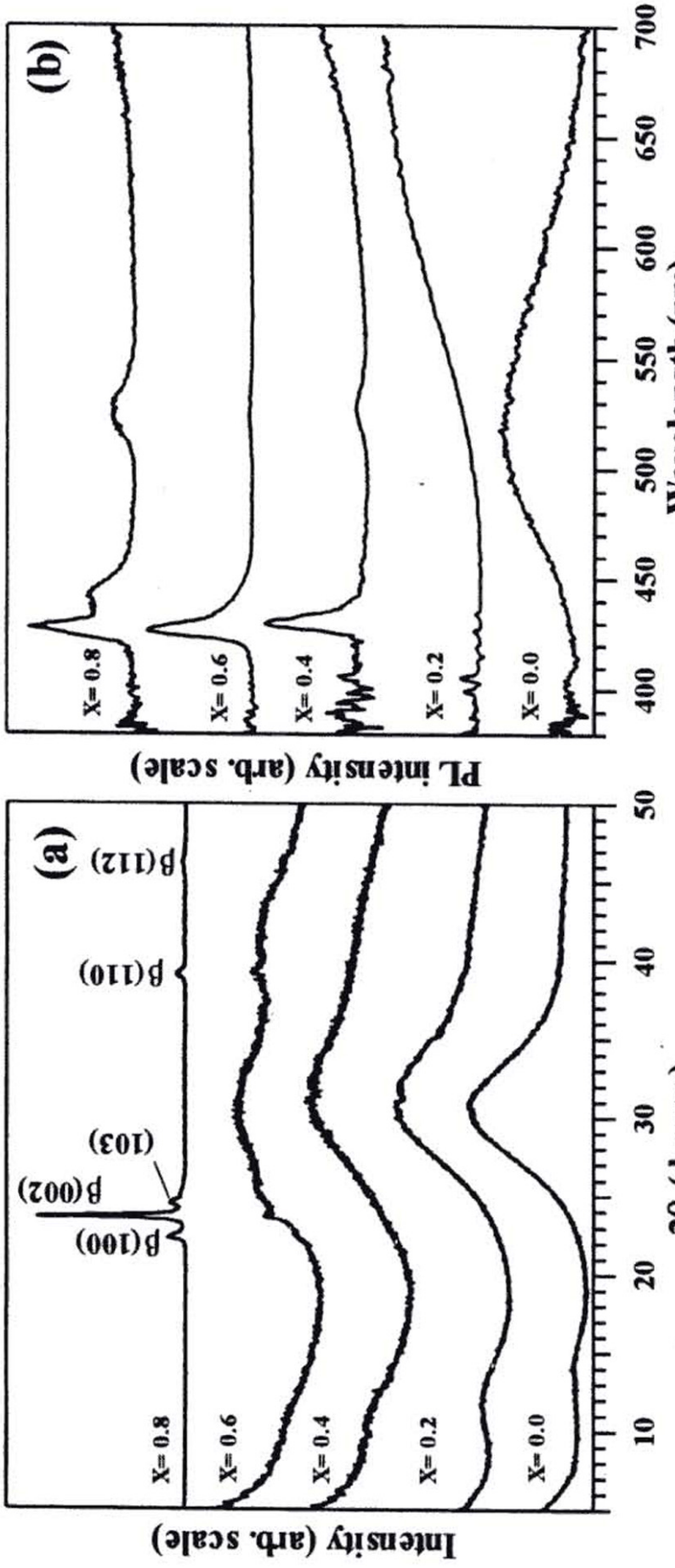

FIGURE 1 $(AgI)_x(AgPO_3)_{1-x}$ glasses (a) XRD patterns at room temperature; (b) PL spectra at 10 K.

angle side. This indicates that the structure of the intermediate range order varies with AgI doping [7]. The present experiment shows that the glass consists of interpenetrating silver phosphate and silver iodide regions with length scales of order 1 nm. For $x > 0.4$, the diffraction pattern shows a superposition of the glass scattering and Bragg powder diffraction of stacking-fault-contained βAgI [8] which precipitate in $AgPO_3$ glass matrix.

Figure 1(b) shows the PL spectra of $(AgI)_x(AgPO_3)_{1-x}$ glasses at 10 K. Pure $AgPO_3$ glass shows a very broad PL band centered at 516 nm. The PL band is Stokes-shifted by about 1.1 eV from absorption threshold and PLE one. Doping a small amount of AgI to this glass weakens considerably the 516 nm-PL band and new broad PL bands appear at about 700 nm and 526 nm. The attenuation of the 516 nm band is mainly due to absorption of doped AgI. Although AgI doping induces this longer wavelength band, the structure of AgI resolved into the glass is not clear at present. With further AgI doping ($x > 0.4$), the intensity of the 700 nm band decreases, together with growing a sharp PL band appears at about 429 nm. This 429 nm band arises from the radiative decay of excitons trapped by shallow level in AgI. It shows that some precipitation of AgI crystallite occurs in $(AgI)_x(AgPO_3)_{1-x}$ glasses, which agrees with the XRD data. The exciton band is accompanied by a shoulder band at about 442 nm. The radiative decay of exciton trapped by defects gives rise to the shoulder band. The 526 nm band has a long decay time is connected to the radiative decay of excitons trapped deeply at the AgI crystallite/matrix glass interface. Since the precipitation of AgI in $AgPO_3$ glass accompanies ionic conductivity increase, the Ag^+–Ag^+ ion exchange through such AgI crystallite/matrix glass interface is thought to be easier at higher x region. The electron of free exciton in AgI crystallite is electrically attracted and trapped by mobile Ag^+ ions at the interface as observed in the present experiments.

Figure 2 shows the PL and PLE spectra of Eu^{3+} ion-doped $AgPO_3$, -$(AgI)_{0.1}(AgPO_3)_{0.9}$ and -$(AgI)_{0.2}(AgPO_3)_{0.8}$ glasses. The spectra consist of a series of resolved bands peaking at 570–700 nm, which are assigned to $^5D_0 \rightarrow {}^7F_j$ ($j = 0,1,2,3,4$) transitions of the Eu^{3+} ions [9]. No difference was observed in the Eu^{3+} PL properties of the glasses with different amounts of AgI. In Figure 3, the PL spectra of the Eu^{3+} ions, subtracted by the background PL due to glass and then normalized in each PL intensity maximum, are plotted. Since the PL spectra are almost the same, it is considered that the glass structure is not changed by doping with AgI. The most striking result of the present study is the spectral feature of the

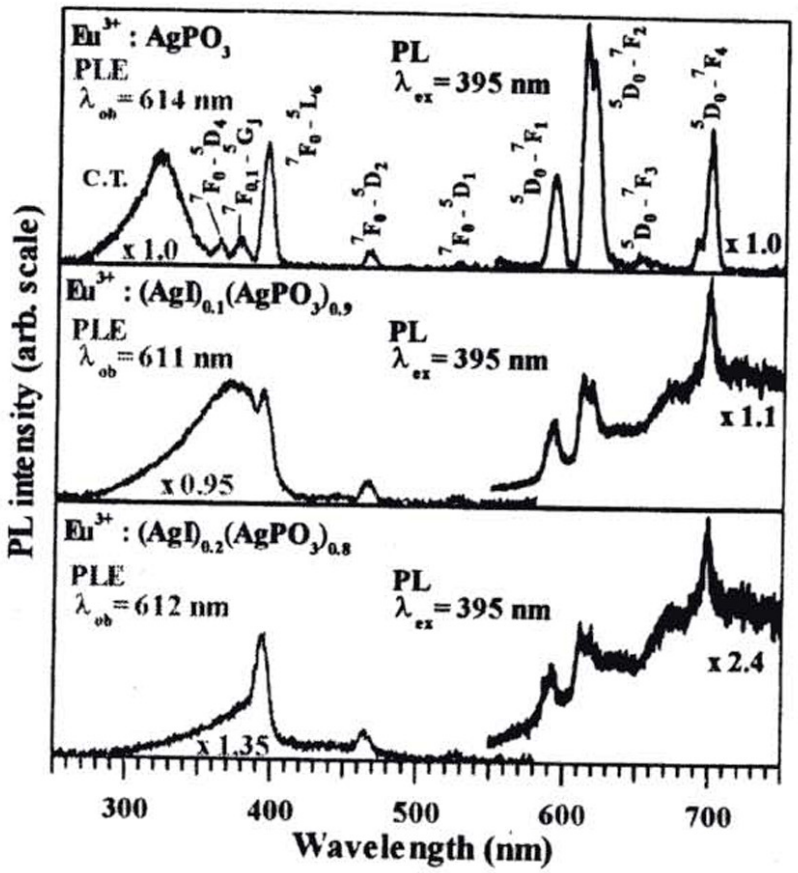

FIGURE 2 PL and PLE spectra of Eu^{3+}-doped $AgPO_3$ glass and two different Eu^{3+} ion-doped $(AgI)_x(AgPO_3)_{1-x}$ glasses at 10 K.

$^5D_0 \rightarrow {}^7F_j$ transitions of the Eu^{3+} ion, which are revealed by the local environment of the Eu^{3+} ions. Among the $^5D_0 \rightarrow {}^7F_j$ transitions, the $^5D_0 \rightarrow {}^7F_2$ band at 612 nm is an electric dipole transition and sensitive to chemical bonds in the vicinity of the Eu^{3+} ion. On the other hand, the $^5D_0 \rightarrow {}^7F_1$ band at 592 nm is a magnetic dipole one and hardly varies with the crystal field strength around the Eu^{3+} ion. Therefore, the PL intensity ratio of $^5D_0 \rightarrow {}^7F_2$ to $^5D_0 \rightarrow {}^7F_1$ transitions, called the asymmetry ratio, gives a measure of the degree of distortion from the inversion symmetry of the local environment of the Eu^{3+} ions in matrix. The asymmetry ratio of the glass is calculated as 1.49, which lies well within the range of values usually found in oxide glasses, indicating that the Eu^{3+} ions occupy high-symmetry sites. It is apparent that the asymmetry ratio is not changed with increasing AgI, suggesting that the random glass-network structure around the Eu^{3+} ions is not changed by doping with AgI. This agrees with the result which the density of $(AgI)_x(AgPO_3)_{1-x}$ glass decreases with increasing x without altering the short-range covalent bonding of the phosphorous–oxygen network, with introducing into voids of the phosphate glass structure [10].

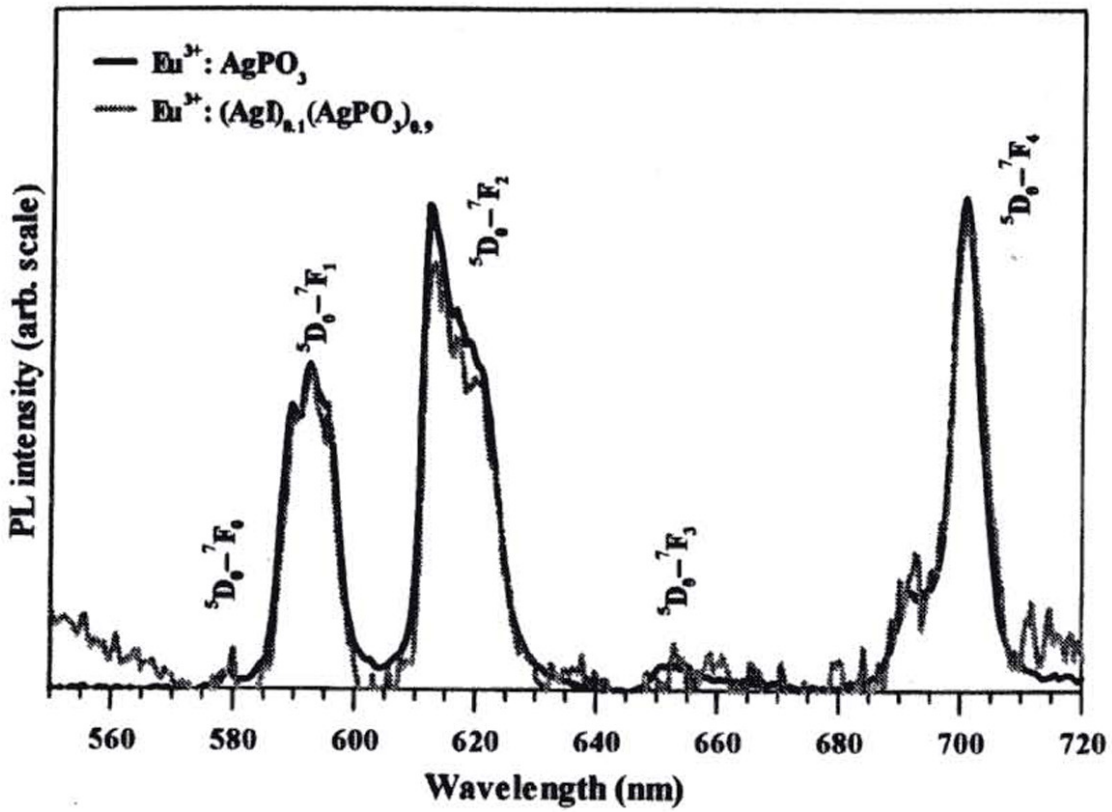

FIGURE 3 PL spectra due to the $^5D_0 \rightarrow {}^7F_j$ transitions in Eu^{3+} ion-doped $AgPO_3$ glass with Eu^{3+} ion-doped $(AgI)_{0.1}(AgPO_3)_{0.9}$ glass at 10 K.

Acknowledgements

This work is partially supported by a Grant-in-Aid for Scientific Research from the Ministry of Education, Science, Sports, Culture and Technology, Japan. This work is partially supported by Interdisciplinary General Joint Research Grant from Nihon University, by Project Research Grant from The Institute of Information Sciences of College of Humanities and Sciences (Nihon University), and by Cooperative Research Grant from The Institute of Natural Sciences of Nihon University.

References

[1] Roling, B. and Ingram, M. D. (1997). *Phys. Rev. B*, **56**, 13619.
[2] Mochizuki, S. and Fujishiro, F. (2002). *Proceeding of the 6th Forum on Superionic Conductor Physics* Kyoto (Japan), May 24–25, 2002, pp. 41–46.
[3] Cardona, M. (1963). *Phys. Rev.*, **129**, 69.
[4] Mochizuki, S. and Ohta, Y. (2000). *J. Lumin.*, **87–89**, 299.
[5] Mochizuki, S. (2001). *Physica B*, **308–310**, 1042.
[6] Mochizuki, S. and Umezawa, K. (1997). *Phys. Lett. A*, **228**, 111.
[7] Kartini, E., Collins, M. F., Indayaninghsih, N. and Svensson, E. C. (2000). *Solid State Ionics*, **138**, 115.

[8] Lee, J.-S., Adams, S. and Maier, J. (2000). *J. Phys. Chem. Solids*, **61**, 1607.
[9] Dieke, G. H. (1968). *Spectra and Energy Levels of Rare Earth Ions in Crystals*. Wiley Interscience, New York.
[10] Wicks, J. D., Borjesson, L., Bushnell-Wye, G., Howells, W. S. and McGreevy, R. L. (1995). *Phys. Rev. Lett.*, **74**, 726.

Nonlinear Optics, 2002, Vol. 29(10–12), pp. 603–608 Taylor & Francis
Taylor & Francis Group

ENHANCED PHOTOLUMINESCENCE OF C_{70}/POROUS GLASS COMPOSITE

TAUTO NAKANISHI* and SHOUSUKE MOCHIZUKI

Department of Physics, College of Humanities and Sciences, Nihon University
3-25-40 Sakurajosui, Setagaya-ku, Tokyo 156-8550, Japan

(Received 22 July 2002; In final form 22 August 2002)

We have investigated the optical absorption (OA) and photoluminescence (PL) spectra of C_{70}/porous-glass (PG) composite at room temperature, comparing with C_{70}-solution and C_{70} film. The composite shows remarkably enhanced PL. The PL spectrum of C_{70}/PG composite is accompanied by several molecular-vibronic side bands of isolated C_{70} molecule. From the time-resolved photoluminescence (TRPL) spectra of the C_{70}/PG composite, the spectral distribution and lifetime show two different relaxation processes. The obtained results are analyzed by taking into account the thermally-activated delayed fluorescence. The long lifetime component of the PL may arise from interactions between C_{70} molecules and porous wall of PG. This interaction is responsible for the observed PL enhancement.

Keywords: Fullerene; Porous glass; Photoluminescence

1 INTRODUCTION

The broadband photoluminescence (PL) of C_{70} fullerene has drawn much interest in recent years. The fullerene powder is easily evaporated to produce homogeneous films on various kinds of substrate and therefore it may well yield materials for light-emitting optical devices. However, the fullerene films exhibit very weak PL at room temperature. Therefore, it is desirable to improve the PL efficiency of C_{70}. Recently, we have

* Corresponding author: E-mail: nakanisi@phys.chs.nihon-u.ac.jp

ISSN 1058-7268 print; ISSN 1029-2500 online
DOI: 10.1080/1058726021000044893

produced C_{70}/PG composites by embedding C_{70} into the pores of nanometer size in PG, and observed a considerable enhancement of the PL efficiency of C_{70} at room temperature [1]. In this paper, we report in detail four types of measurements: the steady-state, the time-resolved, the excitation-light chopping frequency-resolved PL measurements and optical absorption (OA) measurement of C_{70}/PG composite and propose a PL enhancement model.

2 EXPERIMENTAL DETAILS

Nominally pure C_{70} powders (>99.5%) were used without further purification. Corning porous glass (Vycor 7930) with an average pore size of 4 nm was rinsed with acetone and with distilled water, and heated in air at 823 K for several weeks. After immersing the heat-treated porous glass in the 9.5×10^{-4} M C_{70}/toluene solutions for a week at room temperature, the C_{70}-contained PG was heated at 523K in vacuum for 24 hours to remove residual solvent. We examined thus produced C_{70}/PG composite by an atom-forced microscope with the 10 nm resolution, but could not detect any aggregation of C_{70} molecules. The C_{70} film with a thickness of about 1 μm was grown on a silica glass substrate by thermal evaporation in a vacuum of 10^{-4} Pa.

PL spectra were acquired by an optical multichannel analyzer (OMA) consisting of a grating monochromator and an image-intensified charge coupled device (ICCD) system. A Nd^{3+}:YAG laser ($\lambda = 355$ nm, pulse width <5 ns) was used as the excitation source. To avoid photo-polymerization of C_{70} molecules, the excitation power density used was sufficiently weak. The emitted light was led to the same OMA through an optical fiber. Time-resolved photo luminescence (TRPL) spectra were also measured by using the same Nd^{3+}:YAG laser, the same OMA and two delay pulse generators. PL spectra were also measured as a function of excitation-light chopping frequency (f_{ch}) by an apparatus consisting of a monochromatic continuous-wave (cw) light source, a mechanical light chopper, a grating monochromator and a synchronous light detection system. Optical absorption spectra were recorded by using a double beam spectrophotometer. All optical measurements were performed at room temperature.

3 RESULTS AND DISCUSSION

Figure 1 shows the PL spectra (solid lines) of (a) C_{70}/PG composite and (b) C_{70} in toluene and (c) C_{70} film measured at room temperature with the

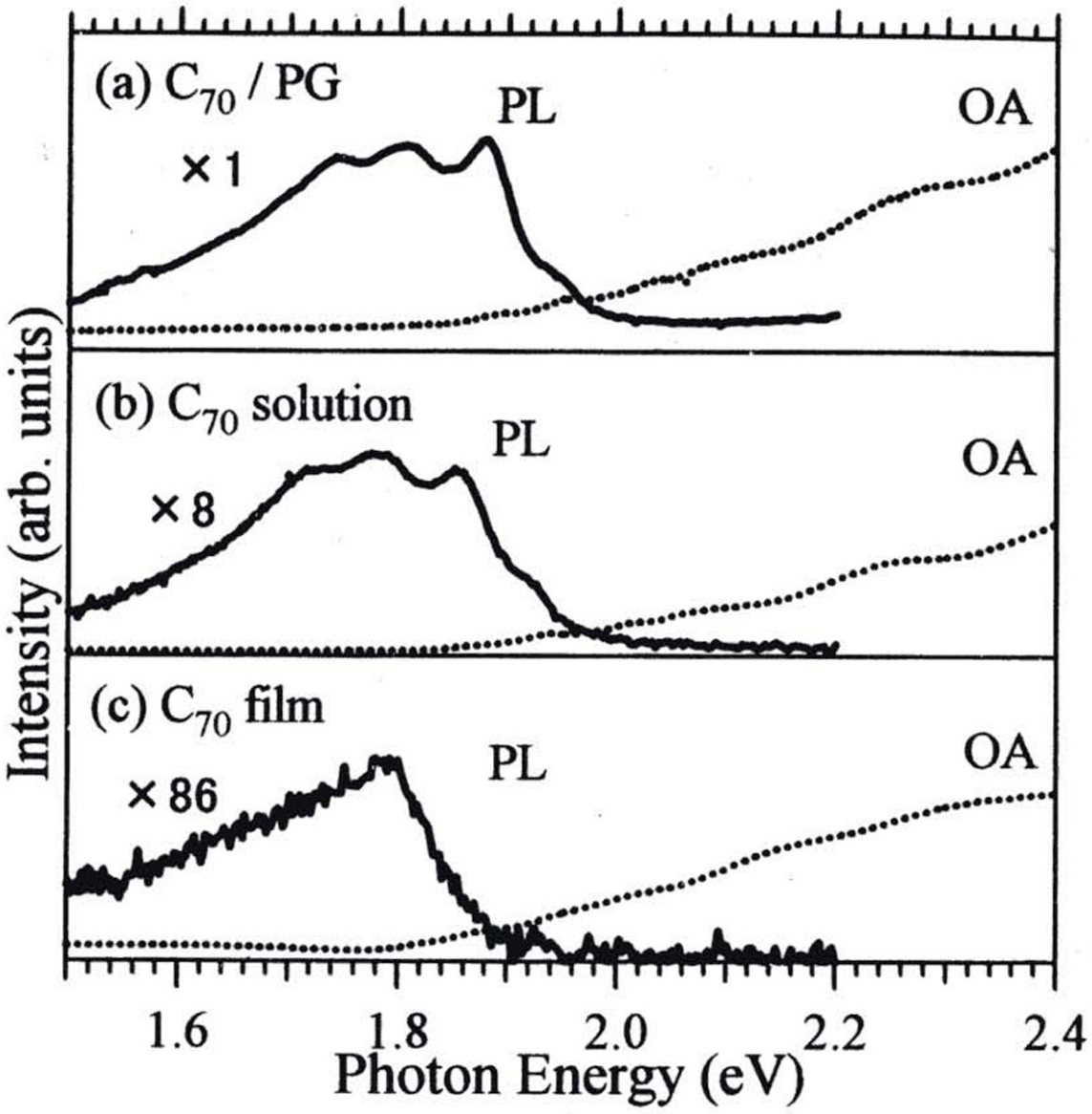

FIGURE 1 Photoluminescence (PL) (solid lines) and optical absorption (OA) (broken lines) spectra at room temperature: (a) C_{70}/PG composite; (b) C_{70} in toluene solution; (c) C_{70} film. Each PL spectrum is corrected for the absorbed light-power.

He–Cd laser line (442 nm). The OA spectra (broken lines) of the same C_{70}/PG composite, C_{70} solution and C_{70} film are also shown. The PL spectrum exhibits some vibronic structures at 1.878, 1.807, 1.741, and 1.945 eV. At the lower energy side, two weak emissions are observed at 1.564 and 1.544 eV. These vibronic structures are similar to those of C_{70} solution (Fig. 1(b)), except for the blue shift of about 25 meV. Any C_{70}-concentration dependence of the peak-energy shift was not observed in the present study. Since the 1.878 eV PL peak of C_{70}/PG composite is close to the first absorption peak at 1.887 eV, we attribute the 1.878 eV band to the 0–0 transition. The 1.878, 1.807, 1.741 and 1.947 eV bands are assigned

to be the vibronic transitions from the excited singlet state S_1 to the ground singlet state S_0. The transitions are induced by the borrowing-intensity mechanism as proposed by Herzberg and Teller (HT) [4,5]. The weak PL bands at 1.544 eV accompanied by the 1.564 eV band are also attributed to the HT-type vibronic transitions from the excited triplet state T_1 to the singlet state S_0 which cannot clearly be observed in C_{70} solution shown in Figure 1(b). At the higher energy side of those PL bands, a tail of the white broad PL band is observed. The tail is due to surface coupling between C_{70} molecule and porous wall, since such tail cannot be observed in pristine porous glass. The white PL band shows the reversible photo-induced spectral changes by irradiation of two different laser-light wavelengths, which will be reported elsewhere. Under cw excitation, C_{70}/PG composite shows strong red-light emissions which can be clearly seen with the naked eye. The PL efficiency of C_{70}/PG composite is about 8 times as large as that of C_{70} solution and 86 times as large as that of C_{70} film. The PL spectrum of C_{70}/PG composite similar to that of C_{70} solution suggests that C_{70} molecules in the PG are well isolated from each other, though the environment of C_{70} molecules differ considerably. An average number of C_{70} molecules per pore of size 4 nm is estimated to be c.a. 0.05 from the observed OA intensity.

Figure 2(a) shows the time-resolved PL spectra of the C_{70}/PG composite for different delay times t_d. The sharp spike at 1.747 eV (twice of 355 nm) is due to the stray scattering of the excitation laser pulse of (355 nm). The PL spectrum at $t_d = 0$ resembles to the steady-state PL one shown in Figure 1(a). The HT-type vibronic PL bands around the 1.878, 1.810, and 1.732 eV (closed circles) are observed even at $t_d = 57$ ms. These decay profiles consist of two exponential components, whereas the 1.769 eV emission (closed triangle) decays with a single exponential. The decay constant of the short component is $\tau_1 = 23 \pm 3$ ms and that of the long component $\tau_2 \gg 100$ ms. Because τ_1 is close to the lifetime of 24.5 ± 2 ms reported by Bachilo *et al.* [5], we have attributed τ_1 to the thermally activated-delayed fluorescence (TDF) due to the reverse S_1–T_1 intersystem crossing. The contribution of the long component was clearly observed as a fluorescence persisting over several seconds with the naked eye.

To study the long-lifetime component in more detail, PL spectrum was measured at different temperatures from 10 K to 300 K as a function of the chopping frequency f_{ch} of the excitation light. The results obtained at room temperature are shown in Figure 2(b). We have subtracted a background PL band due to PG from the raw spectra for different f_{ch} to extract the C_{70}-related emission. It is obvious that the PL intensity of 0–0 transition

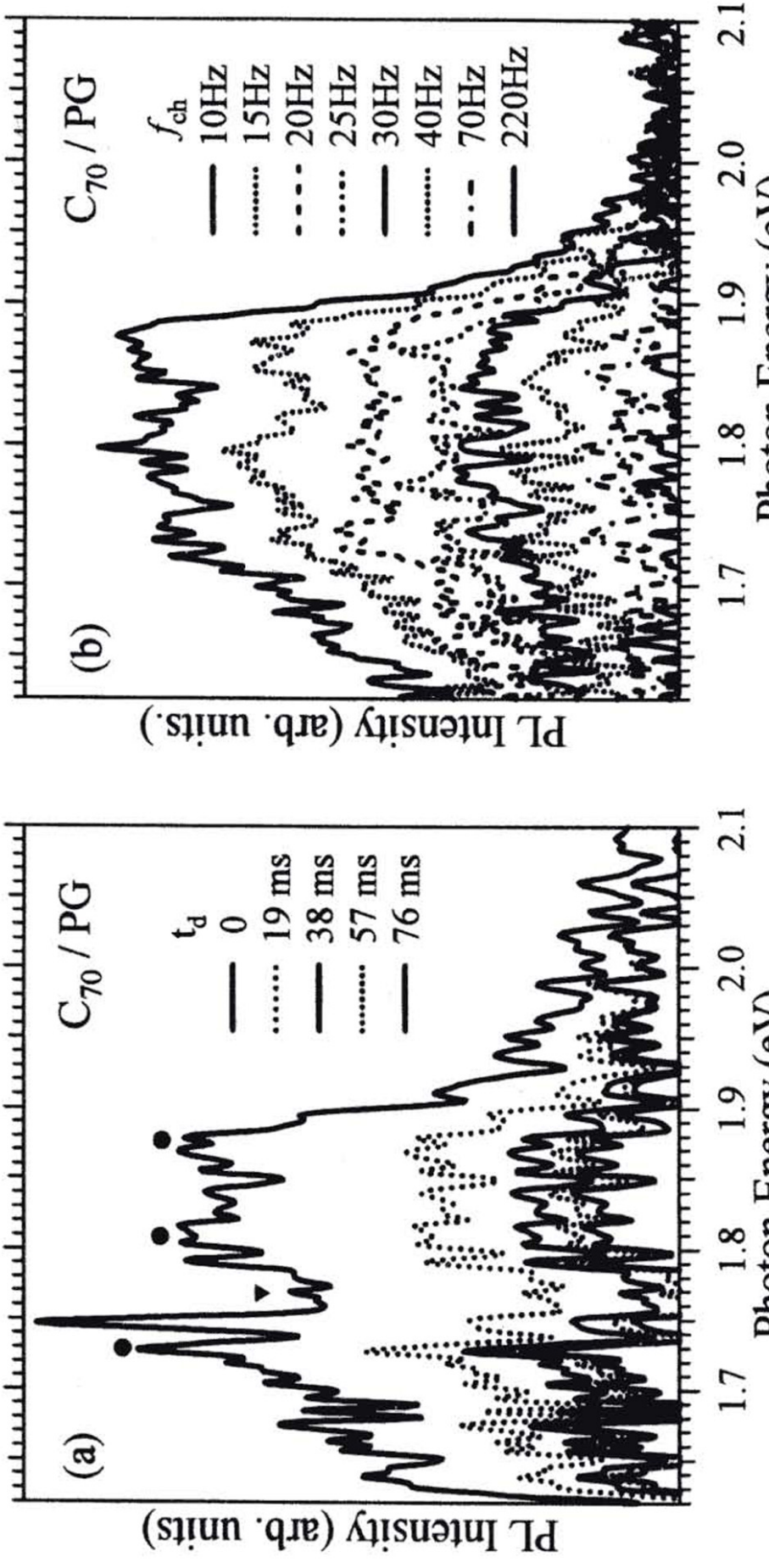

FIGURE 2 PL spectrum of C_{70}/PG at room temperature: (a) Time-resolved photoluminescence spectra at different delay times t_d; with 355 nm excitation, (b) chopping frequency dependence of the excitation light with 442 nm excitation.

decreases with increasing f_{ch}. Note that f_{ch} is related to both the light irradiation time τ_{ir} (*i.e.*, $\tau_{ir} = 1/2f_{ch}$) and the time window for PL measurement. Under 30 Hz, this long τ_2 mainly contributes to the PL, especially at the steady-state PL corresponding to the zero-f_{ch} limit, it plays a significant role to the observed enhanced PL. In addition, with decreasing temperature, the PL intensity decreases considerably. This indicates that the transitions responsible for the PL enhancement are assisted by molecular vibrations, that is, both τ_1 and τ_2 may be due to TDF. The difference in their lifetime is due to the difference in C_{70} molecular environment.

In conclusion, we infer that the following two mechanisms mainly contribute to the longer lifetime of PL in our experiment. (1) The coupling between C_{70} molecule and the OH group at PG pore inner-surface affects the C_{70} molecular vibration and suppresses the transition probability of the vibronically allowed S_1–S_0 transition. (2) The restricted-orientation, -vibration and -collision of C_{70} molecules by the interaction with glass-pore wall should also reduce the radiationless transition. These reduced radiative H-T type vibronic S_1–S_0 transitions and restricted molecular motion and collision in PG give rise to the observed long lifetime. The PL enhancement for integration of the long decay component is expected to be a characteristic of C_{70} molecules inside pore of PG.

Acknowledgements

This work is partially supported by a Grant-in-Aid for Scientific Research from the Ministry of Education, Science, Sports, Culture and Technology, Japan. This work is partially supported by Interdisciplinary General Joint Research Grant from Nihon University, by Project Research Grant from The Institute of Information Sciences of College of Humanities and Sciences (Nihon University), by Cooperative Research Grant from The Institute of National Sciences of Nihon University.

References

[1] Argentine, S. M., Kotz, K. T. and Francis, A. H. (1995). *J. Am. Soc.*, **117**, 11762.
[2] Nakanishi, T. and Mochizuki, S. (2000). *Book of Abstracts*, Part 2. International Chemical Congress of Pacific Basin Societies, Honolulu, Hawaii.
[3] Negri, F. and Orlandi, G. (1998). *J. Chem. Phys.*, **108**, 9675.
[4] Rice, J. H., Galaup, J. P. and Leach, S. (2002). *Chem. Phys.*, **279**, 23.
[5] Bachilo, S. M., Benedetto, A. F., Weisman, R. B., Nossal, J. R. and Billups, W. E. (2000). *J. Phys. Chem. A*, **104**, 11265.

phys. stat. sol. (a) **189**, No. 3, 935–938 (2002)

Magnetic Phase Transition in Antiferromagnetic Materials under High Pressure

Y. MITA[1]) (a), Y. SAKAI (a), M. KOBAYASHI (a, c), S. ENDO (b, c), and S. MOCHIZUKI (d)

(a) Graduate School of Engineering Science, Osaka University, Osaka 560-8531, Japan

(b) Research Center for Materials Science at Extreme Conditions, Osaka University, Osaka 560-8531, Japan

(c) CREST, Japan Science and Technology Corporation, Kawaguchi, Saitama 332-0012, Japan

(d) College of Humanities and Sciences, Nihon University, Tokyo 156-8550, Japan

(Received May 1, 2001; accepted September 30, 2001)

Subject classification: 75.30.Kz; 75.50.Ee; S5.2; S10.1

Pressure dependence of magnon Raman scattering was studied at 1.8 K up to 4 and 60 GPa for solid oxygen and MnO, respectively. In both cases, magnon peaks shift to the higher energy side with increasing pressure. In solid oxygen, the pressure coefficients and intensity of magnon Raman peak are observed to change simultaneously around 0.1 GPa and the peak vanishes at 2.9 GPa. In MnO, the two-magnon Raman peak vanishes around 20 GPa. These results mean that changes in spin configurations (i.e. magnetic phase transitions) occur at these pressures.

1. Introduction It is difficult to study aniferromagnetic materials by conventional magnetization measurement under high pressure, both because the magnetization signal is very weak on account of anti-parallel spin configuration in antiferromagnetic materials and because of the small sample volume possible to be loaded in a pressure cell. On the other hand, only 10^{-8} or 10^{-9} cm^3 of sample volume is required for the accurate Raman detection, which enables us to use a diamond anvil cell (DAC). Furthermore, the Raman shift due to the antiferromagnetic magnon is larger than that of a ferromagnetic one [1]. Since the position and intensity of magnon Raman peak is strongly affected by spin configuration, drastic changes of magnon Raman peak indicate changes in spin arrangement. Thus, magnon Raman scattering is one of the best ways to study magnetic phase transition of antiferromagnetic materials under high pressure. We applied the method to detect magnetic phase transitions of two important materials (solid oxygen and MnO) under high pressure.

Solid oxygen is one of the most interesting molecular crystals because of its behavior as a magnetic material. From many magnetic experiments, it is clarified that the lowest temperature phase (α-phase) is antiferromagnetic with T_N (Néel temperature) = 24 K [2]. However, the highest pressure at which magnetization measurements have been performed is only 0.6 GPa [3]. On the other hand, MnO exhibits antiferromagnetism at temperatures lower than T_N = 118 K. It has type II spin structure in which ferromagnetically ordered (111) sheets are stacked antiferromagnetically in the [111] direction.

[1]) Corresponding author; Tel.: +81-6-6850-6417; Fax: +81-6-6845-4632; e-mail: mita@mp.es.osaka-u.ac.jp

 0031-8965/02/18902-0935 $ 17.50+.50/0

This causes the rock-salt (B1) structure to accompany a small trigonal lattice distortion below T_N, contracting along a [111] direction. No magnetization measurement under low temperature and high pressure conditions has been reported previously.

2. Experiments Raman scattering measurements were performed in backscattering geometry at 1.8 K in solid oxygen and MnO in the pressure range of 0–4 and 0–60 GPa, respectively. Samples were pressurized using a DAC. Solid oxygen was compressed directly and liquid helium was used as a pressure medium for MnO. For pressure calibration, the standard ruby fluorescence method was used. The excitation source was a 514.5 nm line of argon ion laser. Scattered light was detected by a Jobin-Yvon triple monochromator T64000 and a Jobin-Yvon Spex Spectrum-one CCD (charge coupled device) system. In solid oxygen, the measurements were performed at both librational (0–300 cm^{-1}) and vibrational (1500–1600 cm^{-1}) regions.

3. Results and Discussion Figure 1 shows the Raman spectra in librational region under various pressures. Besides two strong libron peaks, a peak due to the one-magnon scattering [4] is also seen around 30–40 cm^{-1} marked by arrows. The relations between applied pressure and Raman peak positions of the vibron (V), librons (L1, L2) and magnon (M) are illustrated in Fig. 2. The pressure coefficients of the L1, L2 and M peaks change around 0.1–0.2 GPa, on the other hand, in vibron (V), the change occurs around 0.4 GPa and the influence remains up to 0.6 GPa. Until now the reason of this discrepancy is unknown. Furthermore, the change in pressure coefficient of vibron is observed also at 2.3 GPa. The pressure dependences of the magnon peak position (open circles) and its peak intensity normalized by L2 (solid circles) are shown in Fig. 3. With increasing pressure the intensity decreases drastically around 0.1 GPa and the change in the pressure coefficient of peak position occurs at nearly the same pressure. The peak intensity decreases with increasing pressure and disappears around 2.9 GPa. The fact that change in magnon peak position and intensity occurs nearly at the same pressure (at 0.1–0.2 GPa) indicates that the change in spin arrangement (i.e. magnetic phase transition) occurs around there. On the other hand, jump in magnon peak energy at 0.1 GPa is not large and the peak shows nearly continuous high

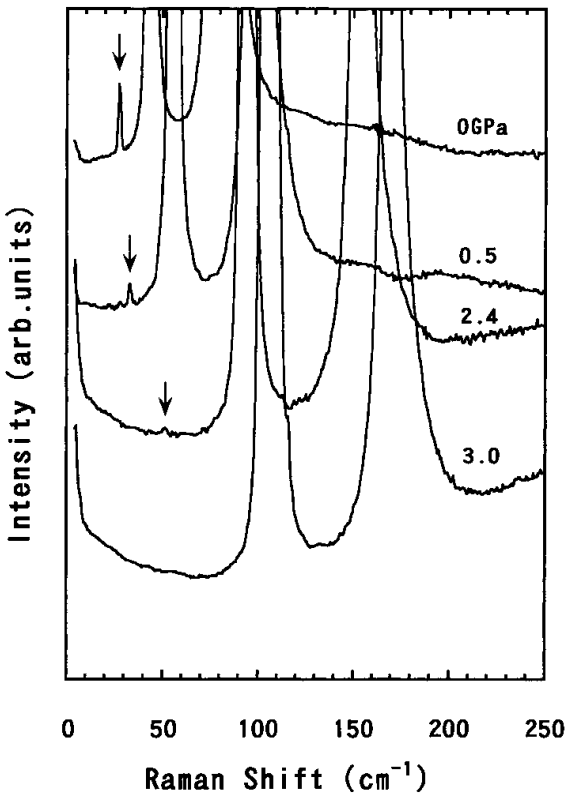

Fig. 1. Raman spectra of solid oxygen at 1.8 K under various pressures

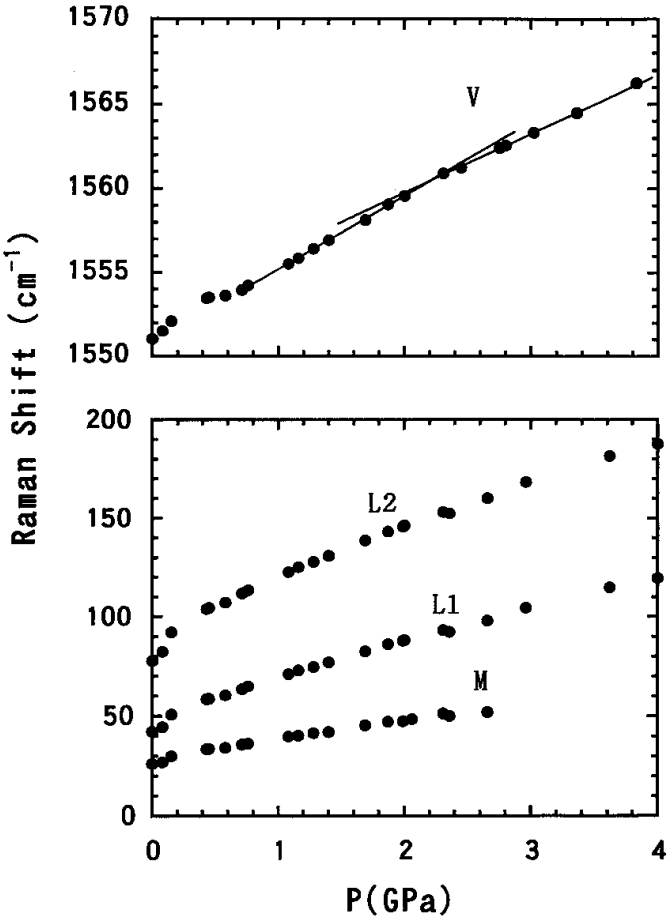

Fig. 2. Pressure dependence of Raman peak positions of the vibron (V), librons (L1 and L2) and magnon (M) in solid oxygen. Lines seen in the upper figure are guides for eye

energy shift with pressure. Therefore, it is deduced that the antiferromagnetic character basically continues at least up to 2.9 GPa and phase transition at 0.1 GPa may be due to a slight change in spin arrangements in the antiferromagnetic phase. Since one-magnon Raman signal reflects the long-range magnetic order ($k = 0$), vanishing of the magnon peak at 2.9 GPa probably means that *this* antiferromagnetic spin order becomes short range. However, it must be emphasized that the phase starts from 2.9 GPa does not necessarily mean that the phase is no more antiferromagnetic. It is also possible the spins align in different type of an antiferromagnetic order.

Figure 4 shows the pressure dependence of Raman spectrum of MnO. In the spectrum obtained at 1 GPa, two peaks are observed clearly around 500 and 540 cm^{-1}. These are a two-magnon (2M) and

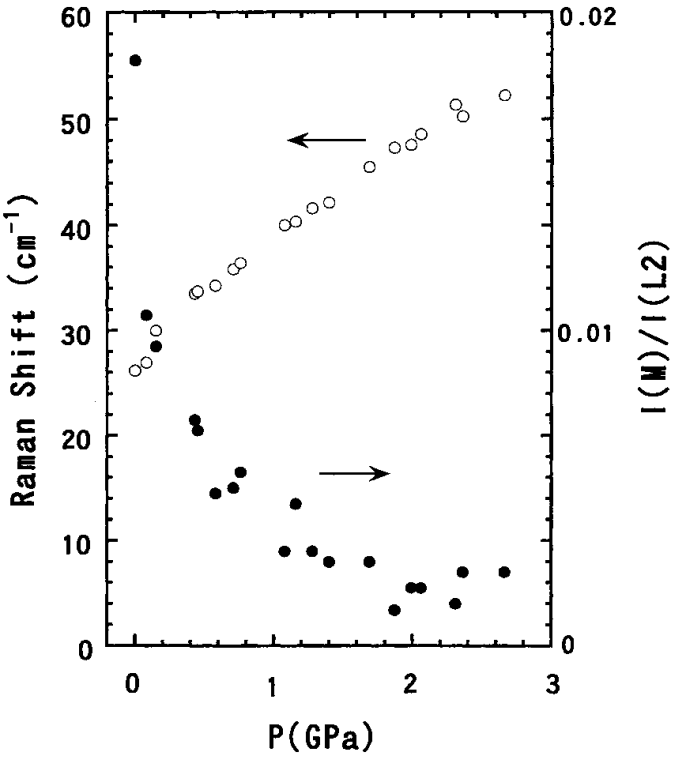

Fig. 3. Relative intensity (solid circles) and peak position (open circles) of magnon Raman peak at various pressures in solid oxygen

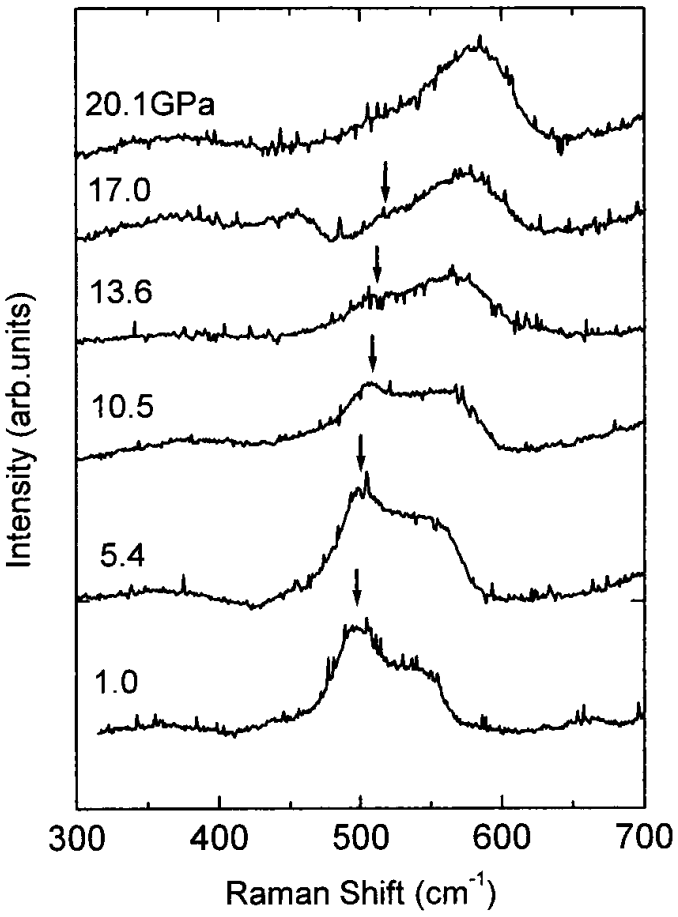

Fig. 4. Raman spectra of MnO at 1.8 K under several pressures

a 2-TO phonon Raman peaks, respectively [5, 6]. With increasing pressure, the 2M and 2TO peaks shift toward higher energy. The 2M peak becomes weak and disappears around 20 GPa. Therefore, the antiferromagnetic spin configuration exists up to 20 GPa and a change in spin arrangement (magnetic phase transition) occurs around 20 GPa. No further phase transition is detected in the pressure region up to 60 GPa.

4. Conclusions Magnetic phase transitions were detected by magnon Raman scattering under high pressure at 1.8 K. In solid oxygen, change in peak intensity and jump of peak position of antiferromagnetic magnon are observed around 0.1 GPa and vanishes at 2.9 GPa. In MnO also, the two-magnon peak shifts toward higher energy with increasing pressure and disappears around 20 GPa. These facts reflect the change in spin arrangements which occurs around the corresponding pressures.

Acknowledgement The authors thank Dr. H. Furuta of Research Center for Material Science at Extreme Conditions of Osaka University for technical support.

References

[1] P. A. FLEURY and R. LOUDON, Phys. Rev. **166**, 514 (1968).
[2] E. KANDA, T. HASEDA, and A. OTSUBO, Physica **20**, 131 (1954).
[3] R. J. MEIER, C. J. SCHINKEL, and A. DE VISSER, J. Phys. C **15**, 1015 (1982).
[4] P. M. MATHAI and E. J. ALLIN, Can. J. Phys. **48**, 1518 (1970).
[5] H.-H. CHOU and H. Y. FAN, Phys. Rev. B **13**, 3924 (1976).
[6] H. Y. FAN, Indian J. Phys. A **55**, 218 (1981).

Available online at www.sciencedirect.com
SCIENCE DIRECT®
Physica B 340–342 (2003) 216–220
PHYSICA B
www.elsevier.com/locate/physb

Structural and optical studies on mesoscopic defect structure in highly conductive AgI–ZnO composites

Fumito Fujishiro*, Shosuke Mochizuki

Department of Physics, College of Humanities and Sciences, Nihon University, 3-25-40 Sakurajosui, Setagaya-ku, Tokyo 156-8550, Japan

Abstract

The electrical conductivity of (x)AgI–$(1-x)$ZnO $(0 \leqslant x \leqslant 1)$ composites at room temperature increases with increasing AgI content and reaches a maximum at about 50% AgI. The results obtained by the scanning electron microscopy, X-ray diffractometry and photoluminescence spectroscopy have clarified high-ionic-conduction pathways related to mesoscopic defect structure at AgI/ZnO interfaces and mesoscopically disordered structure in AgI domain. We have observed also new optical phenomenon, which may arise from excitation energy transfer between AgI-exciton and photoinduced oxygen vacancy at the AgI/ZnO interface.

PACS: 72.80.Tm; 61.72.Nn; 68.35.Fx; 71.35.Cc; 78.55.Hx

Keywords: Defects in oxides; Defects at/near surfaces and interfaces

1. Introduction

The ionic conduction in a composite consisting of AgI and oxide fine particles has received much attention as a model material for searching new solid electrolyte [1,2]. In the composites, electrical conductivity σ was enhanced by a few orders of magnitude higher than that of pristine AgI. Such σ variation is initially explained by taking into account a space charge layer around nucleophilic surface [3]. However, several basic problems were raised about AgI-based composites. How does AgI attach to oxide fine particles? What are the atomic and electronic structures of the AgI/oxide fine particle interface? Why oxide fine particles enhance conductivity? Constituent material AgI shows clear optical spectra due to excitons in the bulk [4], films [5,6] and microcrystals [7]. Besides AgI, most oxides also show exciton spectra. Generally, exciton spectra are very sensitive to the environment in which excitons are moving and, therefore, the optical spectra due to excitons may provide useful information about the AgI/oxide fine particle interfaces. Recently, we have reported the structural, electrical and optical properties of AgI-anatase composites [8]. Very recently, we have fabricated also (x)AgI–$(1-x)$ZnO $(0 \leqslant x \leqslant 1)$ composites and observed σ enhancement. Besides this, we have found new photofunction in the composites. In this paper, we report the structural, electrical and optical studies of AgI–ZnO composites and discuss the

*Corresponding author. Tel./fax: +81-3-5317-9771.
E-mail address: fumito@phys.chs.nihon-u.ac.jp (F. Fujishiro).

0921-4526/$ - see front matter
doi:10.1016/j.physb.2003.09.025

effects of defects at AgI/ZnO interface in these composites.

2. Experimental

AgI–ZnO composites were prepared by mixing AgI powder and ZnO fine particles (with an average diameter of 20 nm), heating the mixture at 873 K for 12 h and then annealing at 373 K for 12 h to remove the stress introduced at the phase transition point of AgI, 420 K. For the σ measurements, the composite powder was uniaxially compressed into pellets under 0.2 GPa for 30 min at room temperature. To avoid the so-called memory effect [9], the pellets were heat-treated at 473 K in air for 12 h and then annealed at 373 K for 12 h, in a lidded crucible. After evaporating silver onto both sides of the pellet, the σ measurements were performed by the impedance method. The composites were characterized by X-ray diffraction (XRD) analysis with Cu $K\alpha_1$ radiation. The morphologies and distributions of Ag, I, Zn and O atoms in the composites were studied by a scanning electron microscope (SEM) (Shimadzu SSX-550). A pulsed Nd^{3+}:YAG laser (wavelength $\lambda = 355$ nm) was used as the excitation source. The photoluminescence (PL) spectra were measured by an optical multichannel analyzer (OMA) consisting of a grating monochromator and an intensified diode-array detector.

Photoinduced-spectral-change experiments were carried out with a continuous wave of He–Cd laser line ($\lambda = 325$ nm) with a power density of 5.4 kW/m^2. The same He–Cd laser line was used to excite luminescence. Emitted light is measured as a function of irradiation time t_{ir} with the same OMA.

3. Results and discussion

The SEM observations and atom-distribution maps indicate that ZnO particles less than 1 μm in size are densely dispersed in AgI matrix and the surroundings of ZnO particles are silver rich. Fig. 1 shows the XRD patterns of (x)AgI–(1−x)ZnO composites at 300 K. All XRD patterns

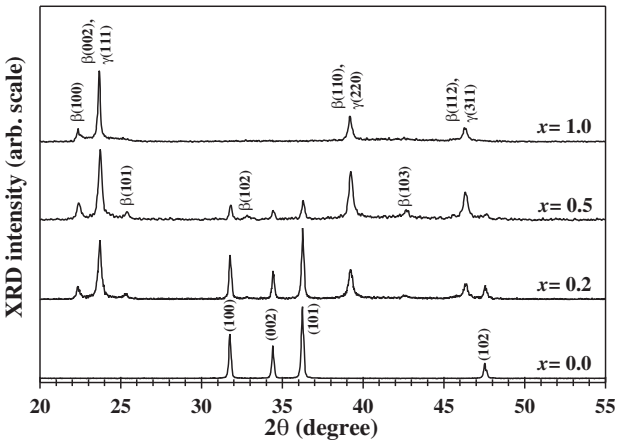

Fig. 1. The XRD patterns of (x)AgI–(1−x)ZnO composites (at 300 K).

in this figure are normalized at the peak intensity. With increasing x, some diffraction lines related to AgI become pronounced and all diffraction lines can be almost assigned to γ-AgI (zincblende structure), β-AgI (wurtzite structure) and ZnO (wurtzite structure), as shown in Fig. 1. The intensity ratio of the β-AgI (0 0 2) line, which coincides with the γ-AgI (1 1 1) peak, to the β-AgI (1 0 0) line tends to increase from about 4 to about 8 while increasing x from 0.1 to 1.0. Such an increase may be explained by either a preferred orientation of β-AgI crystallites or an increase of γ-AgI component in the composites, accompanied by stacking disorder in hexagonal β-AgI. However, it is noted that the β-AgI (1 0 1), β-AgI (1 0 2) and β-AgI (1 0 3) lines become weak in the large x region ($x > 0.5$), which may be connected to stacking disorder in β-AgI lattice [8,10]. Referring to the known result that a silver-deficient AgI solution crystallizes in the γ phase and silver-rich AgI solutions do so in the β phase, this is interpreted as follows. Preferential Ag^+ ion adsorption on ZnO surfaces (silver-rich) induces a concentration gradient of Ag^+ ions in the AgI domain and oxygen vacancies on ZnO particle surfaces. The gradient produces then γ-AgI crystallites and β-AgI ones in the AgI domain. The degree of the gradient is dependent on the ZnO contents and, therefore, the diffraction intensity ratio of the γ-AgI line to the β-AgI line varies with x.

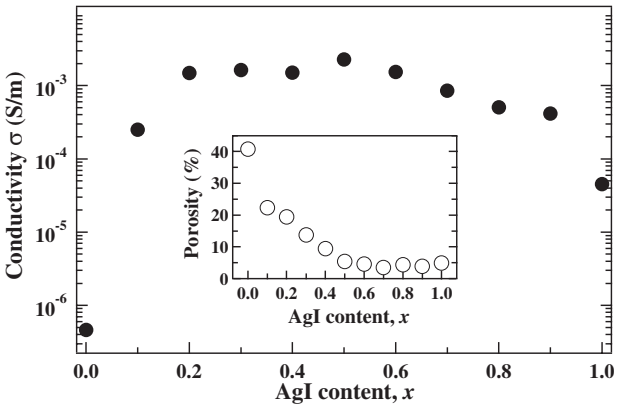

Fig. 2. The σ variation of (x)AgI–$(1-x)$ZnO composites at 300 K. The porosity variation with x is shown in the inset.

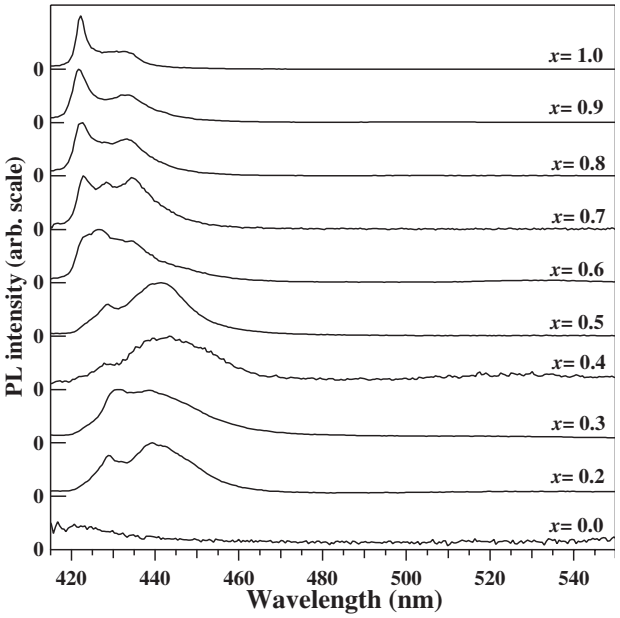

Fig. 3. The PL spectra of different (x)AgI–$(1-x)$ZnO composites at 9 K.

The σ at 1 kHz for (x)AgI–$(1-x)$ZnO composites at 300 K is plotted against x in Fig. 2. No frequency dependence of σ was observed between 42 Hz and 100 kHz. As seen in this figure, σ increase is abrupt against x. On further increasing x, σ reaches a maximum (about 2.3×10^{-3} S/m) at $x = 0.5$. Since the σ for a pristine AgI specimen prepared in the same way is 4.5×10^{-5} S/m, the σ is enhanced by about 50 times. In the x region larger than 0.5, σ falls gradually toward the σ of pristine AgI. In the light of the porosity data shown in the inset of Fig. 2, the σ variation in the small x region may be mainly caused by insulating pore effect. On the other hand, the σ enhancement observed in the intermediate region of x may arise from some composite effects, since the starting materials, pristine AgI and ZnO, have low σ. The composite effects may arise from highly ionic-conductive regions at the AgI/ZnO interfaces. The γ-AgI and β-AgI crystallites may act as Ag^+ ion donor and acceptor, respectively. Thus, we can anticipate high Ag^+ ion conductivity not only at the AgI/ZnO interface but also at the γ-AgI/β-AgI interface. With decreasing x from 1 to 0.5, dispersed ZnO particles approach each other and then the space charge effect spreads over the AgI domain to display a maximum in the σ–x curve.

We have measured the PL spectra of (x)AgI–$(1-x)$ZnO composites at different temperatures between 9 and 288 K. Of them, the PL spectra obtained by 355 nm laser excitation at 9 K are compared in Fig. 3. All PL spectra in this figure are normalized at the peak intensity. Pristine ZnO shows broad PL band ranging from 400 to 700 nm. The PL has been fully studied by many workers and has been attributed to oxygen vacancies [11–13]. The addition of small amount of AgI, $x = 0.2$, leads to a considerable decrease of this ZnO-related PL and gives a sharp PL band at 428 nm and a broad PL band centered at 440 nm. The addition of AgI to ZnO particle may produce oxygen vacancies at the AgI/ZnO interfaces. This may act on the oxygen vacancies to decrease luminescence related to pristine ZnO and may give pathway of Ag^+ ions to enhance σ. Since AgI domain size is small compared with mean free path of free exciton in the small x region, free excitons tend to be trapped at the AgI/ZnO interface. The excitation-laser-light absorption by added AgI should be also taken into account for the decreased luminescence. These PL bands at 428 nm, centered at 440 nm are thus assigned to radiative decay of bound exciton in AgI domain and bound exciton trapped at the AgI/ZnO interface, respectively. Up to the $x = 0.5$, the broad PL band centered at 440 nm increases with increasing x. On further increasing x, from 0.5 to 0.9, the broad PL band centered at the 440 nm comes to disappear and three bands grow

at about 422, 427 and 433 nm. These 422, 427 and 433 nm bands are attributed to radiative decay of free exciton of AgI, bound exciton in AgI domain and another type bound exciton, respectively. Since AgI domain size increases with increasing x, free excitons move with larger mean free path. Some of such excitons are trapped inside AgI domain and then radiatively decayed to increase luminescence intensity, before reaching at the AgI/ZnO interface.

We have found also a reversible photoinduced PL spectral change in the present (0.5)AgI–(0.5)ZnO composite at room temperature, as shown in Fig. 4(a). The arrows indicate the order of the experiments. After fully irradiating with 325 nm laser light in an evacuated specimen chamber for 30 min, the specimen shows a broad PL band centered at 520 nm due to trapped excitons of ZnO at oxygen vacancies, as indicated by curve 1. Oxygen gas is then introduced into the specimen chamber and, with increasing t_{ir}, the broad PL band decreases in intensity and a sharp PL due to AgI-excitons appears at 426 nm, as indicated by curve 2. Oxygen gas is then evacuated from the specimen chamber and, with increasing t_{ir}, the broad PL band becomes prominent, while a sharp PL band due to AgI-excitons degrades as indicated by curve 3. Through many successive experiments, it is found that such spectral changes (curve 2↔curve 3) appear repeatedly. The observed spectral changes may originate from excitation energy transfer between excitons in AgI domain and photoinduced oxygen vacancies at the surface of ZnO particle. The same experiment is also carried out for pristine ZnO. The results are given in Fig. 4(b). The PL intensity change by replacing atmosphere is very similar to that for (0.5)AgI–(0.5)ZnO. In the present experiments, the 325 nm laser light irradiation in vacuum and in oxygen gas may correspond to photoreduction and photooxidation, respectively. Therefore, the PL intensity increase under laser light irradiation in vacuum is thought to be due to the increase in number of oxygen vacancies. The PL band centered at 480 nm and the PL band tail shorter than 410 nm have been assigned to trapped excitons at oxygen vacancies and neutral donor bound excitons, respectively [11–13]. The present photoreduction experiments indicate that both so-called near-ultraviolet PL band and green one of ZnO closely relate to oxygen vacancies.

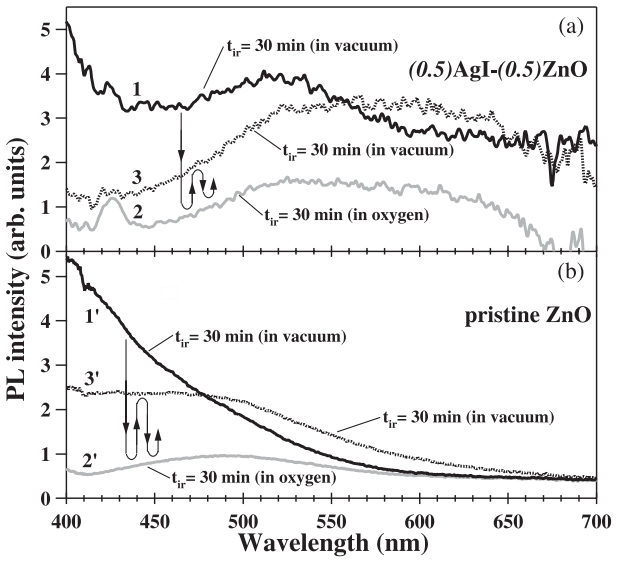

Fig. 4. The photoinduced spectral changes at 300 K in (a) (0.5)AgI–(0.5)ZnO and (b) in pristine ZnO.

Acknowledgements

This work is partially supported by a Grant-in-Aid for Scientific Research from the Ministry of Education, Science, Sports, Culture and Technology, Japan. This work is supported by Interdisciplinary General Joint Research Grant for Nihon University. This work is also partially supported by Project Research Grant from The Institute of Information Sciences of College of Humanities and Sciences (Nihon University) and by Cooperative Research Grant from The Institute of Natural Sciences (Nihon University).

References

[1] K. Shahi, J.B. Wagner Jr., Solid State Ionics 3–4 (1981) 295.
[2] M.C.R. Shastry, K.J. Rao, Solid State Ionics 51 (1992) 311.
[3] T. Jow, J.B. Wagner Jr., J. Electrochem. Soc. 126 (1979) 1963.

[4] S. Mochizuki, F. Fujishiro, Proceeding of the 6th Forum on Superionic Conductor Physics, The Japanese Society of Ion Transport, Kyoto; 2002, pp. 41–46.
[5] M. Cardona, Phys. Rev. 129 (1963) 69.
[6] S. Mochizuki, Y. Ohta, J. Lumin. 87–89 (2000) 299.
[7] S. Mochizuki, K. Umezawa, Phys. Lett. A 228 (1997) 111.
[8] S. Mochizuki, F. Fujishiro, J. Phys.: Condens. Matter 15 (2003) 5057.
[9] G. Burley, Acta Crystallogr. 23 (1967) 1.
[10] J.-S. Lee, S. Adams, J. Maier, J. Phys. Chem. Solids 61 (2000) 1607.
[11] K. Vanheusden, W.L. Warren, C.H. Seager, D.R. Tallant, J.A. Voigt, B.E. Gnade, J. Appl. Phys. 79 (1996) 7983.
[12] S.H. Bae, S.Y. Lee, H.Y. Kim, S. Im, Opt. Mater. 17 (2001) 327.
[13] A. van Dijken, E.A. Meulenkamp, D. Vanmaekelbergh, A. Meijerink, J. Lumin. 87–89 (2000) 454.

Available online at www.sciencedirect.com
SCIENCE DIRECT®
Physica B 340–342 (2003) 913–917
PHYSICA B
www.elsevier.com/locate/physb

Reversible photoinduced spectral transition in Eu_2O_3–γAl_2O_3 composites at room temperature

Shosuke Mochizuki*, Hiroyuki Araki

Department of Physics, College of Humanities and Sciences, Nihon University 3-25-40 Sakurajosui, Setagaya-ku, Tokyo 156-8550, Japan

Abstract

The photoluminescence (PL) intensity of Eu_2O_3–γAl_2O_3 composite has been found to decrease at room temperature with 325 nm laser light irradiation in vacuum, without any accompanying white luminescence. Then, under the same laser light irradiation in oxygen gas atmosphere, the PL intensity recovers. Through many successive experiments, it is found that the spectral change is nearly reversible. In spite of the changing atmosphere (for example, oxygen gas and air exposures), each PL state is stored for a long time at room temperature after the removal of the laser light under room light. This phenomenon is interpreted as results of photoinduced valence-number change of europium ions, the oxygen vacancy formation and some excitation energy transfer. Such a reversible phenomenon may well yield materials for erasable optical storage and oxygen sensor.

Keywords: Defects in oxides; Defects at/near surfaces and interfaces

PACS: 73.20.H; 82.50.F; 42.79.V; 78.55

1. Introduction

There has been a great deal of interest in the study of materials displaying photoinduced reversible spectral change at room temperature [1], because a combination of such reversible phenomenon and the near-field optical microscope [2] is very promising when applied to a high-density optical storage with nanometer resolution. Recently, we have observed a new-type erasable optical memory effects accompanied by intense white light emission in Eu_2O_3 [3,4], at room temperature under 325 nm laser light irradiation. Such optical memory effects arise from photoinduced valence-number change, photoinduced oxygen vacancies or both. It is a hope that we can find new materials having a photomemory function by combining Eu_2O_3 and a photocatalyst oxide (for example, anatase and γAl_2O_3). Very recently, we have fabricated Eu_2O_3–γAl_2O_3 composites and found an erasable photomemory phenomenon without any accompanying white band emission. In this paper, we report the experiments obtained for the $(0.2)Eu_2O_3$–$(0.8)\gamma Al_2O_3$ composite, as a typical example.

2. Experimental

Eu_2O_3–γAl_2O_3 composite powder was prepared by mixing Eu_2O_3 with particle size less than

*Corresponding author. Tel./fax: +81-3-5317-9771.
E-mail address: motizuki@physics.chs.nihon-u.ac.jp (S. Mochizuki).

0921-4526/$ - see front matter © 2003 Elsevier B.V. All rights reserved.
doi:10.1016/j.physb.2003.09.204

5000 nm and $\gamma A1_2O_3$ fine particles (with an average diameter of 60 nm) in air, by heating the mixture in the lidded crucible at 873 K for 69 h in air. Powder compact specimens are prepared by compressing the powder mixture under a pressure of 0.2 GPa for 2 h at room temperature. Microwave (frequency = 2450 MHz, power = 500 W) irradiation was carried out for 50 min. Such microwave treatment not only removes some strain induced by compaction but also induces effective sintering at low temperature [5]. If the microwave power and frequency are set appropriately, sintering may proceed at low temperature without any particle grain growth and, therefore, without losing surface activity of $\gamma A1_2O_3$ fine particles.

The composites were characterized at 300 K by X-ray diffraction (XRD) analysis with $CuK\alpha_1$ radiation. The composite morphology was analyzed by a scanning electron microscope and an optical microscope with a charge-coupled device camera system.

Irradiation is carried out with a continuous wave (CW) of He–Cd laser line (wavelength $\lambda = 325$ nm) with a power density of 318 W/m^2, which is less than 1% of that for previous works in pristine Eu_2O_3 [3,4]. The same He–Cd laser line excites luminescence. Emitted light is dispersed and detected by using a grating spectrograph equipped with a multichannel photodetection system. PLE spectra were recorded by varying the excitation-light wavelength λ_{ex} with an apparatus consisting of a monochromatic light source and detecting the emission light intensity at the fixed observation-light wavelength λ_{ob} as a function of λ_{ex} with a grating monochromator and a synchronous light detection system. All the measurements were carried out at room temperature.

3. Results and discussion

The apparent density of the $(0.2)Eu_2O_3$–$(0.8)\gamma Al_2O_3$ composite is 1780 kg/m^3 and the porosity is 59% at room temperature. The X-ray analysis indicates that the fabricated powder compact is a mere mixture of the C-type (cubic) Eu_2O_3 [6] and γAl_2O_3.

Figs. 1(a) and (b) show the photoinduced PL spectral changes of $(0.2)Eu_2O_3$–$(0.8)\gamma Al_2O_3$ composite under CW 325 nm laser light irradiation. The experiments are carried out in numerical order: $1 \to 2 \to 3 \to 4$. The irradiation time t_{ir} under given atmosphere and the kind of atmosphere are given on each curve. When $(0.2)Eu_2O_3$–$(0.8)\gamma Al_2O_3$ composite is irradiated with 325 nm laser light at room temperature in vacuum of about 1×10^{-4} Pa, the PL intensity decreases with increasing t_{ir}. The PL spectrum of the composite shows red Eu^{3+} emission (curve 1) due to the $^5D_0 \to {}^7F_J$ ($J = 0$, 1, 2, 3, 4) transitions [7]. The pristine γAl_2O_3 displays a broad PL band, as shown in the inset of Fig. 1(a), and pristine Eu_2O_3 displays both sharp PL line and a broad PL band [4], while the broad PL bands due to pristine γAl_2O_3 and Eu_2O_3 disappear in $(0.2)Eu_2O_3$–$(0.8)\gamma Al_2O_3$ composite. This indicates that there are many nonradiative traps (NRT) for photoexcited oxygen vacancies at $\gamma Al_2O_3/Eu_2O_3$ interfaces. The specimen chamber is then filled with oxygen gas of about 0.1 MPa under the same 325 nm laser light irradiation. With increasing t_{ir}, PL intensities due to the $^5D_0 \to {}^7F_J$ ($J = 0$, 1, 2, 4) transitions increases. This change is not accompanied by white light emission, which may be simple materials for photomemory and optoelectronic in comparison with pristine Eu_2O_3 [3,4]. Oxygen gas is again evacuated from the chamber. The red emission becomes weak. The spectral change observed for $(0.2)Eu_2O_3$–$(0.8)\gamma Al_2O_3$ composite appears reversible for replacing kind of atmosphere. In Fig. 1(c), the PL intensity of the line due to the $^5D_0 \to {}^7F_2$ transition is plotted as a function of t_{ir} for each specimen atmosphere. It is also noted that the spectral change becomes more prominent for more specimen-atmosphere change. After removing the 325 nm laser light, both the intense- and weak-red emission states are stored for a long time at room temperature in air.

Figs. 2(a) and (b) show the PLE spectra of $(0.2)Eu_2O_3$–$(0.8)\gamma Al_2O_3$ composite and pristine Eu_2O_3 powder compact. Fig. 2(c) shows the PLE spectrum (solid curve) and PL one (broken curve) of pristine γAl_2O_3 powder compact. In the PLE spectrum of pristine γAl_2O_3 powder compact, two broad absorption bands named X and Y are seen

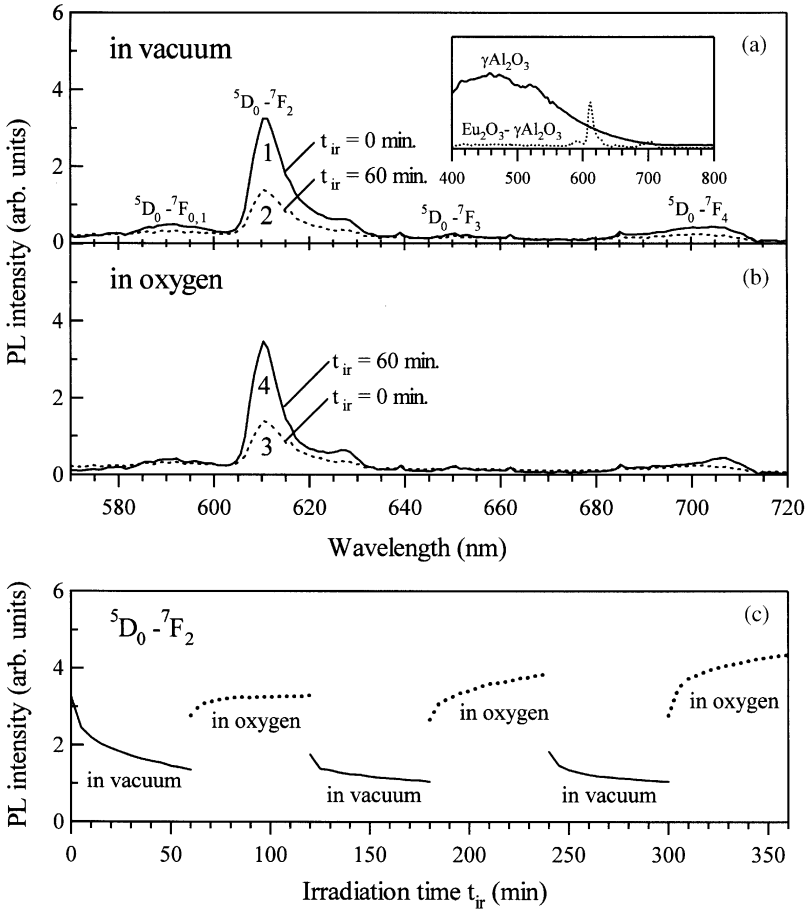

Fig. 1. Reversible photoinduced spectral change of $(0.2)Eu_2O_3$–$(0.8)\gamma Al_2O_3$ composite by replacing specimen atmosphere at room temperature: (a) in vacuum, (b) in oxygen gas, (c) irradiation time dependence of the PL due to $^5D_0 \rightarrow {}^7F_2$ transition. In the inset of (a), the PL spectrum of pristine γAl_2O_3 is compared with that of $(0.2)Eu_2O_3$–$(0.8)\gamma Al_2O_3$.

at 210 nm (= 5.90 eV) and 370 nm (= 3.35 eV), respectively, and a shoulder band named S band is seen at 261 nm (= 4.74 eV). The full-width at half-maximum (FWHM) of the X and Y bands are 1.24 and 0.57 eV, respectively. The Y band centered at 3.35 eV corresponds to deep electronic levels in the energy gap (8.7 eV) of solid γAl_2O_3. The PL spectrum is shifted toward longer wavelength to display quasi-mirror relation with the PLE one. Similar relation has been frequently observed for deeply trapped and spacially localized electrons around oxygen vacancies in metal oxide crystals and in imperfect ionic crystals. We name such localized electronic states due to oxygen vacancies LESOV. In such case, the magnitude of the FWHM depends on the electron–phonon interactions and defect structure. Surely, the PL intensity of the X and Y bands in the pristine γAl_2O_3 powder compact has been found in the present experiments to increase with increasing t_{ir} under 325 nm light irradiation in vacuum. Since the 325 nm laser light irradiation in vacuum corresponds to photoinduced associative detachment of O_2 molecules near the specimen surfaces [4], the X and Y bands are assigned to oxygen vacancies at γAl_2O_3 surfaces. The energy diagram of Eu^{3+} ions is thought to be insensitive to oxygen defects, since the extent of 4f-electron wave functions is extremely small. We note especially the following three of the obtained results.

(1) Eu_2O_3 attachment to γAl_2O_3 creates nonradiative traps to annihilate the broad PL band due to γAl_2O_3 and the white PL due to Eu_2O_3,

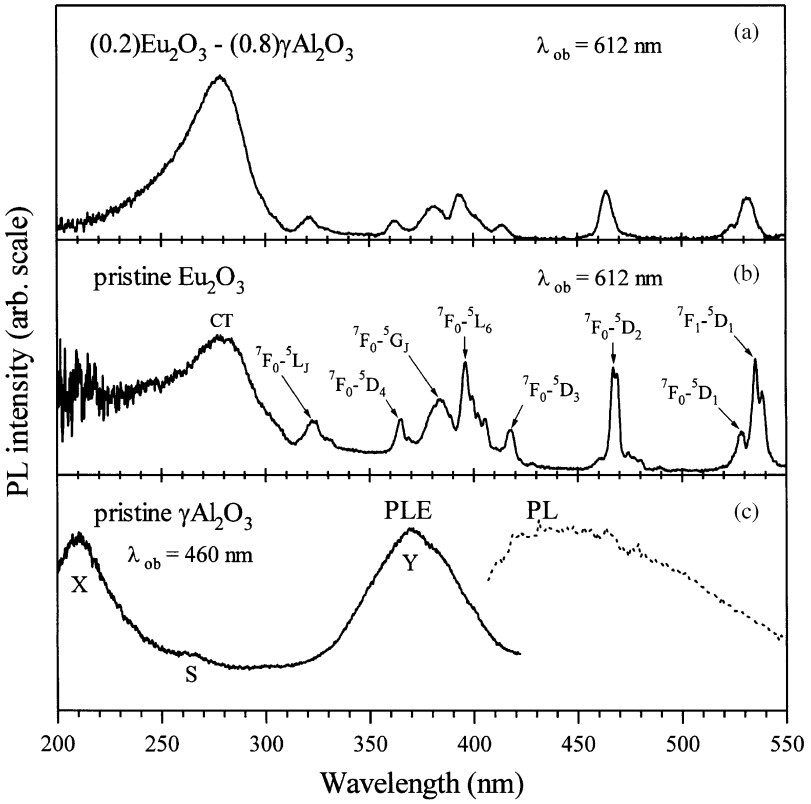

Fig. 2. PLE spectra at room temperature: (a) $(0.2)Eu_2O_3$–$(0.8)\gamma Al_2O_3$ composite, (b) pristine Eu_2O_3, (c) pristine $\gamma A1_2O_3$. The PL spectrum of the pristine γAl_2O_3 is shown in the inset of (c).

(2) 325 nm laser light irradiation in vacuum decreases the PL intensity of Eu_2O_3, while the same laser light irradiation in oxygen gas recovers the PL intensity of Eu_2O_3,
(3) After removing the 325 nm laser light, both the intense- and weak-red emission states are stored for a long time at room temperature in air.

On the basis of present PL and PLE spectra for pristine γAl_2O_3, pristine Eu_2O_3 and $(0.2)Eu_2O_3$–$(0.8)\gamma Al_2O_3$ composite, we have drawn an energy diagram to explain the spectral transitions observed for Eu_2O_3–γAl_2O_3 composite in Fig. 3. Solid arrows and dotted arrows indicate radiative transitions and non-radiative ones, respectively. The 325 nm (= 3.81 eV) laser light wavelength corresponds to the onset wavelength for the charge-transfer (CT) excitation, the wavelength for the $^7F_0 \rightarrow {}^5L_J$ excitation and oxygen defect excitation at Eu_2O_3 surfaces. Gathering up these excitations, they are indicated as a transition from $^7F_0$ to Z. Also, the LESOV in both γAl_2O_3 and Eu_2O_3 can absorb incident 325 nm light and decay nonradiatively to the NRT at $\gamma Al_2O_3/Eu_2O_3$ interfaces. Under CW 325 nm laser light irradiation in vacuum, some of Eu^{3+} ions are excited to higher-energy Z state and others transform to Eu^{2+} ions with creating oxygen vacancies at Eu_2O_3 particle surfaces. In the energy diagram, the electronic states of Eu^{2+} ion, the higher energy levels of Eu^{3+} ion and the LESOV in Eu_2O_3 particle surfaces are not shown for simplicity. The CW 325 nm laser light creates also oxygen vacancies at γAl_2O_3- and Eu_2O_3-particle surfaces in vacuum atmosphere. The valence-number change ($Eu^{3+} \rightarrow Eu^{2+}$) depresses the $^5D_0 \rightarrow {}^7F_2$ emission and the excitation energy of Eu_2O_3 is also transferred to unphotoexcited oxygen vacancies at γAl_2O_3 surfaces, which depress the $^5D_0 \rightarrow {}^7F_2$ emission of Eu^{3+} ions. Since the oxygen-vacancy-related PL has not been observed

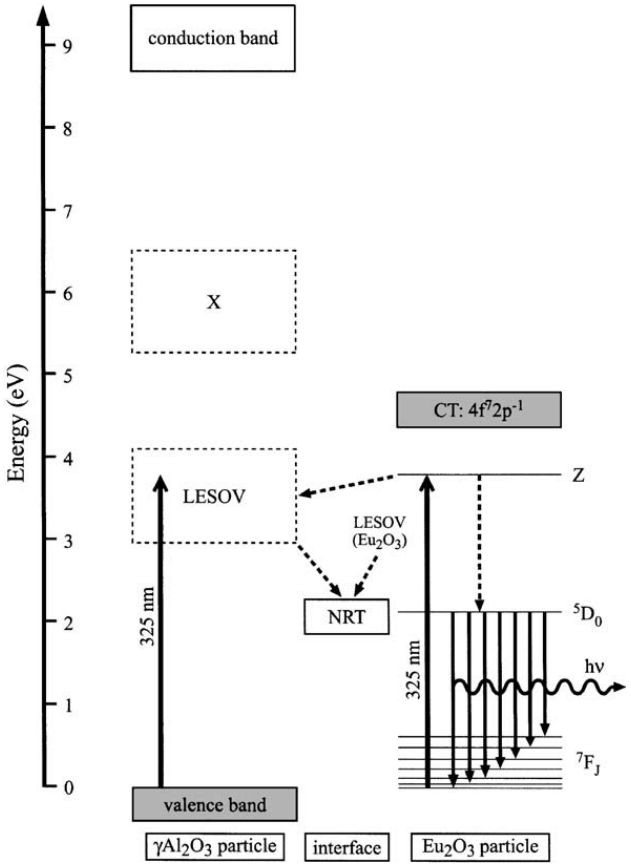

Fig. 3. Energy diagram of Eu_2O_3–γAl_2O_3 composite.

for the present composite, the deexcitation of the oxygen vacancies is accomplished with nonradiative trapping (LESOV → NRT). Under CW 325 nm laser light irradiation in oxygen gas atmosphere, some of Eu^{2+} ions transform to Eu^{3+} ions with annihilating oxygen vacancies at Eu_2O_3 particle surfaces. Simultaneously, at γAl_2O_3 particle surfaces, the annihilation of oxygen vacancies occurs to decrease the number of oxygen vacancies. In the result, the $^5D_0 \rightarrow {}^7F_2$ emission of Eu^{3+} ions recovers in oxygen atmosphere.

Acknowledgements

This work is partially supported by a Grant-in-Aid for Scientific Research from the Ministry of Education, Science, Sports, Culture and Technology, Japan. This work is supported by Interdisciplinary General Joint Research Grant for Nihon University. This work is also partially supported by Project Research Grant from The Institute of Information Sciences of College of Humanities and Sciences (Nihon University) and by Cooperative Research Grant from The Institute of Natural Sciences (Nihon University).

References

[1] K. Tanaka, S. Okamoto, Y. Kanemitsu, T. Kushida, J. Lumin. 94–95 (2001) 519.
[2] E. Bezig, J.K. Trautman, Science 257 (1992) 189.
[3] S. Mochizuki, Y. Suzuki, T. Nakanishi, K. Ishi, Physica B 308–310 (2001) 1046.
[4] S. Mochizuki, T. Nakanishi, Y. Suzuki, K. Ishi, Appl. Phys. 70 (2001) 3785.
[5] M.A. Janney, H.D. Kimrey, M.A. Schmidt, J.O. Kiggans, J. Am. Ceram. Soc. 74 (1991) 1675.
[6] G.H. Dicke, Spectra and Energy Levels of Rare Earth Ions in Crystal, Interscience, New York, 1968.
[7] K.A. Gschneid Jr, L.R. Eyring, in: Handbook on the Physics and Chemistry on Rare Earths, Vol. 3, North-Holland, Amsterdam, 1979.

Available online at www.sciencedirect.com
SCIENCE DIRECT®
Physica B 340-342 (2003) 944–948
PHYSICA B
www.elsevier.com/locate/physb

Intense white luminescence of Sm_2O_3 irradiated with ultraviolet laser light under vacuum

Shosuke Mochizuki*

Department of Physics, College of Humanities and Sciences, Nihon University, 3-25-40 Sakurajosui, Setagaya-ku, Tokyo 156-8550, Japan

Abstract

When Sm_2O_3-powder compact and -microcrystal films are irradiated with 325 nm laser light at room temperature in an evacuated chamber, their photoluminescence (PL) intensities are enhanced enormously. Then, introducing oxygen gas into the specimen chamber, the intense PL state returns to the original weak one under the same laser light irradiation. Through many successive experiments, it is found that the spectral change is reversible under 325 nm laser light irradiation. After removing the 325 nm laser light irradiation, each PL-state is stored for a long time at room temperature under room light, in spite of any change of atmosphere. The PL excitation spectra indicate that the observed phenomenon may arise from photoinduced valence-number change of samarium ions and photoinduced oxygen defects.

PACS: 73.20.H; 82.50.F; 42.79.V; 78.55

Keywords: Defects in oxides; Defects at/near surfaces; White luminescence

1. Introduction

A purpose of the present work is finding new materials which display persistent optical spectral changes at room temperature by laser light irradiation under specific atmospheres (this corresponds to optical recording of information) and then returns to the original optical spectra by laser light irradiation under a different atmosphere (this corresponds to optical erasing of the recorded information). Recently, we have found the reversible change in the photoluminescence (PL) spectra and intense white PL in different Eu_2O_3-powder compacts, -films and -microcrystals at room temperature by changing the specimen atmosphere under 325 nm laser light irradiation [1,2]. The spectral change is closely related to the photo-oxidation and photoreduction, which induces the valence number change of europium ions and oxygen defects. Very recently, we have also found similar photoinduced PL spectral change and intense white PL in Sm_2O_3-powder compact and -microcrystals.

Sm_2O_3 is stable in air and has five phases designated by X, H, A, B and C at atmospheric pressure in order of decreasing temperature [3]. At room temperature, the C type (T_h^7 space group) is thought to be the most stable phase. However, the B type appears also frequently as a metastable phase. The stability of the B-type

*Tel./fax: +81-3-5317-9771.
E-mail address: motizuki@physics.chs.nihon-u.ac.jp (S. Mochizuki).

0921-4526/$ - see front matter © 2003 Elsevier B.V. All rights reserved.
doi:10.1016/j.physb.2003.09.253

(C_{2h}^3 space group) phase may arise from slight nonstoichiometries and other defects. Owing to this quasi-bistability of the C and B types, we can anticipate some photoinduced-structural and -valence changes in Sm_2O_3 under light irradiation. In the present paper, we report the reversible photoinduced spectral change (PISC) of Sm_2O_3 microcrystals, together with that of Sm_2O_3 powder compact, in detail.

2. Experimental

Sm_2O_3 powder compact (PC-Sm_2O_3) was prepared by compressing Sm_2O_3 powder of 99.9% purity under a pressure of 0.2 GPa for 1 h at room temperature and they were then sintered at 1273 K in air for 24 h. The laser ablation target was the same PC-Sm_2O_3 pellet. Sm_2O_3 microcrystal film (μcF-Sm_2O_3) production and deposition on a silica glass substrate (Toshiba Ceramics Co., T-1030) were carried out in oxygen gas of different pressures between 0 and 4 Pa, with pulsed Nd^{3+}:YAG laser (wavelength $\lambda = 355$ nm). The PISC experiments were carried out with a continuous wave (CW) of He–Cd laser line ($\lambda = 325$ nm) with a power density of 5.4 kW/m^2. The same He–Cd laser line excites luminescence. Emitted light is dispersed and detected using a grating spectrograph equipped with a multichannel photodetection system. The PL excitation (PLE) spectra were recorded by varying the excitation-light wavelength λ_{ex} with an apparatus consisting of a monochromatic light source and detecting the emission light intensity at the fixed observation-light wavelength λ_{ob} as a function of λ_{ex} with a grating monochromator and a synchronous light detection system. All the experiments were carried out at room temperature. Vacuum of about 10^{-4} Pa and oxygen gas of about 0.1 MPa were used for the atmosphere around the specimen. Evacuation was carried out by a turbomolecular pump (oil free) system.

3. Results and discussion

The μcF-Sm_2O_3 was characterized, together with the PC-Sm_2O_3 as a laser-ablation target, by the X-ray diffraction (XRD) method at room temperature. The results are shown in Fig. 1, together with XRD histograms for the C- and B-type Sm_2O_3 [4]. All the XRD lines of the PC-Sm_2O_3 are identified with both the B- and C-type lines given in Figs. 1(d) and (e). As shown in Fig. 1(b), the XRD pattern of the as-deposited μcF-Sm_2O_3 consists of a halo-like pattern ganging from 25° to 35° and most of the sharp diffraction lines assigned to the B-type (monoclinic) Sm_2O_3. The halo-pattern may be ascribed to amorphous domains or nanometer-size crystallites in the films. After annealing at 873 K in air for 12 h, the halo-patterns disappear and the C-type lines dominate the B-type ones, as shown in Fig. 1(c). Anyhow, the sintered PC-Sm_2O_3 specimen and different annealed μcF-Sm_2O_3 specimens are the mixture of the C-type Sm_2O_3 and the B-type one.

Preceding showing the spectral data, we report the photoinduced color change in Sm_2O_3. Under 325 nm laser light irradiation in oxygen atmosphere at room temperature, the PC-Sm_2O_3 and

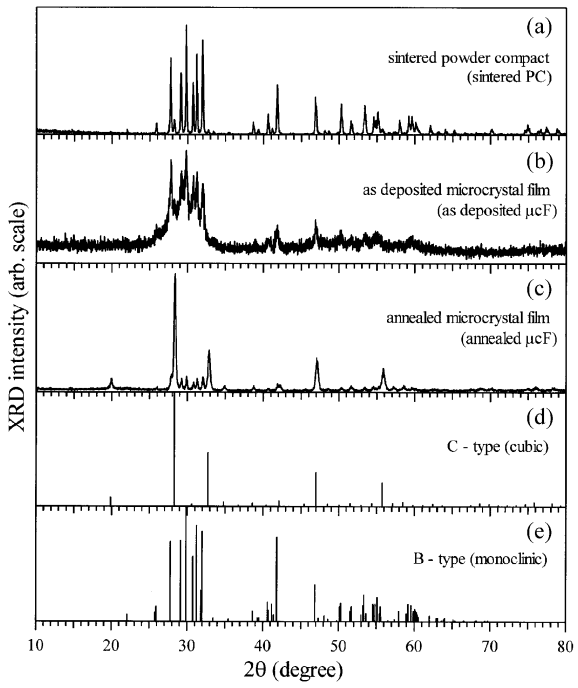

Fig. 1. The XRD patterns of different Sm_2O_3 specimens at room temperature: (a) sintered powder compact (PC), (b) as-deposited microcrystal film (μcF) and (c) annealed microcrystal film (μcF). The diffraction line diagrams of (d) C-type Sm_2O_3 and (e) B-type Sm_2O_3.

the annealed μcF-Sm_2O_3 display weak blue PL color which can be seen with the naked eye. As a typical example, this PL color of the PC-Sm_2O_3 is shown in Fig. 2(a). The specimen chamber is then evacuated under 325 nm laser light irradiation. With increasing irradiation time t_{ir}, the PC-Sm_2O_3 and μcF-Sm_2O_3 show white PL and increase the intensity. At 90 min later, after the evacuation, a bright white PL can be easily seen with the naked eye. As a typical example, this PL color of the PC-Sm_2O_3 is shown in Fig. 2(b). Through many successive experiments, it is found that the PL color changes appear repeatedly at different temperatures from 7 K to room temperature. This result indicates that the observed photoinduced spectral changes are purely electronic phenomena and are not phonon assisted. The color change is induced effectively only by a 325 nm CW laser light, which cannot dissociate directly free O_2 molecules. This result indicates that the phenomenon arises from the photoinduced associative detachment and photoinduced dissociative adsorption of O_2 molecules near the specimen surfaces [1,2]. The results also summarize how color change arises naturally from photoactivated oxidation and reduction. After removal of the laser light, such a white PL state is stored for a long time at room temperature in air under room light, since 3 June 2003. This result indicates that the ground state of the photoreduced state (GSPR) is separated from ground state of Sm_2O_3 by the potential barrier of which height is higher than room-temperature thermal energy to suppress the thermal-forward and -backward transitions between ground state of Sm_2O_3 and that of the GSPR.

Next, we show the spectral data corresponding to the above photoinduced color change. As typical examples, the obtained PISC for the PC-Sm_2O_3 and the annealed μcF-Sm_2O_3 fabricated at 4 Pa are shown in Fig. 3. Experiments are carried out in alphabetical order: (a)→(b) for the sintered PC-Sm_2O_3, (c)→(d) for annealed μcF-Sm_2O_3. Irradiation time t_{ir} under a given atmosphere and kind of atmosphere are indicated by each curve. To display the spectral structure in detail, the spectra are appropriately rescaled. The rescaling factor is given by each curve. Since μcF-Sm_2O_3 is very thin, several hundred nanometers in thickness, the apparent PL intensity is weaker than that of the PC-Sm_2O_3 of 2 mm in thickness. These PL spectra of the specimens fully irradiated in vacuum are quite similar to those of Sm^{2+}-doped materials [5]. The PL contribution from the silica glass substrate is about one-tenth of that of the μcF-Sm_2O_3. As the common feature of the sintered PC-Sm_2O_3 and the annealed μcF-Sm_2O_3, it has been found that the 325 nm laser light irradiation in vacuum increases considerably the PL intensity of both the specimens, while that in oxygen gas decreases the PL intensity to recover. The maximum PL enhancement factor, and the ratio of the integrated PL intensities after evacuation to that before evacuation, are 100 and 17 for the μcF-Sm_2O_3 and the PC-Sm_2O_3, respectively. The spectra shown in Fig. 3(a) exhibit many indistinct structures between 400 and 650 nm. It is known that most of the Sm^{3+}-doped materials exhibit the

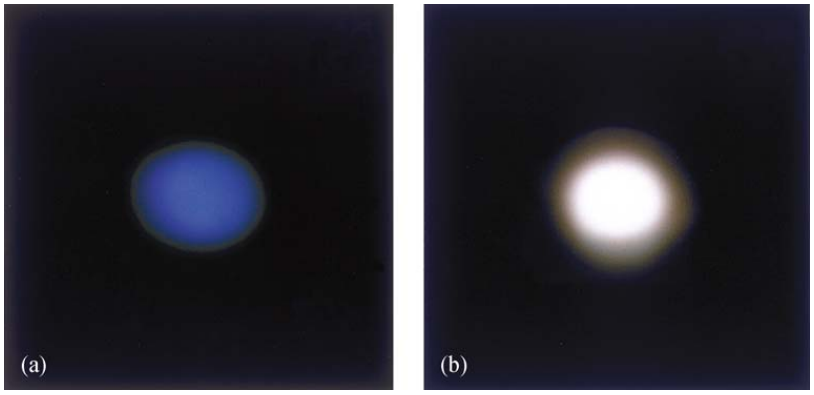

Fig. 2. The PL color change in the sintered Sm_2O_3 powder compact: (a) in oxygen gas, (b) in vacuum.

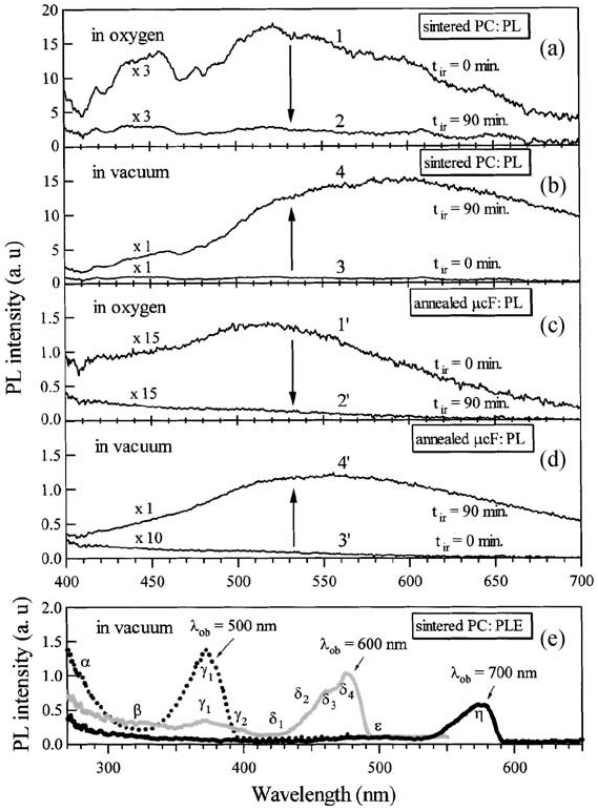

Fig. 3. The PL spectral transition under 325 nm laser-light irradiation: (a) sintered Sm_2O_3 powder compact (PC) in oxygen gas, (b) sintered Sm_2O_3 powder compact (PC), (c) annealed Sm_2O_3 powder microcrystal film (μcF) in O_2 gas and (d) annealed Sm_2O_3 microcrystal film (μcF) in vacuum. The PLE spectra of the intense white light emitting part is also given in (e).

$^4K_{11/2} \rightarrow {}^6H_J$, $^4G_{7/2} \rightarrow {}^6H_J$, $^4H_{3/2} \rightarrow {}^6H_J$, $^4G_{5/2} \rightarrow {}^6H_J$ ($J = (2n+1)/2$) in this wavelength region, while C-type Sm_2O_3 powder do indistinct PL spectral structure [6,7]. Since the energy level structure of 4f electrons depends on the crystal field [7], such indistinct PL spectrum is first explained by the mixture of the B-type Sm_2O_3 in the C-type one, as observed in the XRD data shown in Fig. 1. The defects and the reconstruction of atomic arrangement at surfaces affect also the crystal field, namely, the energy level structure of 4f electrons in microcrystal specimen. Besides them, reabsorption effect is also important, which gives several dips in the PL spectra to become more indistinct [6].

The PLE spectra of the white band have been also measured at different λ_{ob} in the white PL band of the μcF-Sm_2O_3 and the PC-Sm_2O_3. As a typical result, the PLE spectra of PC-Sm_2O_3 are shown in Fig. 3(e). These PLE spectra are very similar to that of Sm^{2+}-doped materials [7,8]. The tail α is assigned to the charge transfer absorption, while the bands β, γ_1, γ_2, δ_1, δ_2, δ_3 and δ_4 between 330 and 500 nm are attributable to the partially allowed 4d–5f transitions of Sm^{2+} ion. The band η may be assigned to the F centers, i.e., electron captured by anion (oxygen) vacancies [9]. The close similarity between the present results and those of Sm^{2+} ion-doped materials indicate that the intense white luminescence closely related to photoinduced valence-number change ($Sm^{3+} \rightarrow Sm^{2+}$) and photoinduced oxygen vacancies.

Finally, the reduction of Sm_2O_3 surface under 325 nm laser light irradiation in vacuum may be accompanied by creation of both valence-number change of samarium ion ($Sm^{3+} \rightarrow Sm^{2+}$) and a electron-captured oxygen defects, which can explain the observed white PL. Since microcrystals have larger specific surface than the sintered powder compact, the photoreduction may occur with high yield. This may be a reason why the microcrystal film specimen has higher enhancement factor for the photoinduced PL spectral change.

Acknowledgements

This work is partially supported by a Grant-in-Aid for Scientific Research from the Ministry of Education, Science, Sports, Culture and Technology, Japan. This work is supported by Interdisciplinary General Joint Research Grant for Nihon University. This work is also partially supported by Project Research Grant from The Institute of Information Sciences of College of Humanities and Sciences (Nihon University) and by Cooperative Research Grant from The Institute of Natural Sciences (Nihon University).

References

[1] S. Mochizuki, Y. Suzuki, T. Nakanishi, K. Ishi, Physica B 308–310 (2001) 1046.

[2] S. Mochizuki, T. Nakanishi, Y. Suzuki, K. Ishi, Appl. Phys. Lett. 70 (2001) 3785.
[3] K.A. Gschneid Jr, L.R. Eyring, Handbook on the Physics and Chemistry on Rare Earths, Vol. 3, North-Holland, Amsterdam, 1979.
[4] Powder Diffraction File: Inorganic Phases Sets 1-50, International Center for Diffraction Data, Pennsylvania, 2000.
[5] Q. Zeng, N. Kilah, M. Rieley, J. Lumin. 101 (2003) 167.
[6] J.-F. Martel, S. Jandl, A.M. Lejus, B. Viana, D. Vivien, J. Alloys and Compounds 275–277 (1998) 353.
[7] J.-F. Martel, S. Jandl, B. Viana, D. Vivien, J. Phys. Chem. Solid 61 (2000) 1455.
[8] M. Nogami, J. Non-Cryst. Solids 259 (1999) 170.
[9] K. Tanaka, S. Okamoto, Y. Kanemitu, T. Kushida, J. Lumin. 94–95 (2001) 519.

Available online at www.sciencedirect.com
SCIENCE DIRECT®
Physica B 340–342 (2003) 956–959
PHYSICA B
www.elsevier.com/locate/physb

Photoluminescence study on defects in pristine anatase and anatase-based composites

Shosuke Mochizuki*, Takashi Shimizu, Fumito Fujishiro

Department of Physics, College of Humanities and Sciences, Nihon University, 3-25-40 Sakurajosui, Setagaya-ku, Tokyo 156-8550, Japan

Abstract

Under 325 nm laser light irradiation at room temperature in oxygen gas, the photoluminescence (PL) intensity of pristine anatase TiO_2 decreases considerably and then it recovers reversibly with the same laser light irradiation at room temperature in vacuum. This result gives important information on the oxygen defects at anatase particle surfaces and may also clarify the origin of largely Stokes shifted broad PL band in pristine anatase. New reversible photoinduced spectral change has been also found in anatase–AgI composites for replacing atmosphere (vacuum ↔ oxygen gas) under 325 nm laser light irradiation at room temperature. This spectral change may arise from the excitation energy transfer between excitons in AgI domain and photoinduced oxygen defects at the anatase particle surfaces.

PACS: 68.35.Fx; 71.35.Cc; 78.55.Hx; 78.68.+m

Keywords: Defects in oxides; Defects at/near surfaces and interfaces

1. Introduction

The physical and chemical properties of pristine anatase TiO_2 and anatase-based composites have received a much attention as novel materials for photocatalyst [1]. Despite much effort, the photoabsorption and photoluminescence (PL) in anatase are still unclear. Pristine anatase single crystal is easily grown by the chemical vapor transport reaction (CVTR) method using halogen as the transport agent and it has been frequently used as the specimen for PL studies. Hitherto, the main interest of physicists was concentrated on the origin of considerably Stokes shifted broad PL band observed for the single crystal grown by the CVTR method [2]. To explain such PL spectrum of pristine anatase, the self-trapped exciton model has been frequently used [3]. However, anatase, as well as rutile, is well known as an oxygen-deficient oxide and the crystal grown by the CVTR method tends to contain impurities and defects related to the agent. Therefore, one should pay attention to defect structures both at the surfaces and on the inside of pristine anatase crystal, for the interpretation of the obtained spectra. It is desired to know how oxidation and reduction affect the optical properties of pristine anatase, except for impurity effects. For reply to these problems, it is better to use powder specimen than bulk specimen, since the powder specimen

*Corresponding author. Tel./fax.: +81-3-5317-9771.
E-mail address: motizuki@physics.chs.nihon-u.ac.jp (S. Mochizuki).

0921-4526/$ - see front matter © 2003 Elsevier B.V. All rights reserved.
doi:10.1016/j.physb.2003.09.172

has large specific surface, and, therefore, it is easily oxidized and reduced to show sensitively the effects related to surface defects. Recently, a broad PL band has been induced in simple oxides and rare-earth metal oxides [4–7] by photoreduction at room temperature. The broad PL band appears at the same wavelength region where anatase displays, and it can be recovered reversibly by photooxidation at room temperature. This photoreduction–photooxidation experiment may promise to clarify effects of oxygen defects on the optical properties of pristine anatase.

In the present paper, we report the photoinduced spectral change in pristine anatase powder compacts, together with single crystal bulk, and new photofunction in anatase–AgI composites.

2. Experimental

Crystalline pristine anatase powder was obtained by heating amorphous titanium dioxide fine particles of 99.9% purity (with an average diameter of 50 nm) at 673 K in air for 24 h. Powder compact specimens were prepared by compressing the powder under a pressure of 0.2 GPa at room temperature. They were then sintered at 673 K in flowing oxygen gas for 3 h. Anatase single crystal was grown by the CVTR method with NH_4Cl agent. Anatase–AgI composites, (x)anatase-$(1-x)$AgI, were prepared by fully mixing AgI powder and anatase powder in air, heating the mixture in the lidded crucible at 673 K for 12 h in air and then annealing at 373 K for 12 h to remove the stress introduced at the phase transition point of AgI, 420 K. The specimens were characterized at 300 K by X-ray diffraction analysis with Cu $K\alpha_1$ radiation.

Photoinduced spectral change experiments were carried out with a continuous wave of He–Cd laser line (wavelength $\lambda = 325$ nm) with a power density of 5.4 kW/m^2. Emitted light was dispersed and detected by using a grating spectrograph equipped with a multichannel photodetection system. All the experiments were carried out at room temperature.

3. Results

Before describing the results of optical measurements on different anatase specimens, we point out general optical properties obtained for anatase powder compacts. When the anatase powder is put in vacuum, the color changes gradually from white to pale yellow even at room temperature under room light (usual fluorescent light). When PL measurement is performed on the anatase specimen in an evacuated specimen chamber, the same change may occur at the thin surface layer of the specimen.

Figs. 1(a) and (b) show the PL spectral change obtained in pristine anatase powder compact under 325 nm laser light by replacing specimen atmosphere. Experiments are carried out in alphabetical order: (a)→(b). Irradiation is carried

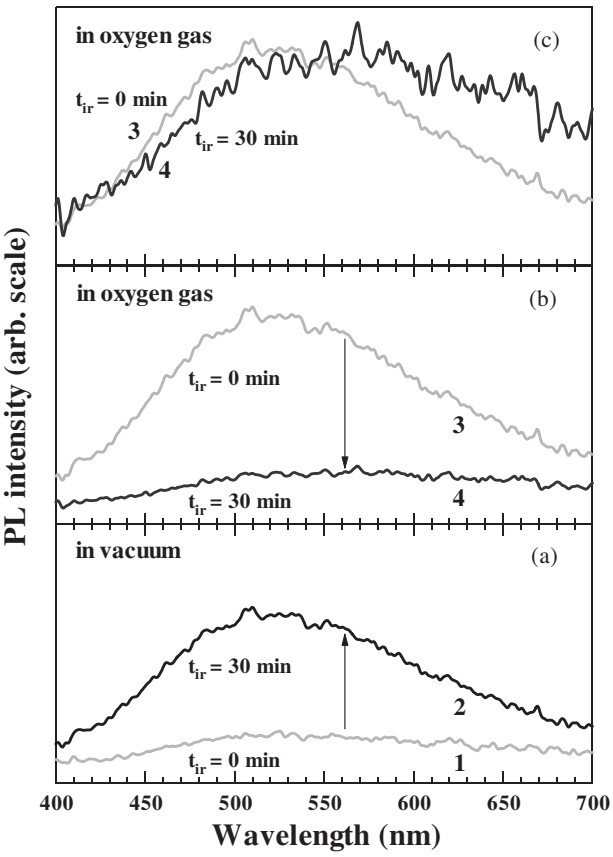

Fig. 1. Reversible photoinduced PL spectral change in anatase powder compact by replacing specimen atmosphere at room temperature: (a) in vacuum; (b) in oxygen gas; and (c) comparison of curve 3 with curve 4.

out at room temperature. Irradiation time t_{ir} under a given atmosphere and the kind of atmosphere are indicated by each curve. The PL intensity of the anatase powder compact is considerably increased by irradiating in vacuum of 1.33×10^{-4} Pa for 30 min, as shown in Fig. 1(a): curve 1 → curve 2. The PL enhancement factor for 30 min, the integrated PL intensity ratio of the curve 2 to the curve 1, is about 3.5. Oxygen gas of 0.2 MPa is then introduced into the specimen chamber under 325 nm laser light irradiation. With increasing t_{ir}, PL intensity decreases, as seen in the spectrum shown in Fig. 1(b): curve 3 → curve 4. To see more clearly the spectral change, the curves 3 and 4 are compared by rescaling the intensity of the curve 4, as shown in Fig. 1(c). The rescaling factor is 4.65. It is noted that the 325 nm laser light irradiation in oxygen gas makes the PL component at longer wavelengths than 520 nm. In the present experiments, the 325 nm laser light irradiation in vacuum and in oxygen gas may correspond to photoreduction and photooxidation, respectively. Oxygen gas is again evacuated. The change from weak PL emission to intense one can be seen with the naked eye. Through many successive experiments, it is found that such the spectral changes are almost reversible, apart from PL intensity. The enhancement factor tends to decrease with further repeating atmosphere change.

It has been also found that single crystal by the CVTR method shows also similar spectral change. The results are given in Figs. 2(a) and (b). To see more clearly the photooxidation effect, the curve 3′ and curve 4′ are compared by rescaling the intensity of the curve 4′ in Fig. 2(c). The rescaling factor is 1.77. However, the spectral change is not so prominent as the powder compact specimen. This may be due to the decreased specific surface of bulk specimen.

Sekiya et al. [8] annealed the CVTR anatase single crystals at different temperatures in oxygen gas and studied their PL properties. They found that PL spectrum consists of three components, F, E and D, centred at about 517, 577 and 636 nm, respectively. The components F, E and D are assigned to excitons bound to partially reduced titanium ions, self-trapped excitons and oxygen vacancies, respectively. If the defect structure of

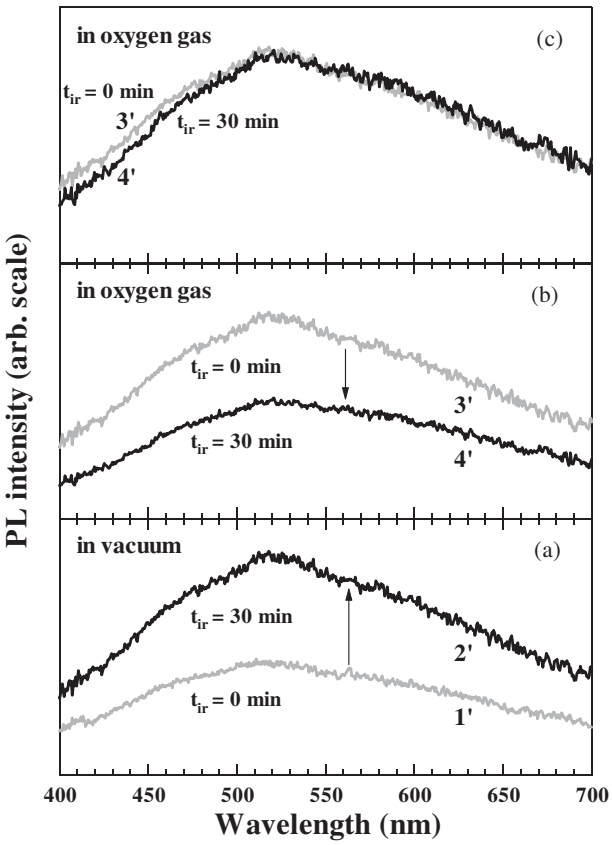

Fig. 2. Reversible photoinduced PL spectral change in anatase single crystal by replacing specimen atmosphere at room temperature: (a) in vacuum; (b) in oxygen gas; and (c) comparison of curve 3′ with curve 4′.

the CVTR anatase single crystal is identical to that of the photoirradiated powder compacts, it may be concluded that the broad PL band reported by many workers arises not from intrinsic self-trapped excitons but from oxygen defects or impurities.

Fig. 3 shows the reversible photoinduced PL spectral change in the (0.5)anatase–(0.5)AgI composite at room temperature. After fully irradiating with 325 nm laser light in an oxygen-gas-filled specimen chamber, the specimen displays a sharp PL band due to the radiative decay of excitons in AgI at about 426 nm [9] and a weak broad PL band related to anatase, as indicated by curve 1″. Oxygen gas is then evacuated from the specimen chamber. With increasing t_{ir}, the sharp AgI-related band becomes annihilated, while the anatase-related broad band becomes pronounced, as indicated by curve 2″. The specimen chamber is

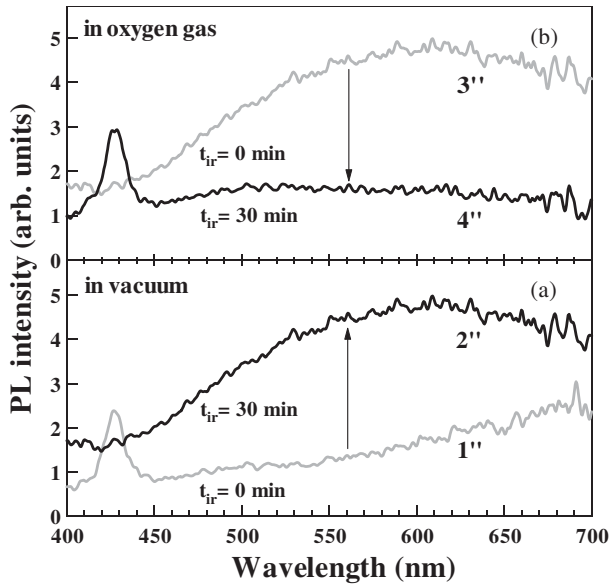

Fig. 3. Reversible photoinduced PL spectral change in (0.5)anatase–(0.5)AgI composite by replacing specimen atmosphere at room temperature: (a) in vacuum; and (b) in oxygen gas.

again filled with oxygen gas. The sharp AgI-related band reappears as shown in Fig. 3(b): curve 3″→ curve 4″, and it prevails against the anatase-related broad band. Through many successive experiments, it is found that such the spectral changes appear repeatedly. The observed spectral changes may be explained by excitation energy transfer between free excitons in AgI domain and photoinduced oxygen defects at the surfaces of anatase particle.

Finally, the spectral changes observed in the present experiments arise from photoinduced dissociative adsorption and photoinduced associative detachment of O_2 molecule near the specimen surfaces [5]. These changes may clarify the origin of the PL observed in pristine anatase and may well yield materials for optical sensor devices, for example, optical oxygen-partial-pressure sensor.

Acknowledgements

This work is partially supported by a Grant-in-Aid for Scientific Research from the Ministry of Education, Science, Sports, Culture and Technology, Japan. This work is supported by Interdisciplinary General Joint Research Grant for Nihon University. This work is also partially supported by Project Research Grant from The Institute of Information Sciences of College of Humanities and Sciences (Nihon University) and by Cooperative Research Grant from The Institute of Natural Sciences (Nihon University).

References

[1] A. Fujishima, T.N. Rao, D.A. Tryk, J. Photochem. Photobiol. C 1 (2000) 1.
[2] H. Bergar, H. Tang, F. Levy, J. Crystal Growth 130 (1993) 108.
[3] H. Tang, H. Berger, P.E. Schmid, F. Levy, Solid State Commun. 92 (1994) 267.
[4] S. Mochizuki, Y. Suzuki, T. Nakanishi, K. Ishi, Physica B 308–310 (2001) 1046.
[5] S. Mochizuki, T. Nakanishi, Y. Suzuki, K. Ishi, Appl. Phys. 70 (2001) 3785.
[6] S. Mochizuki, Physica B (in press 28 July 2003).
[7] S. Mochizuki, H. Araki, Physica B (in press 28 July 2003).
[8] T. Sekiya, S. Kamei, S. Kurita, J. Lumin. 87–89 (2000) 1140.
[9] S. Mochizuki, Y. Ohta, J. Lumin. 87–89 (2000) 299.

Available online at www.sciencedirect.com
SCIENCE DIRECT®
Physica B 340–342 (2003) 969–973
PHYSICA B
www.elsevier.com/locate/physb

UV-laser-light-produced defects and reversible blue–white photoluminescence change in silica

Shosuke Mochizuki*, Hiroyuki Araki

Department of Physics, College of Humanities and Sciences, Nihon University, 3-25-40 Sakurajosui, Setagaya-ku, Tokyo 156-8550, Japan

Abstract

The photoluminescence (PL) color of silica glass changes from weak blue to intense white under irradiation with 325 nm laser light at room temperature in vacuum. Irradiation at room temperature with the same laser light under oxygen gas atmosphere erases the white PL state. Through many successive experiments, it is found that the spectral change is a reversible phenomenon. Such intense white PL state is stored for a long time at room temperature in air under room light after removal of the laser light, in spite of any changes of atmosphere. The observed phenomenon may relate to the photo-induced defect formation at the silica glass surface. Such observed reversible phenomenon may well yield materials for erasable optical information storage, oxygen sensors and white-light emitting devices.

PACS: 73.20.H; 82.50.F; 42.79.V; 78.55

Keywords: Defects in silica; White-light emission; Photomemory

1. Introduction

Silica glass has been widely used as optical element and is of great interest for applications in optoelectronics. Most of commercially available silica glasses, however, display unwanted photoluminescence (PL) bands in the ultraviolet (UV) and visible light regions, and the glasses are damaged by intense UV-laser-light to give additional PL bands [1,2]. On the other hand, it has been well known that UV light induces a Bragg grating in Ge-doped silica glass fiber [3], which gives useful optoelectronics devices. The photo-induced structural and electronic defects, together with pre-existing PL centers, may play an important role for the formation of both the UV-light-induced PL centers and the Bragg grating. Therefore, the defects in silica glass should be fully characterized. Although different types of studies have been carried out in silica glass, the defect structure has been not fully elucidated at present. Very recently, we have observed for the first time the reversible UV (325 nm)-laser-light-induced spectral change and intense white PL state in different silica glasses, as observed in Eu_2O_3 [4,5] and Sm_2O_3. The spectral change may relate closely to photo-induced defects. In this paper, we report the experimental results in detail and discuss UV-laser-light-induced defects in silica glass.

*Corresponding author. Tel./fax: +81-3-5317-9771.
E-mail address: motizuki@physics.chs.nihon-u.ac.jp (S. Mochizuki).

0921-4526/$ - see front matter © 2003 Elsevier B.V. All rights reserved.
doi:10.1016/j.physb.2003.09.271

2. Experiments

In the present study, three different commercially available silica glasses of 1 mm thickness were used as specimens, since laser-irradiation effects are thought to be sensitive to adsorbed OH. One is a T-1030 silica glass (Toshiba Ceramics Co.) which contains a large amount of OH (200 ppm in weight ratio) and it displays considerable optical absorption (optical density OD = 0.36) due to OH at 3650 cm^{-1}. This glass contains also a small amount of aluminum (8 ppm in weight ratio) as main metal impurity. The others are GE-214 and GE-124 silica glasses (General Electric Co.). They contain a small amount of OH (less than 5 ppm in weight ratio). The GE-214 glass never displays the optical absorption due to OH, while the GE-124 glass shows little optical absorption (OD = 0.09) at 3650 cm^{-1}. Both the GE-214 and-124 glasses contain also larger amounts of aluminum (14 ppm in weight ratio) than the T-1030 glass as main metal impurity. More detailed chemical data are given on the Toshiba website (www. tocera.co.jp) and the GE website (www.gequartz.com).

Irradiations were carried out with a continuous wave (CW) He–Cd laser line (wavelength $\lambda = 325$ nm) with a power density of about 5.4 kW/m^2. The same He–Cd laser line excites luminescence. Emitted light is dispersed and detected by using a grating spectrograph equipped with a multichannel photodetection system. Vacuum of about 10^{-4} Pa and oxygen gas of about 0.1 MPa are used for control of the atmosphere around the specimen.

3. Results and discussion

Under 325 nm laser-light irradiation in oxygen atmosphere at room temperature, the T-1030, GE-124, and GE-214 glasses display weak blue PL color which can be seen with the naked eye. As a typical example, this PL color of the T-1030 glass is shown in Fig. 1(a). The specimen chamber is then evacuated under 325 nm laser-light irradiation. With increasing irradiation time t_{ir}, the silica glasses change to show white PL with increasing intensity. About 90 min after the evacuation, a bright white PL can be easily seen with the naked eye. As a typical example, this PL color of the T-1030 glass is shown in Fig. 1(b). Through many successive experiments, it is found that the PL color changes appear repeatedly. After removal of the laser light, the white PL state is stored for a long time at room temperature in air under room light. Figs. 2(a)–(d) show the reversible PL spectral change of the T-1030 glass. Figs. 3(a)–(d) show the reversible PL spectral change of the GE-214 glass. Irradiation was carried out with 325 nm laser line at room temperature. Experiments were carried out in alphabetical order: (a)→(b)→(c)→(d). The t_{ir} under given atmosphere and kind of atmosphere are indicated by each curve. Almost the same spectral change has also observed for the GE-124 glass. Besides the above-described results, through

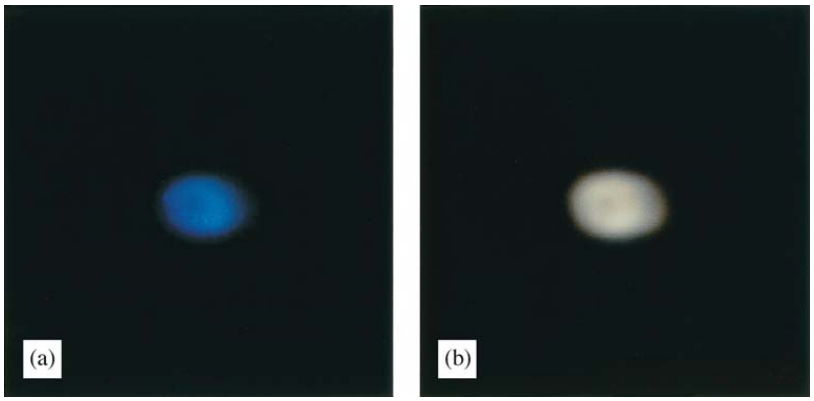

Fig. 1. Photographs of the T-1030 silica glass fully irradiated with 325 nm laser light in each atmosphere: (a) oxygen gas of about 0.1 MPa; and (b) vacuum of about 10^{-4} Pa.

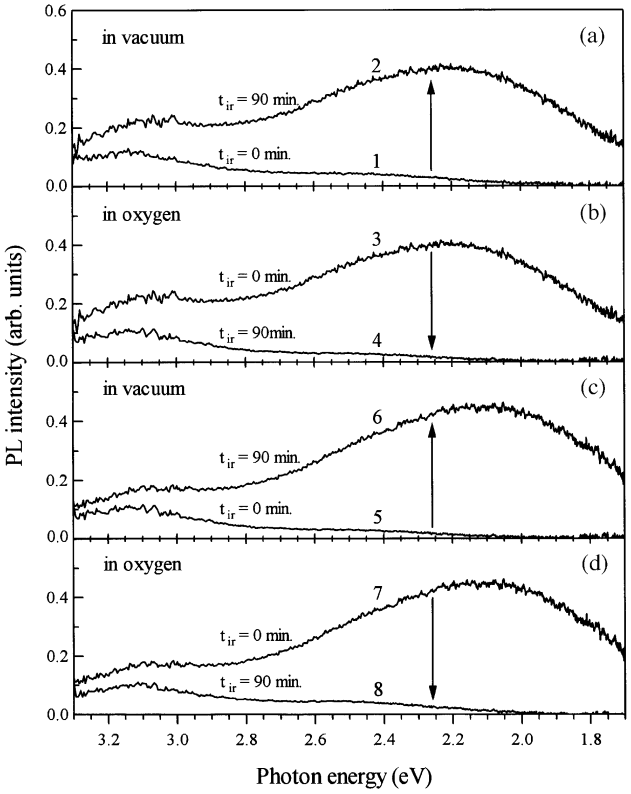

Fig. 2. Reversible PL spectral change of the T-1030 silica glass at room temperature: (a,c) in vacuum; and (b,d) in oxygen.

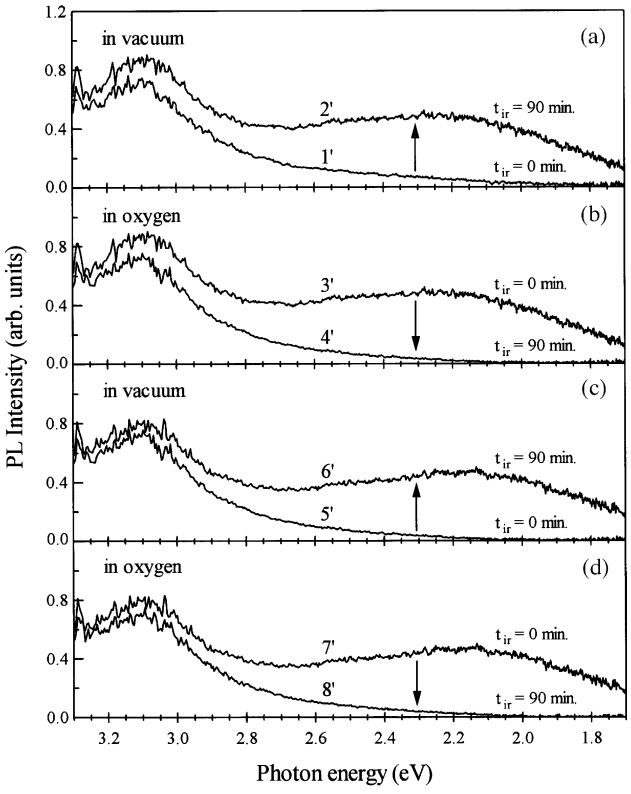

Fig. 3. Reversible PL spectral change of the GE-214 silica glass at room temperature: (a,c) in vacuum; and (b,d) in oxygen.

present experiments, the following conclusions were also found for different silica glasses:

(1) Time is required for the spectral change and the speed of the spectral change increases with laser fluence. They indicate that some nucleation and growth processes dominate the spectral change.
(2) The change to the white PL state occurs even at 7 K under CW 325 nm laser light. This indicates that the spectral change does not arise from a phonon-assisted process and it is a purely electronic mechanism.

The spectral change observed in silica glass arises from photo-induced-associative detachment under vacuum and dissociative adsorption of O_2 molecules under oxygen atmosphere near the specimen surface. Since the 325 nm laser light cannot dissociate directly free O_2 molecules as atmospheric gas, the photo-induced oxidation indicates that the photodissociation energy of O_2 molecules is considerably decreased at the silica glass surface by the interactions, between O_2 molecules and the silica glass.

In order to extract the white PL component, we have calculated the difference spectrum (curve 2–curve 1) for the T-1030 glass. The result is shown in Fig. 4(a). In Fig. 4(b), the difference spectrum (curve 2′–curve 1′) for the GE-214 glass is shown. The T-1030 glass fully 325 nm-laser-light-irradiated in oxygen gas shows a PL band peaked at 3.15 eV and a broad PL shoulder ranging from about 3.0 eV to about 2.0 eV. The T-1030 glass fully 325 nm-laser-light-irradiated in vacuum shows the 3.15 eV PL band and an intense broad PL band centered at 2.20 eV. With repeating atmosphere change, the intense broad PL band redshifts to 2.10 eV. In the GE-214 glass fully 325 nm-laser-light-irradiated in oxygen gas, the PL intensity of the 3.13 eV band is enhanced by twice that of the T-1030 silica glass and extends to about 2.0 eV without showing a clear shoulder. With

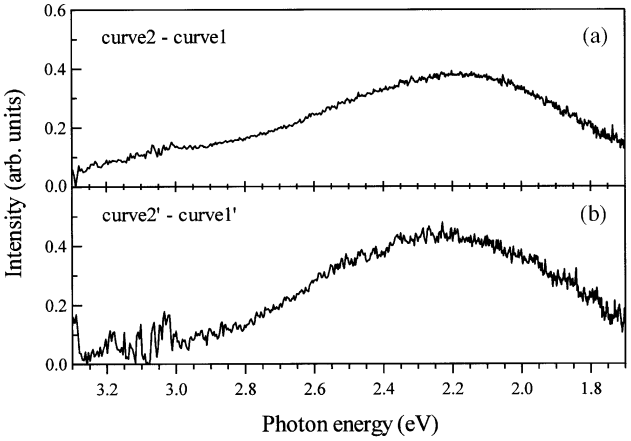

Fig. 4. Difference spectra: (a) (curve 2–curve 1) for the T-1030 glass; and (b) (curve 2′–curve 1′) for the GE-214 glass.

repeating atmosphere change, the intense broad PL band redshifts to 2.15 eV. After fully 325 nm laser-light irradiation in vacuum, the 2.20 eV PL band appears and the PL intensity is nearly the same as that of the GE-124 and T-1030 glasses. The study on the 3.15 eV PL band has been previously reported and the band is tentatively ascribed to the $O_3 \equiv Si-O-O-H$ group, the twofold coordinated silicon lone-pair center ($O-\ddot{S}i-O$) and a germanium impurity [6]. From the weaker 3.15 eV-PL-band observed in the T-1030 glass containing higher OH and lower aluminum than the GE-214 glass may exclude the $O_3 \equiv Si-O-O-H$ group, but we cannot exclude some aluminum-impurity-induced defects as a possible origin of the 3.15 eV PL band.

The white PL band photo-induced under vacuum has a peak energy (E_p) of 2.20 eV and a full-width at half-maximum (FWHM) of about 0.8 eV. Apart from the FWHM, this PL band resembles the PL band observed in γ-ray-irradiated silica glass under 325 nm excitation [7] and silica glasses damaged by high-power laser light [8] in E_p, and spectral shape. The γ-ray induced 2.2 eV PL band has been attributed to the radiation from a paramagnetic defect in which one electron is delocalized over a Si_5 cluster. Such a paramagnetic defect is known as the E'_δ center [7]. Another explanation for the 2.2 eV PL band (γ band) appeared in glass damaged by high-power laser light under 250 nm excitation and is based on the radiative decay of trapped excitons on the vacancy–interstitial pair consisting of an oxygen vacancy and two oxygen interstitials (V_O; $(O_2)_i$) [8]. Since the PL yield of the laser-light damaged silica glass at 325 nm, however, is negligibly small and the FWHM (0.5 eV) of the PL band is relatively small, the defect structure may be different from that induced under 325 nm laser-light irradiation in vacuum. As described above, the 2.2 eV PL band observed at the present study is related to photoreduction at the silica glass surface. In such a case, we assume that E'_δ -like defects and (V_O; $(O_2)_i$)-like states may be produced at the surface. The appearance of defect levels at the silica glass surface decreases considerably the band gap at the surface, as observed in γAl_2O_3 film [9] and then high PL yield at 325 nm can be anticipated.

In conclusion, a new PL color change from weak blue to intense white was observed in different silica glasses under 325 nm laser-light irradiation in vacuum at room temperature. The color change was reversed by the same 325 nm laser-light irradiation in oxygen gas atmosphere at room temperature. The intense white PL state is stored for a long time at room temperature in air under room light after removal of the laser light. The phenomenon is related to the photo-induced oxygen defect formation at the silica glass surface.

Acknowledgements

This work is partially supported by a Grant-in-Aid for Scientific Research from the Ministry of Education, Science, Sports, Culture and Technology, Japan. This work is supported by Interdisciplinary General Joint Research Grant for Nihon University. This work is also partially supported by Project Research Grant from The Institute of Information Sciences of College of Humanities and Sciences (Nihon University) and by Cooperative Research Grant from The Institute of Natural Sciences (Nihon University).

References

[1] S.G. Demos, M. Staggs, K. Minoshima, J. Fujimoto, Opt Express 10 (2002) 1444.

[2] L. Skuja, J. Non-Cryst. Solids 239 (1998) 16.
[3] K.O. Hill, Y. Fujii, D.C. Johnson, B.S. Kawasaki, Appl. Phys. Lett. 32 (1978) 647.
[4] S. Mochizuki, T. Nakanishi, Y. Suzuki, K. Ishi, Appl. Phys. Lett. 79 (2001) 3785.
[5] S. Mochizuki, Y. Suzuki, T. Nakanishi, K. Ishi, Physica B 308–310 (2001) 1046.
[6] Y. Sakurai, J. Non-Cryst. Solids 271 (2000) 218.
[7] H. Nishikawa, E. Watanabe, D. Ito, Y. Sakurai, K. Nagasawa, Y. Ohki, J. Appl. Phys. 80 (1996) 3513.
[8] M. Watanabe, S. Juodkazis, H. Sun, S. Matuo, H. Misawa, Phys. Rev. B 60 (1999) 9959.
[9] B. Ealet, M.H. Elyakhloufi, E. Gillet, M. Ricci, Thin Solid Films 250 (1994) 92.

INSTITUTE OF PHYSICS PUBLISHING JOURNAL OF PHYSICS: CONDENSED MATTER

J. Phys.: Condens. Matter **15** (2003) 5057–5072 PII: S0953-8984(03)60976-8

Structural, electrical and optical studies on AgI–anatase composites

Shosuke Mochizuki[1] **and Fumito Fujishiro**

Department of Physics, College of Humanities and Sciences, Nihon University, 3-25-40 Sakurajosui, Setagaya-ku, Tokyo 156-8550, Japan

E-mail: motizuki@physics.chs.nihon-u.ac.jp

Received 18 March 2003, in final form 3 June 2003
Published 11 July 2003
Online at stacks.iop.org/JPhysCM/15/5057

Abstract

AgI–anatase composites, (x)AgI–$(1-x)$anatase, were fabricated over a wide composition range of 0–100% AgI for the first time. The electrical conductivity at 300 K increases with increasing AgI content and reaches a maximum (about 3×10^{-2} S m^{-1}) at about 40% AgI. The conductivity is enhanced by about three orders of magnitude in comparison with that of pristine AgI. These composite specimens have been characterized by both scanning electron microscopy and x-ray diffractometry. The observations with a scanning electron microscope show that anatase fine particles are densely packed in an AgI particle of several micrometres in size and such composite particles are three-dimensionally connected to each other to form a composite specimen. The photoluminescence (PL), PL excitation and time-resolved PL spectra of these composites have also been measured at different temperatures between 8 and 278 K. The exciton spectra obtained related to the anatase particles and the AgI domains in anatase-packed AgI particles are discussed in the light of the morphological, structural and conductivity data.

1. Introduction

There has been considerable experimental research on ionic conduction in composite solid electrolytes consisting of ionic conductors and insulator fine particles (Liang 1973, West 1984, Shahi and Wagner 1981, Zhao *et al* 1983, Lee *et al* 2000a). The electrical and other properties of the composites can be easily controlled by varying the content of the ionic conductor component. Among various systems of composites, AgI-based composites have been extensively investigated by many workers, because they usually show high ionic conductivity ($\sigma \geqslant 10^{-2}$ S m^{-1}) and pristine AgI is well known as a good superionic conductor at temperatures higher than 420 K (Burley 1963). AgI has three phases designated as α, β and

[1] Author to whom any correspondence should be addressed.

γ at normal pressures in the order of decreasing temperature with the following properties. At the superionic transition temperature T_c (420 K), the superionic α phase transforms into the semiconductor β phase (wurtzite lattice). The α phase has a body-centred cubic arrangement of I^- ions with highly mobile Ag^+ ions randomly distributed through the equivalent interstices, which has been known as the averaged structure. At room temperature, the semiconductor γ phase (zincblende lattice) appears as a metastable state. It is said that the stability of the γ phase is affected by slight nonstoichiometries and other defects. To date, the conductivity of AgI-oxide fine particle composites has been reported in various composites: AgI–Al_2O_3, AgI–SiO_2, AgI–MgO, AgI–Fe_2O_3 (Shahi and Wagner 1981, Zhao *et al* 1983), AgI–ZrO_2, AgI–CeO_2, AgI–Sm_2O_3, AgI–MoO_3, AgI–WO_3 (Shastry and Rao 1992) and AgI–SnO_2 (Gupta *et al* 1996). In all these cases, their electrical conductivities were enhanced by two or three orders of magnitude higher than that of pristine AgI and a maximum conductivity occurred at proper AgI content. For example, the maximum occurs in (x)AgI–$(1-x)\gamma Al_2O_3$ composites with very fine alumina particles at $x = 0.5$–0.6, while composites with larger alumina particles showed the maximum at smaller AgI content. Such conductivity variation is initially explained by taking into account a space charge layer around a nucleophilic surface (Jow and Wagner 1979). However, several basic problems were raised about AgI-based composites. Why do oxides enhance the conductivity? How does AgI attach to oxide fine particles? What are the atomic and electronic structures of the AgI/insulator fine particle interface? In order to solve these problems, it is thought that optical study is effective. Constituent material AgI shows clear optical spectra due to excitons in the bulk (Mochizuki and Fujishiro 2002), films (Cardona 1963, Mochizuki and Ohta 2000) and microcrystals (Mochizuki and Umezawa 1997). Besides AgI, most oxides also show exciton spectra. The exciton behaviour is very sensitive to the environment in which excitons are moving, and therefore the optical spectra due to excitons may provide useful information about the AgI/oxide fine particle interface (Mochizuki and Fujishiro 2003). Very recently, we have fabricated AgI–anatase composites and observed considerable conductivity enhancement. Since AgI is very photosensitive and anatase (TiO_2) is known as a typical oxide photocatalyst for decomposing water and organic matter (Fujishima *et al* 2000), we can anticipate not only a new solid electrolyte nature but also a new photofunction for such an AgI–anatase fine particle composite.

In this paper, we report the morphological, structural, electrical and optical studies on AgI–anatase composites and we discuss the conductivity enhancement of the composites by comparing the scanning electron microscope images with the data obtained.

2. Experimental details

AgI–anatase composites, (x)AgI–$(1-x)$ anatase, were prepared by fully mixing AgI powder and amorphous titanium dioxide fine particles (with an average diameter of 50 nm) in air, heating the mixture in the lidded crucible at 673 K for 12 h in air and then annealing at 373 K for 12 h to remove the stress introduced at the phase transition point of AgI, 420 K. The composition range was from 0 to 100% AgI. At 300 K, the composites were characterized by x-ray diffraction (XRD) analysis with Cu Kα_1 radiation. The composite powder morphology was studied by a scanning electron microscope (SEM) and an optical microscope with a charge-coupled device camera system. Distribution maps of Ag, I, Ti and O atoms in the composites were obtained by using a SEM with an energy dispersive x-ray (EDX) fluorescence spectrophotometer (Shimadzu SSX-550).

Electrical conductivity measurements were performed in a helium gas stream using the impedance method. The applied signal frequency ranged from 42 Hz to 1 MHz. The composite powders were uniaxially compressed under 0.2 GPa for 30 min at room temperature to fabricate

pellets. It has been reported that the γAgI/βAgI ratio is strongly affected by compressing, grinding and the thermal history of specimens. Such an effect, a so-called memory effect, is erased by heat treatment above 445 K (Bloch and Möller 1931, Burley 1967). Therefore, the pellets were heat-treated at 453 K for 12 h in a lidded crucible and then annealled at 373 K for 12 h. Electrical contact with the pellets was obtained by evaporating silver onto both sides of the pellet.

The photoluminescence (PL) spectra were measured by an optical multichannel analyser consisting of a grating monochromator (focal length = 32 cm) and an intensified diode-array detector (gate time: $t_g \geqslant 5$ ns). A Nd^{3+}:YAG laser (wavelength $\lambda = 355$ nm, pulse width < 5 ns) and a monochromatic light source consisting of a 150 W xenon lamp and a grating monochromator (focal length = 20 cm) were used as the excitation source. The photoluminescence excitation (PLE) spectra were recorded by varying the excitation-light wavelength λ_{ex} with an apparatus consisting of the same monochromatic light source described above and detecting the emission light intensity at the desired wavelength as a function of λ_{ex} with a grating monochromator (focal length = 20 cm) and a synchronous light detection system. The time-resolved PL (TRPL) spectra were taken using the same optical multichannel analyser to which two delay pulse generators were attached. The delay time t_d and gate time were set with these delay pulse generators which were controlled by a personal computer. A closed-cycle He refrigerator equipped with a temperature controller was used to change the specimen temperature between 8 and 278 K.

3. Results and discussion

3.1. Characterization of AgI–anatase composite specimens

The apparent density of the (x)AgI–$(1 - x)$anatase composites at about 300 K is plotted, together with the theoretical density, as a function of AgI content x in figure 1. The full line and full circles represent the theoretical and experimental (observed) densities, respectively. Theoretical densities were calculated by using the reported densities of pristine AgI (5960 kg m^{-3}) and pristine anatase (3880 kg m^{-3}). The porosity variation with x is shown in the inset. A remarkable difference between the theoretical and experimental density is observed in the smaller x region. Such a result is known behaviour for the compaction of mixtures of particles with extremely different hardnesses. The porosity variation with x may affect the apparent conductivity of the composites.

We studied the surface morphology of (x)AgI–$(1 - x)$anatase specimens by SEM observations both on the raw surfaces and the fractured ones. Figures 2(a) and (b) show, respectively, the low- and high-magnification SEM images for the surface of the (0.4)AgI–(0.6)anatase composite. The EDX fluorescence measurements indicate that large particles and small particles are AgI and anatase, respectively. As seen in these figures, anatase fine particles are densely packed in AgI particles of several micrometres in size. Henceforth, we call this particle the 'anatase-packed AgI particle'. As shown in these figures, small anatase particles are not so different in size from the initial average particle size of 50 nm, while other anatase particles coagulate to form irregularly shaped particles of several hundred nanometres in size. The EDX fluorescence measurements indicate that iodine-rich parts tend to appear inside pore walls and that the surroundings of anatase particles are silver-rich. The latter suggests that Ag^+ ions are adsorbed onto the anatase particle surfaces.

Figure 3 shows the XRD patterns of (x)AgI–$(1 - x)$anatase composites at 300 K. All XRD patterns in this figure are normalized at the peak intensity. Amorphous titanium dioxide powder, as one of the starting materials, was fully transformed into crystalline anatase by

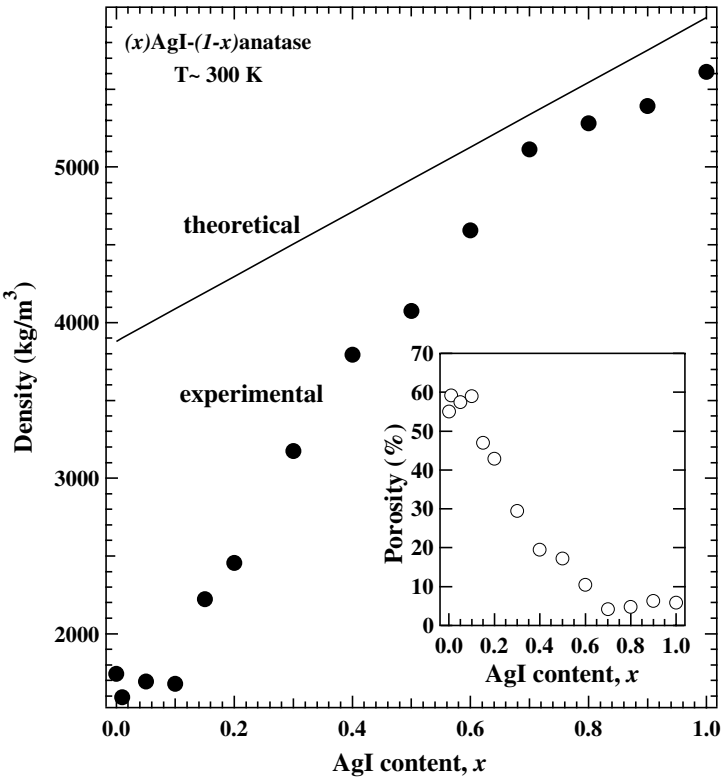

Figure 1. Density of different (x)AgI–$(1-x)$anatase composites at about 300 K. Porosity variation with x is shown in the inset.

heating at 673 K in air for 12 h. With increasing x, some diffraction lines related to AgI become pronounced. All diffraction lines can be almost assigned to γAgI, βAgI and anatase. It seems to be a mere mixture of AgI and anatase. This is very different from that observed in AgI–γAl_2O_3 composites (Lee *et al* 2000a, Mochizuki and Fujishiro 2003). In the AgI–γAl_2O_3 composites, some broadening of the peaks and weakening of the (h0l) and (100) peaks of βAgI become pronounced with increasing x, and some new diffraction lines appear. The new lines can be explained by taking account of the seven-hexagonal-layer polytype AgI (7H-AgI) with the stacking sequence ABCBCAC (Lee *et al* 2000a, 2000b). In the present AgI–anatase composites, however, such polytype-structure lines as observed in AgI–γAl_2O_3 composites never appear, as shown in the inset. In the inset, the full curve represents the XRD pattern of the (0.7)AgI–(0.3)anatase composite, while the broken curve represents that of the (0.73)AgI–(0.27) γAl_2O_3 composite which displays clear (1010) and (1011) lines of the polytype structure. Some broadening is also observed on the βAgI (100) and (002) lines for the small x region. Such line broadening becomes diminished with increasing x. The broadening may arise mainly from reduced crystallite size. The intensity ratio of the βAgI (002) line, which coincides with the γ (111) peak to the βAgI (100) line, increases from 1.919 to 3.384 with increasing x from 0.2 to 0.8. Such an increase may be explained by either a preferred orientation of βAgI crystallites or an increased γAgI component in the anatase-packed AgI particles, accompanied by stacking disorder in hexagonal βAgI. However, it is noted that the βAgI (101), βAgI (102) and βAgI (103) lines almost disappear, while the γAgI (331) line becomes sharpened with

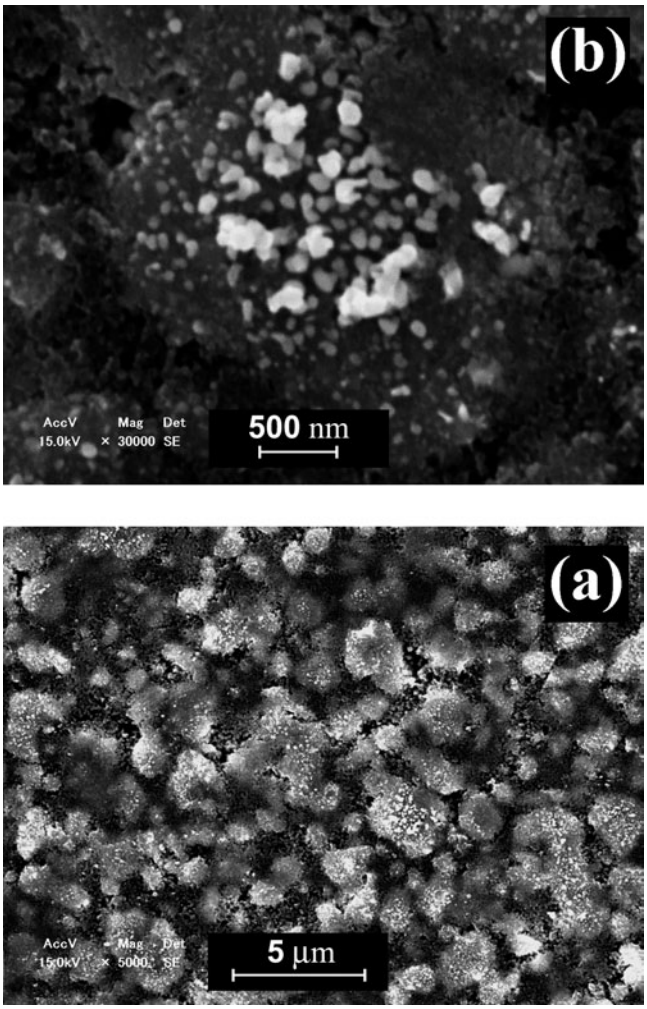

Figure 2. SEM image of the (0.4)AgI–(0.6)anatase: (a) at low magnification (×5000), (b) at high magnification (×30 000).

increasing x, as shown in figure 3. Therefore, to explain the XRD patterns obtained, the contribution from the increased γAgI component should be more taken into account than the preferred orientation. In other words, the AgI domain in the anatase-packed AgI particles consists of many γAgI crystallites and a small number of βAgI crystallites. Referring to the known result that a silver-deficient AgI solution crystallizes in the β phase and silver-rich AgI solutions do so in the γ phase, this is interpreted as follows. Preferential Ag^+ ion adsorption on anatase surfaces, as shown in the SEM and EDX fluorescence data, induces some concentration gradient of Ag^+ ions in the AgI domain. The gradient produces then γAgI crystallites and βAgI ones in the AgI domain. The degree of the gradient is dependent on the anatase content and, therefore, the diffraction intensity ratio of the γAgI line and the βAgI line varies with x, as shown in figure 3. On the other hand, the linewidth of the broad anatase (101) line is found to be almost independent of x. It may indicate that the average size of the anatase particle is not considerably changed by heating. This is consistent with the SEM observation shown in figures 2(a) and (b).

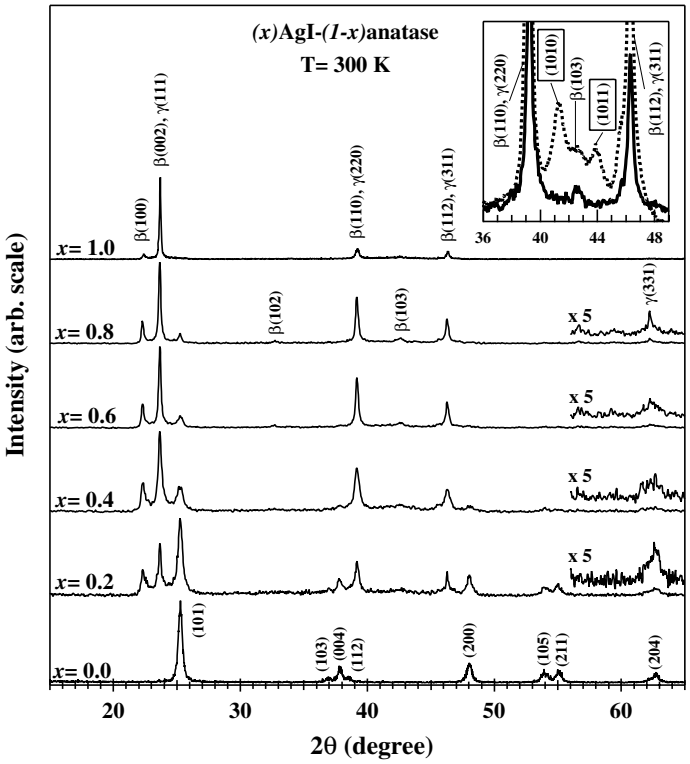

Figure 3. XRD patterns for different (x)AgI–$(1-x)$anatase composites at 300 K. The XRD pattern for (0.7)AgI–(0.3)anatase (full curve) is compared with that for (0.73)AgI–(0.27)$\gamma$$Al_2O_3$ (broken curve) in the inset.

3.2. Electrical conductivity

The conductivity σ of (x)AgI–$(1-x)$anatase composites at 300 K is plotted against x in figure 4. The applied frequency was 1 kHz. No frequency dependence of σ was observed between 42 Hz and 100 kHz. Because of experimental difficulties, the transference numbers for ionic and electronic charge carriers have not been directly determined. However, tentative measurements on the transient current of the asymmetric cell of type (Ag/(x)AgI–$(1-x)$anatase/Au) show a small steady-state current. Therefore, we cannot perfectly exclude the contribution from electronic conduction from the present discussion. As seen in this figure, σ increases abruptly with increasing x. On further increasing x, σ reaches a maximum (about 3×10^{-2} S m^{-1}) at $x = 0.4$. Since the σ for a pristine AgI specimen prepared in the same way is 1.7×10^{-5} S m^{-1}, the conductivity is enhanced by about three orders of magnitude. In the x region larger than 0.4, σ falls gradually toward 1.7×10^{-5} S m^{-1} for pristine AgI. The maximum σ is close to that observed in the AgI–$\gamma$$Al_2O_3$ composite (Uvarov *et al* 2000). Through the present measurements of σ at different temperatures, the following are also found about (x)AgI–$(1-x)$anatase composites:

(1) The σ varies exponentially with temperature below 373 K, while the activation energy for the pristine AgI specimen rises continuously from 0.35 to 0.99 eV with increasing temperature from 300 to 400 K. The activation energy E_σ below 400 K is plotted against x in the inset. The broken curve is the least-squares fit for the plotted E_σ.

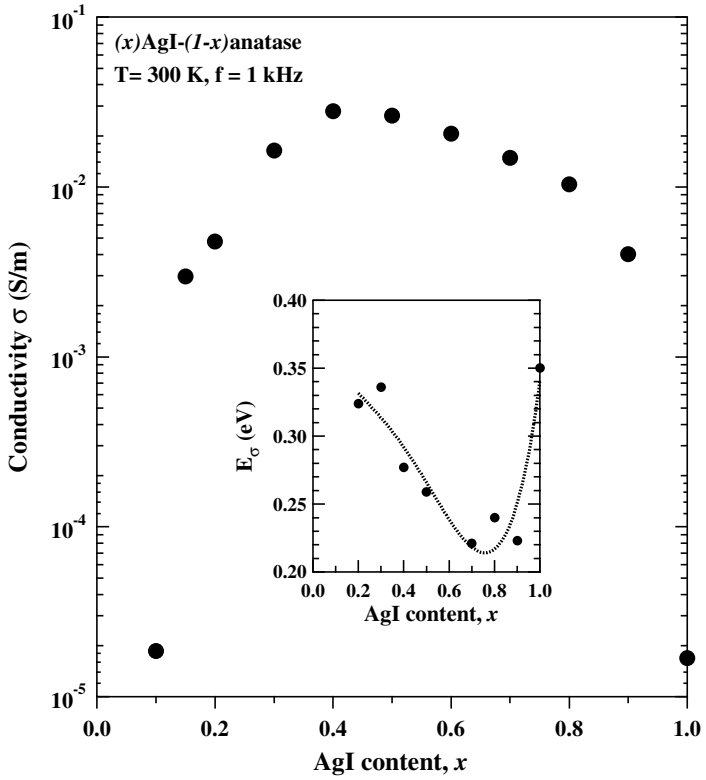

Figure 4. Conductivity of different (x)AgI–$(1-x)$anatase composites at 300 K. The applied frequency was 1 kHz. The activation energy E_σ below 400 K is plotted against x in the inset. The broken curve is the least-squares fit for the plotted E_σ.

(2) The σ at room temperature is not considerably changed for a heating–cooling cycle below T_c.
(3) The composite with larger x ($\geqslant$0.4) exhibits more clearly an abrupt σ change near the T_c (420 K) of pristine AgI with some accompanying transition hysteresis, as observed in the AgI–γAl_2O_3 composite (Lee *et al* 2000a).

In the light of the porosity data shown in figure 1, the σ variation in the small x region ($x \ll 0.4$) may be mainly caused by the insulating pore effect. On the other hand, the conductivity enhancement observed in the large x region ($\geqslant$0.4) may arise from some composite effects, since the starting materials, pristine AgI and anatase, have low conductivities. The composite effects arise from highly ionic-conductive regions at the AgI/anatase interfaces and γAgI/βAgI interfaces in anatase-packed AgI particles. It is known that the adsorption of Ag^+ ions at insulating oxide surfaces leads to the formation of vacancies on Ag^+ sites and the space charge layer. As referred to already in section 3.1, it is also known that a silver-rich AgI solution crystallizes in the γ phase, while a silver-deficient solution crystallizes in the β phase. The γAgI and βAgI crystallites may act as Ag^+ ion donor and acceptor, respectively. Thus, we can anticipate high Ag^+ ion conductivity at the γAgI/βAgI interfaces in anatase-packed AgI particles. With decreasing x from 1 to 0.4, dispersed anatase particles approach each other and then the space charge effect spreads over the AgI domain to display a maximum in the σ–x curve. The activation energy E_σ for σ shows a complicated x

dependence, as shown in the inset of figure 4. The least-squares fitting curve (broken curve) for E_σ exhibits a minimum near $x = 0.7$. It is noted that the porosity variation with x exhibits also a minimum near the same x, as shown in the inset of figure 1. The E_σ of 0.35 eV for the present pristine AgI is smaller than 0.38 eV for an ordered βAgI crystal. This may be explained by the extensive disorder of Ag^+ ions in the stacking faulted structure and such a disordered arrangement of Ag^+ ions may provide a higher energy state than in the ordered βAgI structure with a decrease of E_σ (Lee *et al* 2000b). By adding anatase particles to the pristine AgI, the E_σ decreases. This indicates a generation of new ionic transport pathways. This is due to Ag^+ ion adsorption onto anatase fine particles. On further adding anatase, E_σ becomes affected by both the electronic conduction in anatase particles and the existence of insulating pores. Following more detailed discussion, the transference numbers for ionic and electronic charge carriers should be determined.

The effects of crystalline defects introduced by some strain coming from stress with different thermal expansion coefficients between AgI and anatase should also be taken into consideration (Jow and Wagner 1979).

3.3. Optical spectra

Before describing the results of optical measurements on (x)AgI–$(1-x)$anatase composites, we point out general photoinduced properties obtained for AgI-based glasses (AgI–$AgPO_3$ glasses, AgI–Ag_2MO_4 and AgI–Ag_2WO_4) and AgI-based composites (AgI–γAl_2O_3 and AgI–ZnO (Fujishiro and Mochizuki 2003)). These AgI-based ionic conductors are easily blackened with intense ultraviolet laser light. Such blackening becomes prominent with increasing temperature and increasing AgI content. The blackening is due to precipitation of silver clusters or silver fine particles, which is an irreversible reaction. The blackening gives rise to PL intensity reductions, which is the so-called photodarkening. Therefore, we checked the blackening by examining the reproducibility of measured PL spectra at different laser fluences and then we found a suitable excitation light intensity for the PL measurement for each specimen.

In figure 5, the PL spectra obtained for (x)AgI–$(1-x)$anatase composites with different compositions at 8 K are compared. The PL was excited by the 355 nm laser line of the Nd^{3+}:YAG laser. All spectra in this figure are normalized at the peak intensity. Pristine anatase shows a broad PL band centred at about 536 nm (2.31 eV) with a large Stokes shift of 0.89 eV. The present PLE spectrum measurement of this broad PL band at 8 K shows a sharp PLE edge, corresponding to the optical absorption edge, at about 3.2 eV which is close to the bandgap energy of pristine anatase. This PL band has been tentatively assigned to the radiative recombination of self-trapped excitons in pristine anatase by many authors (Tang *et al* 1994, Hosaka *et al* 1997, Suisalu *et al* 1998). The addition of a small amount of AgI, $x = 0.2$, leads to a considerable decrease of this anatase PL and gives a sharp PL band at 428 nm with accompanying shoulders at about 423 nm and about 438 nm. The spectrum is affected by noise at wavelengths shorter than 415 nm. The decreased PL intensity of the 536 nm band is due to the absorption of excitation laser light by the AgI domain in an anatase-packed AgI particle. In pristine AgI, the bands at about 424 nm and about 429 nm are assigned to the radiative recombination of $Z_{1,2}$ excitons and shallowly trapped $Z_{1,2}$ ones, respectively (Mochizuki and Fujishiro 2002, Cardona 1963, Mochizuki and Ohta 2000, Mochizuki 2001, Mochizuki and Umezawa 1997). No measurable spectral change with x is observed in the 536 nm band. Further addition of AgI, $x = 0.4$, increases the longer wavelength sideband to generate a broad band centred at 442 nm and reduces the 536 nm band, with an accompanying slight bandwidth narrowing at the longer wavelength side ($\lambda > 536$ nm). On further increasing x

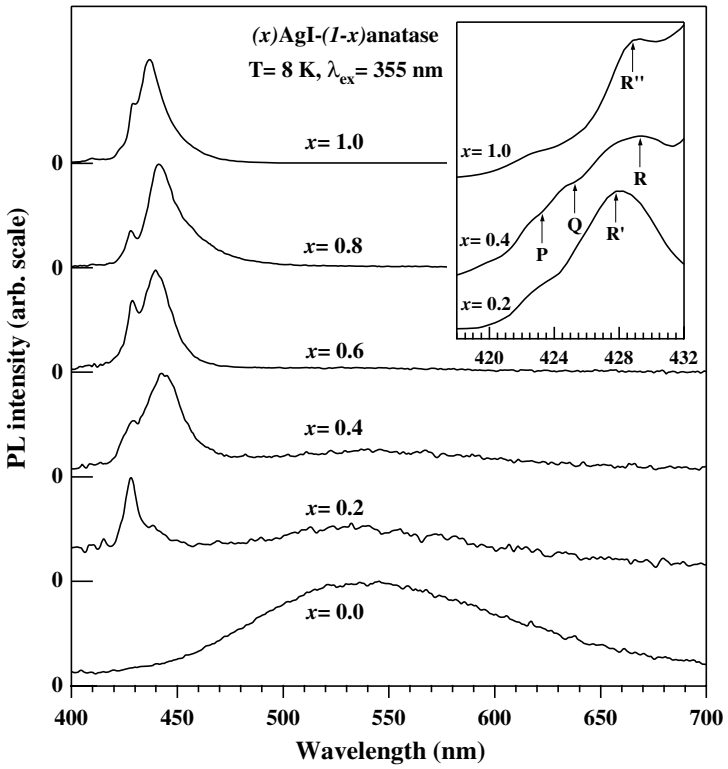

Figure 5. PL spectra of different (x)AgI–$(1-x)$anatase composites at 8 K. Free exciton PL bands for (0.2)AgI–(0.8)anatase, (0.4)AgI–(0.6)anatase and pristine AgI are shown in the inset. The PL bands labelled R, R′ and R″ are due to radiative decays of shallowly trapped excitons.

from 0.4 to 0.8, this broad band becomes narrowed and blue-shifted to 441 nm, which is close to the intensity maximum (437 nm) of pristine AgI. Therefore, it should be interpreted that the broad band consists of the 438 and 442 nm bands. We interpret the observed spectral variation with x, as follows. In the specimens with smaller x, since free excitons are confined in smaller AgI domains, excitons reach AgI domain surfaces and AgI/anatase interfaces and then decay radiatively. Since the energy bandgap (about 3.1 eV) of AgI is close to that (3.2 eV) of anatase, the potential for trapping free AgI excitons is thought to be shallow. In such a case, unlike the AgI–γAl$_2$O$_3$ composite (Mochizuki and Fujishiro 2003), any PL band due to radiative decay of excitons deeply trapped at the AgI/anatase interfaces may not be apparently observed, as shown in figure 5. However, as described below, a small number of excitons deeply trapped at the AgI/anatase interfaces are found through measurements of the excitation-light intensity dependence of the PL spectrum. It should also be pointed out that the fine structure at the higher energy side of the 429 nm band becomes prominent at $x = 0.4$. In the inset, the higher energy side spectral structure for the (0.2)AgI–(0.8)anatase and (0.4)AgI–(0.6)anatase composites is compared with that for the pristine AgI specimen which was prepared in the same way. The shoulders at about 423 nm and about 425 nm, which are respectively labelled P and Q, are seen for the (0.4)AgI–(0.6)anatase composite. As shown in the inset of figure 6, both the P and Q shoulders remain clearly even at 129 K (=11.1 meV) in spite of the small energy separation (13.8 meV) between P and Q. With increasing x, the P and Q shoulders tend to move toward about 424 nm. The $Z_{1,2}$ exciton originates from the doubly degenerate valence band

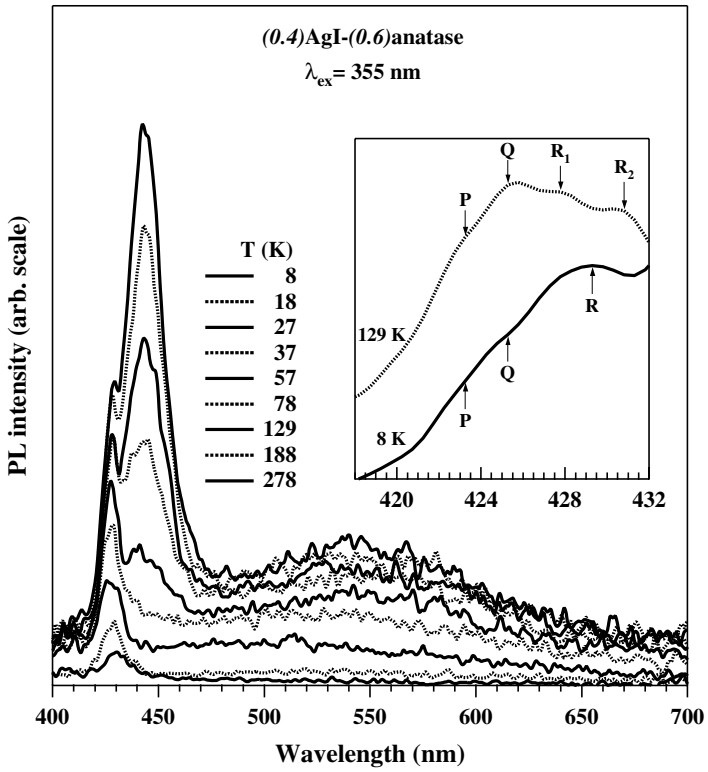

Figure 6. Temperature dependence of the PL spectrum of the (0.4)AgI–(0.6)anatase composite. The temperature increases in the curves from top to bottom. The PL spectra at 8 and 129 K are compared in the inset by rescaling their intensities.

Γ_8 with light and heavy hole masses. The Γ_8 band tends to split by some crystal-field change caused by mixing with the wurtzite structure or some internal stress caused by different thermal expansion coefficients between the AgI and anatase. Therefore, such Γ_8 splitting should be taken into account for rigorous assignment of the 423 and 425 nm shoulder bands. Such an exciton spectrum is similar to that of the microcrystal specimen (Mochizuki and Umezawa 1997). The spectral structure of the 429 nm peak (labelled R) assigned to shallowly trapped $Z_{1,2}$ excitons changes with x as shown in the inset. The changed bands are labelled R′ and R″. This indicates that there are several shallowly trapped exciton states. In such cases, the lower energy trapped excitons tend to populate higher energy trapped exciton states with increasing temperature.

The PL spectra of AgI–anatase composites were studied at different temperatures between 8 and 278 K. The result obtained for the (0.4)AgI–(0.6)anatase composite with maximum σ is shown in figure 6 as a typical example. In comparison with the emission intensities of the P-, Q- and R-emission shoulders, the emission of the 442 nm band decreases prominently with increasing temperature. The intensity peak at about 442 nm was assigned above to radiative decay of excitons trapped by lattice defects and impurities in the AgI domain. On further increasing temperature above 78 K, the 442 nm band almost disappears and absolutely disappears at 278 K. Above 188 K, the intrinsic and extrinsic exciton bands are slightly red-shifted, which is ascribed to the decrease of the bandgap energy of AgI with increasing temperature. Such a redshift was also observed at pristine AgI (Mochizuki and Ohta 2000).

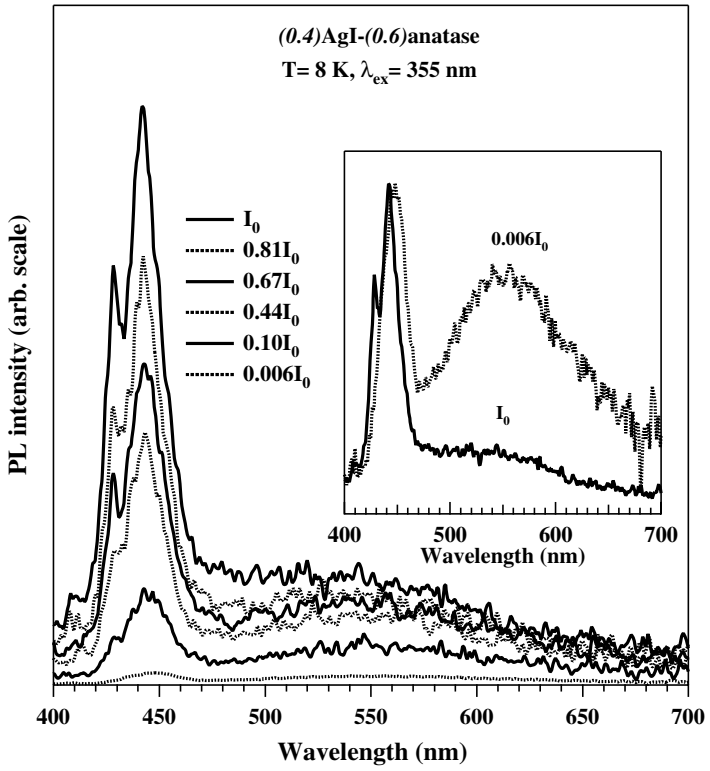

Figure 7. Excitation-light intensity dependence of the (0.4)AgI–(0.6)anatase composite at 8 K. The laser fluence increases in the curves from top to bottom. The PL spectra for the weakest and most intense excitations are compared by rescaling their intensities in the inset.

The disappearance of the 442 nm band may be due to a thermally activated reverse process from trapped states to free exciton ones. The 536 nm band becomes weaker and shifted to shorter wavelength with increasing temperature. Such a blueshift was also observed in the pristine anatase specimen. This indicates the decreased exciton-lattice relaxation energy. As described later, the broad 536 nm band consists of two bands. If these bands have different temperature dependences, such a blueshift of the 536 nm band is possible. The PL intensity decrease of the 536 nm band with increasing temperature from 8 to 98 K is about two times larger than that observed in pristine anatase. This may be attributed to the exciton trapping and nonradiative exciton decay at the AgI/anatase interface.

The excitation-light intensity I_{ex} dependence of the PL spectrum is also studied at 8 K on different (x)AgI–$(1-x)$anatase composites. The result obtained for the (0.4)AgI–(0.6)anatase composite with maximum σ is shown in figure 7 as a typical example. With decreasing laser fluence, the free exciton P- and Q- shoulder emissions and the shallowly trapped exciton R emission decrease linearly with I_{ex}. On the other hand, the 442 and 536 nm emissions decease nonlinearly with decreasing I_{ex}, but their decreases are smaller than those of the P, Q and R emissions. Upon further decreasing I_{ex}, the 536 nm emission intensity becomes comparable to that of the 442 nm emission with accompanying intensity peak wavelength shift from 536 to 552 nm. This indicates that the 442 and 536 nm emissions have higher yields than the free exciton emissions and the shallowly trapped exciton emission. But the 442 and 536 nm emissions become saturated under intense excitation. These saturations arise from a finite

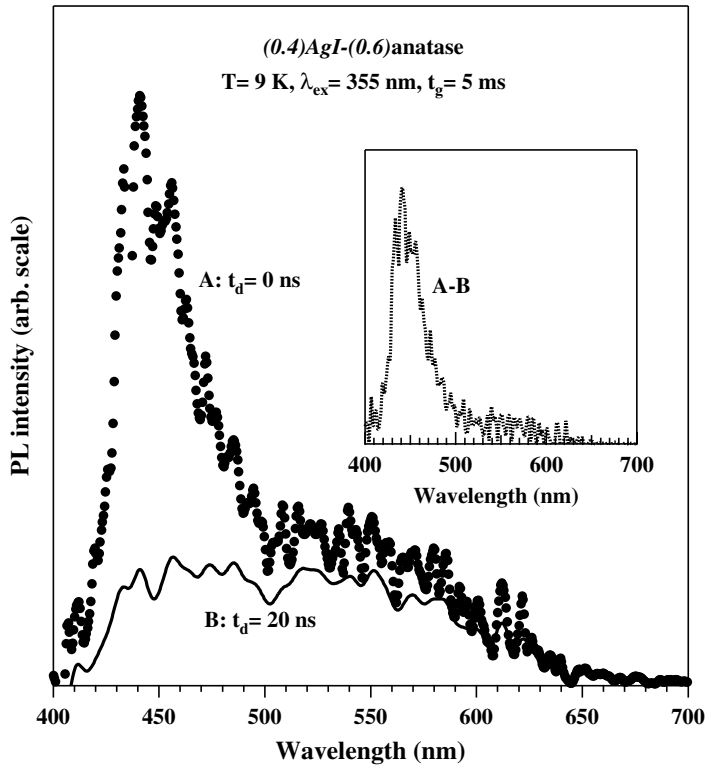

Figure 8. TRPL spectrum of the (0.4)AgI–(0.6)anatase composite at 9 K. Curves A and B correspond to the time-resolved spectra integrated from 0 ns to 5000 μs and integrated from 20 ns to 5000.02 μs after incidence of the laser pulse, respectively. The PL component (curve A − curve B) for short delay time is shown in the inset.

number of shallow- and deep-level PL centres. In the inset, the PL spectra observed under intense ($I_0 = 33$ mJ cm^{-2}) and weak ($0.006I_0$) excitations at 8 K are compared. We have assigned tentatively the 536 nm band to radiative decay of self-trapped excitons in pristine anatase on the basis of both the present PLE spectrum edge (about 3.2 eV) and the assignment made previously in several papers (Tang *et al* 1994, Hosaka *et al* 1997). However, the PL intensity of the composite saturates at a laser fluence larger than 33 mJ cm^{-2}, while we cannot detect any saturation in pristine anatase particles. Therefore, the results may indicate that the excitons in anatase are affected by adding AgI. Deeply trapped excitons in anatase may be formed by exciton–phonon interactions or by interactions between free electrons and trapped holes by defects at the AgI/anatase interfaces or both. Since the number of defects is limited, the emission from such deeply trapped excitons at the interfaces becomes saturated under intense excitation. The observed redshift from 536 to 552 nm with decreasing I_{ex} may indicate that anatase-related emission consists of at least two emission bands, labelled as X and Y bands.

The TRPL spectra of AgI–anatase composites were measured at 9 K. Since the TRPL measurements need longer data-acquisition times and the composites easily became blackened by excitation laser light during the measurements, as stated above, we considerably reduced the laser fluence. As a result, the spectra are considerably affected by noise. In figure 8, the TRPL spectra at 9 K shown for the (0.4)AgI–(0.6)anatase composite with maximum σ are typical

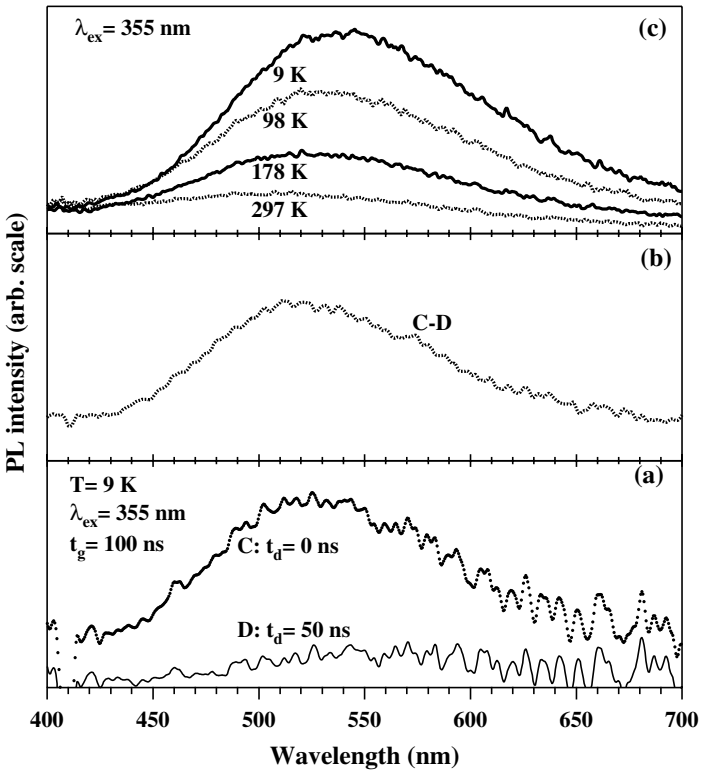

Figure 9. PL spectra of pristine anatase fine particles at 9 K: (a) TRPL spectra, (b) short-delay-time emission, (c) temperature dependence of the PL spectrum.

examples. Curves A and B correspond to the time-resolved spectra integrated from 0 ns to 5000 μs and integrated from 20 ns to 5000.02 μs after incidence of a laser pulse, respectively. At a first glance, the PL spectrum consists of a broad band due to anatase shown as the bottom curve and another broad band due to AgI. In order to extract the short-delay component, we have calculated the difference spectrum (curve A − curve B). The result (curve A–B) is shown in the inset. The difference spectrum gives an image of the 'pure' short-time emission spectrum. Comparing this difference spectrum with those of pristine AgI and pristine anatase shown in figure 5, one can identify the short-time emission spectrum made up essentially of several kinds of AgI-related emission (400 nm $< \lambda <$ 500 nm) and weak anatase-related emission (500 nm $< \lambda <$ 700 nm). On the other hand, the long-time emission spectrum (full curve) may be anatase-related emission, which consists of two components centred at about 465 nm and about 536 nm.

The TRPL spectra of pristine anatase particles are also measured at 9 K. The results are given in figure 9(a). Curves C and D correspond to the time-resolved spectra integrated from 0 to 100 ns and integrated from 50 to 150 ns after incidence of the laser pulse, respectively. In order to extract the short-delay component, we have calculated the difference spectrum (curve C − curve D). The result is shown in figure 9(b). The short time emission (curve C–D) is blue-shifted in comparison with the long-time emission (curve D). The blue-shifted emission indicates that the broad band emission of pristine anatase particles consists of different radiative decays of self-trapped excitons. The PL spectrum of the same pristine anatase specimen was also

measured at different temperatures between 9 and 297 K. The results are shown in figure 9(c). As seen in this figure, the broad PL band is blue-shifted with increasing temperature. This may be related to the above-mentioned multicomponent of the PL band. We should note the spectral structure difference between curve B in figure 8 and curve D in figure 9(a). We compared the PL and TRPL spectra of (0.4)AgI–(0.6)anatase with those of pristine anatase particles and single crystals (Tang *et al* 1994, Watanabe *et al* 2000). In the result, we have reached a view that anatase-related excitons are partially trapped at the AgI/anatase interface. Since an exciton trap is closely related to a defect, the view may yield a conclusion that there are defects at the AgI/anatase interfaces. Assuming that the effect is explained as a space charge effect, the probable reason is the adsorption of Ag^+ ions at the thereby positively charged oxide surfaces and the creation of numerous vacancies at the AgI/anatase interfaces. When the interface has a comparatively large defect density, the interface region may have high ionic conductivity. The detailed report on the PL and TRPL studies on various pristine anatase specimens will be presented in a separate paper (Mochizuki *et al* 2003).

We have already discussed the space charge effects at the AgI/anatase interfaces on ionic conduction. We need to discuss such space charge effects on excitons. The space charges generate a potential gradient, namely an electric field, which drives the self-trapped exciton formation, exciton trapping and exciton dissociation.

4. Conclusion and remarks

The results obtained for (x)AgI–$(1-x)$anatase composites are briefly summarized as follows.

(1) Conductivity enhancement higher than three orders of magnitude is observed.
(2) The SEM and EDX fluorescence measurements indicate that anatase fine particles are packed in large AgI particles of several micrometres in size and such anatase-packed AgI particles are three dimensionally connected to form a composite specimen. We named these composites particles anatase-packed AgI particles. Silver-rich parts appear around anatase particles. This indicates Ag^+ ion adsorption on the surfaces of the anatase particles. The measurements indicate also that some of the anatase particles are nearly isolated and others aggregate with each other to form larger particles.
(3) The XRD pattern of AgI domains in anatase-packed AgI particles is similar to that of type II AgI crystals (Lee *et al* 2000b) and the (311) line of γAgI is observed. The AgI domain in the anatase-packed AgI particles consists of γAgI and βAgI crystallites.
(4) The splitting of the $Z_{1,2}$ exciton spectra of AgI is observed as two shoulder PL bands. These may arise from some crystal-field change caused by the mixing with the wurtzite structure or some internal stress caused by different thermal expansion coefficients between the AgI and anatase.
(5) The anatase-related exciton spectra in the anatase-packed AgI particles are considerably affected in comparison with pristine anatase. Excitons in anatase fine particles are partially trapped at the AgI/anatase interfaces which may contain numerous crystalline defects.

Results (2) and (3) explain well the observed conductivity data for (x)AgI–$(1-x)$anatase composites. It may be concluded that adding anatase fine particles to AgI produces vacancies on Ag^+ ion sites, a space charge layer and a heterostructure for γAgI and βAgI crystallites. In such anatase-packed AgI particles, both the AgI/anatase interface regions of neighbouring anatase particles and the γAgI/βAgI crystallite interfaces would provide pathways for high conductivity.

The main limitation of our technique is that there are no direct mesoscopically space-resolved electrical and optical measurements on the composite specimens. Bearing this

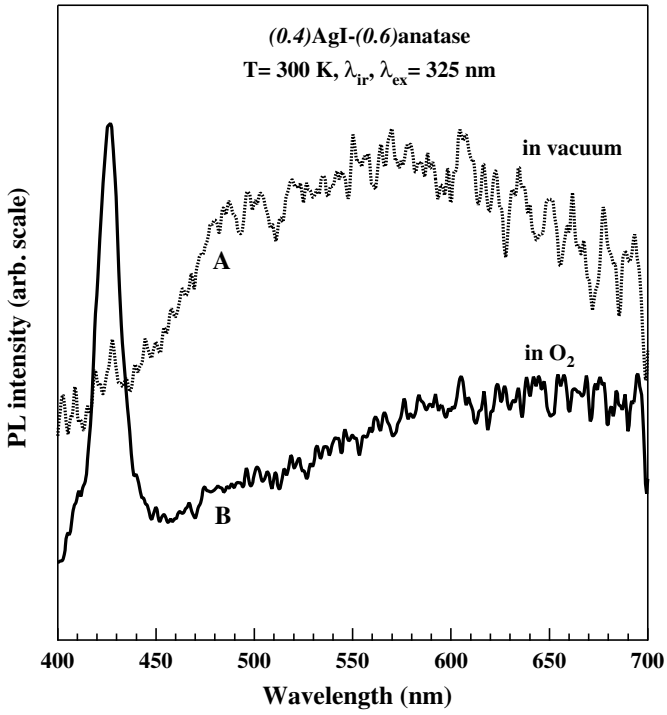

Figure 10. Reversible photoinduced spectral change in (0.4)AgI–(0.6)anatase composites at 300 K. Both the irradiation laser light wavelength λ_{ir} and the PLE laser light wavelength λ_{ex} are the same: 325 nm.

limitation in mind, we have presented some reasonable connections between the measured data and composite effects in the AgI–anatase system. With a near-field optical microscope measurement system and a SEM, the space-resolved optical and structural measurements on different AgI–oxide systems are now in progress in our laboratory.

Very recently, we have measured the Raman scattering spectra of (x)AgI–$(1-x)$ anatase composites at room temperature. The present pristine AgI shows a broad band centred at 88 cm^{-1}. This band is assigned to extra modes coming from defects. When x is decreased to less than 0.2, the band shifts to 78 cm^{-1} and becomes resolved into three bands centred at about 68, 78 and 94 cm^{-1}. Such a spectral change may give more directly information about the defect structure at AgI/anatase interfaces (Mochizuki *et al* 2003).

Finally, we have very recently found a reversible photoinduced spectral change in the present (x)AgI–$(1-x)$anatase composite specimens at room temperature. The spectral change obtained for (0.4)AgI–(0.6)anatase is shown in figure 10 as a typical result. After fully irradiating at 300 K with 325 nm laser light in a vacuum specimen chamber, the specimen shows a broad PL spectrum (curve A) due to trapped excitons in anatase. Oxygen gas is then introduced into the chamber. With increasing irradiation time, the broad PL band becomes weak, while a sharp PL band due to the excitons in AgI grows at 426 nm and the broad PL band prevails, as indicated by curve B. The chamber is again evacuated. The broad PL spectrum reappears. It is found through many successive experiments that the spectral changes appear repeatedly. The enhancement of the broad PL is related to photogenerated oxygen vacancies and is observed for many oxides, for example Eu_2O_3, Sm_2O_3 (Mochizuki *et al* 2001a, 2001b) and SiO_2 (Mochizuki and Araki 2003). The observed spectral changes

may originate from the photoinduced dissociative adsorption and photoinduced associative detachment of O_2 molecules near the composite surfaces and may well yield materials for optical sensor devices, for example, optical oxygen-partial-pressure sensors. The detailed results will be described in a separate paper.

Acknowledgments

This work was partially supported by a Grant-in-Aid for Scientific Research from the Ministry of Education, Science, Sports, Culture and Technology, Japan. This work is also partially supported by a Project Research Grant from The Institute of Information Sciences of College of Humanities and Sciences (Nihon University) and by a Cooperative Research Grant from The Institute of Natural Sciences (Nihon University).

References

Bloch R and Möller H 1931 *Z. Phys. Chem.* A **152** 245
Burley G 1963 *Am. Mineral.* **48** 1266
Burley G 1967 *Acta Crystallogr.* **23** 1
Cardona M 1963 *Phys. Rev.* **129** 69
Fujishima A, Rao T N and Tryk D A 2000 *J. Photochem. Photobiol.* C **1** 1
Fujishiro F and Mochizuki S 2003 *ICDS-22: The 22nd Int. Conf. on Defects in Semiconductors*;; *Physica* B submitted
Gupta R K, Agraval R C and Pandey R K 1996 *Solid State Ionics* ed B V R Chowdary *et al* (Singapore: World Scientific) p 499
Hosaka N, Sekiya T and Kurita S 1997 *J. Lumin.* **72–74** 874
Jow T and Wagner J B Jr 1979 *J. Electrochem. Soc.* **126** 1963
Lee J-S, Adams S and Maier J 2000a *Solid State Ion.* **136/137** 1261
Lee J-S, Adams S and Maier J 2000b *J. Phys. Chem. Solids* **61** 1607
Liang C C 1973 *J. Electrochem. Soc.* **120** 1289
Mochizuki S 2001 *Physica* B **308–310** 1042
Mochizuki S and Araki H 2003 *Physica* B submitted
Mochizuki S and Fujishiro F 2002 *Proc 6th Forum on Superionic Conductor Physics* (Kyoto: The Japanese Society of Ion Transport) pp 41–6
Mochizuki S and Fujishiro F 2003 *Phys. Status Solidi* c **0** 763
Mochizuki S, Fujishiro F and Shimizu T 2003 (in preparation)
Mochizuki S, Nakanishi T, Suzuki Y and Ishi K 2001a *Appl. Phys. Lett.* **79** 3785
Mochizuki S and Ohta Y 2000 *J. Lumin.* **87–89** 299
Mochizuki S, Suzuki Y, Nakanishi T and Ishi K 2001b *Physica* B **308–310** 1046
Mochizuki S and Umezawa K 1997 *Phys. Lett.* A **228** 111
Shahi K and Wagner J B Jr 1981 *Solid State Ion.* **3/4** 295
Shastry M C R and Rao K J 1992 *Solid State Ion.* **51** 311
Suisalu A, Aarik J, Mandar H and Sildos I 1998 *Thin Solid Films* **336** 295
Tang H, Berger H, Schmid P E and Levy F 1994 *Solid State Commun.* **92** 267
Uvarov N F, Vanek P, Savinov M, Zelezny V, Studnicka V and Petzelt J 2000 *Solid State Ion.* **127** 253
Watanabe M, Sasaki S and Hayashi T 2000 *J. Lumin.* **87–89** 1234
West A R 1984 *Solid State Chemistry and Its Applications* (New York: Wiley)
Zhao Z-Y, Wang C-Y, Dai S-Y and Chen L-Q 1983 *Solid State Ion.* **9/10** 1175

INSTITUTE OF PHYSICS PUBLISHING JOURNAL OF PHYSICS: CONDENSED MATTER

J. Phys.: Condens. Matter **16** (2004) 3239–3256 PII: S0953-8984(04)75141-3

In situ real time optical study of films grown on low temperature substrates by vacuum evaporation of iodine and silver iodide: spectral transitions during deposition and annealing processes

Shosuke Mochizuki[1] **and Fumito Fujishiro**

Department of Physics, College of Humanities and Sciences, Nihon University, 3-25-40 Sakurajosui, Setagaya-ku, Tokyo 156-8550, Japan

E-mail: motizuki@physics.chs.nihon-u.ac.jp

Received 20 January 2004
Published 23 April 2004
Online at stacks.iop.org/JPhysCM/16/3239
DOI: 10.1088/0953-8984/16/18/024

Abstract

In order to clarify the growth process and hard to understand reported spectra of iodine film and silver iodide (AgI) film, various spectral transitions have been measured *in situ*: (a) optical density spectra of films grown on low temperature substrates by vacuum evaporation of an iodine lump, during deposition and annealing; (b) optical extinction spectra of vapour zones produced by gas evaporation of AgI powder, during evaporation; and (c) optical density spectra of films grown on low temperature and room temperature substrates by vacuum evaporation of AgI powder, during deposition and annealing. After these *in situ* real time measurements, the film specimens were allowed to recover and were examined by means of comparative measurements of the optical density and photoluminescence spectra at about 12 K. The spectra obtained were analysed and compared with those reported previously by other workers, and the following questions have been optically clarified: (1) How does annealing improve the crystal quality of iodine film? (The annealing at about 200 K improves the crystal quality considerably.) (2) What is the film that is quench deposited on low temperature sapphire surfaces by thermal evaporation of AgI powder? (It is Ag_mI_n ($m, n \geqslant 1$) dispersed iodine film.) (3) How does AgI film grow in the deposited film? (Above about 220 K, iodine evaporates abruptly to grow uniform AgI film on the substrate.) (4) How does excess iodine affect the optical spectrum of AgI? (The excess iodine creates both several exciton absorptions due to polytype structures at wavelengths between 370 and 410 nm, and a tail at wavelengths longer than 430 nm.) (5) What is the best evaporation condition for the fabrication of AgI and iodine films? (The best quality of iodine and βAgI films can be obtained at a substrate temperature of about

[1] Author to whom any correspondence should be addressed.

200 K in the quench deposition method.) Besides this, the present optical experiments have answered the following question: is there truly a strongly enhanced optical absorption in quench deposited AgI films, as reported by Kondo *et al* (1998 *Phys. Rev.* B **57** 13235)? The present studies have elucidated that the enhanced absorption is not due to amorphization of AgI but due merely to intense optical absorption of iodine in the films.

1. Introduction

Because of the practical importance of silver iodide, AgI, in electrolytes, photography and cloud condensation nuclei, the physical and chemical properties have been extensively studied in the last few years. AgI has three phases designated as α, β and γ, in order of decreasing temperature, at normal pressure with the following properties (Burley 1963). At the superionic transition temperature T_c (420 K), the superionic α phase transforms into semiconductor β phase (wurtzite lattice). The α phase has a body-centred cubic arrangement of I^- ions with highly mobile Ag^+ ions randomly distributed through the equivalent interstices; this is known as the averaged structure. At room temperature, the semiconductor γ phase (zinc-blende lattice) appears as a metastable state. It is said that the stability of the γ phase is affected by slight nonstoichiometries and other defects. To date, the optical spectra of pristine AgI (Cardona 1963, Mochizuki 2001, Mochizuki and Ohta 2000) and AgI nanoparticles (Mochizuki and Umezawa 1997, Dulin 1993), AgI-based composites (Mochizuki and Fujishiro 2003a, 2003b) and AgI-based glasses (Fujishiro and Mochizuki 2002, Mochizuki and Fujishiro 2003c) have been reported, by many workers. However, it is well known that the AgI specimens tend to contain excess iodine. The excess iodine species in real AgI specimens are thought to be dependent on the specimen preparation method and thermal history. Iodine clusters I_n ($n > 2$) and films exhibit several intense broad optical absorption bands in the visible and ultraviolet light regions. Although such excess iodine effects have not been reported in detail, we have frequently experienced these absorption bands due to excess iodine disappearing or weakening considerably upon annealing at moderate temperature in vacuum, and found that βAgI film with high optical quality is fabricated by both depositing and subsequently annealing below room temperature. For example, although excess iodine in film specimens is stable at low temperatures ($T < 90$ K) even in vacuum, it rapidly evaporates above about 220 K under heating. Kondo *et al* (1998) prepared films on a low temperature sapphire substrate by evaporating AgI in vacuum and observed extremely enhanced absorption compared to that of crystalline AgI film; the enhanced absorption appearing in thick and thin films disappeared suddenly at temperatures higher than 220 and 180 K, respectively. They explained the enhanced absorption by the p–d hybridization in amorphous AgI and the disappearance of the intense absorption by an amorphous–crystalline transition. However, we have found very recently that such intense absorptions, spectral shapes and sudden spectral disappearances are very similar to those observed for pristine iodine films. Unfortunately, these excess iodine effects have been accorded too little respect in the optical study of AgI and AgI-based materials for a long period of time and they have led many researchers astray.

In the present study, we have performed *in situ* real time measurements of the optical spectra of AgI films and pristine iodine films deposited on the same low temperature sapphire surfaces, during both deposition and heating (annealing) processes. Besides this, we have measured optical extinction spectra of AgI vapour zones and have clarified the vapour species. After these measurements, the AgI film specimens grown were examined by means of comparative measurements of the optical density (OD) and photoluminescence (PL) spectra

at about 10 K. On the basis of these experimental results, we have studied the AgI film growth mechanism below room temperature and elucidated several AgI-related phenomena which were previously reported by other authors but were hard to understand.

2. Experimental procedure

Vacuum evaporation experiments were carried out under a base pressure below 10^{-4} Pa by using a stainless-steel evaporation chamber with two pairs of opposite optical windows. The experimental apparatus was composed of a main evaporation chamber and a spectral measurement system. The apparatus was used previously for cluster and microcrystal studies (Mochizuki 1996, Mochizuki and Ruppin 1993). Optically flat plates of sapphire (R-cut) were used as the substrate. The substrate temperature (T_s) was monitored with a copper–constantan thermocouple. For evaporation of AgI, a platinum crucible containing nominally pure AgI (Alpha, 99.999%) powder was gradually heated indirectly in an alumina crucible on which a tungsten wire heater was wound. The iodine vapour was obtained by evacuating a glass tube which contained nominally pure iodine lumps (Wako, 99.8%) and was connected to the evaporation chamber. In the present experiments, the thickness of film on the substrate increased with time. During the deposition, the OD spectrum of the selected position in the film was recorded as a function of time (t_d) elapsed after the beginning of the measurement with an optical multichannel analyser system. Each measurement was made at the appropriate time window and time interval. A time (t_d) resolved spectrum consists of 64 spectra. In the present paper, some of them are selected and presented. Continuum light from a 150 W xenon lamp was appropriately attenuated to avoid photoinduced blackening and was directed at the whole substrate in a transmission configuration without using a lens. After passing the substrate, only the light through the selected position was collected by a lens and then spectrally analysed and recorded by a multichannel analyser system (Atago, MAX 3000). The transmission T_r at a given position is the intensity ratio at the same position before the beginning of the evaporation. The results for films are expressed with respect to the OD spectra, $-\log T_r$.

Generally, the vapour produced by the vacuum evaporation method is too thin for usual optical absorption measurements and the vapour needs to be confined. In order to confine the vapour, the gas evaporation experiments on AgI were carried out at different gas pressures and the optical extinction spectra were measured at different stages of evaporation, using the apparatus described above to determine optically the vapour species in the AgI vapour, taking into account some aggregation of vapour species due to atmospheric gas. Optical extinction spectra of selected positions in the vapour zones were recorded in the transmission configuration as a function of t_d elapsed from the beginning of the measurement. Since the transmissivity spectra obtained for the vapour zones contain both scattering and absorption effects, the results obtained are expressed as optical extinction spectra, $-\log T_r$.

After the above-described *in situ* real time measurements, the recovered AgI film specimens were put in a helium closed-cycle cryostat, whose temperature could be varied from about 10 to 300 K. PL was excited by different laser lines (360–440 nm) from a Ti^{3+}:sapphire laser excited by a Nd^{3+}:YAG laser. The PL spectra were examined at different laser lines with different excitation intensities. The emitted light was dispersed using a grating spectrograph (Jobin-Yvon HR-320), and an image-intensified multichannel photodetection system (Lambda Vision, LVID) was employed. Both the OD spectra and the PL spectra were measured at about 10 K. The PL spectra were also measured at different temperatures between 7 K and room temperature. The spectral response of the optical system, including the focusing lens and the optical fibre, was carefully measured using a calibrated quartz–halogen lamp and used to correct the raw data. Through the above optical measurements, the lights from the xenon lamp and laser were suppressed to avoid photoblackening.

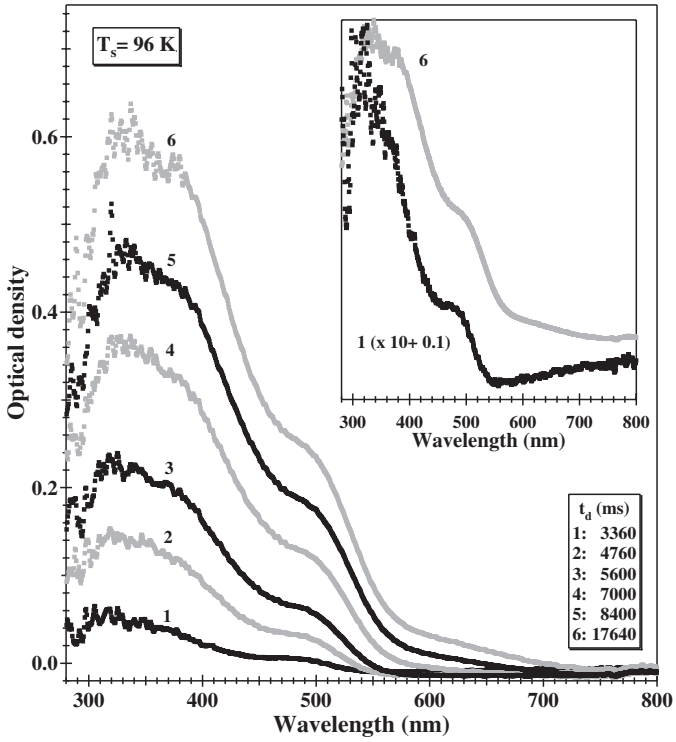

Figure 1. The time evolution of the optical density spectrum of iodine film on a sapphire substrate (T_s = 96 K) during deposition. The spectra at the initial and final stages of the deposition are compared in the inset.

3. Results and discussion

3.1. Time evolution of the optical density spectrum of iodine film deposited on a sapphire substrate during vacuum evaporation of pristine iodine

We evaporated iodine at different evaporation speeds and at different substrate temperatures. Figure 1 shows the time evolution of the OD spectrum of the iodine film deposited on a sapphire substrate whose temperature was 96 K, as a typical example. Each measurement was made for 140 ms at intervals of 140 ms. The time t_d increases for the curves from bottom to top. The time evolution corresponds to the film thickness increase. With increasing t_d, the absorption increases with the spectral broadening. Although the spectra at the transparent region (>600 nm) are affected by some interference effect, curve 1 can be compared with curve 6 by rescaling: $\times 10 + 0.1$. The spectra of iodine film obtained are very different from those of iodine molecules (Mathieson and Rees 1956). This indicates that the strong molecular interaction in solid iodine affects its electronic structure. The absorption of curve 6 starts to rise around about 760 nm, which is comparable to the reported bulk values deduced from optical and photoconduction measurements: 733 nm at 78 K and 779 nm at 200 K (Braner and Chen 1963), 775 nm at 123 K (Yamamoto *et al* 1987), 827 nm at 300 K (Many *et al* 1961), 992 nm at room temperature (Riggleman and Drickamer 1963) and 939 nm at room temperature (Moss 1952). The absorption rises gradually up to about 580 nm, and reaches an inflection point at about 580 nm. After reaching a kink at about 505 nm, the absorption rises steeply to another kink at about 380 nm. Passing through a maximum at about 320 nm, the absorption decreases

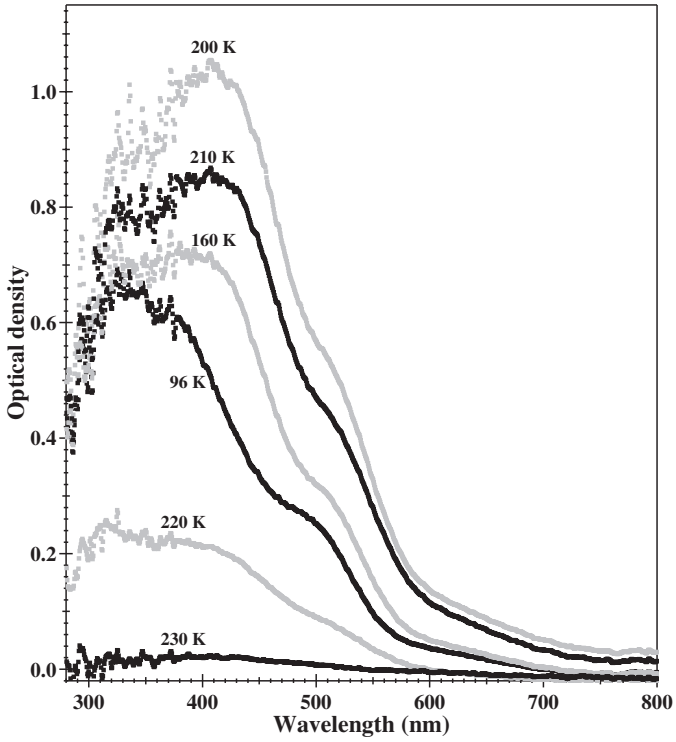

Figure 2. The temperature dependence of the optical density spectrum (curve 6 in figure 1) of iodine film on a sapphire substrate during heating.

steeply. We elevated the specimen temperature to room temperature and measured the spectra at different temperatures. The results are shown in figure 2. With increasing temperature, the absorption continues to increase and reaches a maximum at 200 K. On further increasing the temperature, the absorption decreases monotonically. When the temperature exceeded 220 K, there was a faint exhaust sound from the vacuum pump attached to the specimen chamber and the OD spectrum disappeared suddenly. Both the exhaust sound and the disappearance of the OD spectrum indicate perfect evaporation of the iodine film. Through different experiments, it was found that the spectral disappearance temperature tends to vary with heating rate and film thickness. The temperature dependence of the spectral structure is summarized as follows. The peak wavelength at about 320 nm is not changed with temperature increase. However, the absorption components corresponding to the kinks at about 505 and about 380 nm and to the inflection at about 580 nm shift toward longer wavelengths. The spectrum at 200 K seems to consist of at least three absorption bands centred at about 320, about 410, about 510 nm and a tail at wavelengths longer than 600 nm. They correspond to the 340.0, 411.0, 495.0, 537.0 and 602.5 nm absorption bands observed for iodine single-crystal films (Schnepp *et al* 1965). These five absorptions are assigned to optical transitions from valence bands originating from the π_g, π_u and σ_g orbits in I_2 molecules and to conduction bands originating from σ_u orbits in I_2 molecules (Yamamoto *et al* 1987, Schnepp *et al* 1965). It is known that the iodine films deposited at 123 K were polycrystals of orthorhombic structure (Grimminger and Richter 1956). It has been experimentally known that, when a substance of anisotropic crystal structure is evaporated onto a low temperature substrate, the film produced tends to contain a considerable number of defects. The present film was produced at temperature lower than

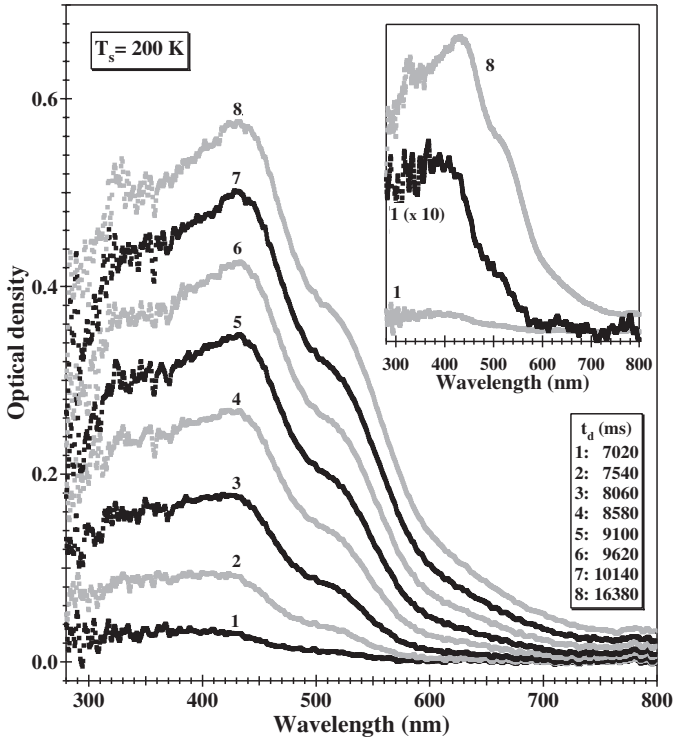

Figure 3. The time evolution of the optical density spectrum of iodine film on a sapphire substrate (T_s = 200 K) during deposition. The spectra at the initial and final stages of the deposition are compared in the inset.

123 K and therefore it may contain some crystal defects. The absorption intensity increase of these bands with increasing temperature from 96 to 200 K may arise from some improvement in crystal quality of the film upon thermal annealing. Therefore, we deposited iodine on a higher temperature substrate ($T_s > 96$ K) and measured the OD spectrum during deposition.

Figure 3 shows the time evolution of the OD spectrum of the iodine film deposited on a sapphire substrate whose temperature was 200 K, as a typical example. Each measurement was made for 130 ms at intervals of 130 ms. In the inset, curve 1 obtained at the initial stage is compared with that obtained at the final stage by rescaling curve 1. A shoulder appears at about 439 nm in an absorption tail (>415 nm) of some higher energy band which seems to consist of several bands. As the deposition progresses, two absorption bands appear at 331 and 435 nm, and at least two shoulder bands appear and become prominent at about 510 nm and below 600 nm. As the deposition progresses further, the absorption intensities of these bands and the shoulder bands increase. The spectral structure is similar to that of the iodine single-crystal film reported by Schnepp *et al* (1965). At the final stage of the deposition, the 331 and 435 nm bands become sharper. The 435 nm band is accompanied by some bands between 370 and 410 nm. After the deposition, the iodine film was cooled down to 96 K and then it was heated to room temperature. During the cooling and heating processes, the OD spectrum was measured as a function of temperature. The result is shown in figure 4. With temperature decreasing to 96 K, the 439 nm band becomes intense and sharp with an accompanying slight red-shift, while the 331 nm one is almost unchanged. The 510 nm shoulder becomes a clear absorption band at about 510 nm. The absorption slope at wavelengths longer than 600 nm grows into a shoulder.

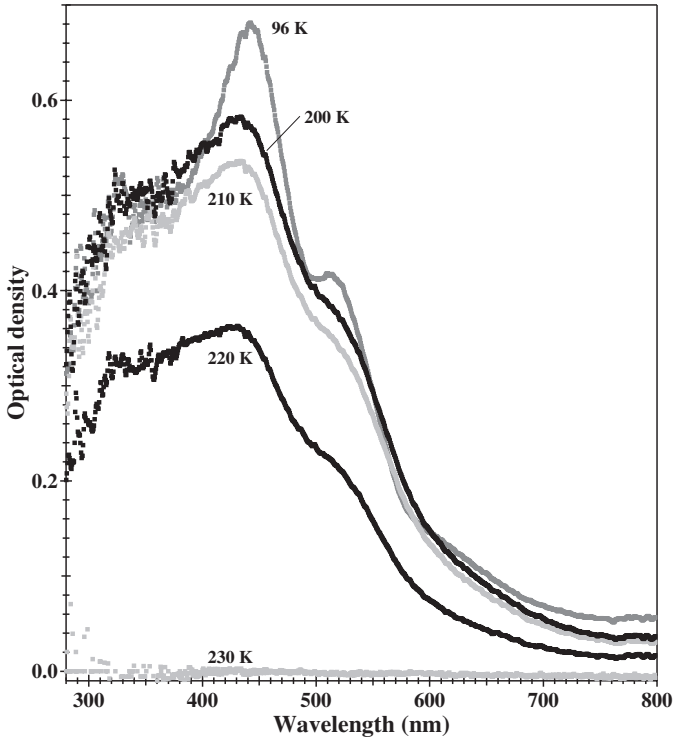

Figure 4. The temperature dependence of the optical density spectrum (curve 8 in figure 3) of iodine film on a sapphire substrate during heating.

With increasing temperature from 96 K, the absorption decreases monotonically. As for the film deposited at 96 K, when the temperature exceeded 220 K, we heard the faint exhaust sound and the OD spectrum disappeared suddenly. The spectral evolution shown in figures 1 and 3 may be explained by the spectral transition from island-like ultrathin film to uniform thick film. In the spectra (curves 1 in the figures) measured at the initial stage of the deposition, small numbers of I_2 molecules are thought to condense to form each island. In such cases, the spectrum tends to resemble that of free I_2 molecules and the apparent optical absorption edge shifts to shorter wavelengths, as shown in figures 1 and 3. The spectral evolution from molecule to solid, together with such an apparent red-shift of the absorption edge, has been explained by calculating electronic energy structures for I_2 and I_n ($n > 2$) (Satoko 2003). Calculation of stable structures of I_n in our laboratory is planned.

3.2. Time evolution of the optical extinction spectrum of vapour produced by thermal evaporation of pristine AgI in helium gas

Figure 5 shows a typical view of the gas evaporation of AgI in helium gas confined at 110 Torr. This photograph was taken at the middle stage of gas evaporation with illumination from a xenon lamp. A dark zone (DZ), ranging from the upper edge of the crucible to a height of about 5.2 mm, and a long conical brown smoky zone (BSZ) can be clearly distinguished. The smoky nature arises from light scattering by particles with sizes comparable to the incident light wavelength. This suggests that the species of the BSZ are large microcrystals. As the gas evaporation proceeds, the BSZ grows to produce a multilayer cone structure which consists of a brown inner zone and a blue outer zone. With decreasing helium gas pressure, the vapour

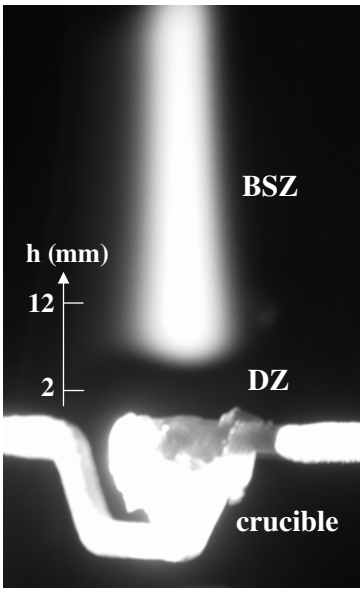

Figure 5. Vapour zones produced by thermal evaporation of AgI powder in He gas confined at 110 Torr. BSZ and DZ are the brown smoky zone and the dark zone, respectively.

zone structure becomes spread and indistinct. As a result, it becomes impossible to measure the extinction spectrum.

Figure 6 shows the time evolution of the optical extinction spectrum of the BSZ at a height of 12 mm from the crucible edge at 110 Torr. Each time t_d is given in the figure. At the initial stage of the gas evaporation, the observed spectrum (curve 2) consists of an absorption band P centred at about 510 nm and another absorption band Q increasing toward about 320 nm. With progressive evaporation, these bands grow as shown by curves 3, 4 and 5. The P band is assigned to the X–B electronic–vibrational transitions in iodine diatomic molecules I_2 (Yamamoto *et al* 1987), while the absorptions due to the X–B transition in isotopes of AgI molecules, ^{109}AgI and ^{107}AgI (Stueber *et al* 1998), and the interband transition in AgI microcrystals (Mochizuki and Umezawa 1997, Dulin 1993) appear in the Q-band wavelength region. In the inset, the optical extinction spectrum of the DZ at a height of 2 mm from the crucible edge is shown. This spectrum was obtained at the steady state of the gas evaporation. The absorption band centred at 515 nm and the absorption which increases toward 270 nm are assigned to the X–B and X–C electronic–vibrational transitions in I_2 molecules, respectively (Yamamoto *et al* 1987). Differing from the case for the gas evaporation of pristine silver (Mochizuki and Ruppin 1993), the absorption lines due to atomic silver Ag_1, the absorption bands due to silver diatomic molecules Ag_2 and silver particles Ag_n ($n > 2$), and the absorption due to the X–A transition in AgI molecules (Metropolis 1939) are not resolved clearly in the broad featureless spectra. However, the existence of silver vapour species is ascertained at the initial stage of the film formation on a substrate whose temperature is 200 K, as shown in the next subsection. Stueber *et al* (1998) already found isotopes of AgI molecules (^{109}AgI and ^{107}AgI) and Ag atoms as species in the molecular beam generated by expansion cooling of vapour which was produced by heating AgI. After the gas evaporation experiments, we found some residual substance in the crucible and thin yellow particles deposited on the upper lid of the evaporation chamber. We examined them by x-ray diffractometry and photoluminescence spectroscopy. The x-ray diffractogram showed that the residual substance in the crucible was silver metal and the thin

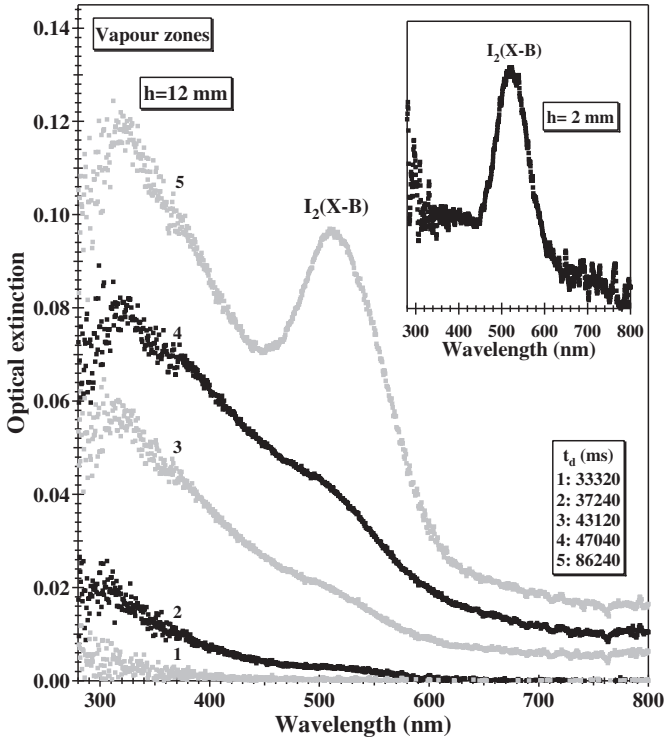

Figure 6. The time evolution of the optical extinction spectrum of the brown vapour zone at a height of 12 mm from the crucible edge during evaporation. The optical extinction spectrum of the dark vapour zone at a height of 2 mm from the crucible edge for the final stage of the gas evaporation is shown in the inset.

yellow deposits were mixtures of βAgI and γAgI microcrystals. Taking account of the vapour species aggregation promoted by atmospheric He gas, it is suggested that Ag_mI_n $(m, n \geqslant 1)$ particles, I_2 molecules and Ag atoms may all be vapour species in vacuum evaporation. The chemical formula Ag_mI_n is the general term for AgI diatomic molecules, AgI clusters $((AgI)_n)$ and nonstoichiometric silver iodide clusters $((AgI)_nAg_\delta$ $(\delta > 1)$ and $(AgI)_nI_\varepsilon$ $(\varepsilon > 1))$. The $(AgI)_nAg_\delta$ and $(AgI)_nI_\varepsilon$ are known as fragment clusters. These vapour species from the crucible are deposited on the high temperature substrate to produce a film. When the substrate temperature is lower than 220 K, the vapour species adsorbed on the substrate may condense to form Ag_n–Ag_mI_n–I_2 composite film. Since the rate of evaporation of I_2 is higher than those for other species, Ag_n and Ag_mI_n are thought to be embedded in an iodine film matrix. This speculation may be ascertained spectroscopically, as reported in later subsections.

3.3. Time evolution of the optical density spectrum of film deposited on a low temperature substrate during vacuum evaporation of AgI

Figure 7 shows the time evolution of the OD spectrum of the film deposited on a sapphire substrate at 109 K during vacuum evaporation. Each measurement was made for 1600 ms at intervals of 4000 ms. In the inset, curve 1 obtained at the initial stage is compared with that obtained at the final stage by rescaling curve 1. The colour of the film was light brown. Although the spectra are broader than those of iodine films, faint inflection points (a, b, c and d) are seen at about 417, about 475, about 544 and about 597 nm at the initial stage of

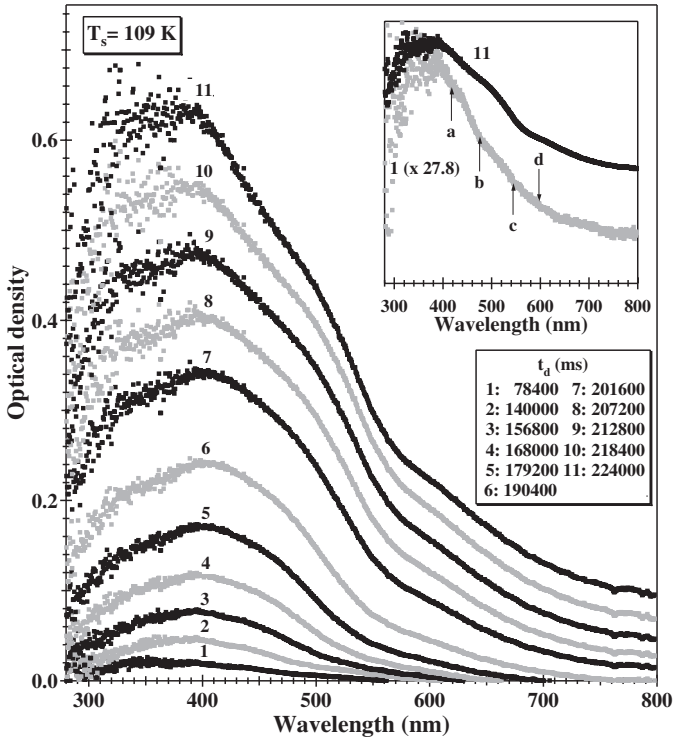

Figure 7. The time evolution of the optical density spectrum of the film deposited on a sapphire substrate ($T_s = 109$ K) during vacuum evaporation of AgI powder. The spectra at the initial and final stages of the deposition are compared in the inset.

the evaporation. As compared with the absorption spectra of pristine AgI (Cardona 1963, Mochizuki and Ohta 2000, Mochizuki 2001) and pristine iodine films described above, the following are found. The inflection at 417 nm is due to the $Z_{1,2}$ exciton absorption (422 nm). The inflections at 475, 544 and 597 nm arise from the absorption bands centred at 340, 411, 495, 537 and 603 nm in iodine films. That is, the film on the low temperature substrate at the initial stage of the deposition is a composite film made of, at least, AgI and iodine. It is hard to deduce the absorptions due to other species from the observed spectra. With progressing deposition, the absorption increases and the absorption edge extends to wavelengths longer than 800 nm. One possible cause of such a spread in absorption is additional optical scattering at the I–AgI interfaces in the I–AgI composite specimen. We elevated the specimen temperature to room temperature and measured the spectra at different temperatures during heating. The results are shown in figures 8(a) and (b). With increasing temperature, the absorption continues to increase and then reaches a maximum at 210 K. The colour of the film becomes dark brown. On further increasing temperature, the absorption decreases monotonically. Similarly to in the above-described experiments for iodine films, when the temperature exceeded 230 K, there was the same exhaust sound. Simultaneously, the intense broad spectrum disappeared suddenly, a weak spectrum peculiar to AgI emerging. Both the exhaust sound and the spectral change indicate the evaporation of excess iodine from the film and indicate also that vapour species related to AgI evaporation are dispersed in an iodine film matrix. Through experiments under different conditions, it is found that the spectral change temperature tends to vary with heating speed and film thickness. With temperature increasing from 240 to 290 K, the tail at wavelengths longer than 430 nm becomes considerably weakened and the absorptions between 370 and 410 nm

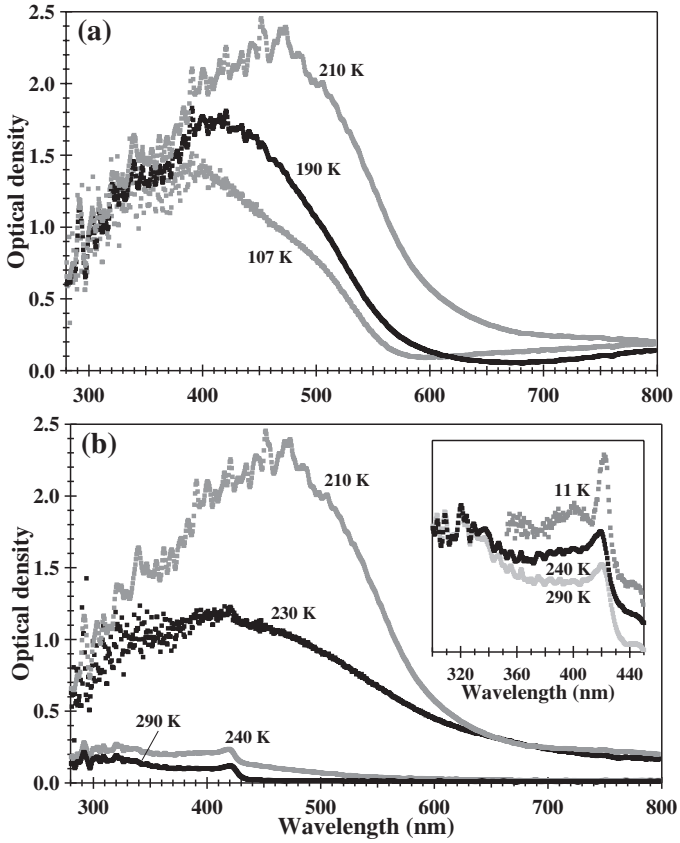

Figure 8. The temperature dependence of the optical density spectrum (curve 11 in figure 7) of iodine film on a sapphire substrate during heating: (a) $T \leqslant 210$ K, (b) $T \geqslant 210$ K. The exciton spectra at 240 and 290 K during heating are compared, together with the spectrum at 11 K, in the inset.

decrease. The tail may be due to excess iodine included tightly in AgI film. The absorptions between 370 and 410 nm correspond to the H_1 and H_2 exciton ones in polytype AgI (Mochizuki 2001), which are induced by some stacking disorder in the AgI lattice. This film was cooled again, down to 11 K, and the OD spectrum was measured. As indicated in the inset, a clear $Z_{1,2}$ absorption peak was observed at 422 nm, which indicates that the film is γ AgI, and this is discussed later in detail. Similarly to that for the iodine film evaporated at 96 K, the absorption increases with increasing temperature from 107 to 210 K. The band centred at about 470 nm, which appears as a shoulder at 107 K, becomes prominent. The spectral change may arise from the improvement in crystallinity of iodine domains upon heating (annealing). However, we cannot exclude effects of some particles (for example, Ag_mI_n) grown at the AgI/iodine interfaces. Therefore, we deposited iodine on a higher temperature substrate ($T_s > 96$ K) and measured the spectrum during deposition, as follows.

Figure 9 shows the time evolution of the OD spectrum of the film deposited on a sapphire substrate at 200 K during vacuum evaporation. Each measurement was made for 1400 ms at intervals of 3990 ms. The colour of the film was light brown. At the initial stage of the deposition, the spectrum consists of a broad band centred at 370 nm and a short wavelength absorption which increases toward some wavelength shorter than 330 nm. In the inset,

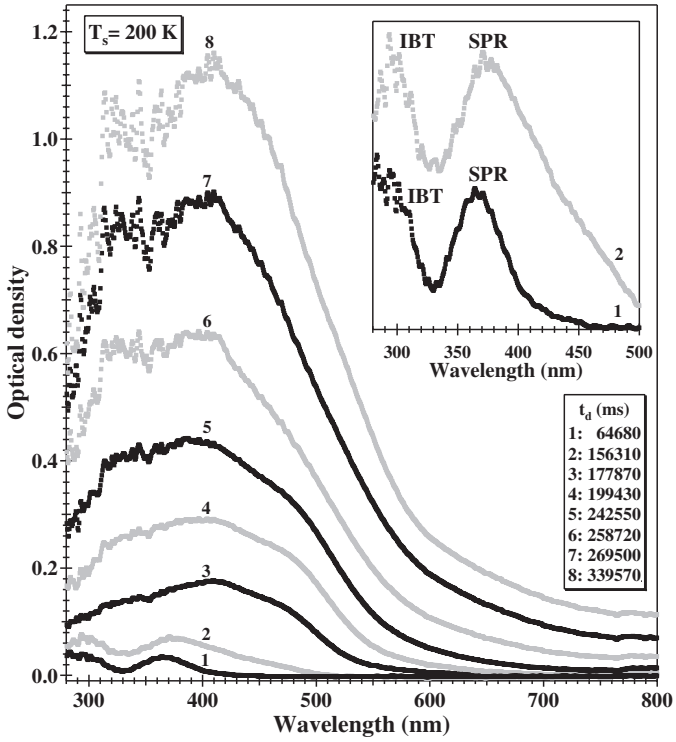

Figure 9. The time evolution of the optical density spectrum of the film on a sapphire substrate ($T_s = 200$ K) during deposition. Curves 1 and 2 are compared in the inset. SPR and IBT denote the surface plasmon absorption band and the interband transition band of silver particles deposited, Ag_n, respectively.

curves 1 and 2 are expanded and shown. These curves are very similar to those observed for silver clusters and microcrystals (Mochizuki and Ruppin 1993). The 370 nm band and short wavelength absorption are assigned to the collective mode resonance of valence electrons (so-called surface plasmon resonance (SPR)) and interband transitions (IBT) of silver particles (Ag_n: $n > 2$), respectively. Such absorptions indicate that silver atoms are also one of the vapour species for vacuum evaporation of AgI powder. At later times of deposition, the SPR band has a long wavelength tail, as shown in the inset. The tail is due to interaction between adjacent Ag_n, which was observed frequently in the spectra of gas evaporated Ag_n films (Hayashi *et al* 1990) and free Ag_n (Mochizuki and Ruppin 1993). Thus, it has been deduced spectroscopically that Ag atoms coming from the evaporation source condense to form Ag_n island film on the 200 K substrate at the initial stage of the deposition. In curve 6, at the middle stage of the deposition, a kink appears at about 415 nm. As discussed later, the kink is connected to the W_1 and W_2 exciton bands of AgI. The appearance of such an AgI-related kink means that vapour species diffuse easily and grow to become AgI particles in the iodine film matrix at 200 K. At the final stage of the deposition, the absorptions at wavelengths longer than 650 nm become prominent, forming the absorption edge structure of solid iodine. We cooled the specimen to 99 K and then elevated the specimen temperature to room temperature. We measured the spectra at different temperatures during the cooling and heating processes. The results are shown in figure 10. With cooling from 213 K, the absorption continues to increase and the maximum at about 420 nm shifts to about 430 nm at 99 K. With temperature increasing from 99 K, the absorption decreases monotonically. When the temperature exceeded 220 K,

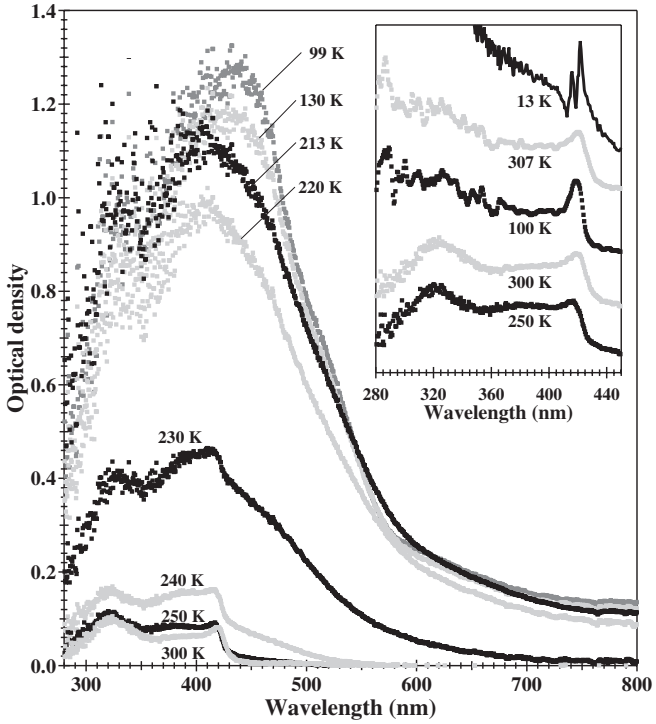

Figure 10. The temperature dependence of the optical density spectrum (curve 8 in figure 9) of the film on a sapphire substrate during cooling and heating processes. The exciton spectra during the cooling and heating processes are compared, together with the spectrum at 13 K, in the inset.

there was a faint exhaust sound from the vacuum pump attached to the specimen chamber, as heard for pristine iodine films. Simultaneously, the intense broad spectrum became weakened and it disappeared suddenly at 240 K, a weak spectrum peculiar to AgI emerging. Through different experiments, it was found that the spectral change temperature tends to vary with heating rate and film thickness. With temperature increasing from 240 to 300 K, the tail at wavelengths longer than 430 nm disappeared and the absorptions between 370 and 410 nm decreased. The tail may be due to some excess iodine included tightly in AgI films. The absorptions between 370 and 410 nm correspond to the H_1 and H_2 exciton ones in polytype AgI, which are induced by some stacking disorder in the AgI lattice. This film was cooled again, down to 13 K, and the OD spectrum was measured. The W_1, W_2 and W_3 exciton absorption bands are observed at 420, 414 and 320 nm, respectively. This indicates that the film is βAgI. In the inset, the spectra measured at 250 and 300 K for the first heating process, 100 K for the second cooling process and 307 K for the second heating process and 13 K for the third cooling process are compared. A remarkable change occurs at wavelengths shorter than 320 nm. A possible explanation for such spectral change is desorption of iodine from the film or reaction of imperfect AgI film with iodine during the heating and cooling processes.

3.4. Time evolution of the optical density spectrum of film deposited on a room temperature substrate during vacuum evaporation of AgI

We measured the time evolution of the OD spectrum of the film deposited on a room temperature sapphire substrate during vacuum evaporation. The evaporation condition is the same as in the experiments with the low temperature substrate. In order to study the optical spectrum for a

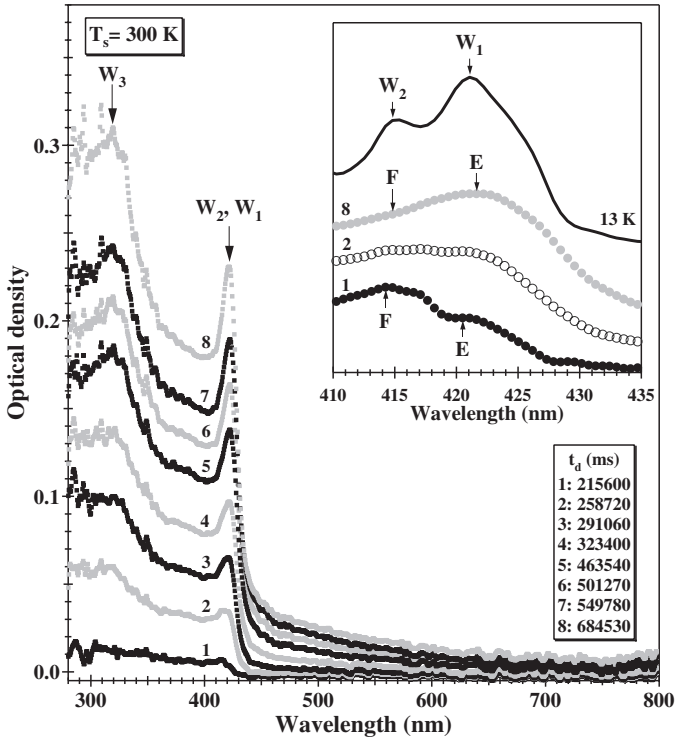

Figure 11. The time evolution of the optical density spectrum of the film on a sapphire substrate (T_s = 300 K) during deposition. The spectra at the initial and final stages of the deposition are compared, together with the spectrum at 13 K, in the inset.

wide thickness range, we performed successively the same depositions on the substrate. The results of the two successive deposition experiments are shown in figure 11. Each measurement was made for 1400 ms at intervals of 3990 ms. In the inset, the exciton spectra (curves 1, 2 and 8) at different stages of the deposition are compared after appropriate rescaling, together with the spectrum measured at 13 K. At the initial stage of deposition, two bands, E and F, appear at 420 and 414 nm, respectively. With progressing deposition, the absorption intensity of the E band becomes superior to that of the F band, and the J band at 320 nm becomes prominent. At the final stage of the deposition, the F band is merged with the E band, while the bands become well resolved at 13 K. At the initial stage of deposition, vapour species may condense on the substrate to form AgI microcrystal film. In the previous paper (Mochizuki and Umezawa 1997), we reported for AgI microcrystals that the $Z_{1,2}$ exciton band split into two bands centred at 420 nm and 415 nm due to the quantum size effects on the doubly degenerate valence band Γ_8 or some crystal field change at the crystallite surfaces due to surface reconstruction or surface defects or the appearance of the wurtzite modification. Since the intensity peak wavelengths of these bands are almost unchanged with progressive deposition, the E, F and J bands are assigned to the W_1, W_2 and W_3 exciton bands of βAgI (Cardona 1963, Mochizuki 2001, Mochizuki and Ohta 2000). Thus, the film deposited on room temperature sapphire substrate is optically identified with wurtzite phase AgI. The relative absorption increase of the W_1 (E) band with increasing deposition time (film thickness) may arise from the decreased exciton confinement and decreased surface (surface reconstruction and defects) effects. After the evaporation experiments, we measured the OD spectrum as a function of ageing time at 301 K.

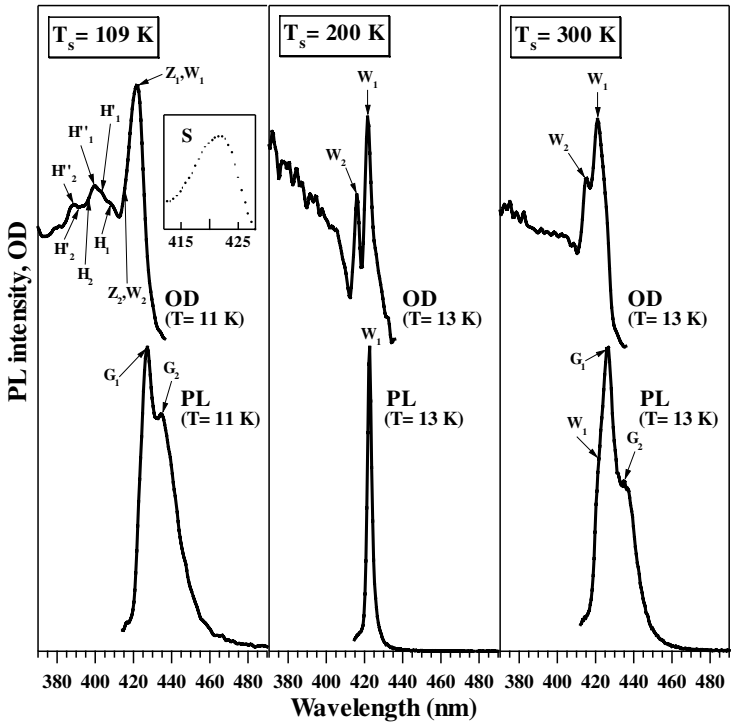

Figure 12. The optical density and photoluminescence spectra of different AgI films near 12 K.

It was found that the absorption at wavelengths shorter than 300 nm grows with increasing ageing time and, after 60 min, the spectrum comes to resemble that of pristine AgI (Cardona 1963, Mochizuki 2001, Mochizuki and Ohta 2000). This result is very similar to the result for the low temperature (200 K) substrate.

3.5. Photoluminescence of AgI films deposited on different temperatures of substrates

Figure 12 shows the OD and PL spectra of the AgI films deposited on the sapphire substrate at three different temperatures (109, 200 and 300 K). First, we discuss the spectra of the film deposited on the 200 K substrate. This film displays sharp well resolved absorption bands at 422 and 416 nm due to W_1 and W_2 excitons, respectively. The PL spectrum shows at 423 nm a sharp emission which has a full width at half-maximum (FWHM) of 79 cm^{-1} (approximately 10 meV) and with a very small Stokes shift (<7 meV) from the W_1 exciton absorption peak. Since the 7 meV shift is within the maximum systematic error between OD and PL measurements, the emission can be assigned to the radiative decay of free W_1 excitons.

The film deposited on the 109 K substrate shows an intense absorption band at 422 nm which coincides with the $Z_{1,2}$ and W_1 exciton wavelengths. However, this band is accompanied by a faint shoulder band (S) on the short wavelength side, as indicated by an arrow in the inset. The shoulder wavelength is close to that of the W_2 exciton. The 422 nm band and the shoulder may be assigned to the Z_1 and Z_2 exciton bands which are split by some crystal field change due to appearance of the wurtzite modification, or to defected βAgI. Incidentally, most of the $Z_{1,2}$ exciton absorption bands previously reported by different authors are also accompanied by a faint shoulder band at about 415 nm. It is also noted that a structured broad absorption band is seen between 380 and 415 nm, which had not been observed for other films. Similar absorption bands was observed previously at 405 and 398 nm for the film specimens (Mochizuki 2001),

which were assigned to the H_1 and H_2 excitons trapped at some stacking-disorder-induced polytype structures of βAgI. The 404 and 392 nm shoulders which are labelled respectively as H_1' and H_2', and the 400 and 389 nm peaks which are designated respectively as H_1'' and H_2'' are the exciton absorptions due to other types of polytype structure of βAgI. The PL spectrum of this film displays at least two broader bands. The intensity peaks at 434 and 427 nm which are designated respectively as G_2 and G_1 are observed, while the emission due to the radiative decay of free W_1 excitons is not clearly resolved. By comparing the PL spectral structure with the OD one, the G_1 and G_2 emissions are assigned to the radiative decays of excitons trapped at crystal defects.

The film deposited on the 300 K substrate shows also the W_1 and W_2 absorption bands which have larger FWHM than those of the film deposited on the 200 K substrate. This indicates the degradation of the crystallinity of βAgI. The G_1 and G_2 emissions are also observed. An extremely faint shoulder is observed at 422 nm. As for the film deposited on the 109 K substrate, the G_1 and G_2 emissions are due to the radiative decays of excitons trapped at crystal defects.

The above optical studies suggest that an optimum substrate temperature for fabricating βAgI film is close to 200 K.

3.6. Film formation by thermal evaporation of AgI powder in vacuum

The present studies have indicated optically that the species in the vapour zones produced by thermal evaporation of AgI powder are Ag atoms (Ag_1), silver iodide clusters (Ag_mI_n) and diatomic iodine molecules (I_2). As defined above, Ag_mI_n is the general term for AgI diatomic molecules, AgI clusters ($(AgI)_n$) and nonstoichiometric silver iodide clusters ($(AgI)_nAg_\delta$ ($\delta > 1$) and $(AgI)_nI_\varepsilon$ ($\varepsilon > 1$)). By the optical and time-of-flight mass spectroscopic methods, Bernstein (2003) has been studying Ag_mX_n (X: Cl, Br, I) particles (clusters) in an effort to understand the structure, dynamics and photochemistry of small clusters, and to explore the properties of larger Ag_mX_n structures as they grow from nanoclusters to the bulk material. We discuss the AgI film formation on the substrate whose temperature is below room temperature. We first note that iodine solid has the highest vapour pressure and I_2 molecules sublimate from the deposited film on a sapphire substrate prominently above 220 K under evacuation, as described above. The vapour species coming from the evaporation source arrive at the substrate surface and, when T_s is low enough to suppress re-evaporation, they are well adsorbed to form a composite film of Ag_1, Ag_mI_n and I_2. Since the rate of evaporation of I_2 is very high, Ag_1 and Ag_mI_n are thought be dispersed homogeneously in an iodine film matrix. These Ag_1 and small Ag_mI_n structures act as condensation nuclei for growing Ag_mI_n in the iodine film at later times. Incidentally, it is known that the cores of photographic sensitization AgI nuclei contain excessive iodine, producing the Ag_mI_n clusters. The composite film may display therefore a slightly different OD spectrum from that of pristine iodine film, as seen already in figures 1 and 7. When T_s is moderate, perhaps approximately 200 K, some of the adsorbed excess I_2 desorbs from the substrate, while Ag_1 and Ag_mI_n grow, generating larger Ag_n structures and larger Ag_mI_n structure, respectively, through some coalescence, absorption and reaction processes. Since the composite film, however, exhibited only the SPR absorption of Ag_n at the initial stage of the deposition, as shown in figure 9, the number of Ag_mI_n structures may be small in the film or the Ag_mI_n structures may be too small to display measurable optical absorption. With progressing deposition, the Ag_n acts as condensation nuclei, absorbing I_2 and small Ag_mI_n structures coming later from the evaporation source, generating larger nearly stoichiometric AgI particles. As a result, the kink at the exciton wavelength may appear in the OD spectrum of the composite film, as shown by curves 6, 7 and 8 in figure 9. Since I_2 neighbouring Ag_mI_n is thought to be bound more tightly in the composite film than in pristine iodine film,

different temperature dependences may be observed in the OD spectra of the pristine iodine and composite films, as shown in figures 4 and 10. Incidentally, the spectral structure is also affected, as shown in figures 3 and 9. When T_s is room temperature, re-evaporation of I_2 from the substrate, reactions and coalescence between adsorbed vapour species are enhanced, generating nearly stoichiometric AgI film, as shown in figure 11. The reactions, coalescences and annealing effects become promoted with T_s, while the re-evaporation and desorption of I_2 with increasing T_s are also promoted, increasing the deviation from the stoichiometric composition of AgI. Therefore, an optimum T_s for fabricating the highest quality AgI film below room temperature may exist. Since the film deposited on the 200 K sapphire substrate showed the sharpest OD and PL spectra, 200 K is thought to be the optimum T_s.

In the present discussion, we have ignored the effects of the kinds of substrate materials and the crystal orientation of the substrate surface. Up to the present, we have found the following substrate effects. When AgI powder is flash evaporated and deposited on different kinds of room temperature substrates (silica glass, sapphire single crystal and GaAs single crystal), βAgI tends to crystallize on the sapphire single-crystal and GaAs single-crystal substrates, while γAgI tends to crystallize on the silica glass. Thus, there is a need to study the substrate effects. More detailed study with different kinds of substrate materials and with different orientations of substrate surfaces is in progress, in an attempt to fully explain the mechanism of AgI film formation.

4. Conclusion

We have evaporated AgI powder in vacuum by setting different evaporation conditions for the evaporation and deposition. The OD spectrum of AgI film on a substrate was measured as a function of the time elapsed from the beginning of the deposition for the first time. The same experiment was carried out for pristine iodine. Besides these vacuum evaporation experiments, we have produced two vertically well separated vapour zones of AgI above the evaporation source in a confined He gas atmosphere and obtained the optical extinction spectra as a function of the time elapsed after the beginning of evaporation. On the basis of these results, we have studied the process of AgI film formation on the low temperature (<room temperature) substrate and the following have been found.

(1) The vapour species produced by thermal evaporation of AgI powder in vacuum are Ag_1, Ag_mI_n and I_2.
(2) The film deposited at low temperatures ($\leqslant$200 K) is a composite film. That is, Ag_1, Ag_n and Ag_mI_n are dispersed in an iodine film matrix to form a composite film.
(3) Intense iodine optical absorption, which is slightly affected by Ag_1 and Ag_mI_n, has led many researchers to the wrong conclusion that amorphous AgI films prepared by quench deposition display strongly enhanced optical absorption in comparison to crystalline film.
(4) AgI film is grown through desorption of excess I_2 from the composite film and a coalescent reaction among film elements (Ag_1, Ag_n, Ag_mI_n and I_2) with increasing temperature.
(5) The composite film grown on the substrate at 200 K becomes transformed to the spectroscopically best βAgI film by heating up to room temperature in vacuum.

The main limit of the present experimental technique is that there is no *in situ* characterization of the film thickness and crystal structure. Bearing these limits in mind, we have presented a reasonable connection between measured optical data and the AgI film formation process, with a convincing coherence with the results on pristine iodine, the vapour zone produced by thermal evaporation of AgI powder in a helium gas atmosphere confined at different pressures and the results obtained by the mass resolved excitation spectroscopy of an expansion cooled AgI beam.

Finally, a comparative study of the OD and PL spectra has also been performed at low temperature for the films deposited at different substrate temperatures. The exciton absorption band at 422 nm, which is usually assigned to $Z_{1,2}$ exciton absorption, has a faint short wavelength shoulder. The absorption intensity of the shoulder is dependent on the specimen preparation and the thermal history. The appearance of the shoulder has been explained by splitting of the doubly degenerate Γ_8 valence band. Such splitting may arise from some stress, with different thermal expansion coefficients for AgI and substrate materials (Mochizuki 2001), or some crystal field change due to mixing of the wurtzite (β) modification and stacking disorder due to nonstoichiometry. This speculation is in agreement with the well known result that γ AgI appears at room temperature as a metastable state and the stability of the γ phase is affected by slight nonstoichiometries and defects. Both the AgI films displaying the less resolved W_2 exciton absorption band and the $Z_{1,2}$ exciton absorption band with the short wavelength shoulder show a broader PL band and the long wavelength PL band. On the other hand, the AgI film displaying well resolved W_1 and W_2 absorption bands shows the sharpest single PL band. Therefore, the PL spectrum measurement could be a useful tool for characterizing the local structure in AgI film. On the basis of this notion, we are now developing nanometre-scale space resolved PL measurement with near-field optical microscopy.

Acknowledgments

This work was partially supported by a Grant-in-Aid for Scientific Research from the Ministry of Education, Science, Sports, Culture and Technology, Japan. This work was also supported in part by an Interdisciplinary General Joint Research Grant from Nihon University. Also, this work was partially supported by a Project Research Grant from The Institute of Information Sciences of the College of Humanities and Sciences (Nihon University) and by a Cooperative Research Grant from The Institute of Natural Sciences (Nihon University).

References

Bernstein E R 2003 http://franklin.chm.colostate.edu/erb/home_metal.htm
Braner A A and Chen R 1963 *J. Phys. Chem. Solids* **24** 135
Burley G 1963 *Am. Mineral.* **48** 1266
Cardona M 1963 *Phys. Rev.* **129** 69
Dulin M N 1993 *Z. Phys.* D **26** 172
Fujishiro F and Mochizuki S 2002 *Nonlinear Opt.* **29** 443
Grimminger V H and Richter H 1956 *Z. Naturf.* a **11** 942
Hayashi S, Koga R, Ohtuji M, Yamamoto K and Fujii M 1990 *Solid State Commun.* **76** 1067
Kondo S, Itoh T and Saito T 1998 *Phys. Rev.* B **57** 13235
Many A, Simhony M, Weisz S Z and Levinson J 1961 *J. Phys. Chem. Solids* **22** 285
Mathieson L and Rees A L G 1956 *J. Chem. Phys.* **25** 753
Metropolis N 1939 *Phys. Rev.* **55** 636
Mochizuki S 1996 *J. Lumin.* **70** 60
Mochizuki S 2001 *Physica* B **308–310** 1042
Mochizuki S and Fujishiro F 2003a *J. Phys.: Condens. Matter* **15** 5057
Mochizuki S and Fujishiro F 2003b *Phys. Status Solidi* c **0** 763
Mochizuki S and Fujishiro F 2003c *Phys. Status Solidi* c **0** 767
Mochizuki S and Ohta Y 2000 *J. Lumin.* **87–89** 299
Mochizuki S and Ruppin R 1993 *J. Phys.: Condens. Matter* **5** 135
Mochizuki S and Umezawa K 1997 *Phys. Lett.* A **228** 111
Moss T S 1952 *Photoconductivity of the Elements* (London: Butterworths)
Satoko T 2003 private communication
Schnepp O, Rosenberg J L and Gouterman M 1965 *J. Chem. Phys.* **43** 2767
Stueber G J, Foltin M and Bernstein E R 1998 *J. Chem. Phys.* **109** 9831
Riggleman B M and Drickamer H G 1963 *J. Chem. Phys.* **38** 2721
Yamamoto H, Seki K, Mori T and Inokuchi H 1987 *J. Chem. Phys.* **86** 1775

Available online at www.sciencedirect.com
SCIENCE DIRECT®
ELSEVIER
Journal of Magnetism and Magnetic Materials 272–276 (2004) 428–429
Journal of magnetism and magnetic materials
www.elsevier.com/locate/jmmm

Pressure-induced phase transition in α-MnS

Y. Ishida[a], Y. Mita[a,*], M. Kobayashi[a], S. Endo[b], S. Mochizuki[c]

[a] *Materials Physics, Graduate School of Engineering Science, Osaka University, Toyonaka, Osaka 560-8531, Japan*
[b] *Research Center for Materials Science at Extreme Conditions, Osaka University, Osaka 560-8531, Japan*
[c] *College of Humanities and Sciences, Nihon University, Tokyo 156-8550, Japan*

Abstract

The IR reflection measurements of α-MnS have been performed at room temperature under various pressures. It is observed that the reflectivity increases drastically at the pressure range of 23–29 GPa and becomes almost constant at the higher pressure. The carrier concentrations obtained from the reflectivity spectra at the pressures higher than 29 GPa are the order of $10^{22}\,cm^{-3}$. Therefore it is concluded that pressure-induced semiconductor–metal transition occurs at the pressure range of 23–29 GPa. This result is quite consistent with the newest results of X-ray analysis.

PACS: 71.30.+h

Keywords: MnS; Pressure; Reflectivity; Phase transition

The discovery of colossal magnetoresistance in $Fe_xMn_{1-x}S$ solid solutions [1] revived interest in studying the physical properties of α-MnS, which is the basic component of these substances. An α-MnS possesses an NaCl-type face-centered cubic (B1) lattice which undergoes a rhombohedral distortion along the cube diagonal in the (1 1 1) plane with decreasing temperature. The antiferro-paramagnetic phase transition occurs at $T_N = 150$ K. In the paramagnetic phase, the α-MnS is a p-type semiconductor with an activation energy $E = 0.3$ eV. In high-pressure region, the luminescence and excitation spectra were studied up to 3.9 GPa and the pressure dependences of crystal field strength Dq and Racah parameter B were obtained [2]. On the other hand, the pressure-induced phase transitions have been explored by many researchers, but their results were inconsistent: Clendenen and Drickamer observed a structure distortion at approximately 10 GPa [3] and Kraft and Greuling detected a structural phase transition from the B1 to the B16 (GeS type) at 7.2 GPa [4]. McCammon performed powder X-ray diffraction at 298 K from 0 to 21 GPa. However the data show no evidence of either transition, and are well fit by a single equation of state at whole the pressure range [5]. In 1993, Sweeney and Heinz observed a phase transition of α-MnS at 26 GPa from B1 phase to a high pressure one whose symmetry is lower than hexagonal but not concluded and it is stable to at least 46 GPa [6]. In that case, change of some optical properties must be observed around the pressure region.

We performed the IR reflection measurements of α-MnS under high pressure up to 37 GPa, which have been obtained by using a diamond anvil cell (DAC) at room temperature. The reflectance spectrum for the interface between the sample and diamond in mid-IR range was measured utilizing a Fourier transform infrared spectrometer FT/IR-610 (JASCO) combined with an infrared microscope installed with two mirror objectives (10×) and an MCT detector. In order to obtain the absolute reflectivity, powdered sample was compressed directly by diamond anvil without using any pressure mediums.

The reflection spectra obtained under various pressures and their pressure dependence at the point of 0.4 eV are shown in Figs. 1 and 2, respectively.

With increasing pressure, the reflectivity shows drastic increase at the pressure range of 23–29 GPa. Note that this pressure coincides with that of the structural change

*Corresponding author. Tel.: +81-6-6850-6417; fax: +81-6-6845-4632.
E-mail address: mita@mp.es.osaka-u.ac.jp (Y. Mita).

0304-8853/$ - see front matter © 2003 Elsevier B.V. All rights reserved.
doi:10.1016/j.jmmm.2003.11.141

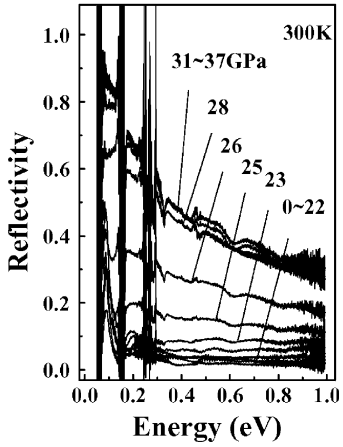

Fig. 1. Reflection spectra of α-MnS obtained under various pressures.

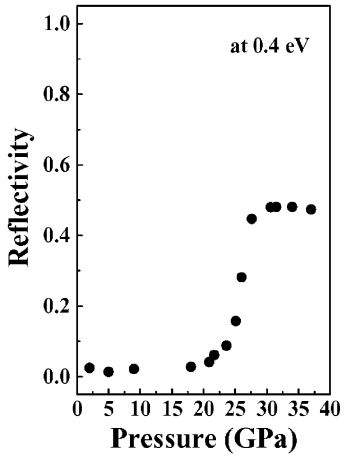

Fig. 2. Pressure dependence of the reflectivity at the point of 0.4 eV. Abrupt increase of reflectivity is seen clearly around 26 GPa.

reported by Sweeney and Heinz (26 GPa) [6] and, in present study, no other optical changes were detected at 7.2 and 10 GPa. According to the Drude model, the dielectric function $\varepsilon(\omega)$ is written as

$$\varepsilon(\omega) = \varepsilon_b - \omega_p^2/(\omega^2 + \Gamma^2) + i\omega_p^2\Gamma/(\omega^3 + \Gamma^2\omega), \quad (1)$$

$$\omega_p^2 = 4\pi Ne^2/m*. \quad (2)$$

Here ε_b, Γ, N and $m*$ are background dielectric constant, damping constant, carrier concentration and effective mass of the carrier, respectively. The normal reflectance $R(\omega)$ is calculated using the Fresnel relation:

$$R(\omega) = |(n_s - n_D)/(n_s + n_D)|^2, \quad (3)$$

$$n_s^2 = \varepsilon(\omega), \quad (4)$$

where n_s and n_D are the reflective index of sample and anvil diamond (=2.4), respectively. Our reflectivity measurements were performed using infrared microscope, which means that the incident condition is not just normal. However deviation angle of the incident light on sample from the normal is smaller than 8° because of high reflective index of anvil diamond. Therefore we regarded the condition as nearly normal. Parameter fitting of the reflection spectra was performed using these relations and the obtained carrier concentrations at high-pressure region ($P > 29$ GPa) assuming $m* = m_0$ are the order of $10^{22}\,cm^{-3}$ which is 10–100 times higher than that of typical semimetal. It is also observed that the reflectivity is independent of the applied pressure at the pressure higher than 29 GPa. These results indicate the band reconstruction to a metallic phase occurs at 23–29 GPa instead of the increased band overlap. Therefore it is concluded that a phase transition occurs at 23–29 GPa in α-MnS and the high-pressure phase is metallic.

The authors thank to Mr. T. Musha of Osaka University for experimental supports.

References

[1] G.A. Petrakovskii, L.I. Ryabinkina, N.I. Kiselev, D.A. Velikanov, A.F. Bovina, G.M. Abramova, JETP Lett. 69 (1999) 949.
[2] M. Kobayashi, T. Nakai, S. Mochizuki, N. Takayama, J. Phys. Chem. Solids 56 (1995) 341.
[3] R.L. Clendennen, H.G. Drickamer, J. Chem. Phys. 44 (1966) 4223.
[4] A. Kraft, B. Greuling, Cryst. Res. Technol. 23 (1988) 605.
[5] C. McCammon, Phys. Chem. Miner. 17 (1991) 636.
[6] J.S. Sweeney, D.L. Heinz, Phys. Chem. Miner. 22 (1993) 63.

Available online at www.sciencedirect.com
SCIENCE DIRECT®
Journal of Luminescence 112 (2005) 267–270
JOURNAL OF LUMINESCENCE
www.elsevier.com/locate/jlumin

The reversible UV-laser-light-induced spectral change and origin of the 2.4 eV luminescence band in $SrTiO_3$

Shosuke Mochizuki*, Seiko Minami, Fumito Fujishiro

Department of Physics, College of Humanities and Sciences, Nihon University, 3-25-40 Sakurajosui, Setagaya-ku, Tokyo 156-8550, Japan

Available online 24 November 2004

Abstract

In order to clarify the origin of the 2.4 eV luminescence band in $SrTiO_3$, as-grown and annealed $SrTiO_3$ single crystals are irradiated with a continuous-wave ultraviolet laser light ($\lambda = 325$ nm) in different atmospheres at room temperature. Under the laser light irradiation in a vacuum, the 2.4 eV luminescence band grows with increasing irradiation time, while it returns to the original weak-luminescence state under the same laser light irradiation in oxygen gas. The excitation-intensity, temperature and time dependences of the photoluminescence spectra are also measured for the crystals. All the results indicate that the 2.4 eV luminescence band arises not from intrinsic self-trapped excitons but from extrinsic excitons trapped around oxygen defects. Near-band-edge emissions have been observed, for the first time, at 3.2 and 2.9 eV under intense excitation.

PACS: 71.35.−y; 78.55.−m; 82.50.−m; 61.72.−y

Keywords: Quantum paraelectric state; Photo-induced defects

A large number of the optical studies have been devoted to clarify the quantum paraelectric state in strontium titanate ($SrTiO_3$). Grabner [1] measured the photoluminescence (PL) properties of doped and undoped $SrTiO_3$ crystals, and observed a near-infrared luminescence band around approximately 1.6 eV and a visible luminescence band around 2.4 eV.These PL bands were Stokes-shifted considerably. He assigned them to intrinsic defects or intrinsic excitons. Recently, Hasegawa et al. [2] measured the optical absorption and PL properties of $SrTiO_3$ crystal. They assigned the Stokes-shifted long-lasting luminescence around 2.4 eV to the radiative decay of intrinsic self-trapped excitons. However, many metal oxides display the similar visible PL, which are related to oxygen defects [3–6]. Unfortunately, such oxygen defect effect has been accorded too low evaluation in the optical study of $SrTiO_3$ and it has led many researchers

*Corresponding author. Tel.: +81 3 5317 9771; fax: +81 3 5317 9771.
E-mail address: motizuki@physics.chs.nihon-u.ac.jp (S. Mochizuki).

0022-2313/$ - see front matter © 2004 Elsevier B.V. All rights reserved.
doi:10.1016/j.jlumin.2004.09.050

astray. Very recently, we have observed that the 2.4 eV luminescence band of $SrTiO_3$ grows under a continuous wave (CW) 325 nm-laser-light irradiation in a vacuum, while it disappears under the same laser light irradiation in oxygen gas [7]. It was found that the observed phenomenon relates closely to the creation and annihilation of oxygen defects under the laser light. Taking account of the oxygen defects in real $SrTiO_3$ crystals [8–10], the PL properties of $SrTiO_3$ should be now restudied in detail. In the present paper, we report the PL properties and reversible photo-induced spectral change of as-grown and annealed $SrTiO_3$ single crystals.

$SrTiO_3$ single crystals were grown by the Vernuil method. As-grown crystals are dark blue and they become transparent by annealing in an appropriate atmosphere. During CW 325 nm laser-light irradiation, we have measured the PL spectra of these as-grown and annealed crystals as a function of irradiation time t_{ir}. Fig. 1 shows the photo-induced PL spectral change of the as-grown $SrTiO_3$ crystal at room temperature in a vacuum as a function of t_{ir} (in min). As seen in this figure, the initial PL spectrum ($t_{ir} = 0$) is very broad, and it has an intensity peak at about 2.8 eV and two faint kinks at about 2.4 and 2.15 eV. With increasing t_{ir}, the intensity increases, growing the PL component below 2.8 eV. With t_{ir} increasing further, the rate of the spectral change becomes decreased. The spectrum at $t_{ir} = 0$ min is rescaled,

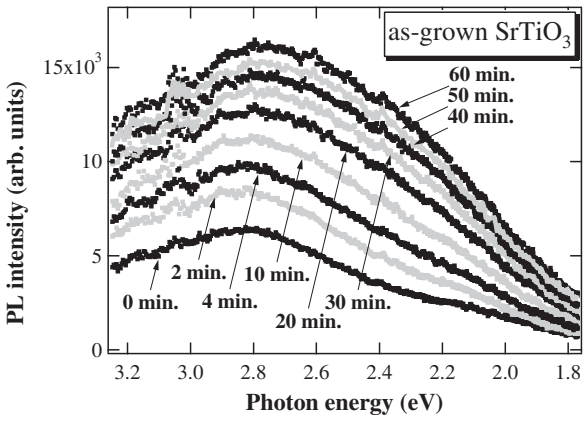

Fig. 1. The CW 325 nm laser light-induced spectral change of an as-grown $SrTiO_3$ crystal at room temperature in vacuum. The t_{ir} is given in min.

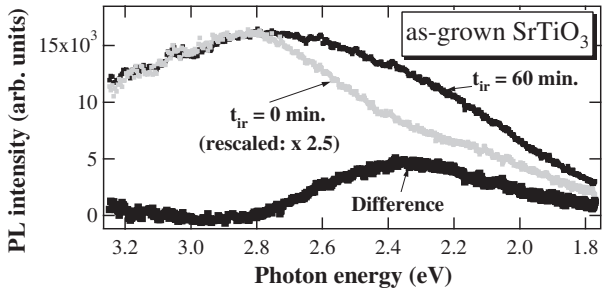

Fig. 2. The CW 325 nm laser light-induced PL component of an as-grown $SrTiO_3$ crystal at room temperature.

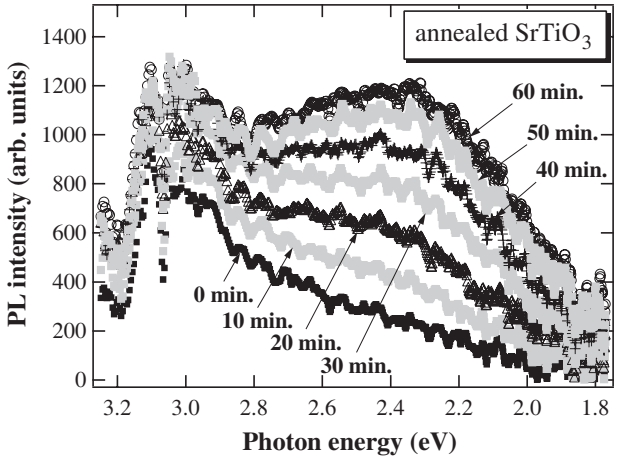

Fig. 3. The CW 325 nm laser light-induced spectral change of an annealed $SrTiO_3$ crystal at room temperature in vacuum. The t_{ir} is given in min.

and then a difference between the spectrum at $t_{ir} =$ 60 min and the rescaled spectrum is calculated, which is shown in Fig. 2. This figure shows clearly that a broad PL band grew at 2.4 eV under 325 nm laser light irradiation in a vacuum. Fig. 3 shows the photo-induced PL spectral change of the annealed $SrTiO_3$ crystal at room temperature in a vacuum. It is noted that the annealing treatment reduces the PL intensity to about one-tenth. The PL component below 2.8 eV grows with increasing t_{ir}. With t_{ir} increasing further, the rate of the spectral change becomes decreased. As done for the results of the as-grown crystal, the difference spectrum is also calculated, which is given in Fig. 4. It indicates clearly that a broad PL band of the annealed crystal grew at 2.4 eV under 325 nm laser light irradiation in a vacuum. The same spectral change in the 2.4 eV band was observed

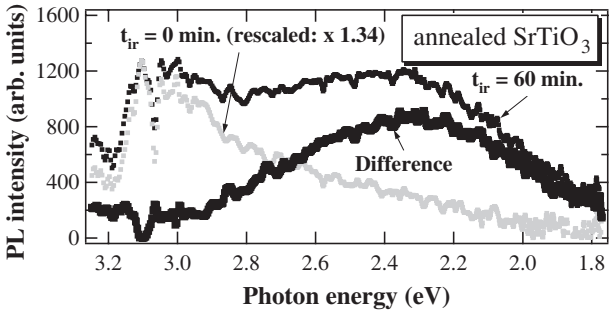

Fig. 4. The CW 325 nm laser light-induced PL component of an annealed $SrTiO_3$ crystal at room temperature.

also at 12 K in our previous study [7]. As well as the as-grown crystal, it is found, under the same laser light irradiation in oxygen gas, the 2.4 eV band disappears, returning to the original weak PL state. Since the 325 nm laser light never dissociates directly free O_2 molecule, the observed spectral changes arise from the photo-induced associative detachment and photo-induced dissociative adsorption of O_2 molecules near the $SrTiO_3$ surfaces [6].

We have studied the PL spectra of the as-grown and annealed $SrTiO_3$ crystals at 13 K as a function of excitation laser fluence of the third harmonics ($\lambda = 355$ nm) of a Nd^{3+}-YAG laser. The results are shown in Figs. 5 and 6. We have confirmed that, unlike CW 325 nm laser light, the pulsed 355 nm laser light cannot induce any reversible spectral change even at 14 mJ/cm^2. At the lowest laser fluence, both crystals exhibit only the intense 2.4 eV band. However, the center energy for the as-grown crystal is slightly smaller than that for the annealed crystal. We compare the PL spectra observed at 4 mJ/cm^2, before and after annealing. The annealed crystal displays more intense 2.4 eV luminescence than that for the as-grown crystal. This may be due to decrease in the number of non-radiative trap by the annealing treatment. With increasing laser fluence, two new PL bands appear at 3.2 eV, which is near indirect gap of $SrTiO_3$ and at 2.9 eV. On the contrary to the 2.4 eV band, the 3.2 and 2.9 eV bands for the as-grown crystal are more intense than those of the annealed crystal. This indicates that the 3.2 eV luminescence and 2.9 eV one are enhanced by oxygen defects. As seen from Fig. 5, with increasing laser fluence, the 2.4 eV band for the as-grown crystal grows and

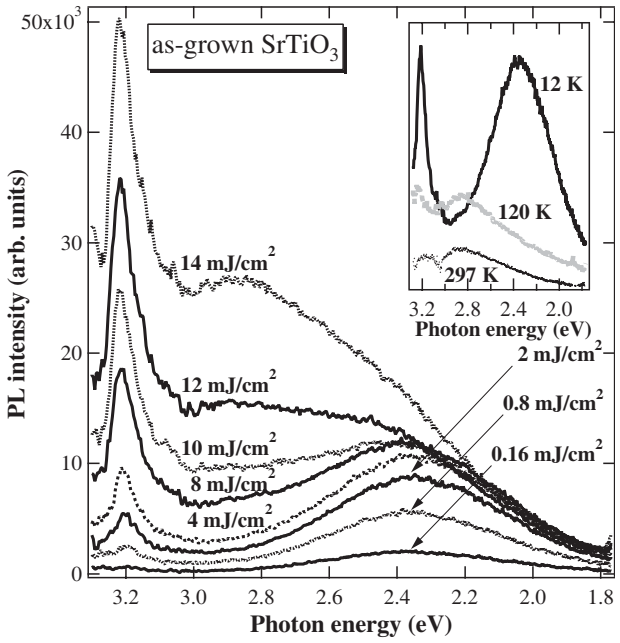

Fig. 5. The excitation laser intensity dependence of the PL spectra of an as-grown $SrTiO_3$ crystal at 12 K. The temperature dependence of the PL spectrum is shown in the inset.

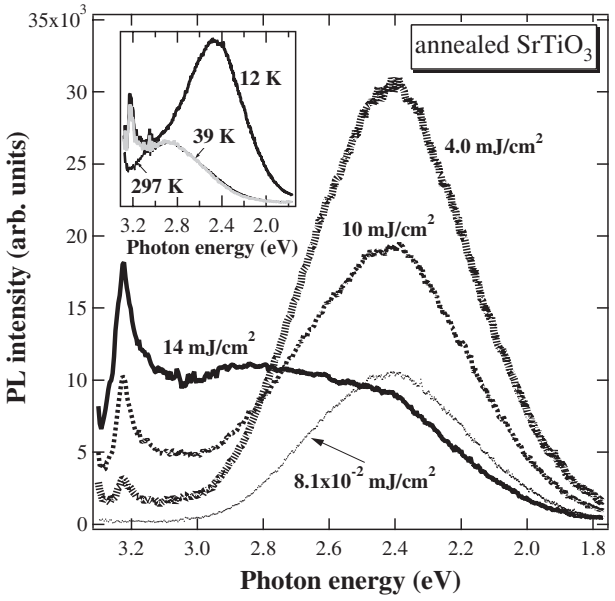

Fig. 6. The excitation laser intensity dependence of the PL spectra of an annealed $SrTiO_3$ crystal at 12 K. The temperature dependence of the PL spectrum is shown in the inset.

then becomes saturated at 8 mJ/cm^2, while the 3.2 and 2.9 eV bands continue to grow without any saturation. As seen in Fig. 6, the PL intensity of the 2.4 eV band for the annealed crystal increases

also with increasing laser fluence, and then it reaches a maximum at 4 mJ/cm^2, while the 3.2 and 2.9 eV bands continue to grow without displaying any maximum. Besides these measurements, the PL spectra were measured at different temperatures between 12 and 297 K. Of them, the PL spectra at 12, 120 and 297 K for the as-grown crystal are given in the inset of Fig. 5, and the PL spectra at 12, 39 and 297 K for the annealed crystal are given in the inset of Fig. 6. As seen from these insets, the 3.2 and 2.9 eV bands grow deteriorating the 2.4 eV band with increasing temperature. The 2.4 eV band observed for the as-grown and annealed crystals disappeared at 120 and 39 K. The 3.2 eV band becomes weak and broad with increasing temperature. The 2.9 eV band remains even at room temperature. We have also measured the time-resolved spectra and found that the 2.4 eV luminescence has long lifetime (≥ 1 ms), while both the 3.2 luminescence and the 2.9 eV one have short lifetime ($\ll 50$ ns), at 12 K [7].

Finally, the experimental results obtained in the present study are summarized and discussed as follows. Since the PL intensity of the 2.4 eV band is affected considerably by oxygen defects and it saturates under intense excitation, the 2.4 eV band is assigned to the radiative decay of extrinsic excitons trapped around oxygen defects. The excitation intensity dependences of the PL shown in Figs. 5 and 6 indicate that, with increasing laser fluence, the 3.2 and 2.9 eV bands grow deteriorating the 2.4 eV band. This intensity relation among these PL bands at 2.4, 3.2 and 2.9 eV with increasing excitation intensity may arise from two causes: (1) finite number of the 2.4 eV luminescence centers, and (2) electron–hole recombination enhanced with higher laser fluence. Since the recombination rate increases with increasing carrier density, the near-band edge emissions at 3.2 and 2.9 eV increase linearly with increasing laser fluence, while the rate of electron (including hole) migration to the 2.4 eV luminescence centers decreases with increasing laser fluence. The excitation-intensity and temperature dependences of the 3.2 and 2.9 eV bands also indicate that two PL bands occur from the same origin. We measured also the PL excitation (PLE) spectrum for the 2.4 eV band and found a sharp PLE edge at 3.26 eV.This edge corresponds well to the indirect gap of $SrTiO_3$. Generally, an indirect-gap-type semiconductor crystal does not exhibit intense PL. However, some impurities and crystal defects activate the PL of indirect excitons, exhibiting intense PL band near band edge. Therefore, the intense PL at 3.2 and 2.9 eV may be assigned to the radiative decay of indirect excitons affected by oxygen defects, creating phonons. The energy difference (271 cm^{-1}) between the PLE edge and the peak energy of the 3.2 eV band is close to the transverse optic (TO) phonon frequency [11]. Thus, the 3.2 eV band is assigned to the one TO phonon sideband, while the broad 2.9 eV band is also assigned to a continuum consisting of other phonon sidebands.

Acknowledgements

This work is supported by a Grant-in-Aid for Scientific Research from the Ministry of Education, Science, Sports, Culture and Technology, Japan. This work is partially supported by Interdisciplinary General Joint Research Grant for Nihon University.

References

[1] L. Grabner, Phys. Rev. 177 (1969) 1315.
[2] T. Hasegawa, M. Shirai, K. Tanaka, J. Lumin. 87–89 (2000) 1217.
[3] S. Mochizuki, T. Shimizu, F. Fujishiro, Physica B 340-342 (2003) 956.
[4] Y. Kawabe, A. Yamanaka, E. Hanamura, T. Kimura, Y. Takiguchi, H. Kan, Y. Tokura, J. Appl. Phys. 88 (2000) 1175.
[5] S. Mochizuki, H. Araki, Physica B 340–342 (2003) 969.
[6] S. Mochizuki, T. Nakanishi, Y. Suzuki, K. Ishi, Appl. Phys. Lett. 79 (2001) 3785.
[7] S. Mochizuki, S. Minami, F. Fujishiro, J. Phys.: Condens. Matter., submitted for publication.
[8] S. Kimura, J. Yamauchi, M. Tsukada M, Phys. Rev. B 51 (1995) 11049.
[9] V.E. Henrich, G. Dresselhous, H.J. Zeiger, Phys. Rev. B 17 (1978) 4908.
[10] R. Astala, P.D. Bristowe, Modell. Simul. Mater. Sci. Eng. 9 (2001) 415.
[11] R.A. Cowley, Phys. Rev. 134 (1964) A981.

Available online at www.sciencedirect.com
SCIENCE DIRECT®
Journal of Luminescence 112 (2005) 71–74
JOURNAL OF LUMINESCENCE
www.elsevier.com/locate/jlumin

Photoluminescence studies on AgI–ZrO_2 composites

Fumito Fujishiro*, Shosuke Mochizuki

Department of Physics, College of Humanities and Sciences, Nihon University, 3-25-40 Sakurajosui, Setagaya-ku, Tokyo 156-8550, Japan

Abstract

AgI–ZrO_2 fine particle composites were fabricated over a wide composition range of AgI. We have measured the X-ray diffractograms and photoluminescence properties of the composites, together with those of pristine AgI and pristine ZrO_2 fine particles. The results give the information about the atomic structure of AgI/ZrO_2 interfaces, which may provide the pathway for the high ionic conduction.

PACS: 78.55.−m; 61.72.−y; 66.10.Ed

Keywords: Exciton; Photoluminescence; Ionic conductor; Interface; Oxygen defect

The ionic conductivity of AgI is considerably enhanced by adding oxide fine particles [1,2]. It is frequently assumed that highly conductive layers are created at AgI/oxide fine particle interfaces. However, it is difficult to clarify experimentally the atomic structure of the interfaces. In order to investigate such interface structure, the photoluminescence (PL) study is effective. Besides AgI [3], most oxides also show structure-sensitive PL. Very recently, we have fabricated AgI–ZrO_2 composites and observed considerable conductivity enhancement [4]. In the present paper, we report the structural and PL studies on AgI–ZrO_2 composites, and we discuss the structure of AgI/ZrO_2 fine particle interfaces.

AgI–ZrO_2 composites were prepared by mixing AgI powder (99.999%, Alfa) and ZrO_2 powder (>98%, Aldrich) with an average diameter of 26 nm, compressing uniaxially the mixture under 0.2 GPa for 30 min into pellets and then heating the pellets in the lidded crucible at 673 K in air for 12 h. The composite pellets were characterized by the X-ray diffraction analysis with Cu Kα_1 radiation. The third harmonics, $\lambda = 355$ nm (= 3.49 eV), of a pulsed Nd^{3+}–YAG laser light was used to excite PL.

Fig. 1 shows the X-ray diffractograms of different (x)AgI–$(1-x)ZrO_2$ composites. All of the diffraction lines observed for a pristine ZrO_2 ($x = 0$) specimen are assigned to the monoclinic

*Corresponding author. Tel./fax: +81 3 5317 9771.
E-mail address: fumito@phys.chs.nihon-u.ac.jp (F. Fujishiro).

0022-2313/$ - see front matter © 2004 Elsevier B.V. All rights reserved.
doi:10.1016/j.jlumin.2004.09.086

phase, except for the tetragonal phase line at 30.2°. Since the diffraction line widths are hardly changed with adding AgI, the average size of ZrO_2 particles in the composites is thought to be almost the same as that of the starting material powder. On further increasing x, the AgI diffraction lines become pronounced. The diffraction intensities of the βAgI(100) line at 22.3° and βAgI(200) line at 45.6° are considerably enhanced in comparison with other AgI-based composites [1], which may be due to preferred-orientations.

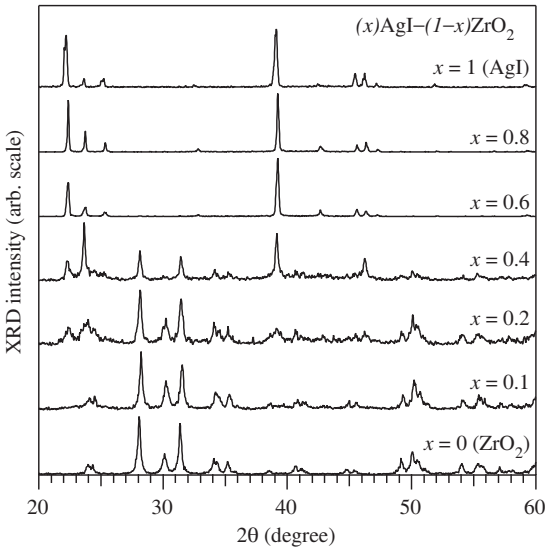

Fig. 1. The X-ray diffractograms for different (x)AgI–$(1-x)ZrO_2$ composites at 297 K.

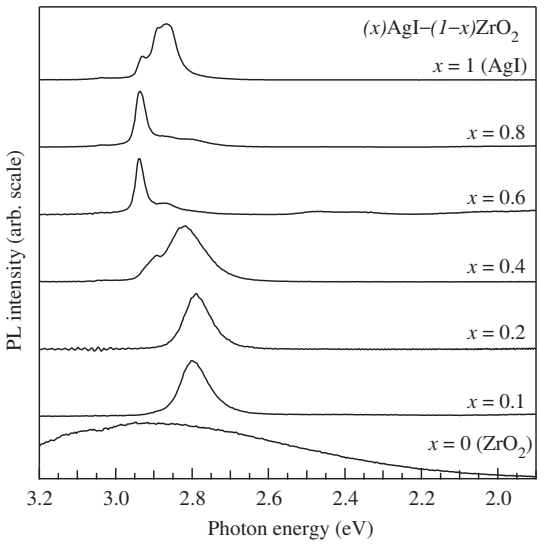

Fig. 2. The PL spectra for different (x)AgI–$(1-x)ZrO_2$ composites at 12 K.

The PL spectra for different (x)AgI–$(1-x)ZrO_2$ composites at 12 K are shown in Fig. 2. The excitation laser fluence I_{ex} was 0.066 mJ/cm^2. Pristine ZrO_2 shows a broad PL band centered at about 2.9 eV. The PL peak energy depends on the excitation photon energy E_{ex}, as shown in Figs. 3(a) and (b). Adding small amount ($0.1 \leqslant x \leqslant 0.2$) of AgI, the intensity of the broad PL band decreases extremely, and a new PL band appears at about 2.80 eV. At $x = 0.4$, two PL bands appear at 2.89 and 2.83 eV. On further adding AgI ($0.6 \leqslant x \leqslant 0.8$), another new sharp PL band appears at 2.94 eV, accompanying by some weak PL bands at its lower energy side. The 2.94 eV band is assigned to the radiative decay of free excitons (FE) in AgI domain [3]. At $x = 1$,

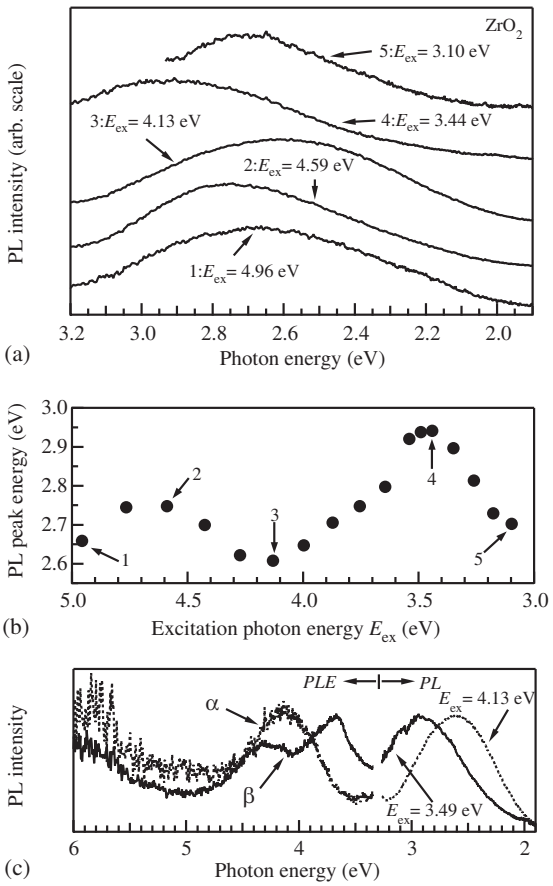

Fig. 3. (a) The PL spectra of pristine ZrO_2 excited with various E_{ex} at 13 K; (b) the PL peak energy plotted against E_{ex}; (c) the PL and PLE spectra for pristine ZrO_2 at 13 K.

namely, pristine AgI, besides the free exciton emission, more intense PL bands grow at 2.89 and 2.86 eV. These intense PL bands are assigned to radiative decays of excitons trapped around defects and grain boundaries in AgI specimen.

In pristine ZrO_2 ($x=0$), we have found that the PL intensity peak energy depends on E_{ex}, as shown in Fig. 3(a). The PL intensity peak energy is plotted against E_{ex} in Fig. 3(b). It is noted that each PL spectrum is considerably Stokes-shifted, which indicates that there are different localized electronic states in the energy gap (5.8 eV) of ZrO_2. The PL and PL excitation (PLE) spectra are also shown in Fig. 3(c). The PLE curve α is monitored at 2.99 eV, which corresponds to the PL intensity peak energy for the excitation $E_{ex}=3.49$ eV, while the PLE curve β is monitored at 2.53 eV which corresponds to the PL intensity peak energy for the excitation $E_{ex}=4.13$ eV. The PLE spectra ascertain the existence of the luminescent localized electronic states in the energy gap. Since the PL intensity of ZrO_2 was decreased remarkably by adding AgI, as shown in Fig. 2, such luminescence centers may be at ZrO_2 particle surfaces.

The temperature dependence of PL spectra for different (x)AgI–$(1-x)$$ZrO_2$ composites was measured. The results are shown in Figs. 4(a) and (b). Each spectrum is normalized in intensity at each maximum. In small x range ($0.1\leqslant x\leqslant 0.2$), with increasing temperature, the 2.80 eV band is considerably weakened and almost disappears above about 100 K. The broad PL band observed at 99 K may arise from ZrO_2. However, the PL spectral shape above 2.85 eV is affected by the optical absorptions due to AgI [3]. At $x=0.4$, the PL intensity of the 2.83 eV band decreases, while the PL intensity of the 2.89 eV band increases in comparison with that of the 2.83 eV band, with increasing temperature. It suggests that phonon-assisted reverse transition from the 2.83 eV luminescence center to the 2.89 eV luminescence center occurs. In large x range ($0.6\leqslant x\leqslant 0.8$), with increasing temperature, free exciton emission decreases in intensity, while another PL band appears at 2.90 eV. This indicates that the 2.90 eV band arises from radiative decay of excitons trapped around thermally ionized defects or thermally ionized impurities.

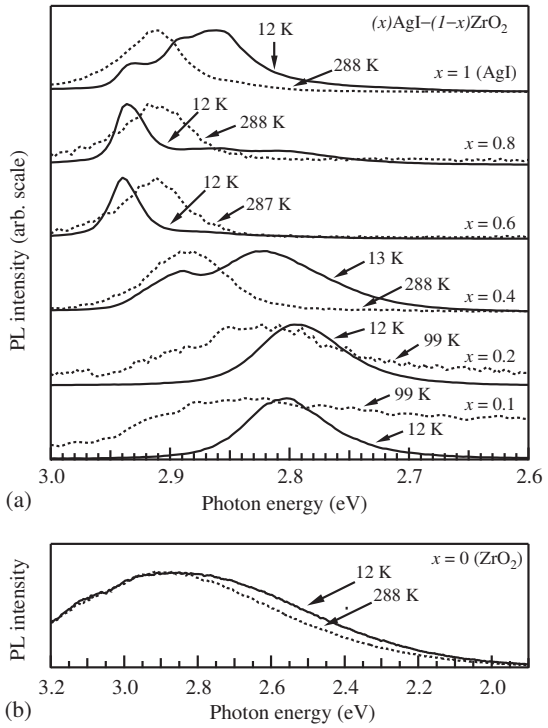

Fig. 4. The temperature dependence of the PL spectra: (a) for different (x)AgI–$(1-x)$$ZrO_2$ composites; (b) for pristine ZrO_2.

Figs. 5(a) and (b) show the I_{ex} dependence of the PL spectra for different (x)AgI–$(1-x)$$ZrO_2$ composites at 12 K. Each spectrum is normalized in intensity at each maximum. Labels, I and W, indicated by the curves denote intense ($\geqslant 1.0$ mJ/cm^2) and weak ($\leqslant 0.1$ mJ/cm^2) excitations, respectively. For small x region ($\leqslant 0.2$), the PL component below 2.80 eV saturates at intense excitation, which indicates that the luminescence center giving this PL component is limited in number, though it has high quantum yield. We note the x dependence of the spectra for weak excitation. With adding AgI, the 2.80 eV band shifts to 2.78 eV at $x=0.2$ and, with further adding AgI, it shifts to 2.81 eV at $x=0.4$. At both $x=0.6$ and 0.8, the band remains as a shoulder of AgI-related PL bands. Since adding AgI to ZrO_2 induces the oxygen defects, $Zr_{1-x}Ag_xO_{2-3x/2}$ $(Vö)_{3x/2}$ [5], the shift may be connected with the change in the electronic states at AgI/ZrO_2 interfaces. On further adding AgI, the shoulders at 2.94 and 2.86 eV become prominent.

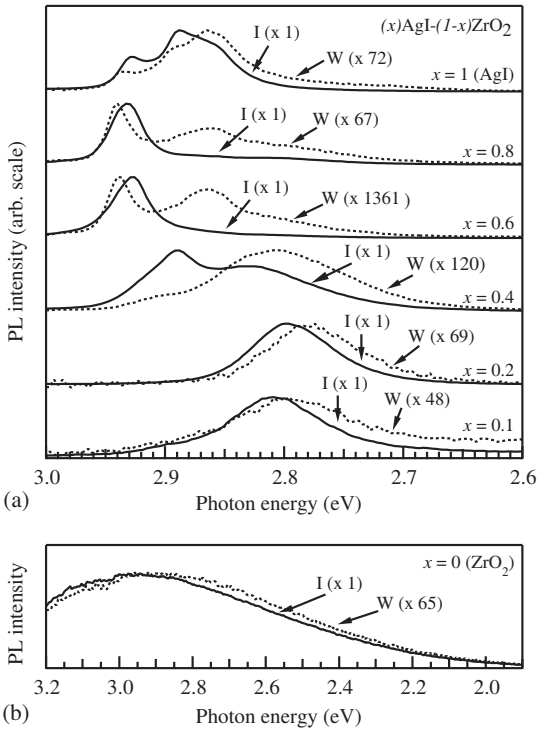

Fig. 5. The I_{ex} dependence of the PL spectra: (a) for different (x)AgI–$(1-x)$$ZrO_2$ composites; (b) for pristine ZrO_2 at 12 K.

The spectral transition with adding AgI is explained as follows. For small x region, the free excitons generated in AgI domain collides frequently with AgI surfaces, and they are trapped at AgI/ZrO_2 interfaces, creating bound excitons. With increasing x, the size of AgI domain increases and free excitons are able to propagate in a long distance. Therefore, before trapping at AgI/ZrO_2 interfaces, a part of free exciton decays spontaneously with generating the 2.94 eV luminescence, and other part of free exciton is trapped at crystal defects and impurities within AgI domain. The radiative decay of these trapped excitons generates the 2.93 and 2.86 eV luminescence.

Besides the above PL properties, we have found also a reversible photo-induced PL spectral change in the present AgI–ZrO_2 composites at room temperature. One of the results is shown in Fig. 6, as a typical example. After fully irradiating with CW 325 nm laser light in an evacuated specimen chamber for 10 min, the specimen shows a broad PL band at 2.57 eV. Oxygen gas is then

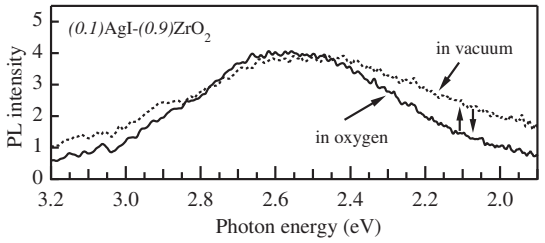

Fig. 6. Reversible photo-induced PL spectral change of (0.1)AgI–$(0.9)$$ZrO_2$ composite at 295 K.

introduced into the specimen chamber and, with increasing irradiating time, the PL component below 2.45 eV decreases in intensity. Through many successive experiments, it is found that such spectral changes appear repeatedly. The observed spectral changes may originate from excitation-energy exchange between the photo-induced oxygen vacancies on ZrO_2 particle and AgI. The spectral transitions yield materials for optical sensor devices.

In summary, we have studied the PL properties of (x)AgI–$(1-x)$$ZrO_2$ $(0 \leqslant x \leqslant 1)$ composites. The PL spectra have shown well the behavior of free and trapped excitons at AgI/ZrO_2 interfaces where Ag^+ ions may move with high-ionic conductivity. The specimen fabrications using different starting-material ZrO_2 powders and more detailed studies are now in progress.

This work is supported by a Grant-in-Aid for Scientific Research from the Ministry of Education, Science, Sports, Culture and Technology, Japan. This work is partially supported by Interdisciplinary General Joint Research Grant for Nihon University.

References

[1] S. Mochizuki, F. Fujishiro, J. Phys.: Condens. Matter 15 (2003) 5057.
[2] M.C.R. Shastry, K.J. Rao, Solid State Ionics 51 (1992) 311.
[3] S. Mochizuki, F. Fujishiro, J. Phys.: Condens. Matter 16 (2004) 3239.
[4] F. Fujishiro, S. Mochizuki, in preparation.
[5] F.A. Kröger, H.J. Vink, Solid State Phys. 3 (1956) 307.

INSTITUTE OF PHYSICS PUBLISHING JOURNAL OF PHYSICS: CONDENSED MATTER

J. Phys.: Condens. Matter **17** (2005) 923–948 doi:10.1088/0953-8984/17/6/011

Photoluminescence and reversible photo-induced spectral change of $SrTiO_3$

Shosuke Mochizuki[1], **Fumito Fujishiro and Seiko Minami**

Department of Physics, College of Humanities and Sciences, Nihon University, 3-25-40 Sakurajosui, Setagaya-ku, Tokyo 156-8550, Japan

E-mail: motizuki@physics.chs.nihon-u.ac.jp

Received 7 June 2004, in final form 4 January 2005
Published 28 January 2005
Online at stacks.iop.org/JPhysCM/17/923

Abstract

When strontium titanate ($SrTiO_3$) single crystal is irradiated at room temperature with a 325 nm laser light in an evacuated specimen chamber, the luminescence intensity increases, creating a broad visible luminescence centred at about 2.4 eV. Then, introducing oxygen gas into the specimen chamber, the photoluminescence spectrum returns reversibly to the original weak luminescence under the same laser light irradiation. After removing the laser light irradiation, each photoluminescent state is stored for a long time at room temperature under room light, regardless of any changes of atmosphere. Such photo-induced spectral change has been observed also at different temperatures from 13 K to room temperature. The observed phenomenon is explained by means of the photo-induced oxygen defect formation at the surfaces of $SrTiO_3$ crystal. For the same $SrTiO_3$ single crystal, we have studied the photoluminescence properties. Besides the 2.4 eV luminescence band, we have observed new two luminescence bands centred at about 3.2 eV and about 2.9 eV. The energy, 3.2 eV, is close to both the photoluminescence excitation edge energy and the reported band edge energy of $SrTiO_3$ crystal. Both the 3.2 eV luminescence and the 2.9 eV luminescence decay rapidly after a pulsed photoexcitation, while the 2.4 eV luminescence lasts for several seconds at 13 K. The excitation light intensity dependence of these luminescence bands has been also measured at 13 K. The 2.4 eV luminescence increases in intensity with increasing excitation intensity up to 4 mJ cm^{-2}, and then it becomes decreased with further increase in the excitation intensity. On the other hand, both the 3.2 eV luminescence and the 2.9 eV luminescence increase in intensity with increasing excitation intensity, without any saturation. Although the 2.4 eV luminescence had been assigned to the radiative decay of intrinsic self-trapped excitons in a superparaelectric state by several workers, the present studies have clarified that the luminescence originates mainly from crystal defects (oxygen defects and chemical heterogeneity in the surface region).

[1] Author to whom any correspondence should be addressed.

0953-8984/05/060923+26$30.00

Both the 3.2 eV luminescence and the 2.9 eV luminescence are discussed qualitatively.

1. Introduction

Considerable attention has been given to clarifying the quantum paraelectric state in strontium titanate ($SrTiO_3$). The lattice of $SrTiO_3$ has the cubic perovskite-type structure at room temperature. At 105 K, it transforms into a tetragonal structure. With temperature decreasing from room temperature, the static dielectric constant increases prominently, and it attains several ten thousands at 4 K without any paraelectric–ferroelectric transition (Müller and Burkard 1979). Between 4 and 0.3 K, the dielectric constant was found to be independent of temperature. Recently, a prominent enhancement of the dielectric constant has been observed under ultraviolet light irradiation (Katsu *et al* 2001, Takesada *et al* 2003, Hasegawa *et al* 2003), but it is now under dispute, involving some complicated problems relating to electrode/$SrTiO_3$ interfaces. In order to explain the quantum paraelectric state, one may assume first that Ti^{4+} ions are fluctuating quantum mechanically in the $SrTiO_3$ lattice, as if they are in the critical state just before the paraelectric–ferroelectric transition in usual ferroelectrics. Müller *et al* (1991) proposed that $SrTiO_3$ is in a coherent quantum state associated with a rotonic minimum in the transverse acoustic mode. For the photo-enhanced dielectric constant, Nasu (2004) assumed that ultraviolet light broke the crystal inversion symmetry, creating ferroelectric microdomains. He assumed also that such microdomains fluctuated and itinerated quantum mechanically in the $SrTiO_3$ crystal. $SrTiO_3$ crystal has an indirect gap and a direct gap in an energy range between about 3.2 eV and about 3.5 eV (Cohen and Blunt 1968, Blazey 1971, Capizzi and Frova 1970, Capizzi *et al* 1972, Cardona 1965, Zollner *et al* 2000, Hasegawa *et al* 2000). It is known that the luminescence intensity is specimen dependent (Grabner 1969). Hasegawa *et al* (2000) measured the optical absorption and photoluminescence spectra at temperatures between 10 K and room temperature. They found that the crystal exhibited a broad photoluminescence band around 2.4 eV. Through time-resolved photoluminescence measurements, they assigned the 2.4 eV luminescence to the radiative decay of intrinsic self-trapped excitons. However, many metal oxides display very similar broad photoluminescence between 2 and 3 eV: for example, Sm_2O_3 (Mochizuki 2003), Eu_2O_3 (Mochizuki *et al* 2001), anatase TiO_2 (Mochizuki *et al* 2003), Al_2O_3 (Mochizuki and Araki 2003a), vitreous SiO_2 (Mochizuki and Araki 2003b) and $LaAl_2O_3$ (Kawabe *et al* 2000). Moreover, their luminescence intensities are specimen dependent, especially as regards the thermal history and crystal preparation method. Unfortunately, this specimen-dependent nature of the 2.4 eV luminescence has been accorded too little respect in the optical study of $SrTiO_3$ and it has led many researchers astray.

Very recently, we have found at room temperature that the 2.4 eV luminescence band of $SrTiO_3$ grows under a 325 nm laser light irradiation in vacuum, while it disappears under the same laser light irradiation in oxygen gas. Through many successive experiments involving replacing the specimen atmosphere, it was found that the spectral change occurs reversibly under the 325 nm laser light irradiation. The observed phenomenon relates to the photo-induced oxygen defects at the surfaces of $SrTiO_3$. Now or never is the time to reinvestigate the photoluminescence properties of $SrTiO_3$ in detail, taking account of such oxygen defects.

In the present paper, we report the photoluminescence spectrum, its excitation intensity dependence, the decay profile, the photoluminescence excitation spectrum, the time-resolved photoluminescence spectrum and the reversible photo-induced spectral change of $SrTiO_3$ single crystal at different temperatures between 12 K and room temperature in detail.

2. Experimental detail

The $SrTiO_3$ crystal was well grown by the Verneuil method and the as-grown crystal is dark blue. The as-grown crystal was then annealed under an appropriate reducing atmosphere. The crystal became perfectly colourless and transparent under the annealing. Several as-grown (dark blue) and annealed (colourless transparent) $SrTiO_3$ single crystals, $10 \times 10 \times (0.5–1.0)$ mm in size, were supplied by Sinkosya Corporation. The broad surfaces of the crystals are optically flat and they are oriented in the [100] direction. It should be noted that such transparent $SrTiO_3$ crystals grown by the Verneuil method have been widely used by many workers for studying electrical and optical properties. As reference specimens, we have used also several $SrTiO_3$ powder compact discs which were sintered at 1273 K and annealed at different atmosphere.

The photoluminescence (PL) spectra were measured by using an optical multichannel analyser consisting of a grating monochromator (focal length = 32 cm, grating = 1200 or 150 grooves mm^{-1}) and an image-intensified diode-array detector (number of channels = 1024, gate time = 5 ns). An Nd^{3+}:YAG laser (wavelength = 355 nm, pulse width = 4–5 ns, repetition = 10 Hz), a continuous wave (CW) He–Cd laser (wavelength = 325 nm) and a monochromatic light source consisting of a 150 W xenon lamp and a grating monochromator (focal length = 20 cm) were used as the excitation source. The excitation light intensity dependence of the PL spectrum was measured by attenuating the incident laser light intensity with glass attenuators calibrated in transmissivity. The PL excitation (PLE) spectra were recorded by varying the excitation light wavelength λ_{ex} with the same monochromatic light source as described above, and by detecting the luminescence light intensity at a desired wavelength λ_{ob} as a function of λ_{ex} with a grating monochromator (focal length = 20 cm) and a synchronous light detection system. The time-resolved PL spectra were taken using the same optical multichannel analyser to which two delay pulse generators were attached. The delay time t_d, which is the measurement start time after a laser pulse incidence, and the gate time t_g, which is the time after t_d of the spectral measurement, were set with these delay pulse generators which were controlled with a personal computer. The actual minimum gate time was 5 ns. The decay curves were measured with an apparatus consisting of a grating monochromator (focal length = 20 cm) equipped with a photodetection system (time constant = about 1 μs) and the Nd^{3+}:YAG laser oscillating at 355 nm. The optical density (OD) spectrum was measured using another optical multichannel analyser.

An optical cryostat was used for the specimen chamber, in which a closed-cycle helium refrigerator equipped with a temperature controller was used to change the specimen temperature between 12 K and room temperature. Another specimen chamber was also used for the measurement of the reversible spectral change at room temperature. An oil-free vacuum system was used for evacuating these specimen chambers.

3. Results

3.1. Photoluminescence spectra of $SrTiO_3$ under weak excitation

Figure 1(a) shows the PL spectra of $SrTiO_3$ at different temperatures under a pulsed 355 nm laser light excitation (pulse width = 4–5 ns, repetition = 10 Hz, fluence = 0.079 mJ cm^{-2}). A broad luminescence band is observed around 2.4 eV at 12 K. The band seems slightly asymmetrical in spectral shape and it consists of two luminescence bands centred at 2.46 and 2.40 eV, which are labelled B′ and B″, respectively. This indicates that this photoluminescence comes from at least two kinds of luminescent centres. The spectral shape and intensity differ slightly with the specimens. We measured also the PL spectra of an as-grown crystal as a function of annealing time at 973 K in a reducing atmosphere. It has been found that the PL

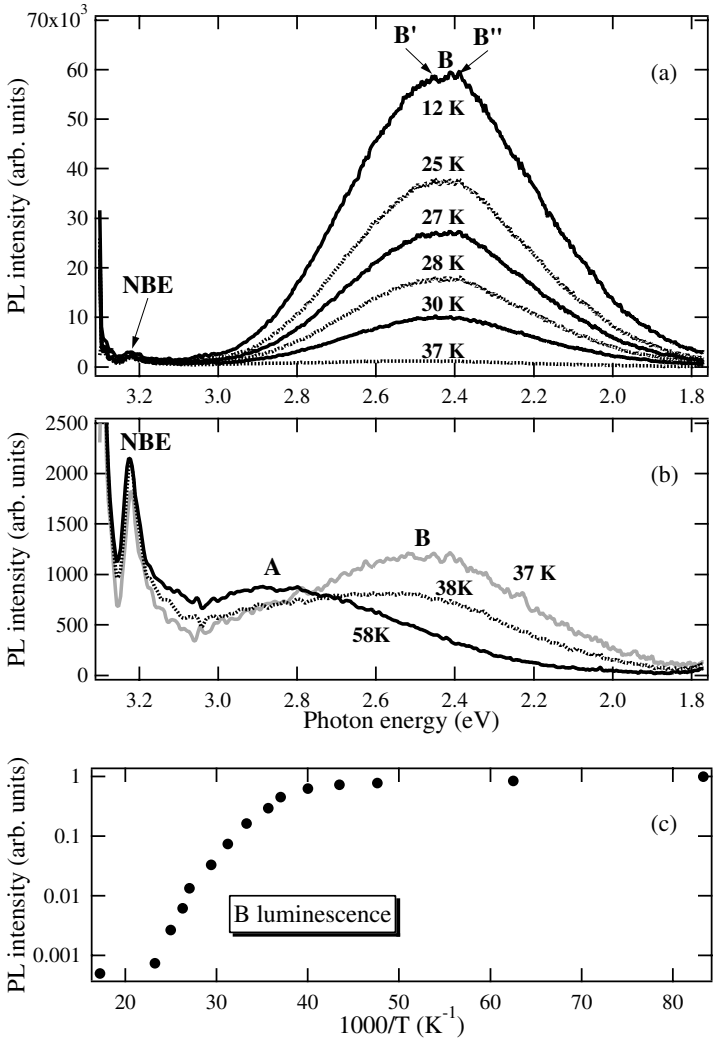

Figure 1. The photoluminescence spectra of $SrTiO_3$ at different temperatures: (a) $T \leqslant 37$ K; (b) $T \geqslant 37$ K. (c) The temperature dependence of the integrated intensity. The excitation laser fluence was 0.079 mJ cm^{-2}. The spectral integration was performed in a photon energy range between 2.9 and 1.77 eV.

intensity increases with increasing annealing time, while the PL intensity peak energy and spectral width are slightly dependent on the annealing time. With increasing temperature, the 2.46 eV luminescence band grows more and then this band becomes together with the 2.40 eV luminescence band, displaying an asymmetrical band centred at about 2.44 eV above 27 K. We call this luminescence band the 'B luminescence band'. On further increasing the temperature, the B luminescence intensity continues to decrease, while a new luminescence band appears at 2.89 eV and becomes prominent, as seen in figure 1(b). We tentatively call this luminescence band the 'A luminescence band'. The A luminescence band seems to extend above 3.2 eV. The A luminescence band grows to the detriment of the B luminescence and it is superior to the B luminescence band above 58 K. The integrated PL intensity of the B luminescence band is plotted against inverse temperature on a semi-logarithmic scale in figure 1(c). The

spectral integration was performed in a photon energy region between 2.9 and 1.77 eV. In this figure, the maximum luminescence intensity is normalized to unity. As seen in this figure, the luminescence intensity decreases gradually with increasing temperature to 25 K and, on further increasing the temperature above 28 K, the intensity decreases exponentially. Approaching 43 K, the intensity becomes constant. Although such temperature dependence approaching a constant has been not reported for $SrTiO_3$, a slight sign of such constant intensity appeared in the reported curve (figure 3(b): Hasegawa *et al* 2000), as some deviation from the curve fitting to the data. The constant intensity is due to the A luminescence component which grows gradually at high temperatures. Although the PL band consists of several luminescence components as described above, we subtract the constant intensity from the data and we assume a phonon-assisted non-radiative decay process for the observed B luminescence. Then, we perform a curve fitting by using the well-known expression for the integrated PL intensity $I(T)$,

$$I(T) = \frac{1}{1 + C\exp(-\Delta E/kT)}, \tag{1}$$

where C is a constant and ΔE is the height of an average potential barrier separating a luminescent state from the ground state. In addition to such a phonon-assisted non-radiative process, thermal ionization of luminescence states is also considered to participate in the intensity decrease with increasing temperature. In such a case, ΔE may correspond to the ionization energy. In the fitting, the data obtained above 40 K are taken off to avoid the effect of the A luminescence. The best-fitted curve is obtained with a $\Delta E = 32$ meV. The value is slightly smaller than the value (43 meV) reported by Hasegawa *et al* (2000). At present, it is not clear whether the difference arises from the specimen-dependent nature or from the error in the specimen surface temperature measurements or from the manner of the curve fitting—performed probably ignoring the effect of the A luminescence.

As seen in figures 1(a) and (b), a sharp luminescence band is also observed at 3.23 eV which is close to the observed PLE edge (3.26 eV) and the reported indirect band gap energy E_g^{id} (3.27 eV) of $SrTiO_3$. We tentatively call this luminescence band appearing near the band edge the 'NBE luminescence band'. The steep rise above 3.26 eV is due to the parasitic luminescence of the optical multichannel analyser used.

3.2. Photoluminescence excitation spectra of $SrTiO_3$

The photoluminescence excitation (PLE) spectra of the same $SrTiO_3$ single crystal have also been measured at different temperatures. Some of the spectra are selected and shown in figure 2, in which the PL spectrum observed at 13 K is also shown. The luminescence intensity was monitored at the intensity peak energy of the B luminescence band. The PLE spectrum displays a sharp edge at 3.26 eV and a kink at 3.42 eV, which are close to the reported indirect gap energy E_g^{id} (3.27 eV) and the direct gap energy E_g^{d} (3.46 eV) of $SrTiO_3$ (Capizzi and Frova 1970), respectively. The PLE spectrum indicates that the B luminescence is caused mainly by the interband excitations. The energy difference of the B luminescence band from the PLE edge is about 0.80 eV. The shape of the PLE spectrum differs in an energy region higher than the PLE edge from the absorption spectra reported by Blazey (1971), Capizzi and Frova (1970), Capizzi *et al* (1972), Cardona (1965) and Zollner *et al* (2000). Generally, there are many crystal defects at the specimen surfaces where photoexcited states tend to decay non-radiatively. Such a luminescence quench effect appears more prominently in an energy region higher than the fundamental absorption edge. The excitation with photons above the band gap energy produces energetic electrons and holes, which are eventually thermalized by emitting phonons. Therefore, the PLE above the band gap is governed not necessarily by the direct

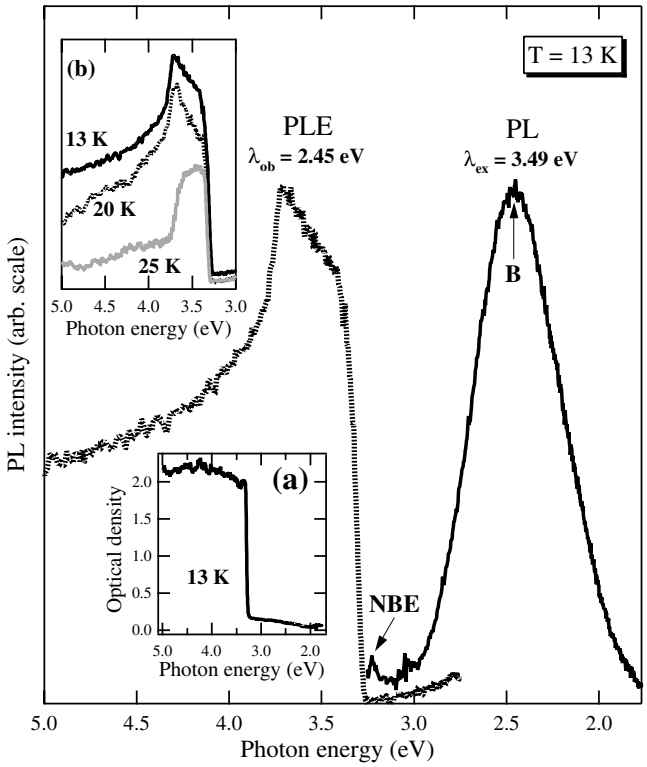

Figure 2. The photoluminescence (PL), optical density (OD) and photoluminescence excitation (PLE) spectra of $SrTiO_3$ at 13 K. The luminescence is monitored at the peak energy (=2.45 eV) of the B luminescence band. The OD spectrum at 13 K and the PLE spectra at different temperatures are shown in inset (a) and inset (b), respectively.

quenching of highly excited electrons at defect sites but by the change in the probability of the interaction of electron–hole pairs with defects.

As shown in inset (a) of figure 2, the OD spectrum has a faint tail below 3.2 eV. It is found that the OD of the tail decreases with annealing in a reducing atmosphere. Although the B luminescence band is well excited by the interband transition, the PLE spectra indicate that the luminescence can also be excited even by photons having energies lower than indirect gap. Under a 442 nm (=2.80 eV) laser light excitation, we have certainly detected the B luminescence spectrum through a laser light sharp cut filter (HOYA: Y48). The B luminescence can also be ascertained clearly by the naked eye through the same filter. Under the same 442 nm excitation, we have also found more intense luminescence for sintered $SrTiO_3$ powder compact specimens (Mochizuki and Fujishiro 2005). These results indicate that there are different defect-related luminescent levels in the energy gap.

As seen in inset (b), the PLE spectral shape changes with increasing temperature, except for the absorption edge profile. The suppression seen at photon energies higher than 3.7 eV becomes prominent with increasing temperature. The suppression may arise from the temperature change in the probability of the interaction of electron–hole pairs with defects.

In the following sections, the observed energy difference (0.8 eV), together with the photo-induced spectral change, will be discussed, and it will be concluded that the B luminescence band comes from the extrinsic luminescent centres around which photo-generated carriers (free electron or free hole, or both) are trapped.

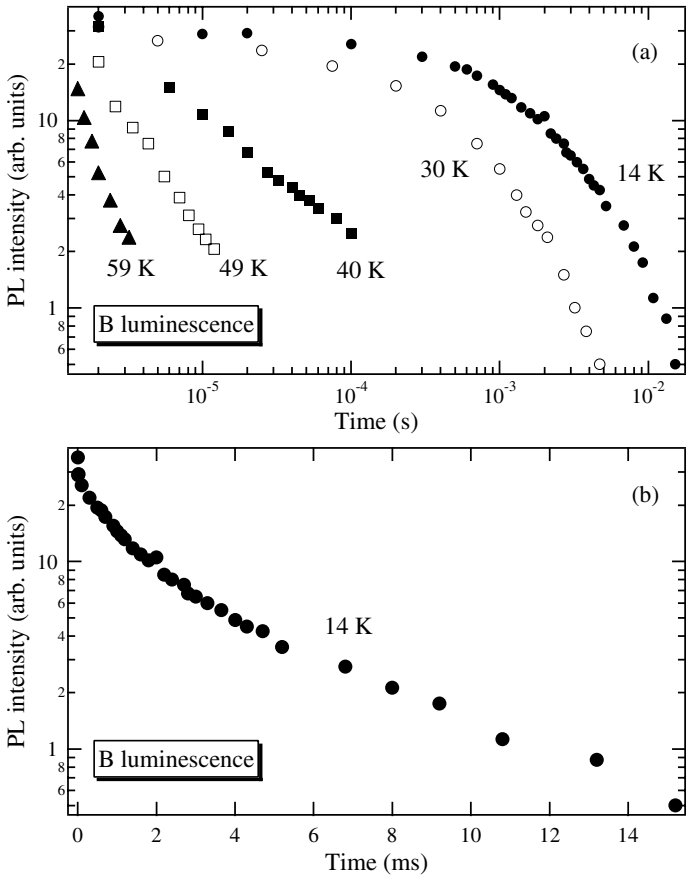

Figure 3. The photoluminescence decay profile of the B luminescence band of $SrTiO_3$: (a) log (PL intensity)–log t plots at different temperatures, (b) log (PL intensity)–t plots at 14 K. The photoluminescence was monitored at 2.45 eV. The 355 nm excitation laser fluence was approximately 0.2 mJ cm^{-2}.

3.3. The photoluminescence decay profile of $SrTiO_3$

We have measured the luminescence decay curves of the B luminescence of the same $SrTiO_3$ single crystal at different temperatures. The luminescence was monitored at an intensity peak wavelength of the B luminescence band. Figure 3(a) shows the PL decay profiles of the B luminescence at different temperatures. The PL intensity is plotted against time on a log–log scale. The decay profile at 14 K is also displayed as a semi-log plot in figure 3(b). It is noted that the crystal displays luminescence for times longer than several tens of milliseconds at 14 K. The profile at 14 K can be well expressed as a three-component exponential decay curve,

$$I(t) = I_1 \exp(-t/\tau_1) + I_2 \exp(-t/\tau_2) + I_3 \exp(-t/\tau_3), \tag{2}$$

with the following parameters:

$I_1 = 15.408$, $\tau_1 = 2.6533 \times 10^{-6}$ s, $I_2 = 11.134$, $\tau_2 = 5.4218 \times 10^{-4}$ s,

$I_3 = 16.909$, $\tau_3 = 2.8396 \times 10^{-3}$ s.

Since the photodetection system used for decay curve measurements has a long time constant (about 1 μs), the shorter lifetime component is not resolved. Therefore, the B luminescence may arise from at least three kinds of luminescence centres.

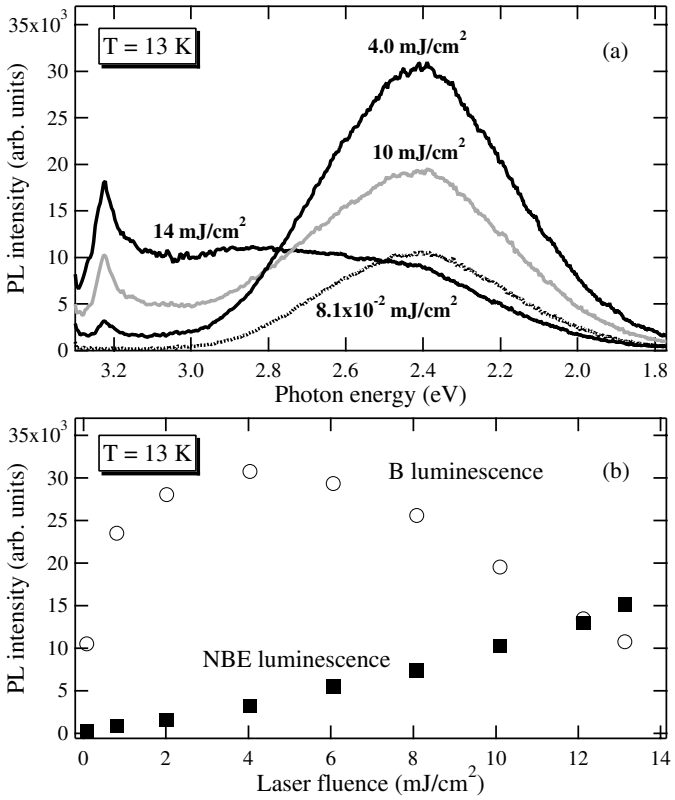

Figure 4. The excitation light intensity dependence of the photoluminescence spectrum of $SrTiO_3$ at 13 K: (a) spectra under intense, medium and weak excitations; (b) the excitation laser fluence dependence of the peak intensities of the near-band-edge luminescence (NBE) band and the B luminescence band. The NBE luminescence peak energy and the B luminescence peak energy are 3.2 and 2.4 eV, respectively.

Alternatively, the same decay data were examined with a power law (t^{-n}). It is found that the curve cannot be uniquely expressed with the t^{-2} law (Tsang and Street 1979); rather it has a t^{-1-2} dependence. Hasegawa *et al* (2000) performed also decay curve fitting with the t^{-n} law, and they inferred suitability of the t^{-2} law for $SrTiO_3$. However, a caution should be required for result to differ greatly by which data points are selected for the curve fitting with the power law.

At the present stage, the observed decay curve should be regarded obediently as an exponential decay curve consisting of different components. The long lifetime component may arise from some radiative transitions of different deeply trapped states. After stopping the laser irradiation of the as-grown and annealed $SrTiO_3$ crystals, we frequently observed faint phosphorescence lasting for several seconds, with the naked eye. Unfortunately, the decay time of such a phosphorescence component ($t \gg 10^{-3}$ s) cannot be determined from the decay curve analysis, because the phosphorescence contribution to the decay curve is too small.

3.4. Photoluminescence spectra of $SrTiO_3$ under intense excitation

We have measured the PL spectra of the same $SrTiO_3$ single crystal at different excitation laser fluences. A typical result is shown in figure 4(a). In figure 4(b), the peak intensities of the

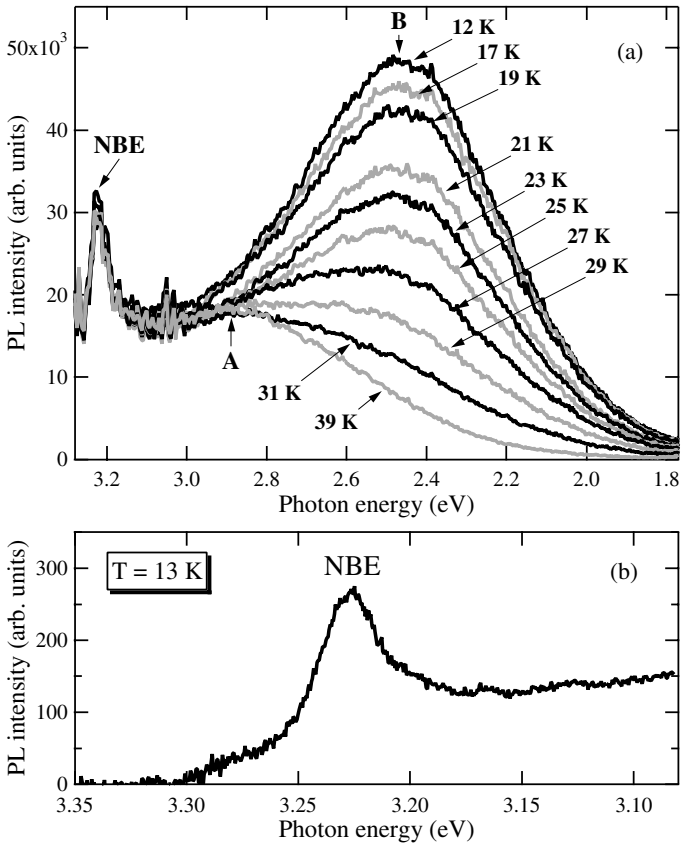

Figure 5. The photoluminescence of $SrTiO_3$ under intense photoexcitation: (a) photoluminescence spectra at different temperatures ($T \leqslant 39$ K). The 355 nm excitation laser fluence was 0.93 mJ cm^{-2}. (b) Near-band-edge (NBE) emission at 13 K. The 355 nm excitation laser fluence was 12 mJ cm^{-2}.

NBE and the B luminescence bands are plotted against laser fluence. Solid squares and hollow circles correspond to the NBE luminescence and the B luminescence, respectively. Under weak excitation, only a B luminescence band is observed. With increasing laser fluence, the B luminescence intensity increases monotonically, and the NBE and A luminescence bands appear. On the laser fluence further increasing up to 4 mJ cm^{-2}, the B luminescence attains a maximum, while both the NBE luminescence and the A luminescence become prominent. On laser fluence exceeding 4 mJ cm^{-2}, the B luminescence intensity begins to decrease monotonically, while both the NBE luminescence band and the A luminescence band continue to grow, degrading the B luminescence band. Incidentally, we have found that the B luminescence intensity maximum appeared at 0.4 mJ cm^{-2} for the sintered $SrTiO_3$ powder compact. This suggests that most of the B luminescence centres are at the specimen surface.

In order to study the NBE, A and B luminescence bands in detail, we have measured the PL spectra at different temperatures under an intense excitation of 0.93 mJ cm^{-2}. This excitation intensity is enough to show up all of the luminescence bands. The results are shown in figures 5(a), 6(a) and (b). We subtract the spectrum measured at 297 K from the spectrum measured at 12 K, in an attempt to extract the B luminescence component. The difference spectrum is given in figure 6(c). By comparing this spectrum with the spectrum (figure 1(a)) observed at the same temperature under a weak photoexcitation, it was found that the spectral

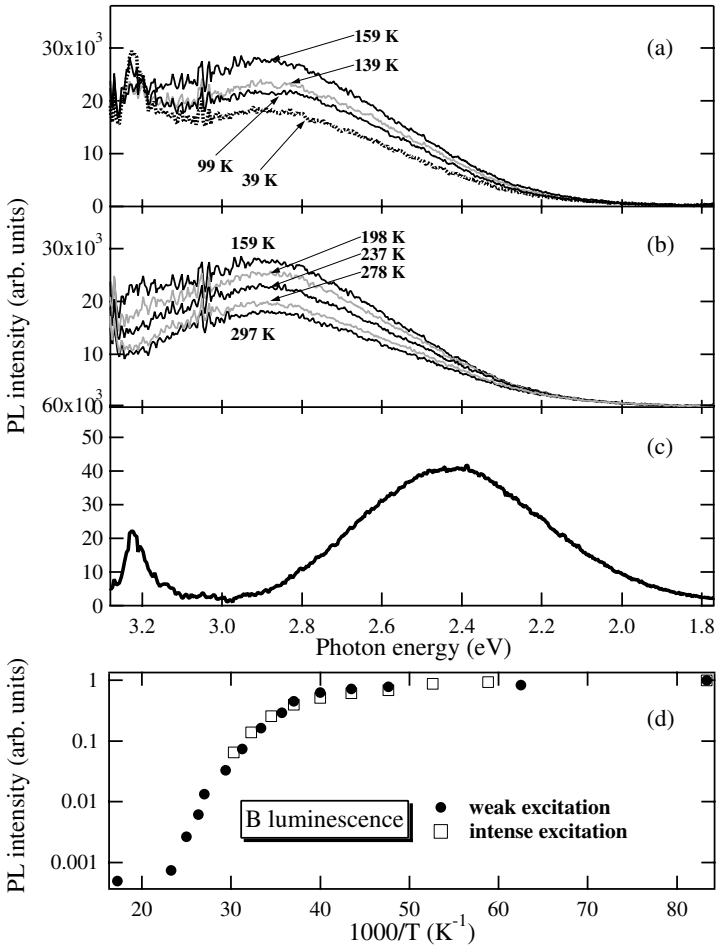

Figure 6. The photoluminescence of $SrTiO_3$ under intense photoexcitation (0.93 mJ cm^{-2}): (a) photoluminescence spectra at different temperatures (39 K $\leqslant T \leqslant$ 159 K); (b) photoluminescence spectra at different temperatures (159 K $\leqslant T \leqslant$ 297 K); (c) the difference spectrum; (d) the temperature dependence of the integrated intensity of the B luminescence band for weak and intense excitations which were 0.079 and 0.93 mJ cm^{-2}, respectively. The spectral integration was performed in a photon region between 2.9 and 1.77 eV.

shape of the B luminescence band is almost independent of the photoexcitation intensity. With temperature increasing up to 39 K, the B luminescence intensity decreases and then it disappears at 39 K, while the NBE and A luminescence intensities are almost constant. With temperature increasing above 39 K, the A luminescence band continues to grow more without changing the spectral shape and then it attains a maximum at 159 K, while the NBE luminescence band becomes weak with the spectral broadening and is merged in the A luminescence band at 198 K. At present, it is not clear why such a phonon-assisted nature of the A luminescence band arose. With the temperature further increasing above 159 K, the A luminescence intensity decreases. This intensity decrease may be due to non-radiative traps. The PL spectrum measured at 297 K was subtracted from that measured at different temperatures, and then the spectral integration was performed over a photon energy range between 2.9 and 1.77 eV. The integrated intensities thus obtained for the B luminescence band are plotted against inverse temperature, as hollow

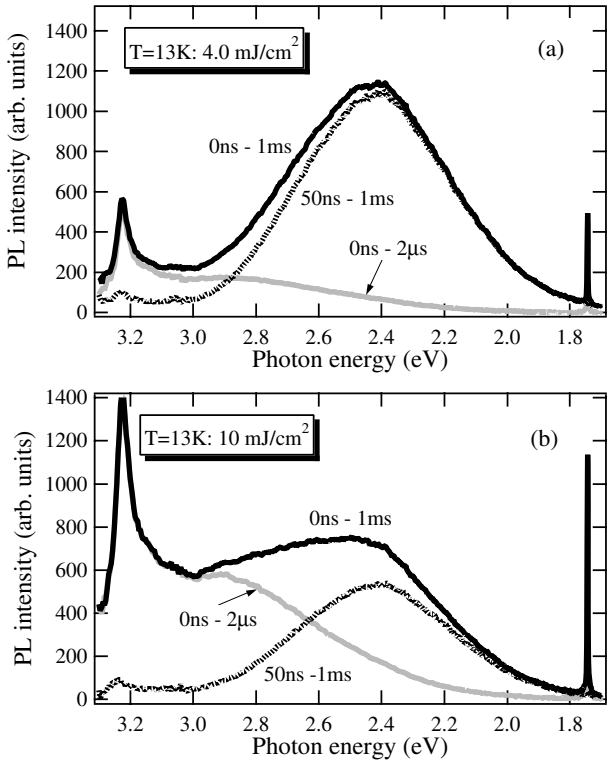

Figure 7. The time-resolved photoluminescence spectra of $SrTiO_3$ at 13 K: (a) laser fluence = 4.0 mJ cm^{-2}; (b) laser fluence = 10 mJ cm^{-2}.

squares, in figure 6(d). The data obtained for weak excitation, which are already shown in figure 1(c), are also plotted as solid circles in this figure.

Under a high laser fluence (12 mJ cm^{-2}), more detailed measurements were performed also on the NBE luminescence and the A luminescence, using a high resolution monochromator. This laser fluence is enough to show up the NBE and A luminescence bands. The result obtained at 13 K is given in figure 5(b). As seen in this figure, the NBE luminescence band is on the rise of the A luminescence band. The NBE luminescence peak is about 77 meV lower in energy than the onset energy of the A band, and it is about 34 meV lower than the PLE edge energy. The NBE luminescence band and the A luminescence have similar temperature and excitation intensity dependences. This suggests that the NBE luminescence and the A luminescence have the same origin.

Most of luminescent metal oxides show some photo-darkening effects under intense photoexcitation. It is found that the PL spectrum and PL intensity of the $SrTiO_3$ single crystal used were almost unchanged, in spite of such intense 355 nm photoexcitation (14 mJ cm^{-2}).

3.5. Time-resolved photoluminescence spectra of $SrTiO_3$

Time-resolved photoluminescence spectra of the same $SrTiO_3$ single crystal have been measured at 13 K under different excitation intensities. To study the time evolutions of all of the luminescence bands, the measurements were performed under intense excitation. The spectra obtained under excitations of 4.0 and 10 mJ cm^{-2} are shown in figures 7(a) and (b), respectively. The measurement times, t_d and t_g, are given by each curve. At the

initial stage of photoexcitation, the laser light pulse is seen at twice the wavelength, 710 nm (=355 nm × 2 = 1.745 eV), of each spectrum, which is common to every grating monochromator. Both the NBE luminescence and the A luminescence disappear rapidly within 50 ns after excitation. Taking account of the parasitic delay, timing jitter times of the apparatus used and the actual laser pulse duration ($\leqslant$10 ns), the lifetimes of the NBE and A luminescences are estimated to be less than 10 ns. The B luminescence band is growing over time between 50 ns and 1 ms, and the spectral shape is almost unchanged with further increase in time. The B luminescence observed between 50 ns and 1 ms is slightly shifted toward the lower energy side of the B luminescence observed between 0 ns and 1 ms, as shown in figure 7(a). The shift is due to the time integration effect on the PL intensity. The measured intensity between t_d and t_g is expressed as follows:

$$I(t) = \sum_j \int_{t_d}^{t_g} \eta_j N_j(t=0) \mathrm{e}^{-t/\tau_j} \, \mathrm{d}t, \tag{3}$$

where η_j, $N_j(t=0)$ and τ_j are the quantum yield, number and lifetime of jth luminescence centre including the extrinsic and intrinsic luminescence centres, respectively. If the luminescence centres responsible for the B luminescence band differ slightly in energy, a small shift may be anticipated, as is in fact observed.

Both the PLE spectrum shown in figure 2 and these time-resolved spectra show clearly that the B luminescence follows the NBE and A luminescence. The long lifetime luminescence, continuing for more than several tens of milliseconds, like the B luminescence, is not peculiar to $SrTiO_3$ but such long lasting luminescence is frequently observed for different metal oxides, for example, ZrO_2 (Fujishiro and Mochizuki 2005). This indicates that the B luminescence cannot necessarily be connected with the nature of the quantum paraelectric state. Such long lifetime luminescence observed for different oxides is thought to arise from accidental recombination of shallowly trapped electrons with distant holes localized around defects. In such a case, the luminescence has slightly different long lifetimes, as seen in figures 3(a) and (b), and the B luminescence spectral shape is almost unchanged with time, as seen in figures 7(a) and (b).

3.6. Reversible photo-induced spectral change in $SrTiO_3$

When the same $SrTiO_3$ single crystal is irradiated with a CW 325 nm laser light at room temperature in an evacuated chamber, the B luminescence intensity is enhanced to about twice. Then, introducing oxygen gas into the specimen chamber, the intense PL state returns to the original weak one under the same laser light irradiation, with increasing irradiation time. Through many successive experiments, it was found that the spectral change is nearly reversible under 325 nm laser light irradiation. After removing the 325 nm laser light irradiation, each PL state is stored for a long time at room temperature under room light, regardless of any changes of atmosphere. A typical example of the photo-induced spectral change obtained is shown in figure 8. The experiments were carried out in the following order: (a) → (b) → (c) → (d). Irradiation times t_{ir} under a given atmosphere and the kind of atmosphere are indicated by each curve. Irradiating under oxygen gas considerably decreases the PL intensity of the specimens. In figure 9, the difference spectrum, curve 7 − curve 8, is shown. The PL spectral change observed for the $SrTiO_3$ single crystal is mainly characterized by an intensity change of the B luminescence band. A slight degradation of the PL intensity is observed, which may be caused by some photo-induced non-radiative centres. The same experiments were carried out by changing the wavelength of the irradiating laser light. No spectral change was observed except for the CW 325 nm laser light. It was found that the speed of the change accelerates on increasing the power density of the activating light.

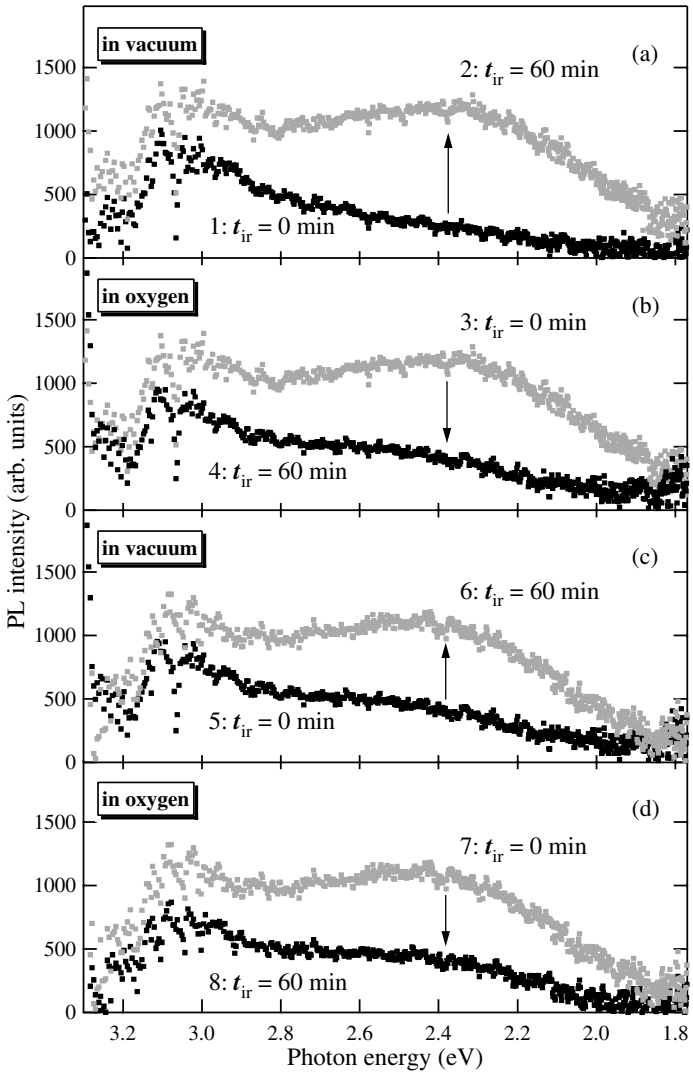

Figure 8. The photo-induced reversible spectral change of $SrTiO_3$ at room temperature: (a) in vacuum, (b) in oxygen gas, (c) in vacuum, (d) in oxygen gas. The experiments were carried out in the following order: (a) → (b) → (c) → (d). Each irradiation was carried out for 60 min under a given atmosphere. Each spectral change is indicated by an arrow. The 325 nm laser fluence was 0.79 W cm^{-2}.

Similar photo-induced spectral change has been observed at different temperatures from 13 K to room temperature. The result obtained at 13 K in vacuum under irradiation with 325 nm laser light is shown in figure 10(a), as a typical result. The t_{ir} in vacuum is indicated by each curve. The peak intensity is plotted against t_{ir} in figure 10(b). With increasing t_{ir}, the intensity increases and then tends to saturate at 90 min. The intensity increase is proportional to t_{ir}^n ($n < 1$). It has been found that the magnitude of the spectral change for 60 min is nearly independent of temperature. After stopping the laser light irradiation, the photoluminescence intensity decreases slightly with increasing time and then reaches a steady state value, which is a photomemory phenomenon.

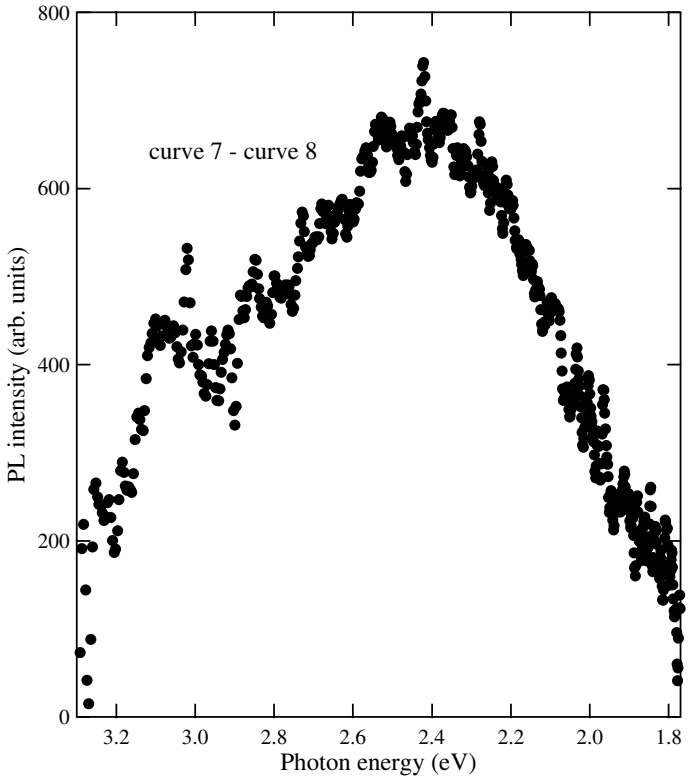

Figure 9. The difference spectrum for curve 7 and curve 8. Curves 7 and 8 are shown in figure 8.

Like for Sm_2O_3 (Mochizuki 2003), Eu_2O_3 (Mochizuki *et al* 2001), anatase TiO_2 (Mochizuki *et al* 2003) and vitreous SiO_2 (Mochizuki and Araki 2003b), the observed spectral transition may arise from photo-induced oxidation and photo-induced reduction.

3.7. Photoluminescence properties of as-grown $SrTiO_3$

In order to elucidate the crystal defect effects on the photoluminescence more directly, we have studied the reversible photo-induced spectral transition for an as-grown Verneuil $SrTiO_3$ crystal at room temperature. The as-grown $SrTiO_3$ crystal is dark blue. The luminescence was excited also with a 325 nm laser line of the He–Cd laser. The result is shown in figure 11(a). Curve 1 is the spectrum of the as-grown crystal. The PL intensity of the as-grown crystal is stronger than several thousands times that of the annealed crystal. The spectrum consists of at least three luminescence bands, at 2.9, 2.3 and 2.2 eV. Curve 2 is the spectrum measured after irradiating in oxygen gas for 60 min. Under 325 nm laser light irradiation in oxygen gas, the PL intensity is decreased considerably. The degradations of the 2.3 and 2.2 eV luminescence bands are especially prominent. The specimen chamber is evacuated again. Curve 3 and curve 4 are the spectra measured at 60 and 480 min after beginning irradiation in vacuum, respectively. Then, oxygen gas was introduced again into the specimen chamber. Curve 5 is the spectrum measured at 840 min after beginning irradiation in oxygen gas. The integrated PL intensity of curve 4 is increased more than 16 times compared with that of curve 5. In figure 11(b), curve 4 is compared after rescaling curve 5 so as to fit to curve 4 at photon energies higher than 2.8 eV. The rescaled curve is shown as curve 5′. Like for the annealed transparent

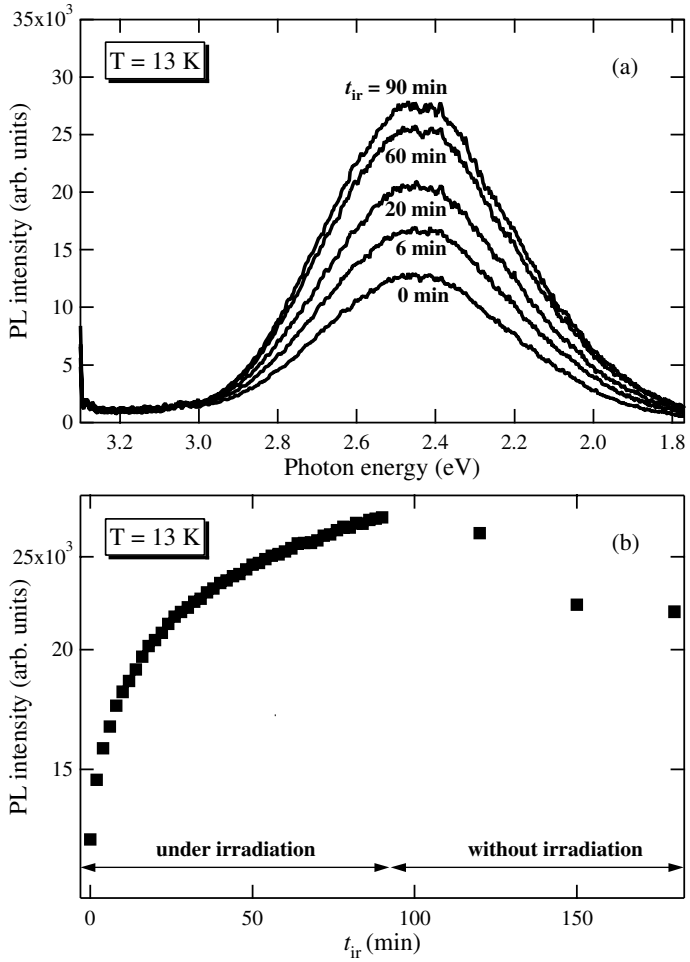

Figure 10. The photo-induced spectral change of $SrTiO_3$ at 13 K in vacuum: (a) photoluminescence spectra for 325 nm laser light irradiation; the irradiation time is indicated by each curve; (b) the irradiation time dependence of the peak intensity of the photoluminescence. The 325 nm laser fluence was 0.79 W cm^{-2}.

$SrTiO_3$ crystal, an A-like luminescence appears in the as-grown crystal: compare curve 5 in figure 11(a) with curve 8 in figure 8(d) and the curve observed at 297 K in figure 6(b). To deduce the information on the B luminescence observed in the annealed $SrTiO_3$ crystal, the difference spectrum (curve 4 − curve 5′) was calculated; it is shown in figure 11(b). We can find a broad luminescence band centred at 2.3 eV, which is slightly shifted to the lower energy side of the B luminescence band of the annealed crystal. It is noted that the B luminescence intensity for the as-grown and the annealed crystals can be varied by 325 nm laser light irradiation in vacuum and in oxygen gas. Since the light penetration depth is very small at 325 nm for $SrTiO_3$ (Zollner *et al* 2000), the observed spectral change of the B luminescence band could be closely related to the change of surface electronic states.

Using the same as-grown crystal, we have measured the photoluminescence spectra at different temperatures under an intense excitation (14 mJ cm^{-2}). As a typical result, the spectrum obtained at 12 K is shown in figure 12. The spectrum obtained at 13 K under the

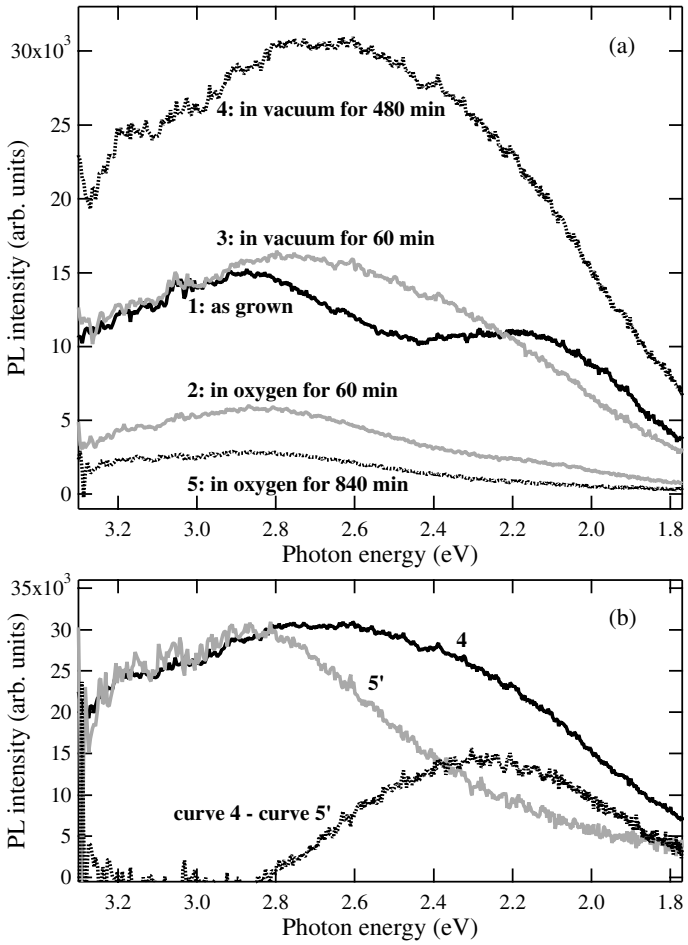

Figure 11. The photo-induced reversible spectral change of as-grown $SrTiO_3$ at room temperature: (a) photo-induced spectral change for replacing specimen atmosphere, (b) comparison of curve 4 with curve 5. The 325 nm laser fluence was 0.79 W cm^{-2}.

same excitation intensity for the annealed crystal is also shown; this was already shown in figure 4(a). The NBE and A luminescence are considerably enhanced in the as-grown crystal. The fine structure and PL intensity of the NBE luminescence band depend on the annealing time. The results suggest that the NBE and A luminescence are assisted by crystal defects.

3.8. Miscellaneous

We have measured the PL spectra of sintered $SrTiO_3$ powder compacts at different temperatures and different laser fluences. The powder specimens show clearly the NBE, A and B luminescences. The NBE and A luminescences remain at room temperature, while the B luminescence disappears above 40 K. Most of the PL properties were very similar to those of single-crystal specimens. Like for other luminescent oxides, the powder compacts were less luminescent and their luminescence decay lifetimes were shorter than those of the single crystals. The main difference between the cases for the powder compacts and the single crystals is that the B luminescence of the powder compacts saturates at lower laser fluence (approximately 0.5 mJ cm^{-2}), while that of the single crystals saturates at 4 mJ cm^{-2}.

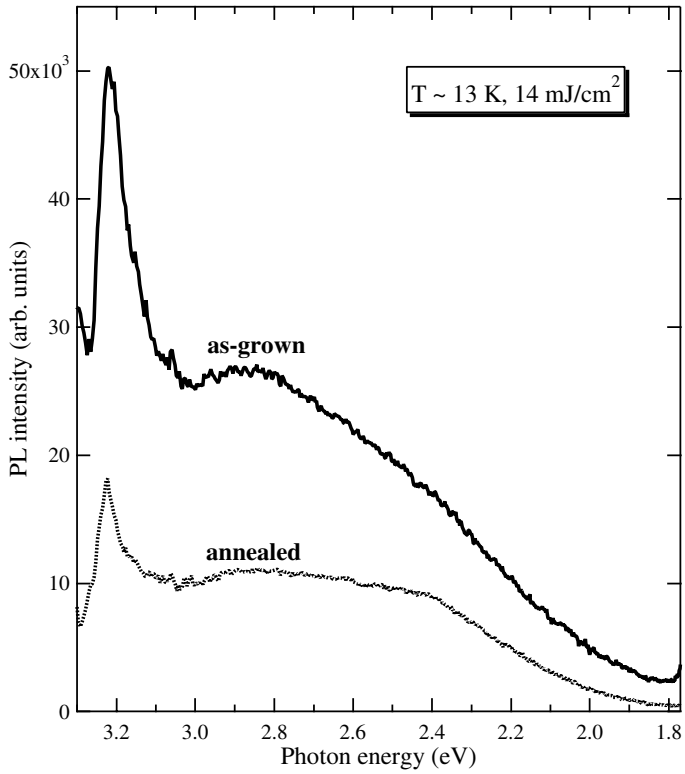

Figure 12. The photoluminescence spectra of the as-grown dark blue and annealed transparent $SrTiO_3$ crystals at about 13 K under an intense 355 nm photoexcitation (laser fluence = 14 mJ cm^{-2}).

4. Discussion

4.1. The reversible photo-induced spectral change

The present experimental results on the reversible photo-induced spectral change of $SrTiO_3$ single crystal may be summarized as follows.

(1) The photo-induced reversible spectral change between weak PL and intense PL can be observed at different temperatures, from 13 K to room temperature. The spectral change takes time. The speed of the spectral change is nearly independent of temperature but it increases with increasing light intensity.
(2) The spectral change tends to saturate at a long light irradiation time (more than 90 min).
(3) The spectral change is induced by changing the specimen atmosphere between oxygen gas and vacuum only under a CW 325 nm laser light. On the other hand, intense pulsed 355 nm laser light (14 mJ cm^{-2}) never induced such spectral change.
(4) After removing the 325 nm laser light irradiation, each PL property persists for a long time even at room temperature under room light, regardless of any changes of atmosphere.

The result (1) indicates that the observed photo-induced spectral changes are purely electronic phenomena and they are not phonon-assisted ones. The result (1) indicates also that the B luminescence is an extrinsic luminescence due to the luminescence centres introduced

by a CW 325 nm laser light. Since the 325 nm (=3.81 eV) laser light never dissociates directly free O_2 molecules, the result (3) indicates that the phenomena arise from the photo-induced associative detachment and photo-induced dissociative adsorption of O_2 molecules near the $SrTiO_3$ surface. In this case, photoexcited $SrTiO_3$ crystal acts as a photocatalyst for decomposing O_2 molecules and also as an oxygen reservoir. The results also summarize how spectral change arises naturally from photo-activated oxidation and reduction.

Although some chemical heterogeneity on the surface has been pointed out for the surfaces of $SrTiO_3$ crystal reduced and oxidized at high temperatures (Szot *et al* 1997, Szot and Speier 1999), we discuss tentatively the observed photo-induced spectral changes at room temperature by regarding the measured $SrTiO_3$ crystal as chemically homogeneous, as follows. The chemical heterogeneity effects will be discussed in the next subsection. The reduction of the $SrTiO_3$ surface under a CW 325 nm laser light in vacuum may be accompanied by the creation of electron-captured oxygen vacancies V''_O, as follows:

$$(O^{2-} \text{ in lattice}) + (\text{CW 325 nm photon}) \rightarrow V''_O + (\text{two electrons}) + \tfrac{1}{2}O_2, \quad (4)$$

where Kröger–Vink notation is used (Kröger and Vink 1956). Using a local spin density approximation plane wave pseudopotential method, Astala and Bristowe (2001) have shown that the doubly positively charged state is the most stable. This is in good agreement with the experimental result that oxygen deficiency in $SrTiO_3$ enhances the electrical conductivity (Jourdan and Adrian 2003) even at low temperatures. This means that most of the electrons around oxygen vacancies are released and, therefore, such oxygen vacancy sites are relatively positively charged. Therefore, the oxygen vacancies tend to trap photo-generated electrons. On the other hand, several authors (Henrich *et al* 1978, Cord and Courths 1985, Kimura *et al* 1995) proposed another type of defect at the $SrTiO_3$ surface as follows:

$$(O^{2-} \text{ in lattice}) + (\text{CW 325 nm photon}) \rightarrow (Ti^{3+}\text{–}V''_O\text{–}Ti^{3+}) \text{ complex} + \tfrac{1}{2}O_2. \quad (5)$$

In the complex, the Ti^{3+} ions act as hole traps, while the vacancy V''_O tends to trap electrons. For $SrTiO_3$ crystal, it is known that electrons determine the transport properties, for example, electrical conductivity and photoconduction, well, while no phenomena related to holes have been observed. This indicates that holes are almost trapped around crystal defects. Incidentally, the high dielectric constant (several tens of thousands) of $SrTiO_3$ crystal suppresses, creating excitons (ex). Toyozawa (1983) proposed three types of symmetry-breaking instability for excitons in the phonon field and, when the electron and the hole have deformation potentials of opposite sign, decomposition into a pair of self-trapped particles occurs. In other words, the instability of an exciton leads to lattice decomposition into an electron centre (an anion vacancy) S_e and a hole centre (an anion interstitial) S_h, if the exciton is formed in the bulk. On surfaces, the hole centre is emitted from the surface, thus leaving only the electron centre. Therefore, such exciton instability may result in oxygen desorption at $SrTiO_3$ surfaces in vacuum and the oxygen vacancies thus produced give rise to B luminescence. Similar desorption has already been discussed for photo-induced breaking of the Si–O bond in a silica (Shluger and Stefanovich 1990). By a quantum chemical calculation, Eglitis *et al* (2004) has demonstrated that the chemical bonding of the perovskite structure contains a considerable covalent component, like the case for silica. It is noted that CW 325 nm laser light is indispensable for spectral change due to the photo-induced oxidation and reduction in $SrTiO_3$. The CW laser fluence in the present experiments was at most 0.8 W cm^{-2}, and therefore any bond-breaking mechanism based on the instability under high density excitation may be excluded from the present discussion. Unlike the case for alkali halides, a single interband excitation never induces the desorption of surface atoms in semiconductors, since the binding energy of atoms is larger than the energy gap. In such photoexcited semiconductor

cases, only atoms around crystal defects at the surfaces can be released (Puchin *et al* 1993, Itoh *et al* 1995, Itoh 1995, Itoh and Stoneham 2000, Song and Williams 1993). Astala and Bristowe (2001) calculated the oxygen vacancy formation energy of about 7 eV, which is approximately twice the bulk energy gap and slightly smaller than twice the CW 325 nm He–Cd laser photon energy, at the TiO_2-terminated (100) surface of $SrTiO_3$. Both the oxygen defects (for example, Ti^{3+}–O''_V–Ti^{3+} and O''_V) inherent to $SrTiO_3$ surfaces and the infinite continuity of the laser light may enable the 325 nm laser photons to release O_2 molecules from the surface. Incidentally, pulsed 355 nm laser light (the pulse width is 4–5 ns), although the photon energy is close to that of the CW 325 nm laser light, never induced spectral change even at 14 mJ cm^{-2}, as a result of (3). Besides the surface defects, a small amount of OH^- ions introduced inevitably during crystal growth by the Verneuil method should also be taken into account for the photo-induced spectral change. Incidentally, Ohmukai *et al* (1999) have observed a 126 nm laser-induced bond breaking and some polycrystalline precipitates on a SiO_2 glass. We could not detect any light scattering due to precipitates on the 325 nm laser light irradiated $SrTiO_3$ crystal.

It has been said that the desorption via such an excited state occurs within 10^{-13} s after laser pulse incidence. However, it is found that a relatively long time (more than 90 min) is taken to complete the spectral change in $SrTiO_3$, as a result of (2). This indicates that the photo-induced oxygen desorption probability is very low at the $SrTiO_3$ surface. The observed saturation tendency with further increasing t_{ir} suggests that photo-induced oxygen defects increase the potential energy of the light irradiated surface. In such a case, equilibrium may be realized in a system composed of matter ($SrTiO_3$ crystal) and a radiation field. It can be assumed that the intensity, coherency and continuity of laser light determine the degree of fluctuation in the system and the dynamics of photo-induced spectral change. Unlike the case for a pulsed laser light, the possibility of successive electronic excitation is not ignored for CW laser light. More detailed experiments with varying frequency, pulse width and duty ratio of a periodic laser light pulse are in progress in our laboratory.

In relation to the UV laser light-induced oxygen defects and white luminescence, it should be noted that the crystals (for example, $LaAlO_3$) grown by light heating methods (for example, the floating zone methods and the arc furnace method) display intense white luminescence. During the growth, the crystals are exposed to intense ultraviolet radiation and, therefore, oxygen defects may be produced, exhibiting oxygen defect-related white luminescence between 3 and 2 eV (Kawabe *et al* 2000).

4.2. The B luminescence band

The present experimental results on the B luminescence of $SrTiO_3$ single crystal may be summarized as having the following features.

(1) The broad B luminescence band is observed well under band-to-band excitation ($>$3.27 eV) in $SrTiO_3$ with a large energy shift (0.80 eV). Although the quantum yield is small, the B luminescence is also observed under a 442 nm (=2.80 eV) laser light excitation.
(2) The B luminescence intensity is considerably increased by photo-induced reduction with 325 nm (=3.81 eV) laser light irradiation in vacuum.
(3) The PL intensity increases with progressive annealing in a reducing atmosphere. The intensity peak energy and spectral width of the B luminescence depend on annealing history.
(4) The B luminescence decay curve consists of at least four components. The phosphorescence component lasts for at least several seconds. It is hard to fit the decay curve uniquely to a power law time (t^{-2}) dependence.

(5) With increasing temperature, the B luminescence intensity decreases, increasing the NBE and A luminescence bands. The B luminescence of both the single crystal and the powder compact disappeared above about 40 K.

(6) With increasing excitation intensity, the B luminescence intensity increases. On further increasing the excitation intensity, the B luminescence intensity attains a maximum at about 4 mJ cm^{-2} and then decreases, increasing the NBE and A luminescence bands. The $SrTiO_3$ power compacts display the B luminescence intensity maximum at approximately 0.5 mJ cm^{-2}.

Feature (1) indicates that the B luminescence arises from several kinds of PL mechanisms. Both feature (2) and the feature (3) indicate that oxygen deficiency is a main cause of B luminescence. Feature (4) indicates that the deviation from stoichiometry creates different types of defect which give different luminescence centres and traps. Most workers have been studying $SrTiO_3$ crystals produced by the Verneuil method. Unfortunately, the compositional deviation of the crystals produced by the Verneuil method is known to be between 10^{-2} and 10^{-4} even for simple transition metal oxides (MnO, CoO, NiO and TiO_2). The chemical purities and isotope separation of the constituent elements (especially strontium and titanium) are not necessarily satisfactory and therefore most of the available $SrTiO_3$ crystals are at most 99.99% pure. These are problems common to many transition metal oxides. Moreover, since a flame consisting of H_2 gas and O_2 gas is used for the Verneuil crystal growth process, some contamination due to OH^- ions may be inevitable. Feature (6) indicates that most of the B luminescence centres are at the specimen surface. Ignoring the above-described chemical impurity effects and noting only the effects due to the deviation from $SrTiO_3$ stoichiometry, we will discuss the results of the PL measurements.

We first discuss the excited states created in $SrTiO_3$ crystal by the third harmonics (355 nm) of the pulsed Nd^{3+}:YAG laser. Unlike CW 325 nm laser light, this 355 nm laser light never induced the spectral changes discussed in the previous subsection. The valence and conduction bands of $SrTiO_3$ mainly consist of the 2p orbits of O^{2-} ions and the 3d orbits of Ti^{4+} ions, respectively. Therefore, the fundamental absorption transfers the electron from the O^{2-} ion to the Ti^{4+} one. After such photoexcitation, some of the photo-produced electrons and holes recombine directly, displaying luminescence via some processes with short lifetime. However, perfect $SrTiO_3$ crystal is an indirect gap semiconductor and, therefore, the PL intensity is so weak that it cannot be measured. Another portion of electrons and holes may be trapped by intrinsic crystal defects at the surface and by the defects related to the deviation from the stoichiometry. In such a case, the PL property differs with the type of defect and also with the sites of defects, as follows.

4.2.1. Oxygen defects at the surface and in the bulk. Stashans and Vargas (2001) have calculated structural and electronic properties of the F centres (two electrons trapped by an oxygen vacancy) in $SrTiO_3$, as have Astala and Bristowe (2001). The results indicate that the wavefunctions of the two extra electrons extend over the titanium atoms closest to the two vacancies and over other nearby atoms, which is the same as the Ti^{3+}–oxygen vacancy complex model proposed by Henrich *et al* (1978), Cord and Courths (1985) and Kimura *et al* (1995). In other words, most of the oxygen vacancies are Ti^{3+}–oxygen vacancy complexes in real $SrTiO_3$ crystal. In this complex, Ti^{3+} ion is one of the candidate hole-trapping centres and the oxygen vacancy is one of the candidate electron-trapping centres. Since electrical conduction due to holes is not observed, most of the photo-generated holes may be deeply trapped at Ti^{3+} sites of the complexes. Unlike such holes, photo-generated electrons may be itinerant, experiencing repeatedly collisions with phonons and trapping by oxygen defects.

When some portions of photo-generated holes and electrons are trapped at distant complexes, a luminescence arises from accidental recombination of shallowly trapped electrons with distant holes localized around the defects, exhibiting a long lasting luminescence. Taking account of the electronic conductivity, both the absorption tail in the OD spectrum shown in the inset (a) of figure 2 and the energy difference of 0.80 eV may guarantee the existence of such deeply trapped hole states and shallowly trapped electron states. The broadness of the OD tail shown in the inset (a) of figure 2 suggests that such hole trap levels and electron trap ones arise from many slightly different defects. Using ultraviolet photoemission spectroscopy (UPS), Henrich *et al* (1978) found that the Fermi level of the fractured $SrTiO_3$ lies about 3 eV above the top of the valence band, which places it within 0.1 eV of the bottom of the conduction band. Also, they observed surface sensitive band gap emission band at energies between the top of the valence band and the Fermi level. These UPS results confirm also the existence of band gap states of the $SrTiO_3$ surface. Thus, the energy difference of 0.8 eV may correspond to the average energy difference between the shallow electron trap levels and the deep hole trap levels in the band gap. Since the observed luminescence decay curve was expressed as a multi-component exponential curve (at most four components), the overlapping between electron and hole wavefunctions is thought to be almost time independent.

With increasing laser fluence, the numbers of photo-generated electrons and holes increase and then the PL intensity may increase. With further increasing laser fluence, photo-generated electrons and holes become diffused more rapidly inside the crystal (bulk), and therefore the PL intensity decreases, as shown in figures 4(a) and (b). This is why the PL intensity maximum appears at 4 mJ cm^{-2}. In other words, this means that most of the defect luminescence centres are at the specimen surface. Since a powder specimen has a large specific surface area, a $SrTiO_3$ powder specimen may exhibit a PL intensity maximum at the laser fluence smaller than that of the single-crystal specimen. This suggestion was certainly confirmed by the present experimental result that the PL intensity maximum of the B luminescence for the powder compacts appeared at laser fluences (approximately 0.5 mJ cm^{-2}) lower than that (4 mJ cm^{-2}) observed for the single crystal. On the other hand, the luminescence arising from the defects in the bulk is thought to saturate at higher laser fluence. In addition to these defect effects, it should be taken into consideration that, at higher laser fluence, the recombination of photo-generated electrons and holes is enhanced and therefore it also reduces the luminescence intensity.

4.2.2. Chemical heterogeneity in the surface region. As stated in the previous sections, a colourless transparent $SrTiO_3$ single crystal is obtained by thermally annealing dark blue as-grown crystal at high temperature under an appropriate reducing atmosphere. Although it is colourless and transparent, the crystal is thought to be affected to some extent by such annealing treatment. In particular, it has been reported that the surfaces of reduced and oxidized $SrTiO_3$ contain not only the above-described oxygen defects but also Ruddlesden–Popper phases (Ruddlesden and Popper 1957, 1958). The combination of x-ray diffraction analysis with surface sensitive techniques has revealed a chemical inhomogeneity in the surface region of single crystals of $SrTiO_3$ prepared under low and high partial pressures of oxygen at elevated temperatures (Szot *et al* 1997). A solid state reaction leads to the formation of a multilayer-type structure. For oxidized crystals, they observed SrO-rich Ruddlesden–Popper phases at the surface and Magnelli phases of Ti in deeper layers of the surface region. The order of the layered structure is reversed for the reduced crystals, with Ti oxides of different oxidation levels at the surface and Ruddlesden–Popper phases in lower parts of the surface region. Measurements by atomic force microscopy are also reported for the (100) and (110) surfaces of $SrTiO_3$ single crystals prepared with different oxidizing and reducing conditions at elevated temperatures (1073–1273 K) (Szot and Speier 1999). The morphology of the surfaces turns

out to be drastically altered for both oxidized and reduced crystals in comparison with the original stoichiometric surfaces. The observed changes on the surface of $SrTiO_3$ due to the applied extensive thermal treatment cannot be explained by the formation of point defects, relaxation of the uppermost surface layer, rumpling or reconstruction due to vacancy ordering. Instead, the results have to be interpreted in terms of segregation processes and solid state reactions at elevated temperatures, which cause the formation of new chemical phases on the surface and in the region underneath. On the surface of oxygen-annealed $SrTiO_3$, this leads to the growth of steps perpendicular to the surface with step heights larger than the unit cell of the perovskite structure. Crystals prepared above 1173 K are shown to exhibit a step height of 1.18 nm which is attributed to the formation of a Ruddlesden–Popper phase $SrO^*(SrTiO_3)_n$ with $n = 1$ on the surface. In the case of reduced crystals, the topographic changes on the surface are caused by the formation of Ti-rich phases such as TiO and Ti_2O on the surface above 1173 K. The complex interplay of the processes at the surface for different temperatures, in particular its dependence on the details of the heat treatment, is discussed. The induced chemical heterogeneity of the surface and in the near-surface region is interpreted in terms of a kinetic demixing.

Certainly, as shown in figures 11(a) and (b), we observed complicated spectral change under CW 325 nm laser light irradiation in oxygen gas and vacuum for the as-grown $SrTiO_3$ crystal, which cannot be explained entirely by the simple oxygen point defect model. Since the as-grown crystal has a higher light absorption coefficient than the colourless annealed crystal, the observed spectral change may be more affected by the surface crystal defects, including the chemical heterogeneity (for example, Ruddlesden–Popper phases) in the surface region.

Bearing these chemical heterogeneities in mind, we have measured the PL properties of the as-grown crystal at different stages of annealing in a reducing atmosphere and also measured those of a colourless transparent stepped TiO_2-terminated $SrTiO_3$ crystal whose step height is 0.4 nm. The detailed results will be reported in a separate paper (Mochizuki and Fujishiro 2005). The results are summarized as follows. The low temperature PL spectral structures of these crystals are almost the same as those of the colourless transparent (100) faced crystal, apart from the PL intensity. However, with progressive annealing, the dark blue colour becomes weak, the intensities of the NBE, A and B luminescence bands decrease and the lower energy tail of the PLE for the B luminescence becomes weak. Moreover, the excitation laser fluence giving the B luminescence intensity maximum (we call this fluence F_{max}) increases with progressive annealing. Like that for the as-grown crystals, the F_{max} for the stepped TiO_2-terminated $SrTiO_3$ crystal decreases considerably in comparison with the F_{max} for the colourless transparent $SrTiO_3$ crystal. The observed change in F_{max} may be due to the change in the probability of electron–hole pairs with surface defects arising from chemical heterogeneity. We have observed also at least five broad optical absorption bands at about 2.9 eV, about 2.4 eV, about 2.1, 1.6 eV and about 0.9 eV for the as-grown crystal at different annealing stages. The dark blue colour of the as-grown crystal is attributed to this spectral structure in which the blue colour wavelength range is a spectral window. With progressive annealing, these absorptions decrease in intensity. These optical absorption bands may be assigned to oxygen defects and some chemical heterogeneity (Szot *et al* 2002). The broad OD tail observed for the colourless transparent crystal is thought to be a trace from these absorption bands; see the inset (a) of figure 2 in the present paper and the figure 4 in the paper reported by Szot *et al* (2002). In order to clarify the optical excitation in the Ruddlesden–Popper phases, more detailed surface sensitive spectroscopic measurements (for example, reflectivity and PL measurements under total reflection conditions) and morphological and structural measurements for the as-grown crystals at different stages of annealing are now in progress in our laboratory.

Taking account of these studies on different kinds of defects in the real $SrTiO_3$ crystal grown by the Verneuil method, we thus assign the B luminescence band to the radiative decay of the crystal defect-related excited electronic states. Alternatively, it is theoretically assumed that a long lasting luminescence arises also from some forbidden transition, and therefore we cannot ignore the contribution from de-excitation of some triplet excited states. Previously, many workers have discussed the long lasting B luminescence on the basis of intrinsic self-trapped electronic (exciton) states, ignoring the effects of crystal defects. As discussed above, it should now be apparent that defect effects are important for such self-trapping, and more careful consideration of them is necessary for deducing the intrinsic nature of $SrTiO_3$ from experimental data.

4.3. The NBE and A luminescence bands

Both the NBE luminescence and the A band luminescence have the following features:

(α) Both luminescences become prominent under higher excitation intensity and do not saturate under intense excitation (14 mJ cm^{-2}). They grow to the detriment of the B luminescence with increasing excitation intensity.

(β) With increasing temperature, both luminescences become prominent to the detriment of the B luminescence and survive even at high temperatures. The spectral structures of the two luminescences at room temperature are hardly changed by changing the excitation laser wavelength from 325 to 355 nm.

(γ) Both luminescences are considerably enhanced in the as-grown crystal.

(δ) Both luminescences appear near the band edge energy region and have very short decay times ($\ll$50 ns).

Feature (α) indicates that both the NBE luminescence and the A luminescence arise not from a small number of impurities and crystal defects, but from numerous luminescent species. Feature (β) indicates also that the NBE and A luminescence centres are stable at high temperatures, without any thermal exhaustion. This feature indicates that both luminescences are assisted by phonons. Feature (γ) indicates that the luminescence is emission assisted by crystal defects. Together with the features (α), (β) and (γ), feature (δ) suggests that the two luminescences arise from the same origin and are assignable to some kind of electron–hole recombination emission assisted by crystal defects and phonons.

We discuss these luminescence bands from two different viewpoints as follows. The frequency shift of the NBE luminescence band from incident 355 nm laser light is about 2207 cm^{-1}. This is too large for assigning this band to non-resonant Raman scattering (Sirenko *et al* 1999). Non-resonant Raman scattering in a cubic centrally symmetric crystal is forbidden by the odd parity of the optical phonons of F_{1u} symmetry, and therefore cubic $SrTiO_3$ crystal displays weak broad Raman spectrum due to second-order Raman scattering in which two phonons are involved in the scattering process. In the tetragonal phase below 105 K, the phonon mode splits into two Raman-inactive modes of A_{2u} and E_u symmetry. When crystal defects (impurities and vacancies) are introduced (Kleemann *et al* 1997) or when uniaxial external fields (electric field and stress) are applied (Akimov *et al* 2000, Worlock and Fleury 1967), these first-order Raman-inactive modes can be observed only below 1000 cm^{-1}. They cannot explain the observed large frequency shift (about 2207 cm^{-1}) of the NBE luminescence. On the other hand, since the photon energy of the incident 355 nm (=3.49 eV) laser light is close to the reported direct gap energy (=3.47 eV; Capizzi and Frova 1970) and the observed PLE edge energy (=3.26 eV), we have to take account of the resonant Raman scattering effects. In this case, the Raman spectrum may display several resonance lines due to the scattering by different phonons near the direct and indirect gap energies, together with other critical points of

the interband transitions (Cardona 1982). As is well known theoretically, the resonant Raman process involves effects due to different intraband and interband scatterings, which display a broad resonance. If we regard the NBE and A luminescences as a result of such resonance Raman scattering, the phonon energy may be estimated from the difference between the indirect band edge energy (PLE edge energy = 3.26 eV) and the NBE luminescence peak energy (= 3.23 eV): the estimated value is 30 meV (=242 cm^{-1}), which is comparable to the transverse optical phonon frequency. Further discussion on the basis of such resonant Raman scattering requires measurements at different incident wavelengths and information about the chemical heterogeneity and defect effects on the Raman scattering.

Next, we discuss the NBE and A luminescence bands as follows. The NBE and the A luminescences were seen even at high temperatures, and they do not exhibit any PL intensity saturation under higher excitation intensity. Although an explanation with so-called donor–acceptor pair (D–A pair) luminescence due to unwanted impurities is frequently given for the intense broad luminescence band with intensity peaks for semiconductors, such D–A pair luminescence related to inevitable impurities may saturate under intense photoexcitation because of the limited numbers of donors and acceptors. Moreover, the luminescence intensity decreases remarkably with increasing temperature. Moreover, such a luminescence spectrum for D–A pairs related to unwanted impurities is thought to be time resolved, since separations between donors and acceptors differ. Therefore, we can ignore the contribution from the impurity-related D–A pair luminescence in the present discussion.

Now, we note that, since ideal $SrTiO_3$ crystal has an indirect gap, the crystal does not exhibit directly any intense intrinsic edge emission. When crystal defects giving shallow levels are introduced at the surface, a PL process becomes possible. We note moreover that the NBE and A luminescence bands are observed even at high temperatures under intense excitation and that these luminescence bands are considerably enhanced for the as-grown crystal, as seen in figure 12. Therefore, we regard the observed NBE and A luminescence bands as defect-induced edge luminescence (emission) ones, in which processes different phonons are created. The NBE luminescence band having a shift of 242 cm^{-1} may be assigned to one of the optical phonon lines. A zero-phonon line anticipated at 3.26 eV is thought to be buried in the rise of the A luminescence band. The full width at half-maximum (FWHM) of the NBE band is about 30 meV. Such a large FWHM is thought be due to some structural inhomogeneity and damping. It is noted that the A luminescence displays an almost smooth and continuous band. This suggests that, besides optical phonons, many longitudinal and transverse acoustic phonons are created during electron–hole recombination.

5. Conclusion and remarks

In summary, we have investigated the reversible PL spectral change and the basic PL properties of as-grown and annealed $SrTiO_3$ single crystals, together with sintered $SrTiO_3$ powder compacts, at different temperatures from 12 K to room temperature. Three luminescence bands, NBE, A and B, are observed around 3.2, 2.9 and 2.4 eV, respectively. The B luminescence intensity changes with CW 325 nm laser light irradiation in oxygen gas and a vacuum. This result indicates that the B luminescence is not intrinsic luminescence but results from radiative decays of the oxygen defect-related photoexcited states and the chemical heterogeneity in the surface region. The NBE and A luminescences remain at high temperatures and they do not saturate under high density photoexcitation (at least 14 mJ cm^{-2}). Their PL properties (temperature dependence, excitation intensity dependence and time dependence) suggest that the NBE luminescence and the A luminescence arise from the same origin. Taking account of crystal defects, the NBE and the A luminescence are discussed qualitatively from two

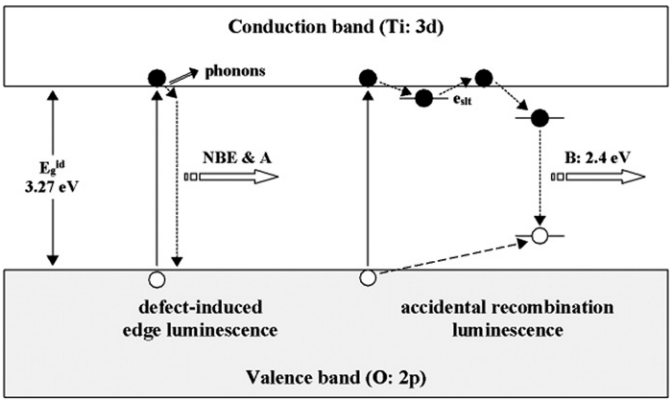

Figure 13. Some of the possible photoluminescence processes in real $SrTiO_3$ crystal. The solid arrow and dotted arrow indicate the optical absorption and radiative transition, respectively. The hollow arrow and double arrow indicate the luminescence and phonon creation, respectively. E_g^{id} and e_{slt} denote the indirect gap energy and the shallow electron trap level, respectively. For the accidental recombination model, the short dotted arrow and the broken arrow indicate the electron trapping and hole trapping, respectively.

different viewpoints: defect-induced resonant Raman scattering and defect-induced electron–hole recombination luminescence accompanying creation of phonons. At present, we do not exclude the possibility of other explanations. Although it constitutes a difficult problem, the surface defect structure and the defect-induced effects on the resonant Raman scattering and the edge luminescence (edge emission) should be considered in more detail.

A tentative energy diagram showing some of the possible PL processes in real $SrTiO_3$ crystal containing crystal defects is given in figure 13. The solid arrow and dotted arrow indicate the optical absorption and radiative transition, respectively. The hollow arrow and double arrow indicate the luminescence and phonon creation, respectively. e_{slt} indicates a shallow electron trap. For the accidental recombination model, the short dotted arrow and the broken arrow indicate the electron trapping and hole trapping, respectively.

Incidentally, Pontes *et al* (2002) found intense PL in amorphous $SrTiO_3$ at room temperature under 488 nm (=2.539 eV) radiation from an Ar^+ ion laser. They ascribed the PL excited by low energy photons to non-bridging oxygen defects, for example, TiO_5. Study of how the non-bridging oxygen defects enhance the PL in amorphous $SrTiO_3$ is also helpful in discussing the PL properties of real $SrTiO_3$ crystal surfaces.

Finally, more detailed PL measurements, with excitation laser wavelengths varying around the band gap energies, on different annealing stages of $SrTiO_3$ crystals are now progress in our laboratory. Experiments with chopped laser light with different duty ratios on the reversible photo-induced spectral change are also now in progress. The results will be reported in a separate paper.

Acknowledgments

This work was partially supported by a Grant-in-Aid for Scientific Research from the Ministry of Education, Science, Sports, Culture and Technology, Japan. This work was supported by an Interdisciplinary General Joint Research Grant for Nihon University. This work was also partially supported by a Project Research Grant from The Institute of Information Sciences of the College of Humanities and Sciences (Nihon University) and by a Cooperative Research Grant from The Institute of Natural Sciences (Nihon University).

References

Akimov I A, Sirenko A A, Clark A M, Hao J-H and Xi X X 2000 *Phys. Rev. Lett.* **84** 4625
Astala R and Bristowe P D 2001 *Modelling Simul. Mater. Sci. Eng.* **9** 415
Blazey K W 1971 *Phys. Rev. Lett.* **27** 146
Capizzi M and Frova A 1970 *Phys. Rev. Lett.* **25** 1298
Capizzi M, Frova A and Dunn D 1972 *Solid State Commun.* **10** 1165
Cardona M 1965 *Phys. Rev.* **140** A651
Cardona M 1982 *Light Scattering in Solids II* (Berlin: Springer)
Cohen M I and Blunt R F 1968 *Phys. Rev.* **168** 929
Cord B and Courths R 1985 *Surf. Sci.* **162** 34
Eglitis R I, Kotomin E A and Borstel G 2004 *Comput. Mater. Sci.* **30** 376
Fujishiro F and Mochizuki S 2005 in preparation
Grabner L 1969 *Phys. Rev.* **177** 1315
Hasegawa T, Mouri S, Yamada Y and Tanaka K 2003 *J. Phys. Soc. Japan* **72** 41
Hasegawa T, Shirai M and Tanaka K 2000 *J. Lumin.* **87–89** 1217
Henrich V E, Dresselhaus G and Zeiger H J 1978 *Phys. Rev.* B **17** 4908
Itoh N 1995 *Butsuri* **50** 704 (in Japanese)
Itoh N, Kansaki J, Okano A and Nakai Y 1995 *Annu. Rev. Mater. Sci.* **25** 97
Itoh N and Stoneham A M 2000 *Material Modification by Electronic Excitation* (Cambridge: Cambridge University Press)
Jourdan M and Adrian H 2003 *Physica* C **388/389** 509
Katsu H, Tanaka H and Kawai T 2001 *J. Appl. Phys.* **90** 4578
Kawabe Y, Yamanaka A, Hanamura E, Kimura T, Takiguchi Y, Kan H and Tokura Y 2000 *J. Appl. Phys.* **88** 1175
Kimura S, Yamauchi J and Tsukada M 1995 *Phys. Rev.* B **51** 11049
Kleemann W, Albertini A, Kuss M and Linder R 1997 *Ferroelectrics* **203** 57
Kröger F A and Vink H J 1956 *Solid State Physics* vol 3 (New York: Academic) p 307
Mochizuki S 2003 *Physica* B **340–342** 944
Mochizuki S and Araki H 2003a *Physica* B **340–342** 913
Mochizuki S and Araki H 2003b *Physica* B **340–342** 969
Mochizuki S, Nakanishi T, Suzuki Y and Ishi K 2001 *Appl. Phys. Lett.* **79** 3785
Mochizuki S, Shimizu T and Fujishiro F 2003 *Physica* B **340–342** 956
Mochizuki S and Fujishiro F 2005 in preparation
Müller K A, Berlinger W and Tosatti E 1991 *Z. Phys.* B **84** 277
Müller K A and Burkard H 1979 *Phys. Rev.* B **19** 3593
Nasu K 2004 *Rep. Prog. Phys.* **67** 1607
Ohmukai M, Takigawa Y and Kurosawa K 1999 *Appl. Surf. Sci.* **137** 78
Pontes F M, Longo E, Leite E R, Lee E J H, Varela J A, Pizani P S, Campos C E M, Lanciotti F, Mastellaro V and Pinheiro C D 2002 *Mater. Chem. Phys.* **77** 598
Puchin V E, Shluger A L and Itoh N 1993 *Phys. Rev.* B **47** 10760
Ruddlesden S N and Popper P 1957 *Acta Crystallogr.* **10** 538
Ruddlesden S N and Popper P 1958 *Acta Crystallogr.* **11** 54
Shluger A and Stefanovich E 1990 *Phys. Rev.* B **42** 9664
Sirenko A A, Akimov I A, Fox J R, Clark A M, Li H C, Si W and Xi X X 1999 *Phys. Rev. Lett.* **82** 4500
Song K S and Williams R T 1993 *Self-Trapped Excitons* (Berlin: Springer)
Stashans A and Vargas F 2001 *Mater. Lett.* **50** 145
Szot K and Speier W 1999 *Phys. Rev.* B **60** 5909
Szot K, Speier W, Carius R, Zastrow U and Beyer W 2002 *Phys. Rev. Lett.* **88** 075508-1
Szot K, Speier W, Herion J and Freiburg C 1997 *Appl. Phys.* A **64** 55
Takesada M, Yagi T, Itoh M and Koshihara S 2003 *J. Phys. Soc. Japan* **72** 37
Toyozawa Y 1983 *Physica* B **112 & 118** 23
Tsang C and Street R A 1979 *Phys. Rev.* B **19** 3027
Worlock J M and Fleury P A 1967 *Phys. Rev. Lett.* **19** 1176
Zollner S, Demkov A A, Liu R, Fejes P L, Gregory R B, Alluri P, Curless J A, Yu Z, Ramdani J, Droopad R, Tiwald T E, Hilfiker J N and Woollam J A 2000 *J. Vac. Sci. Technol.* B **18** 2242

Available online at www.sciencedirect.com
SCIENCE DIRECT®
Polyhedron 23 (2004) 1605–1611
POLYHEDRON
www.elsevier.com/locate/poly

Salts of tetrachloroauric acid with pyridine *N*-oxide having various base/acid ratios of 1/1, 4/3, 3/2 and 2/1: crystal structures, ^{35}Cl NQR and phase transitions

Tetsuo Asaji [a,*], Eigo Akiyama [a], Fukue Tajima [b], Kazuo Eda [b], Masao Hashimoto [b], Yoshihiro Furukawa [c]

[a] *Department of Chemistry, College of Humanities and Sciences, Nihon University, Sakurajosui, Setagaya-ku, 3-25-40, Tokyo 156-8550, Japan*
[b] *Department of Chemistry, Faculty of Science, Kobe University, Nada-ku, Kobe 657-8501, Japan*
[c] *Department of Science Education, Graduate School of Education, Hiroshima University, Kagamiyama, Higashi-Hiroshima 739-8524, Japan*

Received 27 January 2004; accepted 24 March 2004
Available online 30 April 2004

Abstract

We determined crystal structures of $[(PyO)D][AuCl_4]$, $[(PyO)_4D_3][AuCl_4]_3$ and $[(PyO)_3D_2][AuCl_4]_2$ (PyO: pyridine *N*-oxide) at room temperature (1/1, 4/3 and 3/2 D-salts, respectively). The powder X-ray diffraction patterns of these salts (D-salts) were identical to those of the corresponding ones having normal hydrogen (H-salts) unlike the case of $[(PyO)_2D/H][AuCl_4]$. In the crystals of the 4/3 and 3/2 salts, there exist not only the monomer-type protonic adducts of PyO, but also dimer-type adducts in which two PyO units are bridged by a proton. A few types of aggregation of $AuCl_4$ units (sheet and ribbons) were found in these crystals. The variety in the aggregation motif of the anion and that in the structure of the cation seem to be related to the presence of the various salts having several base-to-acid ratios. The isotope effect on the preparation of the salts is discussed. ^{35}Cl NQR and phase transitions of these compounds are also reported.

Keywords: Crystal structure; Phase transition; Isotope effect; Hydrogen bond; NQR; Tetrachloroaurate(III)

1. Introduction

It is known that pyridine *N*-oxide (PyO) forms a monomeric hydrogen adduct $[(PyO)H]^+$ in its salts. Examples can be seen in several compounds [1,2]. In addition, PyO has a tendency to form a monovalent diadduct type cation $[(PyO)_2H]^+$, in which the two PyO units are bridged by a proton. This type of cation exists, for instance, in $[(PyO)_2H][AuCl_4]$ [3] and other compounds [4,5]. There is the possibility that both types of cations are incorporated in a salt. In fact, we prepared a compound $[(PyO)_3H_2][AuCl_4]_2$ having a PyO/$HAuCl_4$ ratio of 3/2, which suggests the coexistence of $[(PyO)H]^+$ and $[(PyO)_2H]^+$ in the crystal [4]. Furthermore, we could separate a compound $[(PyO)_4H_3][AuCl_4]_3$ with another PyO/$HAuCl_4$ ratio of 4/3 by controlling the PyO/$HAuCl_4$ ratio in the solution. These findings led us to determine the crystal structures of these compounds to confirm their composition and the structure of the cation.

As a structural change induced by substitution of D for H atom, we recently reported that the structure of the cation $[(PyO)_2D]^+$ in $[(PyO)_2D][AuCl_4]$ and its whole crystal structure itself were dramatically different from those of $[(PyO)_2H][AuCl_4]$ [4]. Since we have been interested in this phenomenon induced by substitution of a hydrogen isotope, a part of this work was devoted to examine the effect of deuteration on the structures of the various salts mentioned above. We also investigated the stability of $[(PyO)_2D][AuCl_4]$ and $[(PyO)_2H][AuCl_4]$ to show that both of them are in stable phases.

The results of DTA/DSC as well as preliminary ^{35}Cl NQR measurements of $[(PyO)_3(H/D)_2][AuCl_4]_2$, $[(PyO)_4H_3][AuCl_4]_3$ and $[(PyO)D][AuCl_4]$ are reported.

* Corresponding author. Tel./fax: +81-3-5317-9739.
E-mail address: asaji@chs.nihon-u.ac.jp (T. Asaji).

0277-5387/$ - see front matter © 2004 Elsevier Ltd. All rights reserved.
doi:10.1016/j.poly.2004.03.022

We briefly discuss the phase transitions in $[(PyO)_3(H/D)_2][AuCl_4]_2$ and $[(PyO)D][AuCl_4]$.

2. Experimental

2.1. Synthesis

The various complex salts $[(PyO)_m(H/D)_n][AuCl_4]_n$ ($m/n = 1/1$, 4/3, 3/2, 2/1) between PyO and $(H/D)AuCl_4$ were prepared by slow evaporation of aqueous solutions (H_2O or D_2O) containing PyO and $(H/D)AuCl_4$ in the molar ratio shown in Table 1. In the text, following abbreviations will be used; $[(PyO)_m(H/D)_n][AuCl_4]_n$: m/n (H/D)-salt. The 4/3 H-salt was not prepared. $DAuCl_4$ was obtained by dissolving Au_2O_3 in a DCl solution in D_2O. Elemental analyses were carried out at the Center for Organic Elemental Microanalysis, Kyoto University. The results of the analyses have already been reported in [4] for $[(PyO)_2D][AuCl_4]$, $[(PyO)_3H_2][AuCl_4]_2$, $[(PyO)H][AuCl_4]$ and $[(PyO)D][AuCl_4]$. In the following, the results of $[(PyO)_3H_2][AuCl_4]_2$, $[(PyO)_3D_2][AuCl_4]_2$ and $[(PyO)_4D_3][AuCl_4]_3$ are reported. *Anal.* Calc. for $[(PyO)_3H_2][AuCl_4]_2$: C, 18.7; H, 1.8; Cl, 29.4; N, 4.4; O, 5.0. Found: C, 18.4; H, 1.8; Cl, 29.2; N, 4.2; O, 4.8%. *Anal.* Calc. for $[(PyO)_3D_2][AuCl_4]_2$: C, 18.6; H/D, 2.0; Cl, 29.3; N, 4.4; O, 5.0. Found: C, 18.5; H/D, 1.9; Cl, 29.4; N, 4.3; O, 4.8%. *Anal.* Calc. for $[(PyO)_4D_3][AuCl_4]_3$: C, 17.1; H/D, 1.9; Cl, 30.3; N, 4.0; O, 4.6. Found: C, 17.2; H/D, 2.0; Cl, 30.4; N, 4.0; O, 4.3%. The extent of the deuteration has been estimated by use of ^2H NMR measurements of the aqueous solution to be H/D = approximately 15/85 for $[(PyO)_3D_2][AuCl_4]_2$, $[(PyO)_4D_3][AuCl_4]_3$ and $[(PyO)D][AuCl_4]$.

The 3/2 (H/D)-salts and the 4/3 D-salt showed an extraordinarily wide temperature range of melting (see Table 1). This is probably due to gradual decompositions of the salts.

2.2. Physical measurements

X-ray powder patterns were recorded by the use of a Rigaku RINT 2100S diffractometer with Cu Kα radiation. Silicon powder was used as an internal standard of the diffraction angle. DTA and DSC measurements were performed using a home-made apparatus and DSC3100S (Bruker AXS), respectively. For the ^2H NMR measurements of the solution, a JEOL JNM-EX270 NMR spectrometer was employed. The density of the crystal at room temperature was determined by a floating method, using a mixture of *o*-xylene and bromoform or benzene and methylene iodide. A pulsed spectrometer based on the Matec gated amplifier 515A was used for the ^{35}Cl nuclear quadrupole resonance (NQR) measurements. The temperature of the NQR sample was controlled in the range 4.2–300 K using an electronic controller (LakeShore 331) and measured with an accuracy of ±0.5 K by use of a gold +0.07% iron versus chromel thermocouple. Solid-state ^1H NMR experiments were carried out by use of a standard pulsed NMR spectrometer at the Larmor frequency of 42.5 MHz.

2.3. Crystallography

A SMART 1000/CCD diffractometer (Bruker) was employed for the diffraction measurements using graphite monochromated Mo Kα radiation. Data collections were carried out at room temperature. Crystal data and the details of the experiments and refinements are given for the 3/2 D-salt, 4/3 D-salt and 1/1 D-salt in Table 2.

The structures were solved by direct methods and refined by full-matrix least-squares calculations based on F_o^2 with absorption correction (SADABS) using SHELXL-97 [6]. Non-hydrogen atoms of each salt were included in the least-squares calculations with anisotropic displacement parameters.

It was found that the monomeric adduct $[(PyO)D]^+$ in the 1/1 D-salt had a mirror plane, being perpendicular to the ring plane and containing the N–O bond, and a C_2-axis, being normal to the mirror plane and passing through the center of the ring (C_{2h} symmetry) indicating an orientational disorder, in which each of the O, N and relevant C (C1) atoms was located on two sites with an equal population. The positions of the N and C1 atoms

Table 1
The complex salts $[(PyO)_m(H/D)_n][AuCl_4]_n$ ($m/n = 1/1$, 4/3, 3/2, 2/1) between PyO and $(H/D)AuCl_4$ obtained from aqueous solutions (H_2O or D_2O)

Chemical formula	Melting point (K)	Molar ratio in crystal PyO:(H/D)$AuCl_4$	Molar ratio in solution PyO:(H/D)$AuCl_4$
$[(PyO)_2H][AuCl_4]$	368–369	2:1	2:1
$[(PyO)_3H_2][AuCl_4]_2$	428–491	3:2 (1.5:1)	1:1
$[(PyO)H][AuCl_4]$	521–528	1:1	1:2 (0.5:1)
$[(PyO)_2D][AuCl_4]$	367–368	2:1	5:1
$[(PyO)_3D_2][AuCl_4]_2$	438–484	3:2 (1.5:1)	2:1[a]
$[(PyO)_4D_3][AuCl_4]_3$	478–497	4:3 (1.3:1)	2:1[a]
$[(PyO)D][AuCl_4]$	517–520	1:1	2:1[a]; 1:1

[a] From the 2:1 solution, three kinds of crystals were obtained case by case.

Table 2
Crystal data and details of the experiments and refinements

Base/acid	1/1	3/2	4/3
Formula	$C_5H_5DONAuCl_4$	$C_{15}H_{15}D_2O_3N_3Au_2Cl_8$	$C_{20}H_{20}D_3O_4N_4Au_3Cl_{12}$
Formula weight	435.87	966.86	1402.73
X-ray radiation	Mo Kα	Mo Kα	Mo Kα
Wavelength (Å)	0.710730	0.710730	0.710730
Crystal system	orthorhombic	monoclinic	triclinic
Space group	*Pbam*	$C2/c$	$P\bar{1}$
a (Å)	7.673(2)	16.46(2)	9.079(2)
b (Å)	8.526(2)	9.038(9)	9.142(2)
c (Å)	7.944(2)	18.65(2)	12.504(2)
α (°)			78.250(3)
β (°)		110.42(2)	85.110(4)
γ (°)			63.438(3)
Cell volume (Å^3)	519.7(2)	2600(5)	908.8(3)
Z	2	4	1
D_c (g cm^{-3})	2.786	2.471	2.564
D_m (g cm^{-3})	2.78 ± 0.02	2.45 ± 0.02	2.55 ± 0.02
μ(Mo Kα)	15.133	12.118	12.994
$F(000)$	396	1784	644
Crystal color	yellow	yellow	yellow
Crystal size (mm)	$0.09 \times 0.08 \times 0.07$	$0.12 \times 0.07 \times 0.06$	$0.08 \times 0.07 \times 0.06$
Temperature	298	298	296
θ range (°)	2.56–27.47	2.61–27.52	1.66–27.48
Index range	$-9 \leqslant h \leqslant 9$, $-10 \leqslant k \leqslant 10$, $-6 \leqslant l \leqslant 9$	$-18 \leqslant h \leqslant 20$, $-11 \leqslant k \leqslant 7$, $-22 \leqslant l \leqslant 18$	$-11 \leqslant h \leqslant 11$, $-11 \leqslant k \leqslant 11$, $-11 \leqslant l \leqslant 16$
Reflections collected	2722	5684	5316
Reflections unique	585	2593	3617
R_{int}	0.0442	0.0593	0.0302
Reflections ($I > 2\sigma(I)$)	433	1639	2422
$R_1(F)(I > 2\sigma(I))$	0.0334	0.0578	0.0423
$wR_2(F^2)$ for all reflection	0.0836	0.1563	0.0971
Number of parameters	44	156	198
Goodness-of-fit for all reflections (F^2)	0.944	1.062	0.919
Weighting scheme	$w^{-1} = (\sigma^2 F_o^2) + (0.0632p)^2 + 0.00p$, $p = (F_o^2 + 2F_c^2)/3$	$w^{-1} = (\sigma^2 F_o^2) + (0.0721p)^2 + 0.00p$, $p = (F_o^2 + 2F_c^2)/3$	$w^{-1} = (\sigma^2 F_o^2) + (0.0443p)^2 + 0.00p$, $p = (F_o^2 + 2F_c^2)/3$
Maximum shift/esd	0.000	0.000	0.001
ρ_{max} (e Å^{-3})	0.960	2.115	2.044
ρ_{min} (e Å^{-3})	−3.152	−2.077	−1.318

were set to be equal. The D and non-disordered H atoms were found from a difference Fourier map and included in the refinement with isotropic displacement parameters (U_{iso}). The H atom attached to C1 was ignored in the refinement.

The asymmetric unit of the 3/2 D-salt contained a $[(PyO)D]^+$ group having a C_2-axis passing through C6 and C9 as shown in Scheme 1 (C_2 symmetry) and a $[PyO–D–PyO]^+$ group having an inversion center (C_i symmetry).

For the latter group, the bridging D atom was fixed at the center of symmetry, and the positions of the H atoms belonging to the PyO moiety were calculated and they were included in the refinement with U_{iso}. The C_2 symmetry of the $[(PyO)D]^+$ group indicates an orientational disorder of the group. In addition, another disorder was found for the group, because the asymmetric unit of the group had two oxygen atoms (O2 and O2′ shown in Scheme 1) with different populations (0.205 and 0.295, respectively). Owing to this disorder of the $[(PyO)D]^+$ group, the N atom was divided into two sites (N2 and N2′), each overlapping C7 and C8, respectively. The position and U_{ij} of C7 were set equal to those of N2, the population of which being that of O2 (0.205). The same treatment was applied to C8 and N2′. The positions of the H atoms attached to C6 and C9 were calculated and they were included in the refinement with U_{iso}. The rest of the H atoms, as well as the D atom were omitted in the refinement.

The asymmetric unit of the 4/3 D-salt was found to include $[(PyO)D]^+$ and $[PyO–D–PyO]^+$ with a center of symmetry. The positions of H atoms belonging to the PyO moieties in the latter unit were calculated and they were included in the refinement with U_{iso}. The bridging D atom was treated in the way same as that described above. The structure of the PyO moiety of the $[(PyO)D]^+$ unit was considerably distorted and the H atoms could not be found on the Fourier maps. The

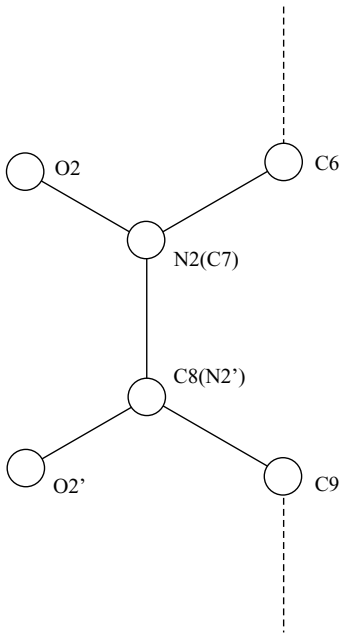

Scheme 1. Asymmetric unit of the disordered $[(PyO)D]^+$ group. The vertical broken line indicates 2-fold axis.

positions of the H atoms were calculated and they were included in the refinement with U_{iso}.

3. Results and discussion

3.1. Effect of deuteration on the crystal structures of the 1/1, 4/3 and 3/2 salts

As an isotope effect on crystal structure, we have reported a novel structural difference between the 2/1 H-salt and the 2/1 D-salt [4]. In relation to this phenomenon, we examined the possibility of such an isotope effect on the crystal structures of the 3/2, 4/3 and 1/1 salts. Their X-ray powder patterns revealed, however, that the deuteration did not change their crystal structures.

Since the quality of the single crystals of the deuterated salts was better than that of the normal ones, X-ray crystal structures of the former salts were determined in the present work.

3.2. Stability of the 2/1 H- and 2/1 D-salts

In order to check the possibility that either of the H- or D-salt is in a meta-stable phase, we carried out DTA measurements to get information on their thermal stability. DTA curves of the two salts measured in the 170–385 K region showed no exothermic heat anomaly corresponding to a monotropic transition of a meta-stable phase. We also examined X-ray powder diffraction patterns measured at room temperature for melt-grown crystals of the H- and D-salts or the crystals annealed at ca. 350 K. The diffraction patterns of the melt-grown or the annealed H- and D-salts were identical to those of the corresponding compounds obtained by crystallization from solutions. These results of the DTA and X-ray experiments strongly suggest that both of the H- and D-salts are in stable phases.

3.3. Crystal structures of the 1/1, 4/3 and 3/2 D-salts at room temperature

The 1/1 D-salt contains only $[(PyO)D]^+$, while there exist both $[(PyO)D]^+$ and $[PyO–D–PyO]^+$ in the crystals of the 4/3 D-salt and the 3/2 D-salt. The molar ratio of the monomeric:dimeric adducts in the crystal is 1:1 in the 3/2 salt and 2:1 in the 4/3 salt. These results are consistent with the chemical compositions of the salts.

The geometries of the monomeric and dimeric adducts are listed in Table 3.

The dimeric adducts in the 4/3 D-salt and the 3/2 D-salt are centrosymmetric (C_i symmetry), while the dimeric adduct in the 2/1 D-salt is non-symmetric (C_1 symmetry) [4]. The O···O distance in the dimeric adduct in the 4/3 D-salt (2.44(1) Å) and that in the 3/2 D-salt (2.41(2) Å) are typical for a symmetric O···H···O

Table 3
Geometries of the dimeric adduct ($[PyO–(H/D)–PyO]^+$) and the monomeric one ($[(PyO)D]^+$)

	$[PyO–(H/D)–PyO]^+$				$[(PyO)D]^+$		
Compounds	2/1 H-salt	2/1 D-salt[a]	3/2 D-salt[b]	4/3 D-salt[b]	3/2 D-salt[c]	4/3 D-salt	1/1 D-salt[c]
N–O distance (Å)	1.362(8)	1.354(9), 1.314(9)	1.32(1)	1.35(1)	–[d]	1.36(1)	1.36(2)
O···O distance (Å)	2.41(1)	2.43(1)	2.41(2)	2.44(1)	–	–	–
N–O···O bond angle (°)	108.24	106.4(5), 116.6(6)	109(1)	106.9(6)	–	–	–
N–O···O–N torsion angle (°)	180	142.7(8)	180	180	–	–	–
References	[3]	[4]	This work	This work	This work	This work	This work

[a] The crystal contains one non-symmetric $[PyO-D-PyO]^+$ in the asymmetric unit.
[b] The crystal contains centrosymmetric $[PyO–D–PyO]^+$.
[c] The monomeric adduct in the crystal is disordered (see text).
[d] The N–O length was not reliable owing to the orientational disorder (see text).

hydrogen bond, being comparable with the corresponding values found, for example, in the 2/1 D-salt [4], 2/1 H-salt [3], $[(PyO)_2H]ClO_4$ [5] and $[(2,6\text{-}(CH_3)_2PyO)_2H]$- $[AuCl_4]$ [7]. The N–O bond lengths of the PyO moiety in $[(PyO)D]^+$ found for the 1/1 and 4/3 D-salts are longer than that of the neutral PyO molecule (1.30 Å) [8]. This observation indicates the hydrogenation of the oxygen atom and/or its participation in the formation of a hydrogen bond.

The crystal of the 1/1 D-salt is built by alternating stacking of the layers of $[(PyO)D]^+$ and $[AuCl_4]^-$ (Fig. 1). $[(PyO)D]^+$ has C_{2h} symmetry to result in its orientational disorder, which can be seen in Fig. 1. It should be mentioned that the $[(PyO)D]^+$ groups in the 1/1 salt form a layer structure as shown in Fig. 2. The short intermolecular O···N contact (3.16(2) Å) suggests a certain interaction between the adjacent $[(PyO)D]^+$ groups. There exists a short intermolecular Cl···Cl contact of 3.391(6) Å, which seems to contribute to connect the layers of $[AuCl_4]^-$. The short intermolecular O1···Cl1 length (3.16(2) Å) indicates possibility of N–O–D···Cl hydrogen bonds.

The crystal structures of the 4/3 D-salt and 3/2 D-salt are depicted in Figs. 3 and 4, respectively. Several aggregation motifs of $[AuCl_4]^-$ ions are found in the 1/1, 4/3, 3/2 and 2/1 D-salts. In the crystal of the 1/1 D-salt, one can recognize a planar sheet structure formed by $[AuCl_4]^-$ ions (Fig. 1). If one takes account of a relatively long Au···Cl contact of 3.509 (3) Å in the sheet structure, the formal coordination number of the Au atom is six and the layer structure is formed by vertex-sharing of the $AuCl_6$ octahedrons. A similar layer structure has been reported for $[EtC(OEt)NH_2][AuCl_4]$ [9].

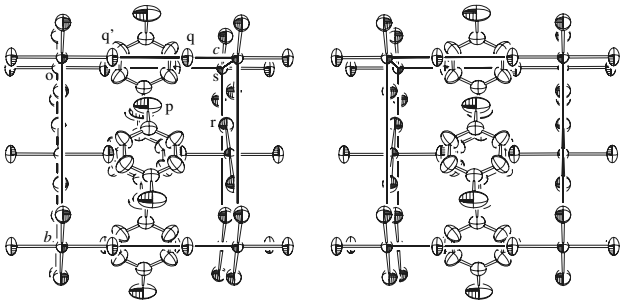

Fig. 1. Crystal structure of the 1/1 D-salt (stereo). Short contacts are Cl1(*q*)···Cl1′(*q*′) (3.391(6) Å), O1···Cl1 (3.16(2) Å) and Cl2···Au (3.509(3) Å). Symbols p, q, q′, r and s denote O1, Cl1, Cl1′, Cl2 and Au, respectively. Symmetry codes: p : $(-x+1.5, y-0.5, -z+1)$; q : $(-x+1, -y+1, -z+1)$; q′ : $(x+1, y-1, z)$; r : $(-x+0.5, y-0.5, -z+1)$ and s : $(x, y-1, z+1)$.

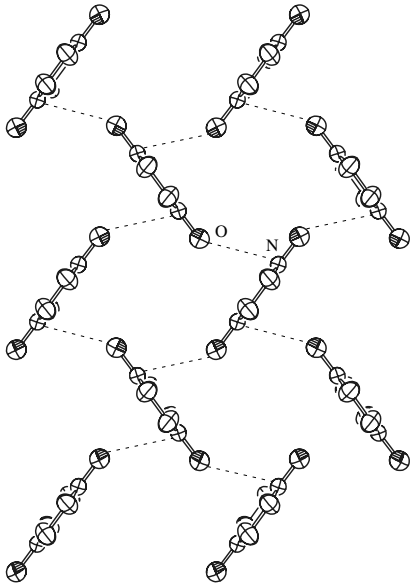

Fig. 2. Layer structure formed by disordered $[(PyO)D]^+$ units in the 1/1 D-salt. The broken lines indicate short O···N contacts of 3.16(2) Å.

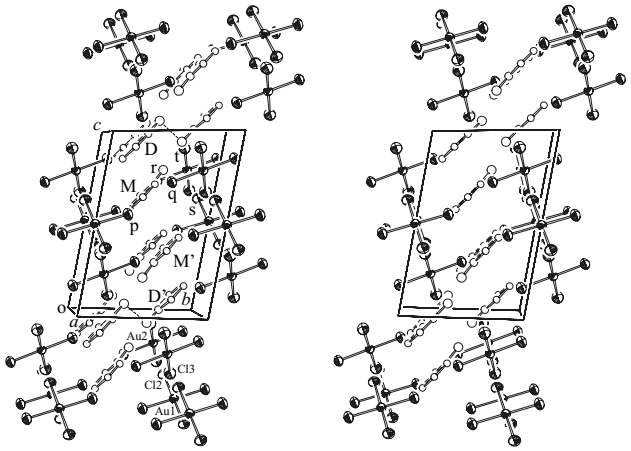

Fig. 3. Crystal structure of the 4/3 D-salt (stereo). D and M indicate $[PyO–D–PyO]^+$ and $[(PyO)D]^+$, respectively. D and D′, M and M′ as well, are related by an inversion center. Symbols p, q, r, s and t are Cl1, Cl4, O1, Cl2 and Cl5, respectively. Symmetry codes: p : $(-x+2, -y+1, -z+1)$; q : (x, y, z); r : (x, y, z); s : $(x-1, y, z)$ and t : $(x-1, y, z)$.

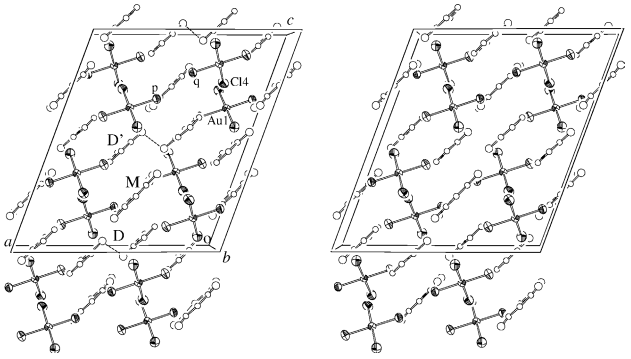

Fig. 4. Crystal structure of the 3/2 D-salt (stereo). D and M denote $[PyO\text{-}D\text{-}PyO]^+$ and $[(PyO)D]^+$ units. Symbols p and q are Cl1 and Cl1′. Symmetry codes: p : $(x+0.5, -y+1.5, z+0.5)$ and q : $(-x+0.5, -y+1.5, -z+1)$.

A ribbon-like aggregation motif of $[AuCl_4]^-$ ions that was found in the 4/3 salt (Fig. 3) can be regarded as a part of the sheet structure observed in the 1/1 D-salt. The Au1···Cl3 and Au2···Cl2 contacts are 3.525(3) and 3.590(3) Å, respectively, being comparable with the Au···Cl contacts found for the chain structures of $[AuCl_4]^-$ ions in [EMIM][$AuCl_4$] and [BMIM][$AuCl_4$] (3.356 and 3.452 Å, respectively) [10]. In the ribbon structure of the 4/3 D-salt, there are six and five coordinations of the Au atom, and vertexes of $AuCl_6$ octahedrons and $AuCl_5$ distorted square pyramids are shared to result in the ribbon.

The crystals of the 3/2 and 2/1 D-salts consist of another type of ribbon structure, each of which can be also regarded formally as a part of the layer structure of the 1/1 salt. The ribbon structure of the 3/2 D-salt has an Au1···Cl4 contact of 3.559(5) Å (Fig. 4). The Au···Cl contact in the 2/1 D-salt amounts to 3.983(2) Å, being comparable to that found for a chain structure of $AuCl_4^-$ ions in $[(H_5O_2)_2(12\text{-crown-}4)_2][AuCl_4]_2$ (3.845 Å) [11].

In the crystal of the 4/3 D-salt, the ribbons are packed along the crystallographic *a*-axis as shown in Fig. 3. A short Cl···Cl contact (3.612(4) Å of Cl1···Cl4) is observed between the ribbons. A columnar cavity surrounded by four ribbons of $[AuCl_4]_n^-$ is filled by a $[(PyO)D]^+$ (M), a PyO moiety of a $[PyO–D–PyO]^+$ (D) and their inversion-related ones (M′ and D′) as shown in Fig. 3. It is interesting to note that one of the two PyO moieties of a $[PyO–D–PyO]^+$ unit is accommodated in a columnar cavity, while the other one in an adjacent cavity. There are two short intermolecular contacts between the chlorine atoms in the ribbon and an oxygen atom in the PyO group: Cl2···O1 (3.31(1) Å) and Cl5···O1 (3.15(1) Å). The planes of the PyO moieties stack parallel to each other (see Fig. 3).

The crystal structure of the 3/2 D-salt is similar to that of the 4/3 D-salt as can be seen by comparing Figs. 3 and 4. The cavity of the 3/2 D-salt is filled by D, D′ (related to D by 2-fold symmetry axis) and M. The number of the PyO moieties accommodated in a cavity of the 3/2 D-salt is smaller than that of the 4/3 D-salt as a result of the decrease in the width of the ribbon structure. D and M stack almost parallel to each other and M, which is flanked by D and D′, exhibits the disorder mentioned above. There is a short Cl···Cl contact between adjacent ribbons (Cl1···Cl1′ of 3.575(9) Å).

3.4. Characterization of the 1/1, 4/3 and 3/2 D-salts by ^{35}Cl NQR and thermal analysis

For the 4/3 D-salt, we observed the five NQR frequencies (ν) of 29.164, 28.727, 28.625, 28.272 and 27.618 MHz at 77 K. There must be one missing line, since there exist six crystallographically non-equivalent chlorine atoms in the crystal. Previously, we have improperly assigned these frequencies to the 1/1 D-salt [4].

The temperature dependence of the ^{35}Cl NQR frequencies of the 4/3 D-salt is shown in Fig. 5. In the temperature range investigated (77–230 K), ν versus T curves seem to have no anomaly corresponding to a phase transition. The thermal analyses (DTA and DSC) carried out in 150–300 K region also could not detect any anomaly due to a phase transition.

For the 3/2 D-salt, a phase transition was detected at 199 K by the thermal analyses with increasing temperature ($\Delta H = 1.3$ kJ mol^{-1}). For the 3/2 H-salt, it was located at 197 K. The transitions exhibited very slight hysteresis, indicating the first-order nature of the transition. It was suggested from the temperature dependence of the ^{1}H NMR spin–lattice relaxation time of the 3/2 D-salt that at least one of the cationic molecules in the unit cell performs a fast reorientational motion above the phase-transition point. This mobility of the cation shows that the disordered structure found in the crystal structure determination is likely to be a dynamic one. So far, we have found four very broad ^{35}Cl NQR lines at 77 K for the 3/2 D-salt. The crystal structure of the low-temperature phase and details of the NMR/NQR results will be reported in a forthcoming paper.

DTA/DSC curves of the 1/1 D-salt measured in 150–300 K region exhibited a very small thermal anomaly at 273 K (T_{c1}) indicating a phase transition ($\Delta H_{c1} = 0.4$ kJ mol^{-1}). Hysteresis (super-cooling of ca. 30 K) of the transition suggested a first-order nature of the transition. It is very interesting that we could not detect any anomaly in the DTA/DSC curves for the 1/1 H-salt in

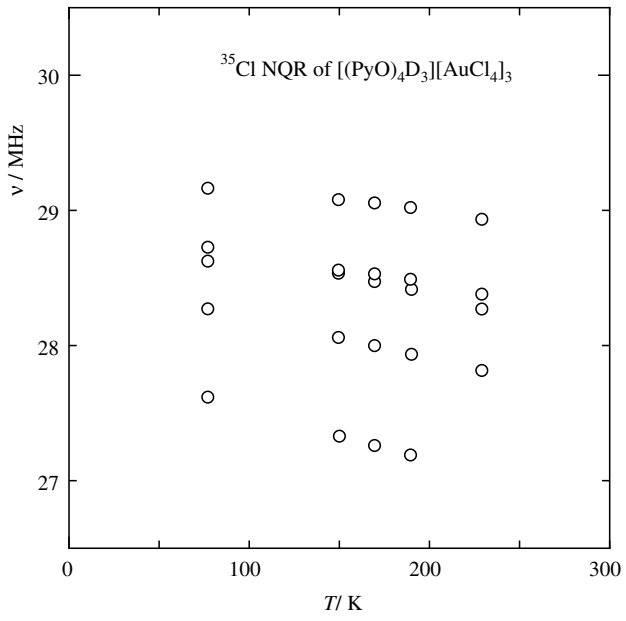

Fig. 5. Temperature dependences of ^{35}Cl NQR frequencies of the 4/3 D-salt.

the temperature range 150–300 K. Such a kind of isotope effect has been reported previously [12,13].

Two ^{35}Cl NQR lines (high- and low-frequency lines) were observed for the 1/1 D-salt at room temperature. When the sample temperature was decreased, the high-frequency line was observed to split drastically into four lines below 70 K (T_{c2}). Thus, from the ^{35}Cl NQR measurements, we have found another phase transition that is more drastic than that at T_{c1}. Moreover, it is interesting that the low-frequency line disappeared before reaching to T_{c2}.

In the region of $T > T_{c2}$, the frequencies (ν) of the two lines decreased monotonously with increasing temperature. No anomaly was detected in the ν versus T curves at T_{c1} within the accuracy of the present frequency measurements. This feature, together with the small value of ΔH_{c1}, indicates quite a subtle structural change at T_{c1}. The presence of the two ^{35}Cl NQR lines is consistent with the crystal structure determined at room temperature having two crystallographically non-equivalent chlorines.

The temperature dependence of the NQR spin–lattice relaxation time T_1 showed an anomalous decrease with decreasing temperature in the region of $T > T_{c2}$. This result suggests a dynamical disorder of the $[(PyO)D]^+$ cations at $T > T_{c2}$, since the ^{35}Cl T_1 behavior can be explained by the relaxation mechanism due to a fluctuation of the electric field gradient caused by reorientational motions between disordered orientations of nearby $[(PyO)D]^+$ cations. The presence of such a motion of the $[(PyO)D]^+$ cation was strongly suggested by the ^{1}H NMR spin–lattice relaxation measurements as well. The details of NMR/NQR measurements will be reported elsewhere.

These conclusions from the NQR and NMR investigations are consistent with the disorder model of the $[(PyO)D]^+$ group proposed in the crystal structure determination. An ordering of the $[(PyO)D]^+$ cation is likely to take place below T_{c2} and hence the transition at T_{c2} seems to be of an order–disorder type.

3.5. Origins of compositional variety and isotope effect on preparation

The present structural analyses revealed that both of the monomeric and dimeric adducts of PyO with proton can be formed in the crystal. In addition, several types of aggregation of $AuCl_4$ units are possible. These structural possibilities found for the cation and anion seem to be a reason why so many salts having different base-to-acid ratio could be formed.

There was a tendency that the base-to-acid molar ratio of the crystal was lower than that of the mother solution in the heavy hydrogen system, while it was found vice versa in the normal hydrogen system (see Table 1). This observation indicates that equilibrium processes in $PyO + (H/D)AuCl_4 + (H/D)_2O$ systems are dependent on the isotopic composition. Similar isotope effects on chemical equilibrium are known, for example, in the enol-enethiol tautomerism of β-thioxoketones [14] and in an acid–base equilibrium [15].

4. Supplementary material

Crystallographic data for the 1/1, 4/3 and 3/2 D-salts have been deposited with the Cambridge Crystallographic Data Centre, CCDC Nos. 219958, 219959 and 219960, respectively. Copies of the information may be obtained free of charge from The Director, CCDC, 12 Union Road, Cambridge, CB2 1EZ, UK (fax: +44-1223-336033; e-mail: deposit@ccdc.cam.ac.uk or www: http://www.ccdc.cam.ac.uk).

Acknowledgements

This work was partially supported by a Grant from the Ministry of Education, Culture, Sports, Science and Technology to promote advanced scientific research.

References

[1] P.G. Tsoucaris, Acta Crystallogr. 14 (1961) 914.
[2] O. Moers, K. Wijaya, T. Hamann, A. Blaschette, P.G. Jones, Z. Naturforsch. 56b (2001) 1052.
[3] M.S. Hussain, E.O. Schlemper, J. Chem. Soc., Dalton Trans. (1982) 751.
[4] T. Asaji, F. Tajima, M. Hashimoto, Polyhedron 21 (2002) 2207.
[5] J. Wasicki, M. Jaskolski, Z. Pajak, M. Szafran, Z. Dega-Szafran, M.A. Adams, S.F. Parker, J. Mol. Struct. 476 (1999) 81.
[6] G.M. Sheldrick, SHELXL-97 Program for the Solution and the Refinement of Crystal Structures, University of Göttingen, Germany, 1997.
[7] M.S. Hussain, Polyhedron 15 (1996) 645.
[8] F.H. Allen, O. Kennard, D.G. Watson, L. Brammer, A.G. Orpen, R. Taylor, J. Chem. Soc., Perkin Trans. II (1987) S1.
[9] R.A. Potts, D.L. Gaj, W.F. Schneider, N.S. Dean, J.W. Kampf, J.P. Oliver, Polyhedron 10 (1991) 1631.
[10] M. Hasan, I.V. Kozhevnikov, M. Rafiq, H. Siddiqui, A. Steiner, N. Winterton, Inorg. Chem. 38 (1999) 5637.
[11] M. Calleja, K. Johnson, W.J. Belcher, J.W. Steed, Inorg. Chem. 40 (2001) 4978.
[12] T. Matsuo, A. Inaba, O. Yamamuro, N. Onoda-Yamamuro, J. Phys.: Condens. Matter 12 (2000) 8595.
[13] T. Gustafsson, M. Ichikawa, I. Olovsson, Solid State Commun. 115 (2000) 473.
[14] B. Andresen, F. Duus, S. Bolvig, P.E. Hansen, J. Mol. Struct. 552 (2000) 45.
[15] S.L.R. Ellison, M.J.T. Robinson, J. Chem. Soc., Chem. Commun. (1983) 745.